Vrije Universiteit Brussel

Faculty of Engineering Sciences
Department of Electronics and Informatics

Cloud properties retrieval for climate studies from geostationary orbit

PhD. thesis submitted in partial fulfillment of the requirements for the degree of Doctor in Engineering Sciences

Alessandro Ipe

Promotors:	Prof. S. Dewitte (RMIB)
	Prof. J. Cornelis
Examining committee:	Prof. L. Van Biesen
	Prof. R. Pintelon
	Prof. R. Deklerck
	Prof. H. Sahli
	Dr. R.P. Allan (University of Reading – UK)
	Dr. R. Roebeling (KNMI – Nederland)

June 30 2011

Print: Silhouet, Maldegem

2011 Uitgeverij VUBPRESS Brussels University Press
VUBPRESS is an imprint of ASP nv (Academic and Scientific Publishers nv)
Ravensteingalerij 28
B-1000 Brussels
Tel. +32 (0)2 289 26 50
Fax +32 (0)2 289 26 59
E-mail: info@vubpress.be
www.vubpress.be

ISBN 978 90 5487 927 5
NUR 973
Legal deposit D/2011/11.161/090

Abstract

The climate system of the Earth is fundamentally determined by the Earth radiation budget (ERB) and its regional distribution. The Earth receives energy from the Sun and radiates energy back to space. In a stable climate system, both incoming and outgoing energy flows are balanced. An external perturbation, e.g. an increase of greenhouse gases or a variation of aerosols concentrations, results in a radiative forcing which is driving a change of the climate system. The final effect of this radiative forcing is influenced by various feedbacks mechanisms.

As we mentioned, the ERB at the top of the atmosphere (TOA) consists of the incoming solar energy and outgoing radiation. While the first component of this budget is known with high accuracy, the exact amount of energy leaving the atmosphere into space is still subject to speculation. This has driven the launch of the Geostationary Earth Radiation Budget (GERB) experiment whose goal is to provide TOA reflected solar and emitted thermal fluxes. This project aims to resolve the diurnal cycle of the outgoing fluxes by providing measurements at high temporal sampling, and combining these to the high spatial resolution of the Meteosat Second Generation (MSG) satellite data. However, these quantities can not be directly measured from narrow field–of–view (FOV) broadband radiometers. Therefore, they need to be estimated from models linking directional radiance measurements to such hemispheric fluxes. This angular modeling plays a central part in the GERB processing. Due to the fixed scene geometry implied by the geostationary orbit, these models must priorly be built from low Earth orbit (LEO) radiometers. These instruments allow to measure the radiance field of several specific scenes in several geometries and thus to derive their associated fluxes. These specific scenes represent broad classes of surface types and cloudy conditions with radiance fields that have a similar angular behaviour for all the scene class members. Thus, to apply such models to GERB measurements, each footprint must be characterized in terms of the features used to stratify these models, i.e. cloud properties (cloud mask, cloud optical depth and cloud thermodynamic phase) and surface geotypes.

In this work, we propose to address this issue. First, we briefly introduce the concepts of physics behind specific cloud parameters needed in such scene identification. Then, we provide an extensive review of the literature about the techniques developed and commonly used to estimate these parameters from satellite–borne sensors. We present the complete design of the method currently implemented in the GERB Edition 1 processing starting from the development and testing of the prototype algorithm on the previous generation satellite data (Meteosat–7) up to its adaptation and validation to the current GERB and Spinning Enhanced Visible and InfraRed Imager (SEVIRI) instruments. We pursue with a proposal for a nighttime cloud detection algorithm which will provide valuable information once included in the end–user products for the next Edition processing. Finally, we conclude this work by providing a critical review of the Edition 1 scene identification and suggesting various improvements of its current weaknesses which will benefit future GERB product editions.

Il est généralement convenu de commencer les remerciements d'une thèse par le ou les promoteurs ainsi que le département de l'université d'accueil du doctorant… Néanmoins, il me semble plus juste de suivre un ordre chronologique qui permet, du moins je le pense, de rendre hommage à tous ceux qui ont eu une importance capitale dans mon existence et mon épanouissement, tant personnel que professionnel.

Je tiens tout d'abord à remercier mes parents pour avoir fait ce qu'ils ont fait il y a maintenant plus de 35 ans mais surtout ma mère pour avoir réussi à me supporter et de continuer à le faire toutes ces longues années[*]. Je dois aussi reconnaître que, si les aptitudes pour les mathématiques et les sciences ont une origine génétique, celles-ci viennent sans aucun doute de mon père. Je tiens aussi à exprimer ma tendre affection à tous les membres de ma famille, sans oublier ceux qui ne sont plus là…

Mon premier chat, Zouki, doit aussi être reconnu à sa juste valeur comme étant celui qui m'a appris (à mes dépends) à respecter les animaux alors que mon jeune âge pouvait peut-être m'excuser de certains actes peu sages. Par la suite, Mickey[†] et Félix ne m'ont apporté que des satisfactions et des moments de réconfort, notamment lors des périodes d'examen. Je dois aussi rendre hommage à un survivant, Bubule le poisson rouge, qui était en fait plutôt orange et qui a échappé à de nombreuses reprises à des parties de pêches improvisées par mes deux derniers chats perchés au bord de son aquarium…

Je tiens à nouveau à remercier ma mère pour avoir souscrit à la télédistribution dès mon plus jeune âge me permettant ainsi d'acquérir une culture audiovisuelle qui peut faire cruellement défaut à certaines personnes lors de conversations empreintes de moments de nostalgie télévisuelle[‡]. Merci à Casimir de « l'Ile aux Enfants », Nounours de « Bonne Nuit les Petits », Pollux[§] du « Manège Enchanté », Les Cités d'Or, Albator, Goldorak, Ulysse 31, Cobra, Ken le Survivant, Starsky & Hutch (Paul Glaser & David Soul), Magnum (Tom Selleck), Rick « ça marche pour moi » Hunter (Fred Dryer), Sergio Leone, Clint Eastwood, Arnold Schwarzenegger, et plus récemment Hugh Hefner[¶], Bar Refaeli, Scarlett Johansson (sans commentaire)… j'en oublie certainement.

Je me remémore avec nostalgie les deux années passées à l'Ecole du Bois de la Cambre n°7 à Ixelles où j'ai découvert les jeux de rôles, les batailles rangées pour garder en notre possession le bac à sable situé sur le domaine de l'Ecole n°8 adjacente et le « jeu » récréatif Papy Boington[‖]…

Je ne m'éterniserai pas sur la période secondaire à l'Ecole Européenne d'Uccle, si ce n'est pour rendre hommage à tous mes professeurs pour la qualité de leurs cours qui m'a permis d'être préparé aux enseignements *volumineux* de la Faculté des Sciences Appliquées de l'Université Libre de Bruxelles (ULB), bien que je ne sache toujours pas pourquoi il a fallu apprendre certains concepts…

Je remercie aussi toutes les « B#tes de Physique » (dixit Xavier P.) pour les nombreux laboratoires inoubliables, notamment quand nous avons dû mesurer le coefficient de viscosité d'un mélange d'eau et de bave du même Xavier ou que nous racontions des blagues d'un humour qui pourrait être considéré comme *douteux* pour les non–initiés.

A nouveau, le rôle prépondérant de ma mère doit être reconnu à sa juste valeur pour m'avoir, en toute circonstance, soutenu, encouragé, aidé lors de mes études secondaires et supérieures. Je la remercie aussi pour sa patience et son support total lorsque j'ai décidé de suivre le cursus du DEA en Physique Théorique à la Faculté de Sciences de l'ULB *pour le fun*…

[*] Comme je lui dis souvent : « *Dieu te le rendra.* », ce à quoi elle me répond : « *Il me l'a déjà rendu…* »

[†] Ce n'est pas le meilleur nom pour un félin, je le conçois…

[‡] Ces personnes se reconnaîtront…

[§] même si j'ai compris assez vite qu'il s'agissait d'un balai à franges…

[¶] pour la qualité des articles de son magazine…

[‖] Xavier sait de quoi je parle.

Je n'oublie pas mes amis (ils se reconnaîtront) connus ou retrouvés à l'université, ceux qui ont d'abord été des collègues ou des adversaires sportifs au badminton (cocktailH3 et 3MT), ainsi qu'une soirée d'anthologie au bar d'un hôtel de Miami Beach où nous avons tenté de goûter tous les cocktails à la carte…

Je tiens à exprimer ma gratitude à mes promoteurs, Steven Dewitte pour m'avoir engagé à l'Institut Royal Météorologique (IRM) et Jan Cornelis pour m'avoir permis d'affilier cette thèse à la Vrije Universiteit Brussel, pour leurs conseils, leur infinie patience et la totale autonomie dont j'ai bénéficié. Je suis également reconnaissant aux docteurs Didier Caprion et Carole Dupuy pour leurs commentaires sur la première partie de ce manuscript, ainsi qu'à Annette Hautecoeur pour la relecture de ces remerciements[**] et tout ce qu'elle (a) fait pour l'équipe GERB. Je tiens également à remercier le docteur Gilles Van Assche pour ses conseils (et son fichier–modèle) en LaTeX sans qui l'aspect final de ce manuscript n'aurait pas été aussi abouti, voire, si je peux me permettre sans vouloir faire de jeu de mots graveleux, « léché »… Je remercie aussi mes (ex–)collègues proches (et plus…) de l'IRM pour m'avoir supporté (au propre comme au figuré) durant toutes ces années, pour les diverses activités extra–professionnelles que nous avons eu l'occasion de faire et qui, j'espère, se poursuivront. Enfin, peut-être le plus important à mes yeux, je remercie des collègues de l'IRM de m'avoir permis, par le passé, d'expérimenter un vrai travail collaboratif, voire symbiotique, sur le projet GERB, même si ces temps sont quelque peu révolus dorénavant…

Finalement, la résistance[††] de mes différents claviers doit être soulignée, en particulier, lors de moments d'exaspération lorsque je tentais de résoudre un problème en supposant que sa résolution dépendait de la force exercée sur la touche « Enter »… ainsi que durant les parties endiablées en *deathmatch* avec certains (ex–)collègues de Doom© 1/2/3, Quake© 1/2/3/4, Half-Life© et Warmux… toujours sous Linux© !

Sponsorisé et/ou financé par:

[**] et la traque des dernières fautes d'orthographe
[††] à des stress mécaniques

A mon coiffeur…

Contents

Chapter 1

Introduction

1.1 Once upon a time...

THE Royal Meteorological Institute of Belgium (RMIB) has been active since the end of the fifties in the study of the radiation balance of the Earth–atmosphere coupled system. This so–called Earth radiation budget (ERB) is simply the difference between the incoming and the outgoing energies of such system as illustrated in figure 1.1. While the incoming source is almost exclusively the incident solar radiation in the shortwave region (0.3 to 4 μm) of the electromagnetic spectrum, the outgoing term is coming from two distinct phenomena: a reflection of a fraction of the solar energy and a thermal emission of an associated imperfect black body*. Both terms are modulated according to the surface geotype and conditions as well as the state of the atmosphere including the presence of clouds and dust.

At a regional scale, the variation of this difference or net energy is the motor of the atmospheric circulation. It is commonly assumed that this balance should be close to zero† over the whole globe. However, even nowadays, space metrology can still not guarantee a sufficient accuracy on these three components to verify the closure of this budget equation in the assumption of an equilibrium climate. It is needless to say that solving this issue would represent a major breakthrough in the assessment and quantification as well as a definitive proof‡ of the *global climate warning* phenomenon which is observed since the end of the last century.

The incoming term of the budget has been studied for more than twenty years at RMIB with spaceborne broadband radiometers (BBRs) [39–43, 50, 51, 106] measuring the solar *irradiance*, i.e. the solar flux density $[\mathrm{W \cdot m^{-2}}]$, and monitoring its temporal variation (the so–called solar sunspot cycles which last about 11 years [187]).

Long–term and continent–scale measurements of the ERB have been done using wide field–of–view (FOV) (with a diameter of about 1000 km) non–scanner instruments on National

* The concept of *emissivity* describes this deviation from the ideal black body radiance modeled by the *Planck* response function.

† Any discrepancy from this null value would result in a net heating (positive) or cooling (negative) of the Earth–atmosphere system with time.

‡ The increase of surface temperature time–series over the last 30 years together with the higher occurrence of extreme weather events were the first indication of this warming.

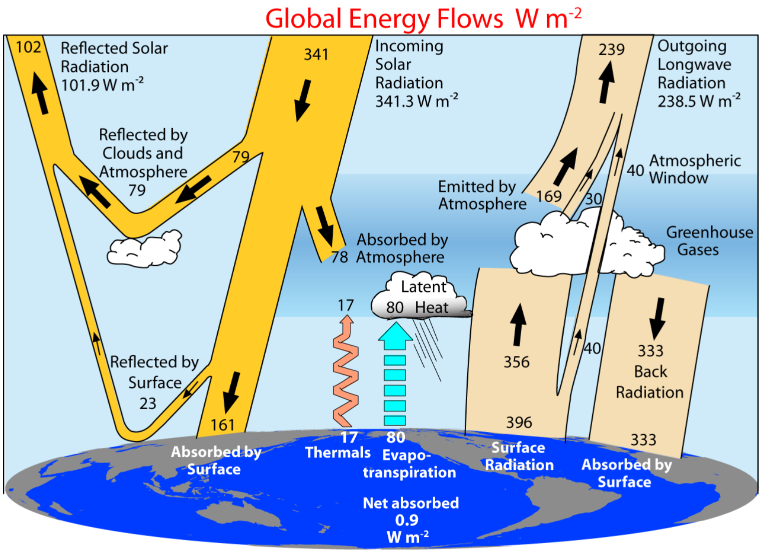

Figure 1.1 – *The Earth's annual global mean energy budget in* $\mathrm{W \cdot m^{-2}}$. *From [167].*

Ocean and Air Administration (NOAA) satellites in the sixties and seventies. Nevertheless, most scientific studies need regional–scale data which is only accessible through higher spatial resolution narrow FOV measurements. Thus, medium and high resolution scanning radiometers with narrow FOV were also placed on board of TIROS and Nimbus low Earth orbit (LEO) platforms. They consist of broad– as well as narrowband spectral devices. However, for narrow FOVs, the directional measurement or *radiance* $[\mathrm{W \cdot m^{-2} \cdot sr^{-1}}]$ has to be converted into a hemispheric quantity, i.e. the flux (density), which is the integration of the energy leaving the top of the atmosphere (TOA) in all the directions.

The Earth Radiation Budget Experiment (ERBE) mission which was launched in 1984 played a pioneering role in such conversion. Its science goal was to measure both outgoing components at a monthly accuracy of 15 $\mathrm{W \cdot m^{-2}}$ over $2.5° \times 2.5°$ regions. ERBE's radiative fluxes were estimated on a monthly basis from several measurements of a given target with a radiance–to–flux conversion scheme. This was performed, for the first time, using a set of 12 angular dependency models (ADMs) [154] to fulfill ERBE's science goal. These models were statistically built to contain information about the anisotropy of the radiance field above typical scenes (4 surface geotypes and 4 fractions of cloudiness). But the poor temporal sampling of the measurements over a given region prevented to use them on less than a monthly mean basis. Nevertheless, the contribution of these results was invaluable and opened new perspectives to climate research. Analysis of the conceptual limitations of ERBE led to the advent of new LEO instruments which improved the temporal and spatial samplings as well as the accuracy of the measurements: the Scanner for Radiation Budget (ScaRaB) [54, 79] on board of Meteor–3/7 and RESURS and more recently the Clouds and the Earth's Radiant Energy System (CERES) [184] on board of the Tropical Rainfall Measuring Mission (TRMM) [89], Earth Observing System (EOS) Terra and Aqua satellites. CERES experiment aims to decrease the uncertainty on monthly regional fluxes to 5 $\mathrm{W \cdot m^{-2}}$ while providing instantaneous flux measurements at about 10 $\mathrm{W \cdot m^{-2}}$ [183].

However, it is only since the launch of the first Geostationary Earth Radiation Budget (GERB) instrument [66] in 2002 that the outgoing component of the ERB is routinely measured several times per day over the same scene while polar orbiting instruments are only able to sample the diurnal cycle twice a day. This instrument is part of the GERB mission [67] which consists in putting on board of the four European Organisation for the Exploitation of Meteorological Satellites (EUMETSAT) Meteosat Second Generation (MSG) satellites* [148] a broadband radiometer as co–passenger to their main payload, i.e. the Spinning Enhanced Visible and InfraRed Imager (SEVIRI). The latter is a multispectral narrowband imager delivering observations every 15 minutes at a spatial resolution of about 3 km at nadir in 11 spectral channels.

The aim of this mission is to take benefit from the geostationary orbit of these platforms to accurately estimate the TOA solar reflected and thermal emitted broadband fluxes from their associated directional measured radiances at high spatial resolution (about 45 km at nadir) and unprecedented temporal sampling (a little more than 15 minutes). To achieve such a goal, it was decided to split this task into two sequential parts [67]:

1. the level 1.5 processing consisting in converting the instrument counts into geolocated† filtered radiances in $W \cdot m^{-2} \cdot sr^{-1}$,

2. the level 2 processing consisting in estimating the unfiltered fluxes in $W \cdot m^{-2}$ from these radiances.

While the Rutherford Appleton Laboratory (RAL) is the prime contractor of the whole processing, the expertise of RMIB in the ERB field was recognized by sub–contracting to RMIB the development of the level 2 processing which is also called the RMIB GERB Processing (RGP). Another aspect of this mission is the near–realtime data dissemination which constraints that level 2 TOA fluxes should be delivered to the science community not more than 3 hours after the measurements. This is a major difference as well as a challenge compared to the CERES project which is only delivering offline products.

1.2 Your mission, should you choose to accept it. . .

As mentioned previously, the GERB team at RMIB is responsible for the development and the operational implementation of the level 2 processing. This is achieved through the synergistic use of SEVIRI to fully characterize each GERB footprint or pixel in terms of multispectral scene analysis at a spatial resolution of 3 km (at nadir) [52]. Such scene analysis allows to perform the unfiltering of the GERB measured radiances, the unfiltered broadband GERB–like radiance estimation using only SEVIRI measurements, the scene identification to adequately select the ADM for the radiance–to–flux conversion and the resolution enhancement. The specific design of this processing allows to deliver several products from the close–to–the–instrument measurements, i.e. convoluted with its point spread function (PSF), up to the higher 10 km resolution and at SEVIRI acquisition times, without any influence of the GERB PSF.

* starting with Meteosat–8

† which means knowing the geographical coordinates on Earth surface of each footprint

However, one has to be aware that the TOA broadband (BB) radiances field can change drastically depending on the spectral and anisotropic characteristics of the surface (ocean or land), the cloud properties and the presence of aerosols. This results in large variations of the flux according to the observed scene within the footprint. Therefore, the radiance–to–flux conversion scheme must use a typical ADM adapted to each scene. Building such ADMs is not possible from the geostationary orbit using solely measured radiances due to the fact that specific areas in the FOV are always observed with the same scene geometries. Indeed, this would introduce a systematic bias in these models. In contrast, LEO precessing BBRs coupled with high spatial resolution multispectral imagers can overcome this limitation*. Indeed, this configuration guarantees that each area of the Earth gives BB radiance measurements for several scene geometries.

While the CERES instruments represent the state–of–art of LEO BBRs, only ADMs derived from CERES measurements on board of the TRMM satellite meet the precessing constraint. Together with the Visible and InfraRed Spectrometer (VIRS) imager, a set of about 600 shortwave and 2000 longwave ADMs were built according to a much more detailed description of the atmospheric and surface conditions [98, 99] than for ERBE.

In this scope, I chose to accept the mission to develop the scene identification of the RGP which has to be compatible with the CERES TRMM shortwave ADMs stratification. As stated above, this step is only needed to select the best suited ADM according to the scene within each GERB pixel. Since the CERES TRMM shortwave ADMs [98, 99] are classified according to the surface geotype, cloud fraction, cloud optical thickness and thermodynamic phase, this scene identification should at least retrieve those four features.

1.3 Plan of this thesis

The work presented in this thesis is limited to the development and validation of what was considered to be the best–suited scene identification scheme for the Edition 1 of the RGP. It follows a two step approach:

1. prior to the launch of Meteosat–8, the first satellite of the MSG series, the development and validation of a near–realtime prototypal scene identification using the operational data stream of the Meteosat–7 imager,
2. the adaptation and validation of this prototyping software to the enhanced capabilities of Meteosat–8 once it became the prime imager.

Therefore, we propose the following structure for this manuscript which is naturally inspired from the published, accepted and submitted papers in the literature describing the work of this thesis. It is worth pointing out that to avoid time–consuming paraphrasing of these papers, we simply transcribed them in separate chapters.

We first briefly introduce in chapter 2 the concepts and definitions in atmospheric physics which will be mentioned throughout this manuscript. The physics basis lying behind the methods commonly used in passive atmospheric remote sensing will also be recalled.

* A precessing orbit allows to sample each region of the globe at different local times over a couple of days as opposed to the sun–synchronous trajectory.

Chapter 3 tries* to give an up–to–date review of the literature on scene identification and more specifically on cloud properties retrieval schemes. We investigate the strengths as well as the weaknesses of the various methods if they had to be applied to the RGP. We then motivate our choice on the adopted strategy for the GERB level 2 processing.

In the following two chapters, the prototyping software developed on Meteosat–7 (MS7) imager data is described. We first present in chapter 4 an innovative method for the estimation of the TOA clear–sky visible reflectances at the native imager spatial and temporal resolutions. Then chapter 5 treats about the cloud properties retrieval as well as their comparison with associated CERES products.

The next two chapters are dedicated to the adaptation (chapter 6) and validation (chapter 7) of this prototyping scene identification to the SEVIRI MSG imagers. As one may note, this adaptation raised some specific issues with the enhanced SEVIRI instruments compared to their previous generation counterparts which had to be solved. As a matter of fact, it is not the doubling of the spatial and temporal samplings but going from 3 broad channels (visible, thermal infrared and water vapor) to 11 narrow bands, which required specific adaptation of the algorithm due to the drastic change of spectral sensitivity to various scene properties.

Chapter 8 suggests a new method to detect clouds using solely thermal infrared information from the imager without requiring realtime ancillary data such as numerical weather prediction (NWP) model fields as it is usually the case in other approaches found in the literature. While this proposed scheme is not part of the Edition 1 processing, it is foreseen to be included in the next Edition 2 software collection.

Finally, we summarize the work performed in this thesis in chapter 9. Future perspectives as well as suggested improvements which should be investigated for a possible implementation in Edition 2 of the RGP close this chapter.

It is worth noting that, while all algorithms have been developed to be applied to the Meteosat constellation of geostationary satellites, they are versatile enough to be almost immediately transposed to similar observing platforms such as the NOAA Geostationary Operational Environment Satellite (GOES) constellation.

* Let us stay humble as it is still possible that we have missed some papers on the subject...

Chapter 2

Interlude in radiative physics

THIS chapter summarizes the main processes occurring when radiation propagates through the atmosphere and introduces the various parameters which will be used throughout of this manuscript. The material used for this summary is directly inspired from [93, 126, 165].

2.1 Radiative quantities

We start this chapter by briefly introducing the common terminology used in the remote sensing community which will be mentioned in the following.

The flux is defined as the total energy per unit time [W] transported by any radiation. However, in meteorological and climate remote sensing, a normalized quantity is of prime interest to study the causes of the variation of radiation at various atmospheric levels. This normalized quantity is the *flux density* defined as the flux per unit area $[\mathrm{W} \cdot \mathrm{m}^{-2}]$ passing through a normal plane to the direction of propagation. It is usual to use the shorter term *flux* instead of *flux density* since no ambiguity can arise. Therefore, from now on, we will use such convention in this manuscript. The flux being a broadband quantity, a monochromatic or spectral flux $[\mathrm{W} \cdot \mathrm{m}^{-2} \cdot \mu\mathrm{m}^{-1}]$ can be introduced as

$$F(\lambda) = \lim_{\Delta\lambda \to 0} \frac{F(\lambda, \lambda + \Delta\lambda)}{\Delta\lambda}, \tag{2.1}$$

where $F(\lambda, \lambda + \Delta\lambda)$ is the flux contributed by radiation in the spectral range between λ and $\lambda + \Delta\lambda$.

The radiant intensity L also called *intensity* or *radiance* describes the amount of flux associated to a specific direction Ω, i.e. the flux per unit solid angle $[\mathrm{W} \cdot \mathrm{m}^{-2} \cdot \mathrm{sr}^{-1}]$,

$$L(\Omega) = \frac{\delta F}{\delta \Omega}, \tag{2.2}$$

where $\delta\Omega$ designates a solid angle element in direction Ω. A spectral radiance can be defined accordingly.

One is generally interested in the incoming or outgoing radiation from either a real or imaginary surface. Therefore, the definition of the outgoing flux follows

$$F^{\uparrow} = \int_{2\pi} L^{\uparrow}(\Omega)\ \cos\theta\, d\Omega \tag{2.3}$$

where the integration is over the upper hemisphere of the surface and θ designates the angle between the normal to the surface and the outgoing direction Ω of the radiance $L^{\uparrow}$. Similar expressions can be derived for incoming and spectral quantities.

Finally, it is convenient to express all these quantities in spherical polar coordinates where the z–axis is aligned with the normal to the surface, the principal plane being defined by the normal and incoming source (sun) vectors which allows to measure the relative azimuth φ between the principal and the sensor planes as illustrated in figure 2.1.

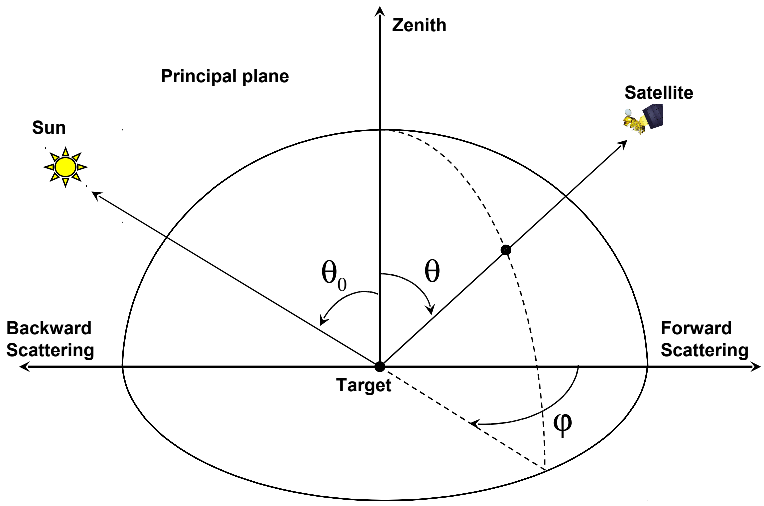

Figure 2.1 *– Scene geometry definition.*

2.2 Energy sources

Radiation in the atmosphere is issued from two emission sources. The first, extraterrestrial, source is the sun while the second is any object in the Earth–atmosphere system at a temperature above the absolute zero, i.e. the Earth surface, clouds, atmosphere, etc…

2.2.1 Solar radiation

Most of the sun's energy reaching the Earth originates from a layer about 500 km thick which is called the *photosphere* and is generally referred to as the surface of the sun, even if it is a gaseous body. The spectral distribution of its emitted energy can be approximated by the theoretical *Planck* function of a black body at a temperature of about 5800 K which is an average over the temperature range of the photosphere. However, the true solar spectrum is more complex, consisting of this continuous emission with a superimposed line structure known as the *Fraunhofer spectrum*. This line structure can be explained from the fact that the radiation inside the sun can be absorbed by atoms according to electronic transitions. The *solar constant*[*] or *flux* which is the total power per unit surface area over all wavelengths reaching the Earth at the mean Earth–sun distance, i.e. 1 A.U., is generally assumed to be $1366 \pm 0.65^{\dagger}$ $W \cdot m^{-2}$. However, this experimental value is still subject to debate in the scientific community and its measurement uncertainty is commonly assumed to be ± 3 $W \cdot m^{-2}$ [90]. As a matter of fact, recent measurements from the Solar Radiation and Climate Experiment (SORCE) Total Irradiance Monitor (TIM) suggest lower values of about 1361 $W \cdot m^{-2}$ [86].

From the left plot of figure 2.2 which represents the approximated continuous spectrum incoming on top of the atmosphere (TOA), we can see that it is extending from the ultraviolet to the infrared regions. It can be shown that about 10 % of the total solar irradiance lies in wavelengths shorter than the visible ($\lambda < 0.4$ μm), 40 % corresponds to the visible region ($0.4 < \lambda < 0.7$ μm) and 50 % to the infrared region ($\lambda > 0.7$ μm), while less than 1 % is associated to wavelengths above 4 μm.

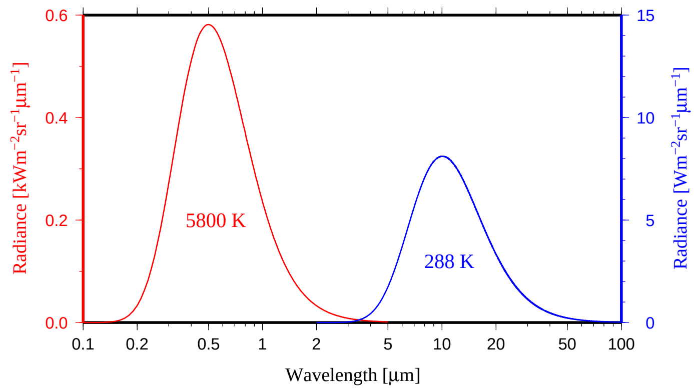

***Figure 2.2** – Blackbody radiance incoming on TOA as a function of wavelength for the average temperature of the sun's photosphere (left) and black body radiation for a typical terrestrial temperature (right).*

2.2.2 Thermal radiation

Since the Earth–atmosphere system absorbs part of the incoming solar radiation, it has to re–emit energy to space to fulfill the global temperature equilibrium condition. The upper bound of this spectral emission is given by the spectrum of the associated *ideal* black body at the same averaged temperature T. However, a black body is only a theoretical construct since no object is a perfect emitter. This deviation of the emitted spectrum $L(\lambda)$ from the Planck function $B(\lambda; T)$ is characterized by the spectral emissivity defined as

$$\epsilon(\lambda, T) = \frac{L(\lambda)}{B(\lambda; T)}, \tag{2.4}$$

[*] The term *constant* is a misnomer since this quantity varies with time.
[†] temporal variability over the 3 last 11–years sunspot cycles

which is ranging between 0 and 1 and is function of other variables such as the geometry and surface, atmosphere or cloud properties, etc... Bodies associated to $\epsilon < 1$ are called *gray bodies*. However, it may be worth noting that most surfaces on Earth emit close to a black body (e.g. oceans). Similarly, the absorptivity $a(\lambda)$ can be defined as the ratio of the absorbed radiation to the Planck function. For a system at thermodynamic equilibrium, the *Kirchhoff* law applies and states that

$$\epsilon(\lambda) = a(\lambda). \tag{2.5}$$

The right plot of figure 2.2 represents the upper bound of spectral emission for a typical terrestrial temperature of 288 K. One can notice a clear cut between the solar and the thermal spectra at about 4 μm due to their limited overlap where more than 99 % of the total emitted energy corresponds to wavelengths above 4 μm. This fact implies a considerable simplification for any radiative transfer (RT) problem since both types of radiation can be treated separately with distinct sources.

Finally, we can define the concept of *brightness temperature* (BT) which is central in infrared (IR) remote sensing. Based on the fact that only gray bodies exist in nature, their brightness temperature [K] is defined as the equivalent black body temperature corresponding to the same observed spectral *radiance* $L(\lambda)$, i.e.

$$\mathrm{BT} = B^{-1}(\lambda; L(\lambda)), \tag{2.6}$$

where B^{-1} designates the inverse of the Planck function.

2.3 Propagation in clear atmosphere

In this section, we review the three main processes occurring when radiation propagates through a clear atmosphere.

2.3.1 Transmission

The variation of the spectral intensity or radiance $L(\lambda)$ of the radiation along its propagating path s into the atmospheric medium can be described locally by the *Beer–Lambert* law, i.e.

$$dL(\lambda) = -L(\lambda)\, \beta_e(\lambda; s)\, ds, \tag{2.7}$$

where β_e [m^{-1}] is called the (volume) extinction coefficient of a specific constituent. This reflects that radiation is attenuated when it propagates through the atmosphere. It can be related to an associated intrinsic quantity, the mass extinction coefficient k_e*, whose product with the constituent density ρ [kg $\cdot$ m^{-3}] in the air must equal the extinction coefficient β_e. It is also convenient to express the volume extinction coefficient relatively to the *number density* or *concentration* N [m^{-3}] of the atmospheric constituent particles. Thus, the extinction *cross–section* σ_e [m^2] can be defined accordingly. To summarize

$$\beta_e = \rho k_e = N\sigma_e. \tag{2.8}$$

*Its dimensions are an area per unit mass, so it can be seen as the extinction *cross–section* per unit mass.

The last equality of the previous equation allows to express the mass extinction coefficient k_e [$\mathrm{m}^2 \cdot \mathrm{kg}^{-1}$] of a spherical particle constituent as

$$k_e = \frac{Q_e(r)\, \pi r^2}{\rho\, \frac{4}{3}\pi r^3}, \tag{2.9}$$

by introducing the extinction efficiency Q_e whose dependency on the wavelength is implicitly assumed and where r designates the particle radius. This extinction efficiency can be seen as a corrective factor to the geometric cross–sectional area of a particle. Mass absorption and scattering coefficients can be defined similarly with their corresponding efficiency.

The extinction coefficient β_e is the sum of the absorption and scattering contributions, i.e. $\beta_e = \beta_a + \beta_s$ and thus similar equalities hold between $\beta_{a,s}$, $k_{a,s}$ and $\sigma_{a,s}$. To quantify the relative importance of scattering compared to absorption, one usually introduces the *single scattering albedo* as

$$\omega = \frac{\beta_s}{\beta_e}. \tag{2.10}$$

The value of this parameter ranges from 0 for strictly absorbing to 1 for purely scattering medium, while its functional dependence with the wavelength is implicitly assumed.

Reconsidering equation 2.7 and solving for L along a path $s_1 \to s_2$, we get

$$L(\lambda; s_2) = L(\lambda; s_1)\, \mathrm{e}^{-\tau(\lambda; s_1, s_2)}, \tag{2.11}$$

where

$$\tau(\lambda; s_1, s_2) = \int_{s_1}^{s_2} \beta_e(\lambda; s)\, ds \tag{2.12}$$

is called the *optical path* (dimensionless) and its exponential the transmittance $t(\lambda; s_1, s_2)$. If the integral of the optical path is along the vertical axis of the atmosphere, τ is called the *optical depth* or *thickness*.

Finally, the generalization of the concept of volume extinction, scattering and absorption coefficients associated to a mixture of constituents as it is the case in the atmosphere is simply the sum of the respective volume coefficient of individual species. Thus, it results that the overall transmittance is the product of the individual constituent transmittances.

2.3.2 Scattering

Radiation experiences various scattering processes depending on the atmospheric constituents. More specifically, the kind of interaction depends on the size of the particle relatively to the typical wavelength of the radiation. The sizes of the atmospheric materials implied in scattering processes cover several orders of magnitude, typically from 10^{-4} μm for gaseous molecules to 1 μm for aerosols, 10 μm for water droplets and 100 μm for ice crystals. For spherical particles, the *size parameter*

$$x = \frac{2\pi r}{\lambda} \tag{2.13}$$

can be defined, where r is the particle radius and λ is the wavelength of the radiation. It also has to be stressed that scattering is a highly directional dependent process. This directional dependency is characterized by the so–called *scattering phase function* $p(\Theta)$ where Θ designates the angle between the directions of incidence and observation (see figure 2.3). It is convenient to assess the amount of forward versus backward scattering of a phase function. Thus, the *asymmetry parameter* g is defined as

$$g = \frac{1}{4\pi} \int_{4\pi} p(\Theta) \ \cos\Theta \ d\Omega, \tag{2.14}$$

where the integration is over the whole unit sphere and $d\Omega$ designates the solid angle element. This parameter is ranging between -1 and 1, $g > 0$ meaning that the forward scattering hemisphere is prominent, $g < 0$ that the backward directions have a higher probability and $g = 0$ that scattering in both hemispheres is likely probable. However, it is worth pointing out that if isotropic scattering is characterized by a null asymmetry parameter, different non–isotropic phase functions can also correspond to $g = 0$.

Particles whose size is small compared to the incident wavelength ($x \ll 1$) result in an elastic scattering of the photons, i.e. the incoming energy is completely transferred to the scattered radiation. It can be shown that the intensity of such scattering follows an inverse fourth power law of the wavelength and it is generally referred to as *Rayleigh* or *molecular* scattering. It results that the intensity of this scattering is the highest at small wavelengths*. This kind of scattering does not only happen along the incoming radiation path. Instead, it follows a directional dependence known as the Rayleigh scattering phase function. It can be demonstrated that for natural unpolarized incident light, this phase function has the form

$$p_{\text{Ray}}(\Theta) = \frac{3}{4}\left(1 + \cos^2\Theta\right). \tag{2.15}$$

while corresponding to a null asymmetry parameter. In clear atmosphere, Rayleigh scattering is the major source of scattering for visible wavelengths due to the typical size of the air constituent molecules. Figure 2.3 illustrates the Rayleigh scattering phase function.

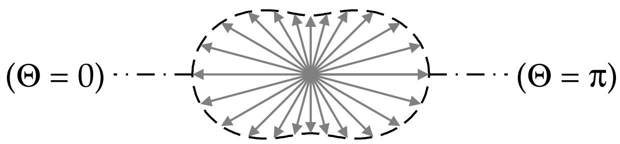

Figure 2.3 *– Polar plot of the Rayleigh scattering phase function* $(r, \theta) = (p_{\text{Ray}}, \Theta)$*. The direction of propagation (horizontal axis) is an axis of symmetry of the phase function.*

When the atmospheric particles are large compared to the wavelength of the incident radiation ($x \gg 1$), the theory of geometric optics or *ray–tracing* can be applied to describe its propagation through the medium. This case is typically occurring with large cloud particles in the visible part of the spectrum and it can be shown that the wavelength dependence of this type of scattering can be neglected.

In the intermediate case where $x \gtrsim 1$, the theory of geometric optics cannot be applied anymore. Instead, the scattering phase function can only be computed through complex formalisms such as the *Lorenz–Mie* theory for spherical particles which considers the *Maxwell* equations for an electromagnetic wave solution. However, this theory is not applicable to

*This explains the blue color of the sky.

non–spherical bodies such as ice crystals or some aerosols. A unified theory dedicated to ice crystals was developed as a combination of the geometric optics and finite–difference time domain (FDTD) methods while for aerosols, the FDTD or T–matrix methods can be applied. The interested reader who is not afraid to dive back into the Maxwell electromagnetic formalism* will find more details on these techniques in [93]. It has to be noted that most of the size distribution of cloud particles falls within that case.

The domain of applicability of these distinct scattering regimes can be summarized in figure 2.4 where the particle radius and wavelength plane is partitioned according to the size parameter x.

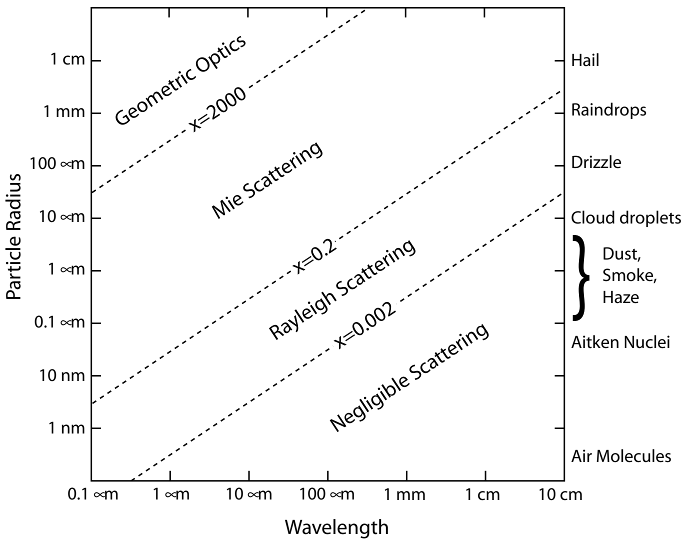

Figure 2.4 *– Partition of the wavelength and atmospheric particle radius plane into the various scattering types according to the size parameter x. From [126].*

In passive atmospheric remote sensing, it is commonly assumed that scattering does not alter the wavelength of the incident radiation. Moreover, the molecules and particles can be considered as independent scatterers, i.e. that each body scatters light in exactly the same way as if all other particles did not exist. This drastically simplifies the multiple scattering problem by a collection of particles since the intensity of the radiation can be used for its propagation into the atmospheric medium instead of its electromagnetic field description.

2.3.3 Absorption

Absorption by the various constituents of the atmosphere varies according to their molecular structure. The incident radiation can lead either to the deformation of the atomic links through translational, vibrational or rotational modes of the gaseous molecules. Moreover, electronic transition can result from the absorption of a photon associated to a specific energy.

*No way for me !

More details can be found in [93]. Since these three phenomena can happen altogether, the absorption spectrum is usually characterized by regions with complex patterns of thin lines and also significantly large spectral absorption bands.

This is illustrated in figure 2.5 where the vertical transmittance of the whole cloud– and aerosol–free atmosphere according to the wavelength as well as for selected gaseous constituents is plotted. It has to be stressed that the overall spectral transmittance curve of the atmosphere is of prime interest for the remote sensing community since it drives the location of the various channels in the design phase of all instruments. Indeed, it is obvious that for meteorological and climate monitoring imagers, absorption regions of the gaseous constituents of the atmosphere should be avoided to accurately observe clouds, aerosols and surfaces. The most noticeable fact from figure 2.5 is that the cloud–free atmosphere is significantly transparent over visible wavelengths.

2.4 Propagation in cloudy atmosphere

This section begins with the definition of a cloud as well as its associated macrophysical parameters. It is followed by an overview of the three main interactions of radiation through a cloudy medium. The expected spectral and spatial signatures of clouds for meteorological remote sensing is then summarized.

2.4.1 What is a cloud ?

Clouds are defined in the literature as visible bodies of condensed water droplets or frozen ice particles found in the atmosphere at altitudes between sea level up to the top of the troposphere (about 11 km). It is obvious that such definition is highly subjective due to the use of the word *visible*. Indeed, the perception of the visibility of a cloud will vary according to the kind of observing instruments, from the human eye to passive or active remote sensing apparatus. One may argue that to some extent clouds are always present in the atmosphere and that what is called *clear–sky* conditions are only a theoretical construct.

If their definition raises some questions, their formation is well known. Clouds form when the air becomes saturated by water vapor. This saturation is either achieved when the air mass cools or moisture is locally added. Lithometeors such as sea salt, sand dust or soot present in the air then act as condensation nuclei where water vapor tends to aggregate, if their concentration is large enough. Depending on the temperature, i.e. the altitude, water droplets or ice crystals will be formed around such hygroscopic aerosols.

Liquid water clouds are usually assumed to be formed by spherical cloud droplets. Typical droplet sizes vary between 1 and 100 μm even if their mean diameter is about 10 μm. Thus it is common in the literature to refer to the *effective radius* r_e defined as

$$r_e = \frac{\displaystyle\int_0^{+\infty} n(r)\, r^3\, dr}{\displaystyle\int_0^{\infty} n(r)\, r^2\, dr}, \tag{2.16}$$

where $n(r)$ [$\mathrm{m}^{-3} \cdot \mu\mathrm{m}^{-1}$] denotes the cloud droplet size r distribution and its integral over r is

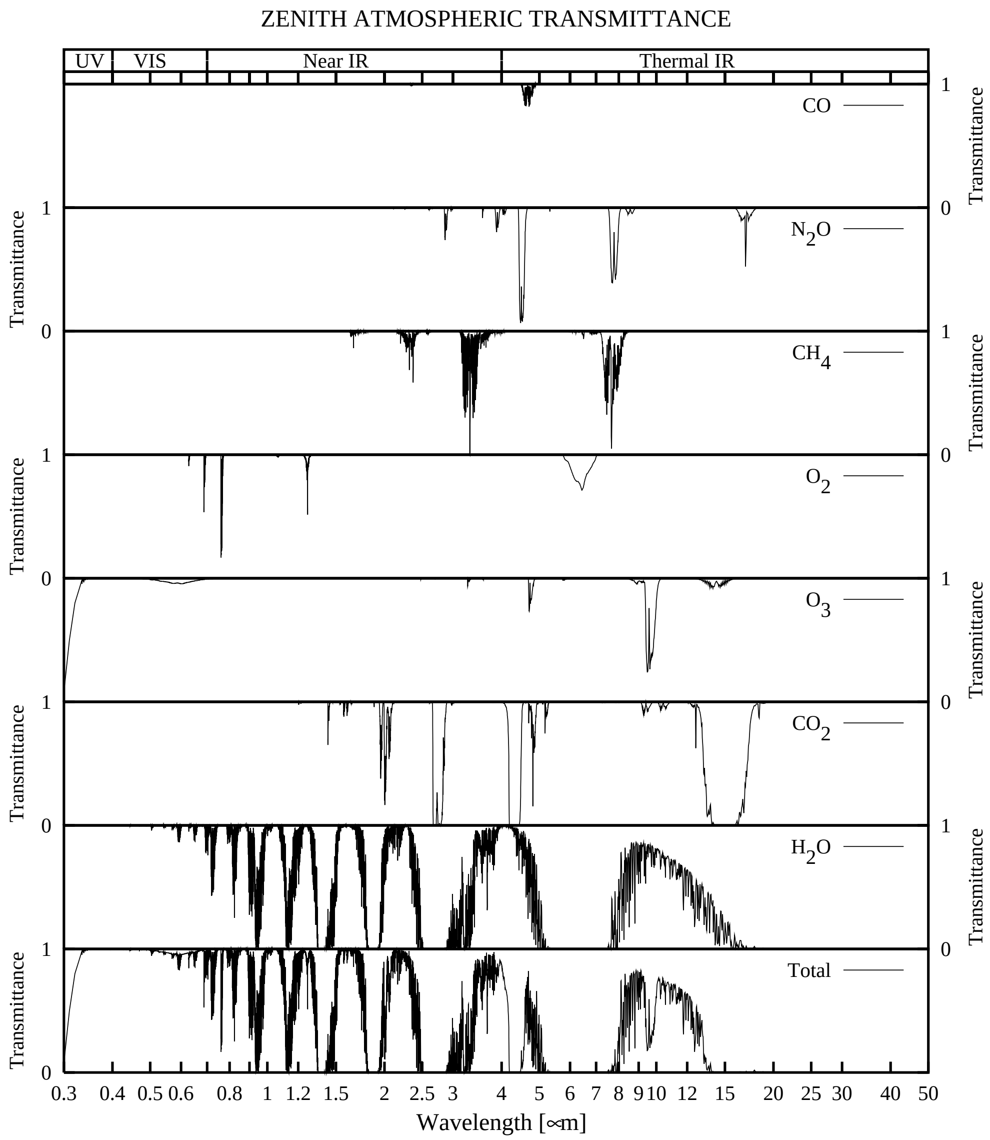

Figure 2.5 *– Transmittance of the cloud and aerosol–free atmosphere for mid–latitude summertime conditions for selected atmospheric gaseous constituents and as a whole. Molecular scattering is not considered. From [126].*

equal to the concentration N of all droplets used in equation 2.8. This distribution is generally unknown in real life cases. However, when radiative transfer model (RTM) simulations are performed, these theoretical models normally assume that it follows a log–normal or a gamma distribution as observed by measurement field campaigns.

Ice cloud particles on the contrary cannot be assumed spherical. They consist instead of mixtures of crystals with varying shapes*. Their larger size generally varies between 10 and 2000 μm with a mean diameter ranging from about 10 μm for thin cirrus to 120 μm for cirrus uncinus. Ice particle size distribution can be similarly characterized like liquid water clouds with the *effective size* D_e

$$D_e = \frac{\int_{L_{\min}}^{L_{\max}} n(L)\ L\ D(L)^2\ dL}{\int_{L_{\min}}^{L_{\max}} n(L)\ L\ D(L)\ dL}, \tag{2.17}$$

where $D(L)$ designates the ice crystal width, $n(L)$ the ice particle length distribution, $L_{\max}$ and $L_{\min}$ the maximum and minimum lengths of ice particles, respectively. Nevertheless, for convenience, we will use the term *radius* indistinctly for liquid water and ice particles in the following of this manuscript.

Having defined these two quantities r_e and D_e, the liquid water content (LWC) [$\mathrm{g} \cdot \mathrm{cm}^{-3}$] can be defined for spherical droplets as

$$\mathrm{LWC} = \frac{4\pi}{3}\, \rho_l \int_0^{+\infty} n(r)\ r^3\ dr, \tag{2.18}$$

where ρ_l is the density of water. A similar expression holds for the ice water content (IWC), i.e.

$$\mathrm{IWC} = \int_{L_{\min}}^{L_{\max}} \rho_i\ n(L)\ L\ D(L)^2\ dL, \tag{2.19}$$

where ρ_i designates the density of ice.

2.4.2 Scattering

The optical properties of polydisperse clouds, i.e. clouds with particles of different sizes, are easily generalized from their definition of monodisperse clouds by integrating them over the size distribution. Indeed, recalling the similar relationship between the scattering coefficient β_s and the scattering cross–section σ_s as in equation 2.8, one gets in the case of a distribution of particles

$$\beta_s = \int_0^{+\infty} n(r)\ Q_s(r)\ \pi r^2\ dr. \tag{2.20}$$

Similar expressions of $\beta_{e,a}$ hold. The combined scattering phase function $p(\Theta)$ is given by the scattering cross–section weighted average of the individual phase functions over the size distribution, i.e.

$$p(\Theta) = \frac{1}{\beta_s} \int_0^{+\infty} n(r)\ Q_s(r)\ \pi r^2\ p(\Theta; r)\ dr, \tag{2.21}$$

and similarly for the asymmetry parameter g.

As shown in figure 2.4, cloud particles typically have sizes where geometric optics can only be applied to the tail of their distribution for the visible wavelengths. Therefore, the Lorenz–Mie formalism for spherical and its counterpart for non–spherical particles must be used to compute the cloud scattering phase function as well as the other scattering parameters. It results from such computations that for visible wavelengths the associated phase

*hexagonal plates, rough aggregates, hollow columns, planar rosettes, spatial rosettes and solid columns function is rather complex with strong forward scattering and diffraction peak and it cannot be expressed analytically. This is illustrated in figure 2.6 where the phase functions associated to two extreme effective particle radii are plotted for liquid water and ice clouds for a given visible wavelength.

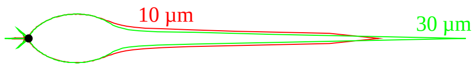

(a)

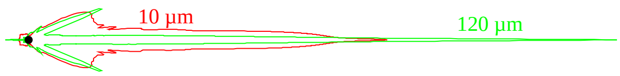

(b)

Figure 2.6 *– Polar plots of the scattering phase functions $(r, \theta) = (\log p, \Theta)$ for (a) liquid water (spherical particles) [188] and (b) ice (mixture of crystal habits) [13–15, 192] cloud at a wavelength of 0.6 µm. The sizes designate the effective particle radii and the direction of propagation (horizontal axis) is an axis of symmetry of the phase functions.*

RT theory demonstrated the usefulness to decompose this complex phase function into a truncated series of Legendre polynomials since it drastically simplifies the formulation of the RT equation. This parameterization "simply" consists in evaluating the coefficients of the series according to the wavelength and particle microphysical properties. Since such evaluation can be time–consuming, approximation of the true phase function has been suggested for flux RT simulations. The mostly used is the *Henyey–Greenstein* phase function whose parameter g playing a similar role than the asymmetry parameter is tuned to have some resemblance to the shape of the real phase function. It is defined as

$$p_{\mathrm{HG}}(\Theta, g) = \frac{1 - g^2}{(1 + g^2 - 2g\cos\Theta)^{3/2}}, \tag{2.22}$$

with $g > 0$. However, even if this function is adequate for the forward scattering peak, it fails to capture the backward peak. Therefore, the double *Henyey–Greenstein* phase function was introduced to address such issue:

$$p_{\mathrm{HG2}}(\Theta, b, g_1, g_2) = b\ p_{\mathrm{HG}}(\Theta, g_1) + (1 - b)\ p_{\mathrm{HG}}(\Theta, g_2), \tag{2.23}$$

where $g_1, g_2 > 0$ and $0 < b < 1$. Such empirical phase functions are also used by convenience for radiance computations in RTMs due to the complexity required to accurately parameterize $p(\Theta)$ for ice clouds. However they are unable to capture the detailed structure of the true phase function (see figure 2.6) thus leading to high uncertainties.

2.4.3 Absorption

As it will be reviewed in the following chapter, all major cloud phase detection algorithms found in the literature and based on multispectral threshold techniques rely on the spectral differences between liquid water and ice properties. The propagation of light in any homogeneous medium in the absence of diffraction is characterized by the dimensionless *index of refraction n*. This spectral parameter allows to describe such propagation in purely geometrical terms. This index can be separated into a real and imaginary part. The real part n_r defined as the ratio of the speed of energy propagation in vacuum to that in the medium rules the transmission of the radiation within the medium*. But it is the imaginary index of refraction n_i which characterizes the absorption through its relationship with the absorption coefficient and the wavelength of the radiation

$$\beta_a = \frac{4\pi\, n_i}{\lambda}. \tag{2.24}$$

In figure 2.7, we have plotted the imaginary index of refraction of both liquid water and ice according to the wavelength.

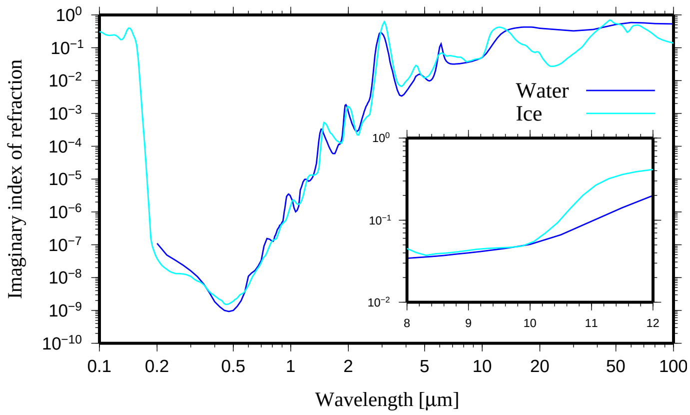

Figure 2.7 *– Imaginary index of refraction n_i for liquid water [65] and ice [178] according to the wavelength.*

Even if a cloud cannot be considered as a homogeneous medium, figure 2.7 gives a qualitative insight of the spectral behavior of clouds according to their thermodynamic phase. It is obvious why cloud phase detection algorithms mainly rely on brightness temperature differences (BTDs) of the 11 μm channel with one of the 8.5 and 12 μm channels. This is due to the fact that the spectral absorptions of liquid water and ice are almost identical around 8.5 μm while being significantly different at about 11 and 12 μm. Since liquid water absorption increases more between 11 and 12 μm than between 8.5 and 11 μm while it is the opposite for ice, BTD_{11-12} and $\mathrm{BTD}_{8.5-11}$ can further be used together to delineate liquid water and ice clouds. From the near–infrared (NIR) perspective, measurements around 1.6 and 3.7 μm are also promising candidates for liquid water and ice clouds separation even if the 3.7 μm channel signal contains both reflected solar as well as emitted thermal radiation during day–time (see figure 2.2).

By keeping in mind the atmospheric spectral transmission curve of figure 2.5, the sign of $\mathrm{BTD}_{8.5-11}$ allows to separate clear–sky from cloudy conditions. Indeed, around the 8.5 μm

*Gradient of n_r results in ray bending.

region, both liquid water and ice absorption are minimal and atmospheric water vapor absorption is moderate, while particle absorption is maximal with minimal water vapor absorption in the 11 μm region. Thus, clear–sky conditions are usually characterized by negative $BTD_{8.5-11}$ compared to positive values associated to clouds.

2.4.4 Transmission

Once the absorption and scattering properties are resolved, the single scattering albedo of clouds can be computed with equation 2.10. Its spectral behavior is illustrated in figure 2.8 where it is plotted for liquid water and ice clouds characterized each by two particle size distributions, i.e. different effective radii. This is in agreement with the fact that clouds are almost exclusively scattering radiation in the visible wavelengths* and therefore justifies to neglect absorption in this region of the spectrum when performing RTM calculations. On the contrary, scattering and absorption are occurring both in the IR domain.

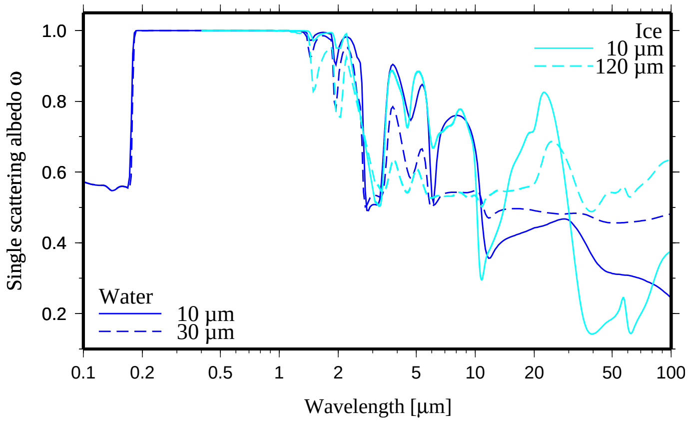

***Figure 2.8** – Single scattering albedo ω for liquid water [188] and ice (composed of a mixture of crystal habits) [13–15, 192] clouds according to the wavelength and various effective radii for particle size distribution.*

Knowing the geometric thickness of the cloud layer Δz, the liquid water path (LWP) and ice water path (IWP) are simply defined by the product of Δz with the associated water content for a homogeneous plane–parallel cloud, i.e. a cloud whose distribution of particles does not vary along the vertical axis z. Recalling the definition of the cloud optical depth in equation 2.12 and the expression of the extinction coefficient similar to equation 2.20 with the previous assumption, we get

$$\tau(\lambda) = \Delta z \int_0^{+\infty} n(r)\, Q_e(r;\lambda)\, \pi r^2\, dr. \tag{2.25}$$

In the visible part of the spectrum, one generally assumes that the extinction efficiency Q_e is approximately equal to 2 irrespectively of r for water droplets. Therefore, by further combining equations (2.16) and (2.18), an approximate expression of the cloud optical depth *in the*

*This explains why we observe clouds as white objects.

visible is given by

$$\tau \approx \frac{3\,\mathrm{LWP}}{2\rho_l\, r_e} \tag{2.26}$$

for liquid water clouds. However, outside of the visible domain, one usually considers empirical regressions for various spectral intervals, such as

$$\tau \approx \mathrm{LWP}(ar_e^b + c) \tag{2.27}$$

which are faster to compute than equation 2.25. Similarly for random oriented non–spherical ice particles, empirical expressions have also been derived for various crystal habits and spectral intervals, such as

$$\tau \approx \mathrm{IWP} \sum_{i=0}^{3} \frac{a_i}{D_e^i} \tag{2.28}$$

through non–linear regressions [83]. These parameterizations are generally used in general circulation models (GCMs) and RTMs such as STREAMER [82] which is used extensively in chapters 5 and 6 for the Geostationary Earth Radiation Budget (GERB) cloud properties retrieval algorithm.

2.4.5 Cloud spectral signature

If we consider plane–parallel cloud properties, the TOA radiance can be predicted by known asymptotic expressions for optically thick layers overlying a lambertian surface [84]. For non–absorbing wavelengths, the associated expression of the reflection of such thick clouds is essentially depending on the surface albedo α and the scaled optical thickness τ' defined by

$$\tau' = (1-g)\tau \tag{2.29}$$

where g is the asymmetry parameter. It results that for wavelengths below 1 μm characterized by $\omega \approx 1$ (see figure 2.8), the radiance of a cloud only exhibits limited sensitivity to cloud particle size (through g) but instead is highly dependent on the cloud optical depth τ. In contrast, for wavelengths where absorption is occurring ($\omega < 1$), the expression given by the asymptotic theory is fundamentally varying with the surface albedo and the similarity parameter s defined by

$$s = \sqrt{\frac{1-\omega}{1-\omega g}} \tag{2.30}$$

where ω is the single scattering albedo. Since this similarity parameter is primarily dependent on the cloud effective particle size r_e [118], the reflection function is also primarily sensitive to the cloud particle size for specific radiance measurements around 1.6 and 2 μm.

This is illustrated in figure 2.9 which summarizes the relationship between RTM simulations performed at the non–absorbing 0.6 or 0.8 μm and the absorbing 1.6 μm wavelengths for various cloud optical depths, particle effective radii and both cloud thermodynamic phases. The dashed curves represent iso–τ cloudy conditions while the solid lines denote iso–r_e cloudy conditions. The minimum value of the reflectance in each wavelength is associated to TOA clear–sky conditions over the underlying surface. It is obvious from this figure that the nearly orthogonality between equi–τ and equi–r_e curves implies that non–absorbing channels can be used to retrieve the cloud optical depth with little influence of the cloud effective particle radius while measurements in absorbing bands are mainly affected by cloud effective particle radius. Such fact is directly used in all major algorithms to estimate the cloud optical depth and cloud particle size. From figures 2.9 and 2.10, one can note that the accuracy of such technique is directly linked to the difference between clear–sky and cloudy conditions. Since the response to cloudy conditions tends to saturate for high values of the cloud optical depth, Earth surfaces associated to low spectral signature will decrease the uncertainty on the cloud retrievals. Nevertheless, one can notice that conditions associated to thin clouds ($\tau < 2$) cannot be anymore retrieved unequivocally. Indeed, as the cloud optical depth decreases, the iso–r_e curves associated to low cloud effective particle radius are converging. This results in multiple pairs of (τ, r_e) which are all compatible with the same spectral reflectance measurement pair at (0.6 μm, 1.6 μm) or (0.8 μm, 1.6 μm).

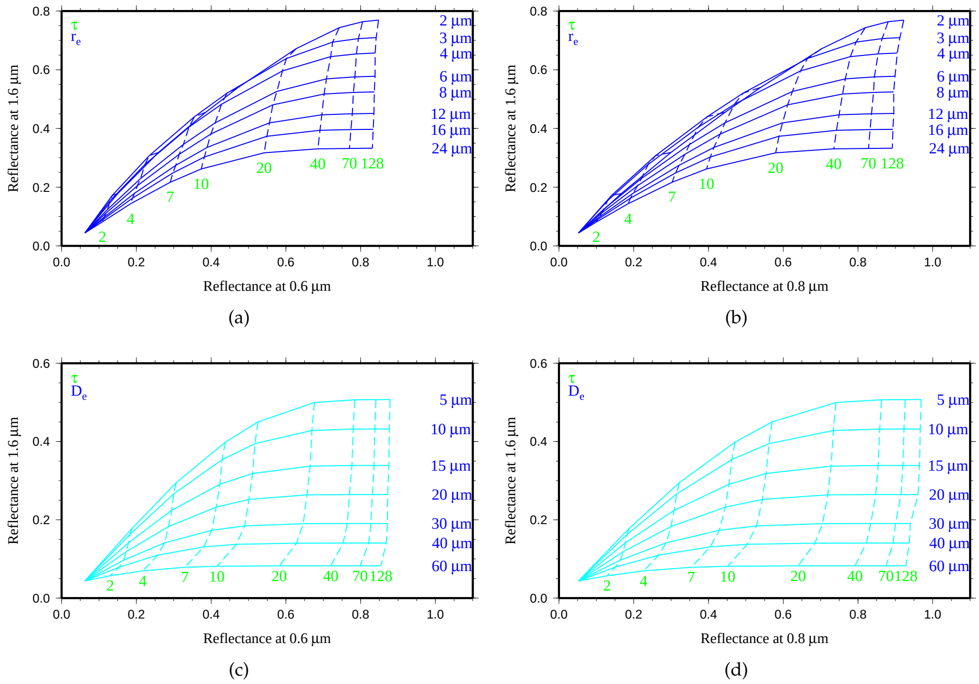

Figure 2.9 – RTM [105] simulated relationship between the reflectance at 0.6 or 0.8 and 1.6 μm for liquid water (blue) and ice (cyan) clouds. Solid lines represent iso–r_e curves while dashed lines designate iso–τ curves for various cloud optical depths and cloud particle effective radii. Scene geometry is $\theta_0 = 26°$, $\theta = 40°$ and $\varphi = 42°$. Surface albedo α is set to 0.05. Ice crystals are solid–column habit.

The spectral response of clouds is commonly exploited for their detection in major threshold techniques found in the literature. Indeed, thick high clouds are generally associated to significantly colder temperatures than their underlying Earth surface thus allowing them to be easily identified by brightness temperature (BT) threshold tests from IR window measurements around 11 and 12 μm. Since such measurements vary according to the water vapor profile and the surface emissivity, channels impacted by H_2O and CO_2 absorption can be a good alternative over polar regions because most of the measured signal is coming from the upper part of the atmosphere. Thin clouds and cloud edges on the contrary can not be detected using a single BT measurement due to their small impact on satellite measurements. Their detection can usually be performed by the so–called *split window* technique which relies on the BTD of a pair of IR bands such as BTD_{11-12} or $BTD_{8.5-11}$. The physics behind such method is based on the differential water vapor absorption in both channels. If low water clouds characterized by a similar temperature than the surface can also be detected using $BTD_{11-3.7}$, visible and NIR measurements at non–absorbing wavelengths around 0.8 μm provide a simpler method during day–time. Indeed, thick clouds are generally associated to higher visible reflectances than their underlying Earth surface* but depending on the geotype, this contrast can be reduced. Nevertheless, single visible and NIR reflectances at 0.6 and 0.8 μm, i.e. associated to low Rayleigh scattering by air molecules, as well as their ratio $\rho_{0.8}/\rho_{0.6}$ exploiting the fact that thick clouds do not exhibit large spectral differences efficiently manage to detect these clouds†. However, specific geotypes may require to use other combinations of channels as for example the 0.8 and 1.6 μm for bright desert. Of course, refinements of these basic detection recipes are used depending on the spectral characteristics of the imagers to achieve a higher sensitivity towards specific cloud objects.

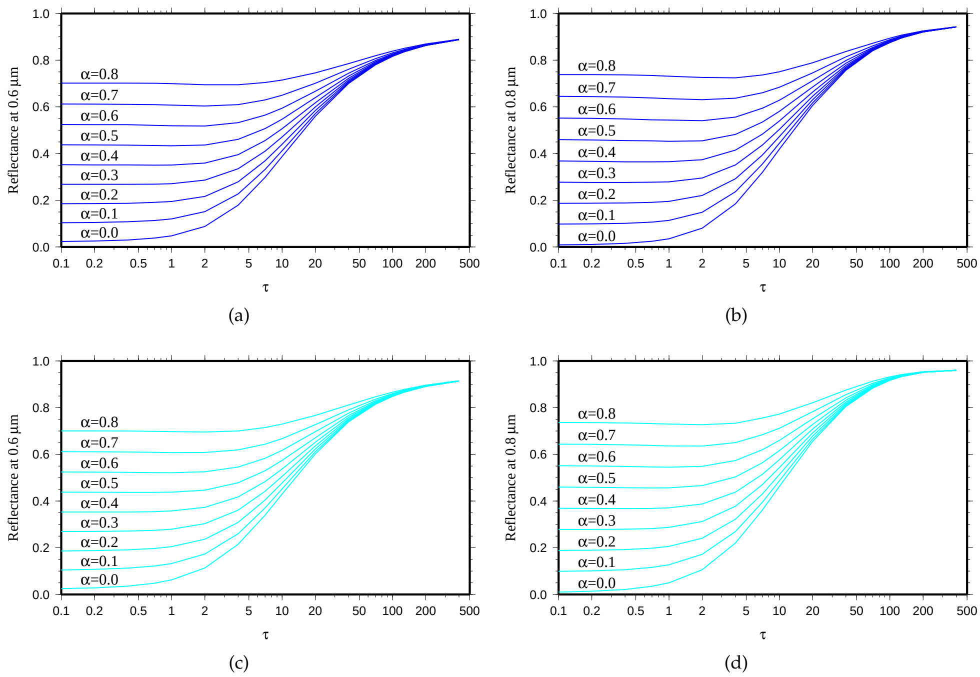

***Figure 2.10** – RTM [105] simulated relationship between the reflectance at 0.6 or 0.8 and the cloud optical depth τ for liquid water (blue) and ice (cyan) clouds for various surface albedos α. Cloud particle effective radius is 8 μm for liquid water clouds and 50 μm for ice clouds (solid–column crystal habits). Scene geometry is $\theta_0 = 26°$, $\theta = 40°$ and $\varphi = 42°$.*

* the exception being snow/ice covered surfaces
† for regions unaffected by the sun–glint

2.4.6 Cloud spatial signature

Local variance within a given channel can also be used to discriminate different cloud types. At 11 μm, cirrus are associated to large variance due to the fact that the signature of these thin objects is perturbed by the underlying surface response while for low stratiform cloud fields, their BT is more homogeneous locally resulting in small variance. However, in the visible part of the spectrum (0.6 and 0.8 μm), it is the opposite with low variance for cirrus while high variance values correspond to low stratus since it is the roughness of the cloud top which is constraining the reflected radiation towards the instrument. Broken cloud fields are also associated to high variance of their 11 μm BT signal. Therefore, this justifies why some cloud detection techniques found in the literature are making use of *spatial uniformity tests* on neighboring pixels within specific channels.

However, local variance is only one of possible textural features available from general image analysis theory. Indeed, features such as entropy, homogeneity, angular second moment, contrast, cluster shade and prominence are generally used in supervised as well as unsupervised cloud detection and classification algorithms [11, 55]. We will not detail such textural features since it is beyond the scope of this work.

2.5 Surface boundary conditions

Once the incoming radiation has passed through the atmosphere and the clouds and has gone through various interactions (scattering and absorption) in clear and cloudy atmospheric parts, it reaches the surface of the Earth. For most applications in remote sensing, such surface can be considered as a non–transmissive medium*. When observing a scene from a satellite platform, i.e. where a pixel can be considered as the average of the outgoing radiation from a large area, its detailed characteristics and physics parameters are not needed even if this area is far from being either smooth or homogeneous. In fact, a precise theoretical treatment of the interaction between the incoming radiation and the surface would be too complex to handle. Instead, we have to rely on empirical determination of its radiative properties.

We can generally assume, no matter how strongly irregular or inhomogeneous a surface is, that it can be approximated by a plane located just above the irregularities. The region below that plane can then be considered as a *black box*. Therefore, the interaction of radiation with this imaginary plane simply consists of the absorption of some fraction of it, while the other part is reflected up in the atmosphere. By defining the *absorptivity* $a(\lambda)$ and the *reflectivity* $r(\lambda)$ as the absorbed and the reflected fraction, respectively, we have for any direction of incident radiation Ω_0 in the virtue of the principle of energy conservation†

$$a(\lambda, \Omega_0) + r(\lambda, \Omega_0) = 1. \tag{2.31}$$

Recalling the Kirchhoff law applying to the medium at thermal equilibrium, one gets with equation 2.5

$$\epsilon(\lambda) + r(\lambda) = 1, \tag{2.32}$$

linking the emissivity (thermal radiation) and the reflectivity (solar radiation) of any surface where the dependence on the direction of incoming radiation is implicitly assumed.

*except for those interested in oceanography and atmosphere–ocean coupled systems

†Since the medium is opaque, there is no transmission.

Due to the complex nature of the surface, the reflected radiation usually exhibits an angular dependency behavior Ω according to the direction of incidence Ω_0. Such angular relationship is expressed by the spectral *bidirectional reflectance distribution function (BRDF)* ρ [sr^{-1}] defined as [146]

$$\rho(\lambda, \Omega_0, \Omega) = \frac{dL^{\uparrow}(\lambda, \Omega_0, \Omega)}{dL^{\downarrow}(\lambda, \Omega_0)} \tag{2.33}$$

where $L^{\uparrow}$ is the upwelling radiation while $L^{\downarrow}$ is the downwelling radiation on the surface. Typical examples of reflective behavior are illustrated in figure 2.11. One can notice the two extreme cases which are normally not observed in remote sensing: (a) the specular reflection wherein the reflected and incident direction are uniquely related and (c) the *lambertian* reflection wherein the angular distribution of the reflected radiation is uniform.

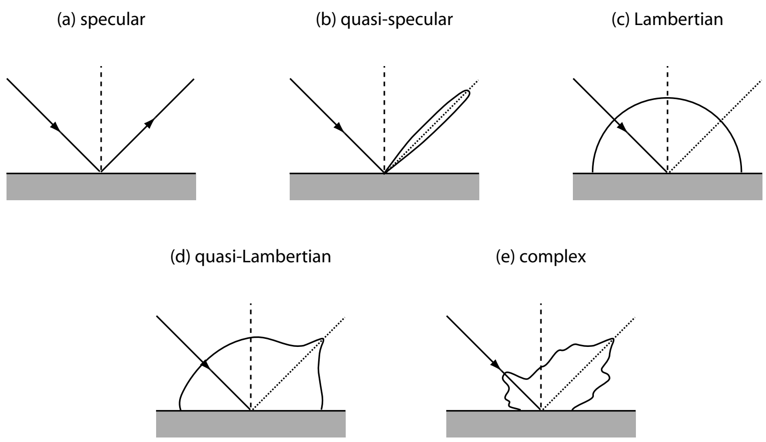

Figure 2.11 *– Examples of various types of surface reflection as polar plots where the radius represents the fraction of reflected intensity for an associated direction. From [126].*

To assess to overall reflective characteristic of a surface, one usually introduces the *albedo** α as the ratio of the reflected flux to the incident flux

$$\alpha(\Omega_0) = \frac{\int_{2\pi} dL^{\uparrow}(\Omega_0, \Omega)\, d\Omega}{\int_{2\pi} dL^{\downarrow}(\Omega_0)\, d\Omega_0} \tag{2.34}$$

where the integrals run over the upper hemisphere relative to the surface [146]. Similarly, we can introduce the *spectral* albedo $\alpha(\Omega_0, \lambda)$ of a surface. Both concepts ease the comparison of the reflectivity between various surface types. Such spectral albedos of typical natural surfaces are given in figure 2.12. One can note that snow has one of the highest albedos over the visible spectrum which can be larger than the response of thick clouds, while it drastically decreases around 1.6 μm to reach an even lower value at about 3.7 μm. Desert and dry vegetation on the other hand exhibit a gradual increase of their albedo up to the NIR domain and are the only surface types with a significant albedo ($\approx$ 20 %) around 4 μm. This implies a specifically lower emissivity at those wavelengths for these surfaces in virtue of equation 2.32. Even

*also called the *bihemispherical reflectance* if vegetation has a pronounced peak at about 0.55 μm*, its higher response around 0.8 μm is typical. Finally, one can observe that the albedo of water and by extension of ocean is very low at 0.4 μm (< 5 %) while slowly decreasing up to 2.7 μm. However, for *sun–glint* geometries between the sun and the observer, quasi–specular reflection occurs on the water surface which results in intense reflected radiation in a narrow viewing direction† (its reflective profile is illustrated by figure 2.11(b)).

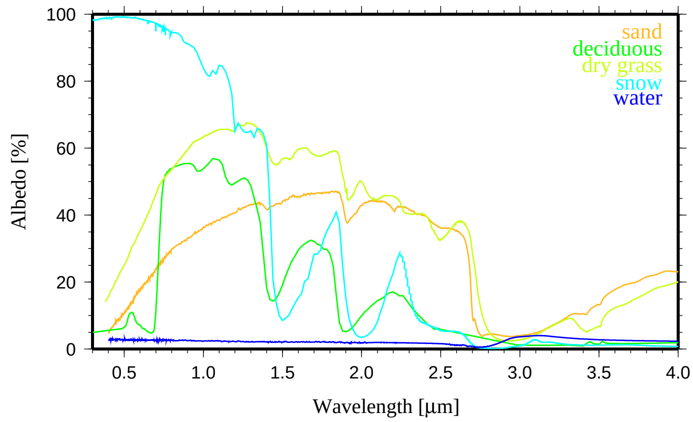

Figure 2.12 *– Albedos of various natural surfaces as a function of wavelength. From [8].*

The various spectral behaviors of the surface types implies a variation of the dynamical range between the clear–sky and the cloudy signal measured by the instrument. Therefore, cloud optical depth retrieval algorithms generally rely on measurements in the 0.6 μm channel for land geotypes while the 0.8 μm band is used over the ocean to maximise their sensitivity and obviously reduce the uncertainty of the retrievals.

2.6 Imagers spectral design

The previous sections demonstrated that to properly characterize cloud properties such as their thermodynamic phase and their optical depth, measurements must be performed around specific wavelengths. These generally avoid absorption bands of atmospheric constituents while trying to maximize their sensitivity to some specific feature.

This is therefore why all contemporary multispectral imagers targeted for meteorological and climatological monitoring include the following basic set of spectral channels for which we have summarized the main purposes:

* corresponding to the green portion of the visible spectrum and due to the chlorophyll

† This direction is modulated by the size and orientation of the waves according to the wind at the surface.

0.6 μm	clouds detection and optical depth retrieval over the land, aerosols optical depth retrieval
0.8 μm	clouds detection and optical depth retrieval over the ocean, aerosols optical depth retrieval
1.6 μm	cloud thermodynamic phase and effective particle size retrieval
3.7 μm	cloud thermodynamic phase and effective particle size retrieval, low water clouds detection
8.5 μm	thick cold clouds at altitude z_1, cloud thermodynamic phase
11 μm	thick cold clouds at altitude z_2 ($z_2 > z_1$), thin cirrus and cloud edges detection, low water clouds detection, cloud thermodynamic phase
12 μm	thick cold clouds at altitude z_3 ($z_3 > z_2$), thin cirrus and cloud edges detection, low water clouds detection, cloud thermodynamic phase

To this basic set, imagers from the latest generation include additional channels providing an increased sensitivity to specific conditions or phenomena such as clouds over polar regions*.

In this chapter, we only have introduced the basic prerequisites of radiative physics which are needed to comprehend the following chapters. As suggested throughout this chapter, we are far from having performed an exhaustive review of such a complex field. However, this should be sufficient to understand the principles behind the various cloud properties retrieval techniques, as well as their strengths and weaknesses, which are discussed in the following chapter.

*Indeed, at wavelengths commonly used to retrieve cloud properties these regions are characterized by high albedo snow or ice covered surfaces which are colder than clouds above them.

Chapter 3

Cloud properties retrievals

In this chapter, we try to give the most up–to–date overview of the techniques found in the literature to detect clouds and retrieve their physical properties from an air– and satellite–borne platform using only passive sensors*. In the next section, we briefly perform a critical analysis of the three main strategies which can be adopted for these retrieval schemes. We then focus in the following sections on the 3 cloud parameters which are required to properly select a Clouds and the Earth's Radiant Energy System (CERES) Tropical Rainfall Measuring Mission (TRMM) shortwave angular dependency model (ADM) for the Geostationary Earth Radiation Budget (GERB) solar flux processing, i.e. the cloud detection, the cloud thermodynamic phase and the cloud optical depth retrievals†. Finally, the last section (3.7) justifies the strategy that we have chosen for the RMIB GERB Processing (RGP).

3.1 General approaches

Since the transmission of the first image of the Earth from the TIROS–1 satellite in 1960, there has been a growing interest in the use of space instruments to collect cloud cover data and in building cloud climatologies datasets. In 1964, the first successful attempts to derive cloud amounts from satellite imagery required human expertise in a time–consuming process [6, 31]. Fortunately, with the advent of modern computers, numerous automated techniques have been developed to extract cloud physical parameters. Even if the majority and their underlying concepts were and are still developed for LEO imagers, they have been successfully adapted to geostationary instruments and to their specific scene geometries. These techniques are mainly relying on the typical spectral characteristics of the clouds compared to cloud–free conditions while some of them additionally make use of textural knowledge as, for example, spatial coherence information within a given channel. As already mentioned, multispectral imagers are designed to provide spectral bands which allow maximum discrimination between cloudy and cloud–free scenes based on their underlying physics, thus similar spectral

*During the last decade, several active instruments have been launched on board of low Earth orbit (LEO) platforms to supplement passive sensors. Indeed, their synergistic use improves drastically the vertical characterization of the atmosphere along their swath, both in terms of cloud and aerosol information, as for example in [45].

†The fourth parameter which is the surface geotype is defined as the fixed CERES surface map projected on the Spinning Enhanced Visible and InfraRed Imager (SEVIRI) field–of–view (FOV).

features are used in almost all techniques. They can generally be divided into three classes:

- those which rely on supervised methods,
- those relying on unsupervised frameworks,
- those based on comparisons with radiative transfer model (RTM) computations combined with some threshold tests to detect cloudy pixels.

3.1.1 Supervised techniques

Supervised methods are rarely developed. A maximum likelihood estimator technique has been implemented for cloud typing in polar regions using textural and spectral features from the four bands (a visible, two near–infrared (NIR) and an infrared (IR)) of Advanced Very High Resolution Radiometer (AVHRR) on National Ocean and Air Administration (NOAA)–7 [55]. A similar estimator demonstrated its applicability to Moderate Resolution Imaging Spectroradiometer (MODIS) data [91]. It consists in using the MODIS official cloud mask product to derive an initial learning dataset and then successively use the output classification as training set for the next iteration. A similar learning approach was adopted to train a discriminant analysis classifier to perform cloud detection on SEVIRI [4]. Another approach using AVHRR on NOAA–11 is based on the fuzzy logic formalism to detect single– as well well as multi–layer clouds using spectral (including ratio of reflectances and brightness temperature differences (BTDs)) as well as textural features [11]. A training dataset of such features is used to build the membership functions for each targeted cloud class. The result of the classification is a probability to belong to every class, calculated for pixel tiles, thus at a lower spatial resolution. The neural network (NN) formalism [37] allows to consider horizontal inhomogeneous cloud fields and to estimate the mean and standard deviation of cloud parameters. It has been successfully applied to SEVIRI to estimate a probability of cloud cover using spectral and temporal features derived from 8 SEVIRI channels [133]. The main asset of this algorithm is its independence to numerical weather prediction (NWP) ancillary data even if it relies on a cloudy and a clear–sky training dataset, the latter being inferred from the analysis of 10.8 μm brightness temperature (BT) time–series*. A temporally adaptive classifier has also been developed for Geostationary Operational Environment Satellite (GOES)–8 visible and IR channels [143, 175]. Basically, it relies on a probabilistic NN. This NN is trained by the classification result of the previous repeat cycle of the satellite using Bayesian theory on the spatial and temporal neighborhood of every pixel while the initial training dataset is classified by human experts. It is obvious that such approach is defeated in case of a missing repeat cycle and that errors in classification tend to exhibit a memory effect with time.

Usually, the main drawback of supervised methods is the need to firstly extract a representative training database which can be a time–consuming manual process while the logic of the classification is buried inside the classifier *black box*. These methods also suffer from several drawbacks such as the sensitivity of the classifier to the training samples with the risk to overfit them and thus delivering poor results for real life cases.

*Basic comparison was performed on synoptic data. However, it was recognized that such comparison is uncertain due to the ambiguity in the definition of *octa* and human observations.

3.1.2 Unsupervised techniques

Unsupervised techniques are not considered for operational purpose. However, already in 1982 a clustering algorithm using the three Meteosat channels (visible, infrared and water vapor) was investigated for potential cloud type classification [48]. This classifier was also used to develop a cloud detection scheme on Meteosat–4 data [5]. It consists in applying a k–nearest neighbours (kNN) clustering technique on directional textural features for the segmentation of the data. It was demonstrated that such method is especially efficient over snow and ice covered surfaces to detect clouds, when compared to multispectral threshold algorithms which are hampered by the lack of spectral contrast between the clouds and the surface. Another approach based on the spatial clustering of Medium Resolution Imaging Spectrometer (MERIS) pixel tiles has been tested [59]. The features used are based on the spectral behavior of clouds in the visible region of the spectrum (high and relatively constant albedo) and on the distinct atmospheric transmission when a cloud is observed in the O_2 and water vapor bands. Moreover, clustering techniques have been proved to be specifically suited in the case of partially cloudy pixels as it is the case for low resolution radiometers [7].

Nevertheless, they suffer from inherent issues such as sensitivity to initialization, the need to adequately choose the number of representative clusters, the significant increase of computing power due to an iterative scheme or the a posteriori identification of meaningful classes from the final clusters.

3.1.3 Comparison techniques

The vast majority of algorithms are based on comparisons of the multispectral measurements to radiative transfer (RT) simulations. As mentioned previously, the photon transport in a cloudy atmosphere is a complex problem depending on the 3–dimensional (3–D) description of the surface–atmosphere system. Therefore, the retrieval "simply" reduces to infer the parameters associated to 3–D fields from RTM simulations by matching them to the measured radiances at the top of the atmosphere. It is obvious that such problem is ill–posed because the unknown parameters drastically outnumber the measurements (instrument channels). Moreover, even if the complete 3–D structure could be known, 3–D RTMs which are usually based on probabilistic Monte Carlo formalisms [75, 102, 121] can not be used extensively due to the tremendous computing time requirements. Thus, most of the routine retrievals are based on the simplified *plane–parallel* or 1–dimensional (1–D) theory which models the atmospheric medium as horizontally homogeneous slabs with vertically varying parameters. To quote A. Davis [44]

> *"Homogeneous plane–parallel clouds may not exist in nature but they are the only ones for which we know how to solve the radiative transfer in a small amount of computer time."*

These algorithms treat each pixel within the FOV independently. They assume that every pixel can be considered either as completely cloudy or clear and that the cloud field is horizontally homogeneous within the pixel. These assumptions imply that horizontal photon transport is neglected as well as the radiative contribution of cloud edges and oblique illumination of 3–D cloudy structures. It is expected that results from such algorithms exhibit a dependence on the resolution of the instrument. Specifically, for high resolution imagers (less than 1 km at nadir), the 3–D effects become significant for cloud detection [193] and large errors can result when estimating cloud optical depth and effective radius [81] or top of the atmosphere (TOA) solar albedos [25] over broken clouds or convective cells. Even if the implementation of a 3–D cloud properties retrieval scheme is unpractical due to the fact that the 3–D cloud fields are unknown and that it would be computationally prohibitive, it is worth pointing out that several correction schemes for the 1–D theory are available in the literature [76, 103, 122, 191]. Moreover, approximations of the horizontal photon transport exist and allow to estimate the domain of validity of the plane–parallel assumption [128].

Recently an optimal cloud analysis (OCA) approach based on optimal parameters estimation has been developed [179] for SEVIRI data. This technique is still based on what is called the independent pixel approximation (IPA) but it is not relying anymore on threshold tests. Instead, it consists in searching the optimal input parameters (cloud optical depth, phase and cloud particle size and pressure) of a simplified *forward* RTM for its simulated TOA radiances to match as close as possible the multispectral measurements of each imager pixel. However, the huge amount of computing power required by this 1–D variational method currently prevents its use in an operational environment even if its main advantage is to deliver consistent parameters with all the multispectral measurements of each pixel which are spatially coherent*.

In the following of this chapter, we will be focussing on the schemes based on comparisons between multispectral radiance measurements and plane–parallel RT computations. Since these schemes are almost all relying on a prior cloud detection [115, 117, 134], we first start by investigating cloud masking techniques in the literature. We then review the common methods to discriminate between liquid water and ice clouds to finally end on the cloud optical depth retrieval algorithms.

3.2 Cloud masking

This section gives an overview of the common cloud detection algorithms found in the literature associated to projects or programs dedicated to climate studies. These schemes are implemented either on LEO or geostationary Earth orbit (GEO) instruments. It has to be noted that depending on the targeted applications of each project or program, the cloud detection scheme is either *cloud–* or *clear–sky conservative*. More precisely, a *cloud conservative* algorithm tries to minimize false cloud detection with an increased probability to miss thin clouds, so that scenes which are flagged cloudy can be fully trusted. In contrast, a *clear–sky conservative* algorithm tries to minimize false clear–sky detection with the risk to falsely identify some clear–sky scenes as cloudy. Such algorithm classifies clear–sky scenes with the highest confidence. Nevertheless, as stated in section 2.4.1, there is no *absolute* criterion to decide whether a scene is clear–sky or cloudy. Such *relative* classification depends in fact on the purpose of the cloud mask within each experiment.

3.2.1 LEO instruments

The AVHRR Processing scheme Over cLoudy Land and Ocean (APOLLO) was developed to detect clouds initially over western Europe area in AVHRR imagery [144]. Its processing con-

*No discontinuities are foreseen in areas of geotype transition as it can be the case for threshold techniques, the latter making use of specific values according to the surface type.

sists of threshold tests on 2 visible, a NIR and 2 IR channels during day–time while only the NIR and IR bands are used during night–time. These tests are grouped according to their purpose and sequentially applied. The cloud–free group uses the visible reflectance $\rho_{0.6}$, BT_{12}, $BTD_{10.8-12}$ (thin cirrus and cloud edges), ratio of reflectances $\rho_{0.8}/\rho_{0.6}$ and spatial uniformity on BT_{12}. Then, the remaining pixels are tested by the totally–cloudy group using ratio of reflectances $\rho_{0.8}/\rho_{0.6}$ and spatial uniformity on BT_{12}. The remaining unclassified pixels are flagged as partially cloudy. Finally, a snow/ice detection is applied to cloudy pixels using the NIR reflectance $\rho_{1.6}$. The logic of the night–time algorithm still exploits $BTD_{10.8-12}$, BT_{12} and spatial uniformity on BT_{12} in the threshold tests in addition to $BTD_{10.8-3.7}$ (fog and low stratus) and $BTD_{3.7-12}$ (medium– and high–level thick clouds). The various thresholds are dynamically computed from the analysis of histograms over pixel tiles in the processed imagery. From the previous description, this scheme can be categorized as clear–sky conservative. It was further improved for robustness over the entire globe and specifically over non–vegetated surfaces by updating the computation of the dynamic thresholds [88, 145].

Another algorithm is also available for AVHRR. The NOAA Cloud Advanced Very High Resolution Radiometer (CLAVR) scheme in its most current version relies on a sequential decision tree of multispectral threshold tests [156, 166]. These include: (1) contrast signature tests using visible and NIR reflectances and IR BTs, (2) spectral signature tests using ratio of reflectances and BTDs and (3) spatial signature tests based on uniformity of reflectances and BTs. The thresholds are again dynamically estimated using clear–sky radiance statistics computed from the previous 9–days repeat cycles* of NOAA satellite. The results of such scheme is either clear, cloudy, mixed–cloudy or mixed–clear. The mixed–cloudy class is assigned to pixels satisfying the contrast and spectral signature cloudy tests while being spatially non–uniform. The mixed–clear class is associated to clear–sky scenes according to the contrast and spectral signature tests which exhibit a spatial uniformity.

The launch of MODIS instruments on board of the Terra and Aqua satellites represents a major milestone in the design of cloud detection algorithms. Indeed, such imagers provide an extensive number of spectral channels which were carefully chosen among others to be sensitive to specific characteristics of the surface, atmosphere, aerosols and clouds.

The MODIS Atmosphere Science Team (MAST) developed a cloud mask based on threshold tests [2, 85, 130]. These tests use 20 out of the 36 available spectral bands either individually when applied on reflectances and BTs, or combined when applied on BTDs and ratios of reflectances. Basically, they are organized into 5 successive groups, each group being devoted to detect a specific cloud type: thick high, thin, low, upper tropospheric thin and cirrus clouds. The thick high clouds are detected using single BTs (11, 13.9 and 6.7 μm) while thin clouds are characterized with BTD_{11-12}, $BTD_{8.6-11}$, $BTD_{11-3.9}$ and $BTD_{11-6.7}$. Low warm clouds are then usually detected using solar channels by means of single reflectances (0.6, 0.8 and 0.9 μm) and reflectances ratio tests $\rho_{0.8}/\rho_{0.6}$ as well as $BTD_{3.9-3.7}$. The upper tropospheric thin clouds are further identified by a single threshold test on the NIR channel sensitive to H_2O absorption located around 1.38 μm. Finally similar BTD tests than the thin clouds group are used for cirrus with specifically tuned threshold values. Even if the thresholds used in the various tests are static, their values are varying across the FOV. In fact, each test is defined by a low and high threshold allowing to estimate a confidence level of being clear†. Within each group, these confidence levels are combined by considering the minimum value. The overall confidence "probability" is then computed as the geometric mean of the group confidence

*i.e. the 9 previous acquisitions at the same time of the day

†The confidence level is a linear function between the two thresholds.

levels. The final result of the cloud mask follows by partitioning this probability: confident clear, probably clear, uncertain and cloudy. It is obvious that such approach is clear–sky conservative because any test which has a null clear confidence, i.e. which is totally sure of the occurrence of a cloud, will propagate its value up to the overall confidence probability.

Recently, another cloud mask scheme was suggested for MODIS [74]. The motivation for its development was to design a *neutral* cloud detection algorithm that is neither clear–sky– nor cloud conservative. Even if it is inspired from the MAST cloud mask scheme by using similar threshold tests and the concept of confidence level, these have been reorganized into two distinct groups. The first group is composed of the cloud conservative set of threshold tests and delivers a clear confidence level accordingly while the second group is clear–sky conservative. Both clear confidence levels are then combined by a geometric mean and therefore the result of this cloud mask is a continuous clear confidence level between 0 and 1 allowing the user to select the sensitivity of the algorithm according to its needs. Moreover, to avoid any false identification of bright surfaces as clouds, a minimum surface albedo map over one month is used as threshold for the single reflectance tests instead of a static value.

The launch of the series of CERES broadband radiometers on board of the TRMM, Terra and Aqua satellites triggered the development of a cloud detection scheme on their companion Visible and InfraRed Spectrometer (VIRS) (on TRMM) and MODIS (on Terra and Aqua) imagers. Since the CERES project aims to monitor the climate of the Earth on a several–decade basis as well as providing a set of constraints for climate model assessment and improvement, the whole CERES processing including its cloud detection must use time consistent algorithms, ancillary data and calibrations across instruments. Since the MAST scheme uses many MODIS channels preventing its application to VIRS and ancillary data which may not be consistent with time, it was decided to implement a distinct scene identification (sceneID) for the CERES processing system. Such sceneID must remain versatile as this system ingests LEO and GEO imager products through complex time–space averaging to derive radiative fluxes at various levels of the atmosphere. Thus, the main purpose of the CERES cloud mask is to (1) detect clouds with the greatest radiative impact on the radiation budget, (2) suitably apply anisotropic directional models, i.e. ADMs, to CERES radiance measurements and (3) allow to quantify the direct and indirect aerosol effects through the identification of clear–sky scenes. As one may expect, an inter–calibration must first be performed across the LEO and GEO imager data to ensure that all derived cloud properties will give consistent results [112, 113]. The cloud detection algorithm is based on different cascading multispectral threshold techniques for day– and night–time [116]. Basically, it relies on the 0.6, 1.6, 3.7, 10.8 and 12 μm measurements and uses them either alone or through ratios of reflectances and BTDs. Its ancillary input data include vertical profiles of temperature, water vapor, wind, ozone and aerosols from re–analysis of NWP models allowing to estimate the skin surface temperature. A daily map of the snow/ice extent is also used as auxiliary input data. Clear–sky reflectances in visible and NIR channels are computed from associated monthly derived clear–sky albedos and directional modeling [160] while monthly surface emissivities allow to infer clear–sky radiances in IR spectral bands. Even if the cloud detection scheme is run at the pixel–level, its ancillary clear–sky properties and atmospheric corrections are constant over 16×32 and 32×32 km^2 tiles for VIRS and MODIS, respectively*. It results that uncertainties on the clear–sky thresholds can be estimated, and hence a *good* or *weak* cloudy flag and clear flag can be provided based on the BT, reflectance, BTD and reflectance ratio tests and depending on the availability of the visible and NIR channels. Moreover, it has to be noted that the resulting clear–sky pixels are not only used in the following cloud properties retrieval module but also in updating the

*This in fact corresponds to an area of 8×16 pixels.

ancillary clear–sky data within their respective tile for the cloud detection scheme. However, using constant ancillary data over such tiles has also a drawback since artifacts at tile borders can appear in the resulting cloud mask.

3.2.2 GEO instruments

In 1983, the World Climate Research Program (WCRP) initiated the International Cloud Climatology Project (ISCCP). Its main objective was "to obtain more information on how clouds alter the radiation balance of Earth" [147]. Specifically, ISCCP was developed to collect and analyze weather satellite radiance datasets to produce a global cloud climatology [137, 139, 140, 147]. To identically process all these GEO and LEO instruments, only a visible 0.6 and an IR 11 μm channels common to all platforms were retained for the processing. Prior to any analysis a careful inter–calibration of the imagers is required. Then, a cloud detection based on threshold tests is performed. These thresholds are dynamically derived from composite clear–sky values. Thus, the ISCCP processing relies on an accurate composite clear–sky estimation scheme. This scheme consists of 5 steps: (1) a spatial contrast test in a single IR image, (2) a time contrast test on 3 successive IR images at a given day–time, (3) a merge of space and time statistics for both channels, (4) the estimation of clear–sky composites for both bands every 5 days at a given day–time as well as their uncertainties. The cloud mask thresholds are then computed as the sum of the clear–sky values and their associated uncertainties. Finally, each scene is flagged *cloudy* provided that at least one of its visible and IR radiances is above the corresponding threshold while it is declared *clear* otherwise. It is obvious that this algorithm is cloud conservative, i.e. it minimizes false cloud detection but it misses thin clouds whose signal is lower than the inherent noise of the clear–sky estimation.

Minnis et al. [108] proposed a bispectral threshold technique to estimate clear–sky radiances and infer an associated cloud mask on GOES imager data. A minimum reflectance approach is used for the visible 0.65 μm channel to derive a global clear–sky bidirectional reflectance distribution function (BRDF) model for ocean and a set of longitudinal and latitudinal clear–sky BRDF models for land. Such approach is augmented by a clear–sky diurnal cycle BT modeling for the IR 11.5 μm measurements. Then, visible and IR cloudy thresholds are estimated based on their respective clear–sky models and the bidimensional visible and IR local histogram.

An operational cloud detection technique was also developed for Meteosat–7 whose aim was to initialize a short–term cloud forecasting scheme [57]. It relies first on an 11 μm BT threshold test. The threshold is estimated using the skin surface temperature field from a NWP model. These temperatures are corrected for bias between clear–sky BT and skin surface temperature by using selected cloud–free synoptic measurements. Another test is performed on the 0.7 μm visible channel. The associated threshold is computed using a two–week time–series frequency distribution to build a surface reflectivity map based on IR cloud–free flagged pixels. Finally, both tests are repeated once with lower threshold values to detect thin clouds near cloud edges.

Even more recently, European Organisation for the Exploitation of Meteorological Satellites (EUMETSAT) initiated their Satellite Application Facility (SAF) program focussing on meteorology and climatology. Among the SAF network, the Nowcasting and Very Short–Range Forecasting SAF (NWCSAF) aims to provide data for nowcasting purpose. To achieve such goal, an operational cloud detection scheme has been implemented [47]. Its logic relies on a cascade of multispectral threshold tests which are similar to those used for MODIS and are based on BTs, sea surface temperature (SST) estimation, reflectances, BTDs and spatial texture analysis. A significant difference between MODIS and NWCSAF methods lies in the fact that NWCSAF thresholds are dynamically computed according to the scene geometry, using look–up tables (LUTs) from RTM calculations as well as ancillary NWP model profiles and various climatologies. Moreover, an objective tuning of these thresholds has been performed based on a training dataset manually generated by human experts. The processing is ended by a spatial filtering which reclassifies isolated pixels with a different cloud flag from their neighbors. This scheme has successfully been applied to LEO imagers such as AVHRR or MODIS, even if it was initially designed for the Meteosat Second Generation (MSG) geostationary platform.

3.3 Cloud thermodynamic phase

An accurate cloud phase detection is of prime interest for climate studies because liquid water clouds and ice clouds influence differently the surface energy balance. While liquid water clouds tend to reflect much of the shortwave radiation, ice clouds tend to absorb and re–emit thermal radiation back to the surface. In this section, we review common approaches found in the literature to determine the cloud thermodynamic phase at a macrophysical scale from satellite imagery. It turns out that these techniques can usually be divided into 3 groups depending on the kind of spectral information used:

- those using thermal IR radiances,
- those utilizing visible and NIR reflectances,
- those combining visible, NIR and IR radiances.

Nevertheless, all approaches consider the differential absorption behavior between liquid water and ice (see figure 2.7) in selected spectral regions.

3.3.1 IR channels retrieval

The main advantage of using exclusively thermal measurements lies in the fact that such schemes provide cloud phase both during day– and night–time. However, the thermal contribution of the Earth surface can be a significant part in the satellite's measured signal when observing thin or broken clouds. Warm surfaces underneath such clouds can mask them and even lead to cloud phase misclassification as it is the case, for example, for thin cirrus clouds overlying desert. Moreover, thresholding on BTs assumes a sudden transition between liquid water and ice clouds at a given value while the transition between the two states does not normally occur at some unique value in real life. Instead it is merely dependent of the cloud dynamic and microphysical properties and therefore varies from case to case. Finally, it is demonstrated that cloud phase retrieval from IR channels is more representative of the phase near the cloud–top since these BTs are good estimators of the cloud–top temperature. It is expected from thermal RT theory [126] that IR window channels around 11 μm have the highest sensitivity to clouds altitude. This explains why such channels have been historically used for that purpose.

The ISCCP project uses in its processing a threshold test on the estimated cloud–top temperature derived from the 10.8 μm BT to separate liquid water from ice clouds [140, 147]. This estimation is based on the computation of the cloud emissivity according to the cloud optical depth at 10.8 μm [110] and on the clear–sky radiance. However, the cloud optical depth at 10.8 μm needs to be inferred from its associated value at 0.6 μm, thus requiring the availability of day–time visible measurements.

The usefulness of the 3.7 μm channel was later demonstrated on AVHRR data [7]. Indeed, the use of the 3.7 jointly with the 10.8 μm channel allows to select the most adequate microphysical cloud particle model and thus to reduce the uncertainty on the estimation of the cloud–top temperature.

The trispectral method was first introduced on High–spectral resolution Interferometer Sounder (HIS) data to detect cirrus clouds [1]. Such technique relies on the difference of microphysical and optical properties between water droplets and ice crystals in specific spectral bands located in the 8–12 μm window allowing to discriminate liquid water and ice clouds using their BTD. Indeed, the absorption efficiency of liquid water and ice is almost identical around 8 μm while ice is more absorbing around 11 and 12 μm resulting in a lower BT (see figure 2.7). Moreover, from the latter figure, one sees that the absorption efficiency of ice is larger between 8 and 11 μm than between 11 and 12 μm while it is the opposite for liquid water. It is therefore possible to partition a BTD_{8-11} versus BTD_{11-12} scatter diagram according to the cloud thermodynamic phase, liquid water clouds being generally identified below the unit slope, ice clouds above, mixed–phase clouds around and clear–sky conditions exhibiting negative BTD_{8-11} and small BTD_{11-12}. This method was also applied to collocated High–Resolution Infrared Sounder (HIRS) and AVHRR as well as on MODIS Airborne Simulator (MAS) data [157]. This last study demonstrated that the trispectral technique efficiently allows to discriminate clouds with emissivities below 1 (typically thin clouds), while high emissivity (thick) clouds are expected to exhibit almost zero BTDs. However, their thermodynamic phase can be easily inferred according to their 11 μm BT. It was also noted that the BTD_{8-11} threshold associated to clear–sky conditions is varying with the total column water vapor amount.

If the trispectral method seemed promising for the operational MODIS processing when applied to the MAS, it was not implemented due to issues which were raised during its operational testing. Indeed, it turns out that scenes containing clouds at multiple levels where never observed at the high spatial resolution of MAS (about 50 m) while they were in the large MODIS swath width. Moreover, slopes between $\mathrm{BTD}_{8.5-11}$ and BTD_{11-12} values were often close to zero leading to confusion in the scatter diagram. Thus, the MAST decided to opt for a simplified bispectral algorithm using the 8.5 and 11 μm channels which can be applied to any individual pixel without relying anymore on an analysis of a scatter diagram [85, 130]. It is still based on optical and physical properties through thresholds on $\mathrm{BTD}_{8.5-11}$ and BT_{11}, respectively, allowing to partition the $(\mathrm{BT}_{11}, \mathrm{BTD}_{8.5-11})$ space into 4 classes: liquid water, ice, mixed and undefined. Moreover, this algorithm and its threshold values have been successfully adapted to the SEVIRI instrument [190].

3.3.2 Visible and NIR channels retrieval

The retrieval methods based on visible and NIR reflectances exploit the optical properties of liquid water and ice cloud particles in this region of the spectrum. The behavior of the

NIR reflectances is dominated by the cloud thermodynamic phase and particle size through absorption (see figure 2.7) and scattering (see figure 2.8), whereas it is almost independent in the visible wavelengths.

Such concept is considered in a method which jointly retrieves the cloud thermodynamic phase together with the cloud particle size from a non–absorbing 0.67 and an absorbing 1.6 μm channel [77]. Even if it has been initially developed on Along Track Scanning Radiometer (ATSR) data, it was designed to be applied to AVHRR and SEVIRI. It assumes that the cloud type is homogeneous over small pixel boxes and assigns a cloud phase according to the scatter diagram between $\rho_{0.67}/\rho_{1.6}$ and $\rho_{0.67}$ of the pixels in each box. Such assignment is performed through a matching of the shape of the scatter diagram with RT simulated curves of varying cloud particle type* and effective radius.

However, simpler approaches have also been considered using threshold tests on single reflectance ratios. The cloud phase discrimination of the Multispectral Thermal Imager (MTI) processing relies on a threshold test on the ratio $\rho_{0.86}/\rho_{1.62}$ [29] while the ratio $\rho_{2.13}/\rho_{0.66}$ was initially investigated by the MAST. Comparisons of these two techniques with the MAST bispectral BTD method on MODIS data pointed out that the MTI algorithm gives consistent results and the one based on the ratio $\rho_{2.13}/\rho_{0.66}$ is biased toward the ice phase [30]. Spectral threshold tests were also investigated on single AVHRR 1.65 and 3.75 μm channels [124]. These tests manage to correctly detect the thermodynamic phase of thick clouds due to different spectral behavior (see figure 2.7), but they cannot discriminate thin clouds ($\tau < 1$) since thin liquid water and ice clouds tend to exhibit similar reflectances at these NIR wavelengths.

3.3.3 Visible, NIR and IR channels retrieval

Methods relying on the combination of visible, NIR and IR measurements offers the best accuracy because they allow to exploit cloud properties from various perspectives, i.e. according to their solar and thermal characteristics. However, the asset of these techniques is also their major limitation as these can only be applied during day–time.

The Cloud Physical Properties algorithm which is part of the Climate Monitoring SAF (CMSAF) operational processing chain falls in that category [134, 190]. The cloud thermodynamic phase is iteratively inferred together with the cloud optical depth and effective particle size. Such retrievals are performed through comparison between measured and simulated RTM reflectances in the 0.6 and 1.6 μm SEVIRI bands. Once the scheme has converged, a threshold test is applied on the emissivity–corrected cloud–top temperature to ensure that no cloudy pixel is assigned to ice phase while its temperature exceeds 265 K.

The MAS trispectral method was further enhanced by the addition of the visible 0.65 as well as the NIR 1.63 and 1.9 μm bands [12]. This proved to increase its reliability in regions of mixed cloud thermodynamic phases and of thin cirrus overlying low–level liquid water clouds. It is achieved through the use of threshold tests exploiting locally measurements associated to neighboring clear–sky pixels. Another study demonstrated that the addition of a single threshold test on the 1.63 μm channel also improved the thin cirrus identification for MODIS [28].

*liquid water droplets or ice crystal habits

3.3.4 Thin cirrus and multi–layer cloud detection

When retrieving the cloud thermodynamic phase of any pixel, we generally assume that the cloud field within this footprint is single–layered and sufficiently thick to modulate the response from the surface contribution in specific spectral channels. However, recent studies tend to show that multi–layer cloud configurations do occur frequently at all latitudes. Others estimated that thin cirrus can be present as much as 80 % of the time over the tropics while covering over 50 % spatially [27, 177]. Thin cirrus and multi–layer cloud detection are still an active research field since their radiative effect is significantly different from clear–sky and single–layer cloudy conditions. Currently, most multi–layer cloud detection algorithms manage to detect such clouds, but no detailed analysis on the phase of each layer is performed.

Cirrus clouds are composed of ice crystals at high altitude. While thick cirrus are easily detected, the identification of thin cirrus due to their optically semi–transparent nature still represent nowadays a challenge. Their signal is usually masked by the contribution of the surface radiation or the response of lower water clouds. Nevertheless, specific techniques are proposed.

The detection of single layer configurations of thin cirrus can be achieved by applying the split–window test, i.e. a threshold test on the BTD between the 10.8 and 12 μm AVHRR channels, according to 10.8 μm BT and the scene geometry [145]. However, this simple approach has to be supplemented since it suffers from misidentification of fractional liquid water cloud–filled pixels as thin cirrus while its accuracy is reduced over land geotypes.

Combination of the previous technique [145] with a thresholding on the AVHRR bispectral reflectance ratio $\rho_{3.7}/\rho_{0.6}$* increases the accuracy of thin cirrus detection over the ocean and vegetated surfaces but tend to miserably fail over sparsely vegetated areas such as desert [72]. Moreover, the use of the 1.6 μm channel for thin cirrus detection is limited since the cirrus contribution is almost completely overwhelmed by the response of highly reflective surfaces in that band.

The MODIS 1.38 μm spectral band is designed for its sensitivity to thin cirrus. Indeed, the strong water vapor absorption band in the vicinity of 1.38 μm (see figure 2.5) implies that the reflectance measured around this wavelength is almost entirely resulting from upper tropospheric clouds since all of the atmospheric water vapor is located below common cirrus altitude. Thus, the 1.38 μm channel can be used instead of the 3.7 μm one in the bispectral reflectance ratio technique together with the BTD between 8.6 and 11 μm channels [135] which is sensitive to the cloud thermodynamic phase through the differential absorption. By using the 1.38 μm channel the influence of the Earth surface geotype is removed. However, in this study the adopted logic was to combined into a single index, *the high cloud screening parameter*, both the reflectance ratio $\rho_{1.38}/\rho_{0.6}$ and the $BTD_{8.6-11}$ and use a single threshold test on this index to identify thin cirrus clouds. A modified method considering only the 1.38 μm channel with the $BTD_{8.6-11}$ and threshold values estimated from RTM computations was also investigated with success [136].

Recently, a novel cirrus detection technique was specifically developed for SEVIRI [87]. It is based solely on thermal IR channels which allows it to be applied day and night. Basically, it relies on two split–window tests on $BTD_{10.8-12}$ and $BTD_{8.7-12}$. To decouple the surface contribution from these BTD values, the BTD for every pixel is subtracted by the asso-

* where the thermal component of the 3.7 μm radiation is priorly removed

ciated cloudless value determined either from NWP fields or from the pixel's neighborhood. Furthermore, additional morphological high–pass filter tests are performed on SEVIRI water vapor channels. Indeed, due to the strong water vapor absorption in these bands, the surface and low clouds will have only a limited impact compared to high cirrus clouds. Their occurrence will result in significant small–scale variability patterns. Split–window threshold values are estimated from comparisons to comprehensive RT calculations while those for the morphological tests are empirically fixed by visual inspection of satellite images.

Multi–layered cloud configuration can be detected using the method initially developed on MAS data [10] and applied to the MODIS instrument [120]. This method uses tiles of neighboring pixels (typically 200×200) and starts to identify single layer liquid water and ice clouds using the bispectral technique on the 8.5 and 11 μm BTs. Then, cloud layer discrimination relies on the analysis of the scatter diagram of a NIR (1.6 or 2.1 μm) and IR (e.g. 11 μm) band together with clear–sky pixels information from a cloud mask. Specifically, single–layer liquid water and ice cloudy as well as clear–sky pixels clusters are identified. Then, average cluster centers are computed in this diagram and a region is defined where pixels could be associated to multi–layer clouds. Finally, the robustness of this technique is increased by not only performing a single pass analysis for every pixel, but by staggering the tiles for each pixel to be analyzed up to 100 times but at the expense of an increased computation time.

Another approach developed for AVHRR uses solely single pixel's measurements and applies RTM thresholds on 0.6 μm and BTD between 11 and 12 μm channels [123]. It assumes that a cirrus cloud overlap significantly deviates from the predicted plane–parallel behavior of a single liquid water cloud in the BTD_{11-12}. This method was further extended for the Visible–InfraRed Imaging Radiometer Suite (VIIRS) by adding threshold tests on the 1.65 and 1.38 μm reflectances [124].

3.4 Cloud optical depth

As we mentioned in the beginning of this chapter, we will only investigate methods based on comparisons with RTM computations. Nevertheless, these are representing the vast majority of implemented techniques for commonly used datasets in the climate and meteorological community. We know from section 2.4.5 that both cloud optical depth τ as well as the effective particle radius r_e or D_e can be retrieved simultaneously from two spectral measurements, one at water non–absorbing wavelengths and the other at absorbing wavelengths. Moreover, as illustrated in figure 2.9, properly selected channels allow to almost completely decouple one cloud property from the other and associate the variability of each spectral measurement to either τ (see figure 2.10) and r_e or D_e, providing that the cloud optical depth is not *too small**. It has to be noted that such result is derived from theoretical RT modeling and thus illustrates the usefulness of RTMs. The common approach is usually to retrieve the cloud optical depth for all pixels flagged as cloudy from a previous cloud detection processing by applying specific LUTs according to an a priori cloud thermodynamic phase estimation.

These retrieval schemes can generally be grouped into non–iterative and iterative methods. While direct, i.e. non–iterative, approaches can be used to estimate the cloud optical depth by making assumptions on the cloud effective particle radius, iterative schemes are developed to overcome the need of such approximations.

*It could not be more vague…

3.4.1 Non–iterative retrieval

A pioneer study was performed in 1980 and consisted in inferring the effective particle radius r_e of liquid water clouds [168]. It demonstrated that this quantity can be estimated using reflectance measurements at water absorbing wavelength (1.6 or 2.2 μm) provided that the cloud optical depth is priorly known. Such knowledge was achieved with measurements at a non–absorbing wavelength.

The joint retrieval of the cloud optical depth and top temperature was performed for the first time on NOAA TIROS–N AVHRR data [7]. This retrieval is based on RTM comparisons with the 0.73 and 11 μm channels through the selection of the LUT for this inversion. Such selection is first achieved by the 3.7 μm band to estimate the most adequate microphysical model of cloud particles, i.e. the effective radius size of spherical liquid water and ice droplets, used to stratify the LUTs.

The derivation of asymptotic analytical expressions from RT plane–parallel theory has later proved that such relations accurately predict the reflected solar measurements for thick clouds ($\tau \geq 9$) [84]. Thus, their inversion can be used to retrieve the *scaled cloud optical depth*, i.e. $(1-g)\tau$ (see equations 2.12 and 2.14 in chapter 2). Moreover, these expressions give an insight about the dependence of the reflectance of thick clouds with the cloud optical depth, surface albedo and asymmetry factor. It results in a significant reduction of the size of the LUTs required for the inversion. Moreover, this study stressed that the choice of a realistic cloud phase function for the RTM LUT computations is of prime interest.

The adopted approach for Polarization and Directionality of the Earth's Reflectances (POLDER) processing as well as initially for the ISCCP cloud analysis was to retrieve the cloud optical depth using a single visible channel and a prior cloudy knowledge [23, 139]. Assuming that all clouds can be modeled as homogeneous plane–parallel layers composed of liquid water droplets with an effective particle radius of 10 μm, RTM LUTs are used to invert the measured reflectance into the associated cloud optical depth according to the surface albedo and scene geometry. Nevertheless, it is worth pointing out that assuming spherical particles for ice cloud parameterization leads to relative discrepancies up to 70 % on the cloud optical depth retrievals [56].

An improved version of the previous method was developed and applied globally on NOAA–5 data [138, 141]. It consists in retrieving the cloud optical depth through RTM LUTs using ancillary NWP temperature and water vapor profiles but without any prior cloudy knowledge. Instead, the cloud optical depth is estimated for all pixels and a cloud flag is set for pixels associated to values above some threshold τ_{th}. However, as any cloud optical depth retrieval scheme, this approach requires first to estimate the clear–sky surface visible reflectance and window IR BT. This is achieved through the collection of monthly statistics from locally homogeneous reflectances and BTs around each pixel which allows to generate clear–sky surface maps together with an estimation on their uncertainties. Specifically, the error on clear–sky surface reflectance is used to compute τ_{th}. Finally, this study demonstrated that a significant increase in cloud detection sensitivity directly results from a more accurate clear–sky signal estimation compared to fixed climatological datasets of surface albedos.

It was during the First ISCCP Regional Experiment (FIRE) aircraft campaign that for the first time a technique was developed to simultaneously retrieve the cloud optical depth τ and effective particle radius r_e of stratiform liquid water clouds [118]. To achieve such goal, two measurements around 0.75 and 2.16 μm are used. This technique relies on the minimization of the cost function χ^2 defined by

$$\chi^2 = \sum_{\lambda} \left[\log \rho^{\lambda}_{\text{meas}}(\mu_0, \mu, \varphi) - \log \rho^{\lambda}_{\text{theo}}(\tau, r_e, \mu_0, \mu, \varphi) \right]^2 , \tag{3.1}$$

where the summation extends over the two measurement channels λ, μ_0 and μ are the cosine of the solar and viewing zenith angles and $\rho^{\lambda}_{\text{theo}}$ is the theoretical reflectance of channel λ for a specific plane–parallel cloud cover (τ, r_e). Due to the non–linear dependence of the reflectance on τ and r_e, no analytical solution can be derived. Instead of using RTM computations for all cloudy configuration, the method combines such calculations for thin clouds with the asymptotic radiative relationships for thick clouds to assume a parameterization of τ as a function of r_e. Thus, the minimization of χ^2 over the two unknowns (τ, r_e) reduces to a non–linear least–squares problem in r_e. Nevertheless, this simplification does not mitigate the fact that multiple solutions do exist for thin clouds and that additional channels (e.g. 1.65 or 3.7 μm) do not remove this ambiguity in the retrievals. Furthermore, a detailed theoretical analysis showed that the underlying surface albedo is directly related to the uncertainty of the cloud optical depth retrievals of this method.

This approach was selected by the MAST in the MODIS operational cloud product algorithm [85, 130]. Depending on the underlying geotype, a non–absorbing channel is selected to minimize the surface reflectance, i.e. the 0.65, 0.86 or 1.2 μm band for land, ocean or ice/snow covered surfaces, respectively. The cloud optical depth and effective radius are then retrieved independently for each of the 1.6, 2.1 and 3.7 μm absorbing bands, thus allowing to estimate the uncertainties on the retrievals. However, it has to be noted that a climatological surface albedo map is still currently used for the selection of the RTM LUTs.

3.4.2 Iterative retrieval

One of the first iterative methods to retrieve simultaneously the cloud optical depth and effective particle radius from semi–transparent to thick clouds was developed for the NOAA AVHRR multispectral imager [119]. It is relying on the visible 0.63 and NIR 3.7 μm bands, while the IR 11 μm channel is used to remove the thermal contribution to the 3.7 μm measured signal. The iterative scheme is based on a theoretical plane–parallel RT formalism of the expected radiance in these 3 channels where the surface is modeled by a lambertian reflector (see figure 2.11). This parameterization allows to decouple the contribution of the cloud layer from the thermal and ground radiance components in the measurements. Thus, by using RTM LUTs to model the reflectivities and transmissivities of the 3 channels according to a limited set of τ and r_e values, the algorithm iterates on τ with fixed r_e until the 0.65 μm observed and LUT radiances reach similar values. Then, the iteration is run on r_e with fixed τ where a similar criterion on the 3.7 μm radiances is tested, and so on... The convergence is met when measured and RT modeled radiances in the 0.65 and 3.7 μm bands do not significantly differ anymore.

While relying on the SEVIRI 0.6 and 1.6 μm channels, the cloud optical depth and effective particle radius retrieval scheme developed for the CMSAF processing is also proceeding iteratively [134]. The retrieval consists of a direct comparison between RTM LUT simulated reflectances with the measurements of cloudy flagged pixels. Previously, pixels were flagged as cloudy when the observed TOA 0.6 μm reflectance was higher than the LUT simulated clear–sky reflectance from fixed ocean and land albedos. The NWCSAF cloud mask [47] is now used as input. The iterative approach retrieves simultaneously both cloud properties from previous guesses since the updated cloud optical depth estimated from the 0.6 μm reflectance is used to update the cloud particle size from the 1.6 μm reflectance. If initially, this scheme was assuming constant albedos for ocean and land surfaces in the 0.6 and 1.6 μm bands, its most recent version [190] relies on the MODIS white–sky surface albedo product [130].

As mentioned previously, a specific sceneID has been implemented for the CERES project. This is motivated to guarantee that all products are generated by similar algorithms relying on controlled ancillary data even when the co–passenger imager to the CERES radiometer is changed from VIRS to MODIS. Similarly to the cloud mask, two dedicated retrieval schemes have been developed for day– and night–time [117]. The day–time Visible Infrared Solar–Infrared Split Window Technique (VISST) relies on measurements from 4 channels located around 0.65, 3.9, 10.8 and 12 μm, hence the name of the method. It aims to retrieve a detailed description of the cloud layer, including the cloud optical depth and effective radius together with its thermodynamic phase, the liquid water and ice paths, the cloud top and base pressures and temperatures and the cloud emittance. It is based on the comparison between observations and RTM LUT radiance computations through an iterative scheme. Basically, from an initial guess on the cloud effective particle size r_e for a water cloud, the cloud optical depth τ is computed according the 0.65 μm reflectance measurement. Next, the cloud temperature is estimated from the 3.9 and 10.8 μm channels and the previous two cloud properties τ and r_e. The cloud thermodynamic phase is then assumed once and for all from a threshold test on the cloud temperature. This allows to compute from LUTs the $\mathrm{BTD}_{3.9-10.8}$ for the current r_e or D_e and τ values according to the proper cloud microphysical model. By matching the measured $\mathrm{BTD}_{3.9-10.8}$ with their RTM counterpart, one is able to update the cloud effective particle radius r_e or D_e. This updated radius allows to update τ according to the assumed cloud phase from the 0.65 μm measured reflectance and so on... The convergence criterion is met when the updated cloud particle size does not significantly change anymore. As one may expect, the VISST algorithm relies on ancillary input data including the CERES cloud mask [116] as well as dynamic clear–sky estimations of the 0.65 μm reflectance and of the IR BTs over tiles of 16×32 and $32 \times 32\,\mathrm{km}^2$ for VIRS and MODIS, respectively [160]. Moreover, it has also successfully been adapted to other imagers on geostationary orbiting platforms such as MSG and GOES.

3.5 Retrieval over snow and ice covered surfaces

As one may expect, snow and ice covered surfaces are mainly occurring over polar and mountainous areas but also during wintertime over temperate regions. The lack of contrast between cloudy objects and such surfaces in the visible as well as in the window IR part of the electromagnetic spectrum implies the development of dedicated cloud detection and thermodynamic phase retrieval schemes. However, this subject which is still currently under investigation is beyond the scope of this literature review. The reader may simply note that, over non–polar regions, it is common to detect snow and ice covered surfaces without attempting to further retrieve any cloud properties.

The cloud optical depth retrieval canvas consisting in using a non–absorbing visible channel such as the 0.6 or 0.8 μm to derive cloud optical depth cannot be applied anymore to snow and ice covered surfaces. As we already mentioned, this is due to the fact that such surfaces have a response of the same order of magnitude than clouds while exhibiting large variability.

This results in a significant increase of the uncertainty of cloud properties retrieval (see figure 2.10). However, these surfaces are characterized by a much lower response in NIR bands (see figure 2.12) and thus the standard cloud optical depth retrieval canvas can be adapted by using the 1.6 and the more absorbing 3.7 μm channels [129]. However, the relative orthogonality between the measurements and the cloud optical depth and effective radius, that is observed for 1.6 μm versus 0.6 and 0.8 μm in figure 2.9, is lost.

3.6 Uncertainties in retrievals

Several sources are contributing to the errors on the various cloud properties retrievals from satellite measurements. These can either be categorized depending on their intrinsic physical nature, due to the instrumental design or the assumptions made for their retrievals.

3.6.1 Physics–based sources

3.6.1.1 Rayleigh scattering

As defined in section 2.3.2, the magnitude of the Rayleigh scattering is wavelength dependent, varying as its inverse fourth power. It results that this phenomenon can only significantly contribute to the measured signal at low wavelengths. Transposed in the context of meteorological space–borne instruments and cloud properties retrieval algorithms, it is mainly affecting channels around 0.6 and to a smaller extend 0.8 μm*.

A detailed analysis was performed during the Atlantic Stratocumulus Transition Experiment (ASTEX) campaign on the expected errors from retrieved cloud optical depths when Rayleigh scattering is not considered in the retrieval scheme [176]. It turns out that such scattering in the 0.6 μm channel can result up to an error of 60 % on the cloud optical depth for thin clouds and for all clouds at high solar zenith angles. Moreover, even if its contribution decreases in the 0.8 μm channel, errors as high as 25 % can be observed when retrieving cloud optical depth at high solar zenith angles. Therefore, Rayleigh scattering must be taken into account in RTM LUTs when these are used to perform retrievals from direct comparison with TOA measurements. For other retrieval approaches based on the estimation of intermediate cloud parameters such as their emissivity, top temperatures or radiances, an iterative method is suggested to correct the TOA measurements using the cloud albedo and cloud top pressure before ingesting them in any retrieval scheme [176].

3.6.1.2 Aerosols

Aerosols generally designate suspended matter or liquid particles in the atmosphere. Such particles can be made from dust–like, water–soluble, soot, oceanic, sulfate, mineral, water and organic materials [93]. Depending on their nature, aerosols exhibit distinct behaviors in the visible, NIR and thermal IR. While dust–like aerosols are mostly reflective, biomass burning aerosols tend to be more absorptive in the visible wavelengths.

*Lower MODIS spectral bands which are designed for aerosols and ocean state monitoring are, of course, increasingly affected, but these are not used in cloud properties retrieval.

If such aerosols are located above clouds, cloud properties retrievals such as cloud optical depth and effective particle radius are impacted. This is observed during austral winter off the coast of southern Africa due to the transport of smoke from biomass burning [186]. It results that satellite measurements in the visible part of the spectrum is decreased compared to unpolluted scenes, thus leading to a negative bias on the cloud optical depth retrievals whose magnitude is directly proportional to these retrievals.

On the contrary, dust–like reflective aerosols tend to increase visible measurements. If this has only a limited impact over high albedo land surfaces, major dust outbreaks can exhibit a larger signal than clear–sky ocean in the 0.8 μm channel (see figure 2.12). Thus, cloud detection techniques solely based on visible information will falsely detect such outbreaks as "water clouds" and flag them accordingly. Nevertheless, a dedicated method to recover these false cloudy scenes based on the specific spectral behaviour of dust–like particles compared to water clouds in the IR have been developed for SEVIRI [21].

3.6.1.3 Cloud shadowing

Shadowing of the ground or clouds by clouds systematically occurs for specific scene geometries which are common for both LEO as well as GEO imagers. This effect results in a drastic extinction of the measured signal over such regions for the solar radiation domain. Cloud shadows casted over a cloud field due to their roughness (cloud bumps) can be falsely detected as clear–sky over the ocean. Hence, techniques have been developed for the detection of cloud shadows over land surfaces [150, 152]. Their strength relies on the fact that no assumption is made on the cloud height. Instead, once cloud location is known from a clustering approach on the visible and thermal IR AVHRR channels, the extent of cloud shadows is derived from geometrical (relative position of the Sun, cloud and satellite) and spatial IR homogeneity considerations over neighboring regions to the cloud edges. Finally, the cloud shadow extent allows to estimate the cloud top height from basic geometric formulas [151].

3.6.1.4 Surface albedo

To accurately retrieve the cloud optical depth, the surface contribution to the measured signal has to be assessed carefully. Indeed, as illustrated in figure 2.10, simulated plane–parallel RTM relationships between the TOA visible radiances and the cloud optical depth exhibit a strong dependence on the surface albedo. It was demonstrated that any uncertainty on the surface albedo leads to systematic bias on cloud optical depth retrievals [84, 118] as well as to a reduction of the cloud detection sensitivity [138, 141]. Moreover, for optically thick clouds ($\tau \geq 9$), asymptotic theory demonstrated that any uncertainty in the surface albedo $\Delta\alpha$ results in a systematic offset on cloud optical depth retrievals by an amount given by

$$\Delta\tau = \frac{4}{3(1-g)(1-\alpha)^2}\,\Delta\alpha, \tag{3.2}$$

where g is the asymmetry factor of the cloud scattering phase function [84]. This implies that RTM LUTs used for the cloud optical depth inversion must be parameterized accordingly. Furthermore, it results that the surface albedo must be estimated for each observed scene prior to any inversion.

From the previous literature review, we can note that various assumptions are being made for the estimation of the surface albedo in the cloud properties retrieval techniques which have been reviewed previously. Some approaches use climatological surface albedo maps [85, 130] which are usually only available at lower spatial resolution while their temporal sampling is either monthly or seasonal. Others assume constant behaviour at a given time over pixel tiles [116, 117] which result in geometric "patchy" artifacts and discontinuity of cloud properties at tile borders, but are dynamically refreshing surface albedo with time by using *detected* clear–sky scenes. However, a cruder approximation has also been used by some schemes [134]. It consists in assuming a fixed surface albedo for both ocean and land.

3.6.2 Instrumental sources

3.6.2.1 Digitization

The energy measured by the sensor at TOA is converted as discrete brightness levels or *counts* by the on board acquisition electronics. Therefore, every measurement has an intrinsic uncertainty of ± 0.5 count. Such uncertainties result in errors on the cloud optical depth retrievals reaching up to 20 % for an 8–bit digitization* and showing a strong dependence on cloud optical depth and solar zenith angle [127].

3.6.2.2 Calibration

To relate discrete voltage measurements from sensors to a physics quantity, i.e. the radiance, one needs an equation between the radiance and the counts. This relationship is usually called the *calibration* of the instrument. Unfortunately, even nowadays, visible channels of meteorological imagers are not calibrated in an absolute sense as it is the case for their IR bands†. Since sensors suffer from aging due to the extreme space weather conditions, any pre–launch calibration must be replaced by its vicarious counterpart. Such calibration is based on the comparison between measurements of clear–sky regions associated to almost constant surface albedos such as bright desert and ocean and RTM simulations of the associated TOA radiances (see [63] for SEVIRI). This obviously introduces errors to the converted imager radiances. It can be shown that a 5 % uncertainty in the calibration results in errors on the cloud optical depth retrievals reaching up to 50 % and showing again a strong dependence on cloud optical depth and solar zenith angle [127].

3.6.3 Assumption sources

3.6.3.1 Scene geometry and spatial resolution

It is obvious from a purely geometrical point of view that the viewing zenith angle has an influence on the estimated cloud fraction of a scene. Indeed, this subject has been addressed in a study using coincident GOES–E and GOES–W measurements [107]. It was demonstrated

*SEVIRI uses a 10–bit digitization [148].

†This is generally achieved by a controlled black body cavity within the instrument which is checked regularly during its lifetime to monitor any drift from the pre–launch measured specifications.

that the cloud fraction can be enlarged up to 30 % for all cloud types due the resolution change of the footprints according to the viewing zenith angle. However, distinct parameterization of the cloud fraction according to the viewing zenith angle have been derived for various broken cloud shapes to reduce such bias in climatological datasets.

Besides any scene geometry considerations, the spatial resolution of the instrument has also a direct effect on the estimated cloud fraction [182]. Landsat thematic mapper (TM) data were used to test this hypothesis allowing to simulate various spatial resolution imagers up to meteorological instruments. While the impact of sensor resolution is small for pixel sizes less than 0.25 km, it is significantly larger for pixel sizes above 1 km due to the increase of partially cloud filled pixels and thus, the estimated cloud fraction exhibits a dependence according to the cloud type.

3.6.3.2 RTM input atmospheric parameters

As mentioned previously, RTM LUTs are generated for a small set of ideal scenes. Such scenes assume fixed background tropospheric and stratospheric profiles of aerosols, cloud effective particle radii and standard atmospheric gaseous profiles. However, observed scenes exhibit natural variations of these parameters which thus lead to errors in the cloud optical depth retrievals. By using realistic uncertainties on these 3 parameters, it was shown that the error on the cloud optical depth is not larger than 5 % for the atmospheric parameters. In contrast, a variation of cloud effective particle radius from 10 to 22 μm leads to errors reaching up to 15 % and showing again a strong dependence on cloud optical depth and solar zenith angle [127].

3.6.3.3 Cloud phase function

As noted in section 2.4.2, the cloud phase function used in the RTMs plays a central role when LUTs computations are performed at high angular sampling. Indeed, any accurate radiance calculation requires a detailed modeling of the cloud phase function. Moreover, it is obvious from figure 2.6 that liquid water and ice clouds exhibit significantly different angular scattering behaviors. Therefore, any parameterization of the cloud phase function using the Henyey–Greenstein approximation or the assumption of spherical particle for ice clouds results in discrepancies of the simulated radiances. Recent studies demonstrated that the influence of ice crystal shape results in relative differences of up to 70 % for cloud optical depth retrievals [56]. This can be explained by the fact that the asymmetry parameter as well as the single scattering albedo are more sensitive to crystal shape than to particle size distributions, especially at non–absorbing visible wavelengths [101].

3.6.3.4 RTM LUT nodal interpolation

All cloud properties retrieval algorithms based on RTM comparisons for the inversion of radiances or reflectances are relying on a fixed set of LUTs parameterized according to selected scene geometries*. But the retrieval of the cloud optical depth from a satellite scene requires to interpolate the LUTs to its specific geometry for the inversion. Therefore, this step necessarily

*They are generally chosen linearly in the angle or the cosine of the angle.

introduces some level of uncertainty in the retrievals [110]. It turns out that the largest errors occur for scattering angles where the cloud phase function is rapidly varying (see figure 2.6) since no interpolation scheme is able to capture its complex features from a coarse angular sampling. It was demonstrated that the linear interpolation method on the scene geometry and logarithm of the cloud optical depth is the best trade–off between the reflectance errors due to interpolation and computational requirements.

3.6.3.5 Plane–parallel modeling

As already mentioned in section 3.1.3, the plane–parallel assumption can result in significant bias with respect to the exact 3–D RT formalism. From the previous literature review, the vast majority of cloud properties retrieval schemes based on comparison with RTM simulations assume the validity of the IPA, i.e. that each pixel within the FOV can be treated independently from its neighbors. However, horizontal photon transport from adjacent pixels can affect the TOA measurements in various ways:

- The radiance of clear pixels located in the vicinity of cloud edges can be enhanced due to the extra scattering of radiation from the side of the cloud.
- Inversely, the radiance of cloudy pixels located in the vicinity of cloud edges can be reduced due to the fraction of the radiation exiting from the side of the cloud.
- The radiance of cloudy pixels can be reduced due to the shadowing from neighboring higher cloudy pixels.
- The radiance of cloudy pixels can be enhanced due to the extra scattering from neighboring illuminated sides of clouds.

It is therefore obvious that 3–D effects tend to increase the uncertainty of any cloud detection and cloud properties retrieval scheme.

Depending on its "conservativeness" (see section 3.2), a cloud detection scheme will be biased differently with respect to the true cloud amount. Indeed, cloud conservative algorithms underestimate the cloud fraction, while clear conservative approaches highly overestimate it [193].

The systematic enhancement of clear–sky pixel reflectances in the vicinity of cloud edges due to 3–D effects has been demonstrated by several studies. The analysis of a large MODIS dataset has shown that such enhancement can extend to about 15 km from the cloud edges and is larger near illuminated than shadowy cloud sides [173]. Moreover, these enhancements are stronger at shorter wavelengths and in the neighborhood of optically thicker clouds. It results that any IPA aerosol optical depth retrieval scheme will exhibit spurious correlation between cloud optical depth and overestimated aerosol concentrations in those clear–sky areas.

Theoretical simulations of 3–D cloud fields for typical MODIS footprints have shown that 1–D cloud optical depth retrievals almost exhibit no bias from their true values for spatial resolutions of meteorological imagers* [171]. It was also demonstrated that the magnitude of the uncertainty on 1–D cloud optical depth retrievals due to 3–D effects tends to increase

*from a few hundred meters to a couple of kilometers with cloud optical depth and solar zenith angle. Such increase of the uncertainty with respect to the solar zenith angle as well as its decrease according to the viewing zenith angle is also found for overcast marine stratus layers due to their undulating cloud tops even if they are generally considered as the prototypical plane–parallel clouds [80, 94]. Finally, analysis of one year of MODIS global cloud optical depth retrievals illustrated a stronger dependency of these retrievals to the viewing zenith angle for inhomogeneous than homogeneous cloud fields[*] at oblique sun illumination [172].

3.7 Adopted strategy for GERB

As already mentioned in section 1.2, the purpose of this work is to adapt or develop a sceneID for the RGP allowing to select the CERES TRMM shortwave ADMs for the radiance–to–flux conversion scheme. Since these ADMs have been stratified according to 4 features — a fixed surface map, the cloud fraction, the cloud optical depth and cloud thermodynamic phase — any implemented sceneID must at least retrieve this minimal set of parameters for every observed scene.

The most obvious strategy would consist in adapting the complete CERES sceneID to the SEVIRI imager characteristics. Indeed, this would guarantee almost no discrepancy between CERES scenes used to compute the ADMs and GERB scenes on which the ADMs are applied. Unfortunately, the CERES sceneID cannot meet the operational near–realtime constraint of the GERB processing. Such constraint requires that the complete processing should not last more than the time between two SEVIRI repeat cycles, i.e. 15 minutes[†]. Similarly, the implementation within the RGP of other iterative cloud optical depth retrieval approaches is discarded for the same reason. It is thus clear that the sceneID, at least in its first version[‡], will only estimate the four features needed to adequately select the ADMs through a non–iterative cloud properties retrieval scheme.

Since the sceneID is primarily used for the ADM selection, a systematic bias could be introduced in the GERB fluxes if the GERB and CERES estimations of the cloud fraction significantly differ due to distinct spatial resolutions of their imager. Indeed, it would mean considering different scenes[§] for the computation of the CERES TRMM ADMs and their use in the GERB radiance–to–flux conversion. Nevertheless, such problem is mitigated by the fact that the VIRS imager (on board of TRMM) used to build these ADMs and SEVIRI have similar spatial resolutions of 2.4 and 3 km (at nadir), provided that both cloud detection schemes exhibit compatible results.

Since the GERB project was created to perform climate studies and monitoring, it aims to produce long records of data with a constant accuracy[¶]. This can only be achieved by controlling all processing steps, from the acquisition to the delivery of end–user products. Therefore, this does not require the best but the most *stable* and *robust* sceneID with respect to ancillary data and changes of imager calibration. It results that any sceneID relying on external

[*] based on the local gradient of 11 μm BT

[†] In fact, the current implementation of the CERES sceneID on SEVIRI data takes about 3 hours to process a single repeat cycle.

[‡] Edition 1 software collection

[§] i.e. associated to different cloud fractions

[¶] This is needed to detect any trend on TOA fluxes over a decade which could result from the global warming.

data such as NWP fields does not meet this stability criterion*. We do not even mention the philosophical dilemma which could arise if the RGP would rely on any NWP model since the GERB experiment is also aiming to validate NWP and climate models.

These constraints pushed us to develop a *home–made* sceneID satisfying all these requirements. We choose to rely on non–iterative retrieval of the cloud optical depth from direct comparison between TOA visible measurements and RTM LUTs assuming fixed effective particle radii for liquid water and ice clouds. Moreover, for consistency, we decide to rely on a threshold test in the cloud optical depth retrieval for the cloud mask which thus implicitly classifies our approach among the *cloud conservative* algorithms. However, it was demonstrated in the section 3.6.1.4 that a significant part of the uncertainty in the cloud optical depth retrievals arises from the misestimation of the TOA clear–sky surface signal. Therefore, we have developed a dedicated technique to estimate composite TOA clear–sky reflectances for GEO imagers at pixel–scale resolution. The prototype of this method is detailed in the next chapter. It was developed and validated on Meteosat–7 data.

*For example, the operational NWP model can be updated anytime.

Chapter 4

Pixel–scale composite TOA clear–sky reflectances for Meteosat–7 visible data*

This chapter describes the development and validation of an algorithm applied to the Meteosat–7 imager and allowing to estimate composite top–of–the–atmosphere clear–sky visible reflectances at native pixel–level.

Abstract

A new method to estimate composite top of the atmosphere (TOA) visible clear–sky reflectances for wide narrowband geostationary satellites such as the Meteosat constellation is presented. This method relies on a priori knowledge of angular variations of TOA broadband reflectances associated with clear–sky conditions above mean surface types through the use of the clear–sky Clouds and the Earth's Radiant Energy System (CERES) shortwave broadband angular dependency models (ADMs). Each pixel (or Earth location) viewed from such geostationary imager at a given day–time is associated with a reflectance time–series made up of its chronological daily measurements. This time–series can be seen as a clear–sky visible narrowband reflectance curve of the associated pixel surface plus an additive random noise modeling cloudy conditions above it. Based on this assumption, TOA clear–sky broadband reflectances extracted from the CERES ADMs are used to compute curve driven 5th percentiles on these time–series in order to estimate the TOA clear–sky visible narrowband reflectance curves for all pixels while the percentile approach exhibits only a reduced sensitivity to cloud shadows. Benefits of our method are discussed towards its application to 7 months of Meteosat–7 day–time visible narrowband measurements. Finally, the performance of our algorithm is assessed through comparisons with its predicted and associated International Cloud Climatology Project (ISCCP) DX clear–sky values with respect to a visually generated clear–sky pixels database.

*Adapted transcription of Ipe, A., N. Clerbaux, C. Bertrand, S. Dewitte, and L. Gonzalez, Pixel–scale composite top–of–the–atmosphere clearsky reflectances for Meteosat–7 visible data, *J. Geophys. Res.*, 108(D19), 4612, doi:10.1029/2002JD002771, 2003.

4.1 Introduction

INFERENCE of the top of the atmosphere (TOA) visible clear–sky reflectances from satellite narrowband imagers is crucial in remote sensing. Such a scheme is the first step of nearly all cloud algorithms which aim to retrieve cloud parameters (see [141] for a non–exhaustive historical survey of cloud algorithms) in order to study, for example, cloud radiative feedbacks. The TOA visible clear–sky reflectances are usually used by these algorithms to detect the presence of clouds in the observed scenes. Moreover, with the use of radiative transfer models, these TOA visible clear–sky reflectances can be inverted to derive surface properties such as biomass estimation over vegetation through vegetation indices and surface albedos. In addition, a monitoring of these surface properties may also be indicative of climate variations.

A number of algorithms devoted to perform this clear–sky determination can be found in the literature. These are generally based on the common assumptions that (a) clear–sky visible reflectance variations are smaller in time than in space (especially over land), and (b) surface reflectance variations are smaller than variations associated with the cloud reflectances. As an example, [108] generated composite clear–sky images from the Geostationary Operational Environment Satellite (GOES) data by applying a minimum reflectance threshold criterion to identify clear scenes as a function of surface type and geographic region. Unfortunately, to avoid cloud contamination, the threshold values have to be extracted from some sub–sampling of minima values in the reflectance time–series with respect to some standard deviation criteria. This therefore requires more information on the reflectance distributions than simply the minimum values. Moreover, as pointed out by [104] such a technique of clear–sky determination is sensitive to the scene geometry variations and to the atmospheric noise such as cloud shadows. Regarding the International Cloud Climatology Project (ISCCP), [137] developed an algorithm based on a spatial and temporal homogeneity test (as well as several geotypes) to be applied at the regional grid cells. In addition, scene geometry variations are corrected to the first order according to the solar zenith angle. ISCCP also relies on the empirical bidirectional reflectance model from [108] for clear–sky ocean and assumes isotropic clear–sky reflectance over land although it has been established that the anisotropy of the land scenes is significant [109].

Being involved in the Geostationary Earth Radiation Budget (GERB) radiometer ground segment (which aims to deliver near–realtime estimates of the TOA radiative broadband fluxes at the high spatial resolution of 10 km at nadir with the help of the Spinning Enhanced Visible and InfraRed Imager (SEVIRI) for the limited geographical area covered by Meteosat Second Generation (MSG) satellite), one of Royal Meteorological Institute of Belgium (RMIB) pre–operational activities was to test the RMIB GERB Processing (RGP) on Meteosat–7 (MS7) data and to derive GERB–*like* products without any associated broadband radiometer information. Such data after adequate validation with real GERB products will certainly prove to be valuable to the future GERB users by extending back in time the availability of GERB data prior to the routine exploitation of MSG. In order to process MS7 data by the RGP as suggested, we need to generate clear–sky images for the MS7 visible narrowband channel at every 30 minutes sampling day–time. Algorithms as previously developed to deal with the Scanner for Radiation Budget (ScaRaB) data [159] and/or the ISCCP data are not suited for GERB data processing since we need to retain the high spatial resolution of MS7 visible images (2.5 km at nadir). Moreover, the composite clear–sky images as produced by using such algorithms are time–averaged over a couple of hours which is incompatible with the high temporal resolution of MS7 (30 minutes) and the geostationary platforms (large variations in the Sun–Earth–satellite viewing geometry).

This chapter aims therefore to present an innovative method which accounts for high Sun–Earth–satellite (or scene) viewing geometry variations (see figure 4.1(b)) and a high spatial resolution of the imager when estimating composite TOA clear–sky visible reflectances from narrowband geostationary satellite measurements. The benefits and simplicity of this new approach are discussed towards its application to 7 months of MS7 day–time visible measurements. In order to assess the performance of this new method compared to region–based algorithms found in the literature, comparisons are performed between those two approaches and a database of MS7 clear–sky pixels.

In the following *visible* has to be understood as visible narrowband and *shortwave* refers to the spectral interval of $0.3 - 4.0$ μm.

4.2 Clear–sky detection algorithm

As noted by [141], grassland and desert surface reflectances can exhibit large spatial variations. Thus, considering each pixel (i.e., fixed location on Earth surface) independently, we only have to deal with a visible reflectance distribution affected by the surface temporal variations, the illumination and the cloudiness. Surface variations are mainly known to occur over vegetated surfaces and are a function of the vegetation age and fractional coverage. According to [104] the seasonal surface reflectance variations over Africa (which is located in the center of the field–of–view (FOV) of MSG) are small due to the presence of large areas of desert and evergreen forests. Therefore, assuming that vegetated surfaces are stable over a restricted time period, the signal measured by the instrument during this period can be considered as only a function of the scene viewing geometry and cloudiness. For a given day–time hour (i.e., time slot) and a given pixel viewed from a geostationary imager we can associate the visible reflectance time–series made up of its chronological daily visible measurements. This time–series can then be split into two components: (1) a base curve representative of the clear–sky conditions, and (2) a noise component representing the clouds contributions above the ground surface associated to the pixel. Note that for areas with broken clouds, an additional effect has to be taken into account: the cloud shadows on neighboring pixels decrease the reflectance below the expected clear–sky value. Such an effect is well highlighted in figure 4.1 where the sudden and abrupt decrease of the reflectance value measured on day 343 compared to the other displayed MS7 reflectances can easily be explained by the neighboring pixels cloud shadow contamination, when looking at the images.

MS7 visible narrowband images have been used to illustrate the performance of our algorithm, but this technique is obviously applicable to any geostationary imager with a similar wide visible channel. Registered visible MS7 count images (coded on 8 bits) were retrieved from the Meteosat Archive and Retrieval Facility (MARF) in 5000×5000 pixels. These count values were then converted into reflectances with the help of the EUMETSAT time–dependent count–to–radiance calibration scheme from [63]. This scheme provides coefficients which are linearly and continuously varying with time, thus it is expected that no discontinuities in the measured reflectances are introduced, due to updated calibration information as could be the case for other imagers.

Here, we propose to use the clear–sky Clouds and the Earth's Radiant Energy System

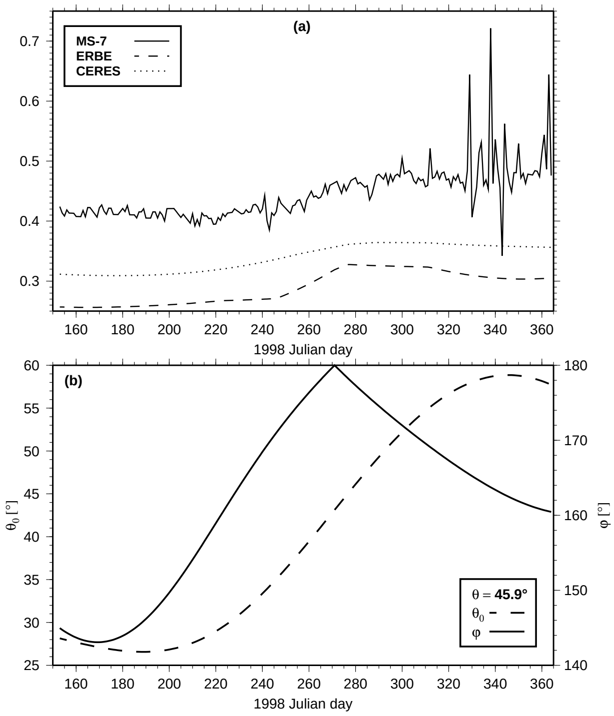

Figure 4.1 *– (a) Meteosat–7 visible reflectance time–series, ρ_m, and associated clear–sky shortwave ERBE and CERES reflectances, ϱ, according to (b) scene viewing geometry variations (θ_0 = solar zenith angle, θ = viewing zenith angle and φ = relative azimuth angle) from the 12:00 UTC daily measurements over a bright desert pixel (27.18°N, 30.12°E).*

(CERES) shortwave broadband angular dependency models (ADMs) [99] and their associated geotype classification (see figure 4.2) to extract the visible clear–sky base curve from the MS7 signal. ADMs used in this chapter follow the definition from [163]. They are built for some scene stratifications—surface geotypes, cloud fractional covers, cloud phase and cloud optical depth for CERES, coarser surface geotypes and cloud fractional covers for Earth Radiation Budget Experiment (ERBE)—and some angular bins for scene viewing geometry (see table 4.1). Basically, an ADM is constituted by an anisotropic function R

$$R(\theta_0, \theta, \varphi) = \frac{\pi\, L^{\uparrow}(\theta_0, \theta, \varphi)}{F^{\uparrow}(\theta_0)} \tag{4.1}$$

and a broadband albedo A

$$A(\theta_0) = \frac{F^{\uparrow}(\theta_0)}{E_0\, \cos\theta_0} \tag{4.2}$$

where, θ_0, is the solar zenith angle, θ, is the viewing zenith angle, φ, is the azimuth angle relative to the solar plane ($\varphi = 0$ corresponds to forward scattering), $L^{\uparrow}$, is the mean TOA outgoing broadband radiance for given scene type $[\mathrm{W} \cdot \mathrm{m}^{-2} \cdot \mathrm{sr}^{-1}]$, $F^{\uparrow}$, is the mean TOA outgoing broadband flux for given scene type $[\mathrm{W} \cdot \mathrm{m}^{-2}]$ and E_0, is the solar constant corrected for Sun–Earth distance [W · m^{-2}]. By multiplying equation 4.1 and 4.2, we obtain

$$R(\theta_0, \theta, \varphi) \cdot A(\theta_0) = \frac{\pi L^{\uparrow}(\theta_0, \theta, \varphi)}{E_0 \cos\theta_0} = \varrho(\theta_0, \theta, \varphi)$$

where, ϱ, is the TOA shortwave bidirectional reflectance distribution function (BRDF) for the associated mean scene type. Thus, clear–sky ADMs allow us to compute mean TOA shortwave BRDFs associated with some surface types under clear–sky conditions.

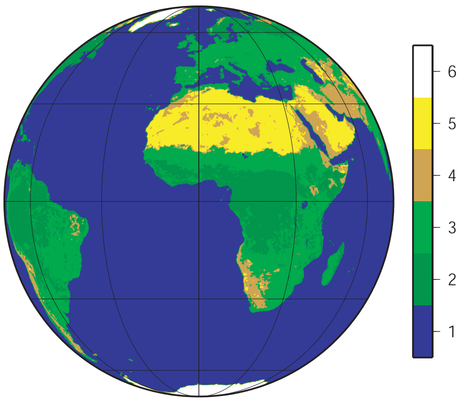

Figure 4.2 *– CERES ADMs surface geotypes as seen by Meteosat–7 imagers (1 = ocean, 2 = moderate–to–high vegetation cover, 3 = low–to–moderate vegetation cover, 4 = dark desert, 5 = bright desert, 6 = snow or ice) [99]. ERBE ADMs surface classification is obtained by grouping dark and bright deserts in one desert class and low–to–moderate and moderate–to–high vegetation covers in one land class.*

Table 4.1 *– ERBE [162] (first of each pair of columns) and CERES [99] (second of each pair of columns) ADM angular bin definitions in degrees.*

Solar zenith angle (θ_0)		Viewing zenith angle (θ)		Relative azimuth (φ)	
0–26	0–10	0–15	0–10	0–9	0–10
26–37	10–20	15–27	10–20	9–30	10–30
37–46	20–30	27–39	20–30	30–60	30–50
46–53	30–40	39–51	30–40	60–90	50–70
53–60	40–50	51–63	40–50	90–120	70–90
60–66	50–60	63–75	50–60	120–150	90–110
66–73	60–70	75–90	60–70	150–171	110–130
73–78	70–80		70–80	171–180	130–150
78–84	80–90		80–90		150–170
84–90					170–180

While ERBE and CERES ADMs are built from shortwave measurements, they provide some qualitative knowledge on angular variations of TOA visible BRDFs for associated surfaces. This is illustrated in figures 4.1(a) and 4.1(b), where we plotted TOA Meteosat–7 visible reflectance and ERBE and CERES clear–sky shortwave reflectance time–series for a given pixel and its associated scene viewing geometry variations. We can observe that ERBE and CERES curves have shapes similar to the clear–sky visible reflectance base curve that we want to estimate, although they are offset from each other. As shown in figure 4.1(a), the use of CERES ADMs leads to a TOA broadband reflectance time–series which is less broken than when using ERBE ADMs due to their coarser angular resolution. The offset between the CERES and ERBE curves can be explained from differences in surface type classification and in clear–sky conditions (cloud fractional cover up to 5 % for ERBE and 0.1 % for CERES) for the ADMs. By contrast, the offset between Meteosat–7 and these shortwave reflectance curves is due to the fact that the ADMs were built from shortwave measurements and global averaging of each geotype's responses. For a given day ($d^\star$= current Julian day) and time slot ($t^\star$= hour) we build the composite TOA visible clear–sky image ρ_{cs} by using for each pixel the following formulation:

$$\rho_{\mathrm{cs}}(x,y,d^\star,t^\star) = \alpha(x,y,d^\star,t^\star,N)\cdot\varrho_c(x,y,d^\star,t^\star)$$

where, x and y, are the pixel coordinates in images and α, is a multiplicative factor determined for a given time period of N days. This factor is used to shift the shortwave CERES reflectance curve, ϱ_c, in such a way that only 5 % of the measured visible reflectances over the given time period, ρ_m, are kept below the CERES curve. This can be seen as a curve driven 5th percentile search which reduces to estimate:

$$\alpha(d^\star,t^\star,N) = \text{5th percentile of } \frac{\rho_m(d,t^\star)}{\varrho_c(d,t^\star)} \text{ for } d = d^\star - N,\ldots,d^\star.$$

(Note that we implicitly assumed the pixel coordinates dependence in our formulation). It must be noted that such a scheme relies on the assumption that clear–sky shortwave CERES BRDF, ϱ_c, curve and clear–sky visible Meteosat–7 base curve, ρ_{cs}, only differ by a constant multiplicative factor over some temporal extent, N, (i.e., some limited range in the scene viewing geometry). Restating differently the previous assumption, we are supposing that these two curves only differ by their respective albedos, A, and not by their anisotropy functions, R. Note that cruder approximations can be found in the literature. As an example, [64] assume equality of narrowband and broadband albedos. [109] derive regression equations from coincident measurements of narrowband and broadband reflectances according to scene conditions. However, as suggested by [92], no significant improvement is found on the regressions of either viewing and solar zenith angles. In figure 4.3, we have plotted the ratio between ρ_m and ϱ_c associated to the values of figure 4.1. As one can see in figure 4.1(b), the maximum variation of θ_0 over 60 days is about 20° while the corresponding variation of the base curve of the ratio (associated to clear–sky conditions) is limited to about 6 %.

4.3 Choice of parameters

It is worth pointing out that the time period, N, over which the percentile is computed can not be too short, otherwise the method reduces to a search for the minimum value of $\rho_m(d,t^\star)/\varrho_c(d,t^\star)$. This will therefore lead to an unacceptable sensitivity towards cloud shadows (characterized by an abrupt and sudden decrease of the measured reflectance) as previously mentioned. On the other hand, a too large time period could violate our assumption regarding the stability of vegetation. According to [104] some portions of the African tropical land area present persistent cloudiness over more than 30 days. This can lead to large errors in the retrieved clear–sky reflectances from algorithms using a base period of time lower than 60 days. The influence of the time period length on the computed visible clear–sky reflectance

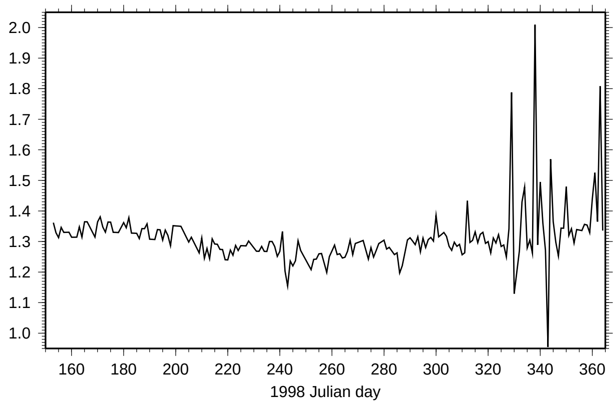

Figure 4.3 *– Ratio of the Meteosat–7 visible reflectances, ρ_m, and associated clear–sky shortwave CERES reflectances, ϱ_c, for the same pixel as in figure 4.1.*

values is displayed in figure 4.4. As we can see, the smoothness of the clear–sky curve increases with increasing N. This is a direct effect of our statistical approach. Moreover, our implicit assumption regarding the proportionality between the shortwave CERES and the visible clear–sky reflectance curves over a given time period is not necessarily valid for large N. Indeed, figure 4.4 clearly indicates that as the value of N increases, the computed clear–sky visible reflectances tend to be underestimated. For all these reasons, setting N equal to 60 days appears to be a good compromise.

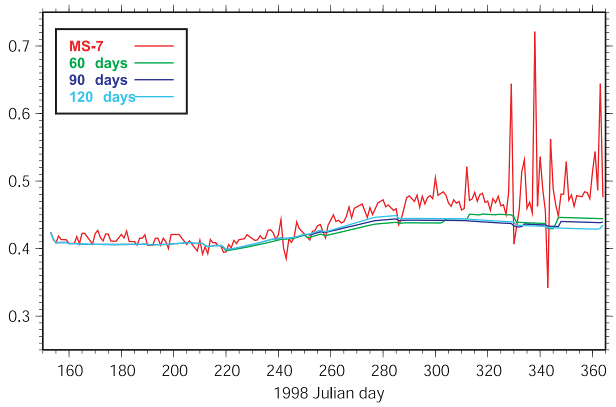

Figure 4.4 *– Reflectance time–series, ρ_m, of the same Meteosat–7 pixel as in figure 4.1 and TOA visible clear–sky values, ρ_{cs}, for several N as predicted by our algorithm.*

In the previous section, we chose 5 % as the percentile value for our algorithm. As already mentioned, the measured signal can be seen as the clear–sky base curve plus a random additive noise representing the clouds contribution (positive) and the cloud shadows effect (negative). A too small threshold on the percentile value would lead to unacceptable sensitivity to shadow occurrences, while a too high value would result in the selection of a cloudy

α value to compute the clear–sky reflectance. Thus, fixing the threshold to 5 % guarantees that we will successfully filter in our scheme up to 3 measurements associated to cloud shadows within 60 days, while requiring at least 4 clear–sky reflectances on the same time period. Qualitative tests have shown the spatial and temporal robustness of this value.

Nevertheless, in the following section, these values will be implicitly validated. Note that the applicability of our algorithm is not limited to land surfaces. Figure 4.5 illustrates its results over an ocean surface pixel.

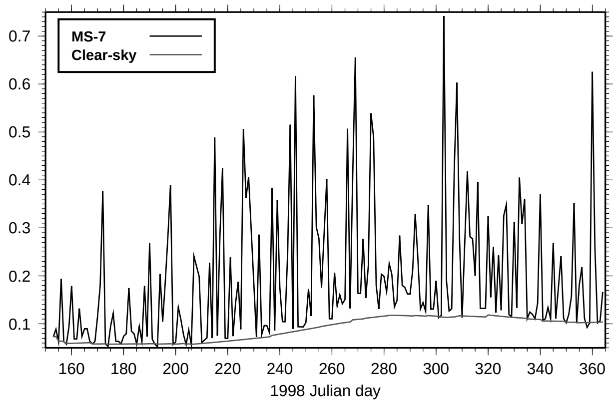

Figure 4.5 *– Meteosat–7 visible reflectance time–series,* ρ_m*, and TOA visible clear–sky values,* ρ_{cs}*, as predicted by our algorithm (*$N = 60$ *days) from the 12:00 UTC daily measurements over an ocean pixel (*$4.42°S$*,* $1.28°E$*).*

4.4 Algorithm performance

In order to assess the improvement of our method with regards to region–based algorithms such as the one implemented in ISCCP, we have built a clear–sky pixels database by visually selecting cloud–free pixels. However, it is almost impossible to guarantee that such pixels are truly clear (see chapter 2, section 2.4.1). But cloud contamination is expected to be limited since the selection of these pixels was carried out by enhancing the contrast of both the MS7 visible and thermal infrared (IR) channels and considering neighboring textural information to discard thin clouds in the FOV. Contamination by aerosols on the other hand implies a larger impact on the visible measurements over the low albedo ocean surfaces. However, this issue is difficult to overcome due to the limited aerosol estimation capabilities of MS7. Due to the exhaustive manual work this step requires, we only have selected 3 days with one month interval between each others, i.e. the firsts of August, September and October 1998. Those clear–sky pixels were selected from 8:00 to 16:00 UTC on a hourly time step basis and in every surface geotype. For convenience, we have chosen to stratify them according to the simple ERBE surface classification (ocean, vegetation and desert). Note that the day and hour samplings in this database does not decrease its generality because we are capturing during these three months the main temporal changes in the reflectance of vegetation coverage. However, to easily compare our results with ISCCP, we only considered pixels belonging to ISCCP time slots, i.e., 9:00, 12:00, and 15:00 UTC (reduced database). Table 4.2 gives the population within each ERBE surface class. Finally, for each pixel of this database, we have computed its clear–sky reflectance as estimated by our algorithm with the 5th percentile and $N = 60$ days. The comparisons between these values and the real ones are shown in tables 4.3 and 4.4.

Table 4.2 *– Number of pixels for each ERBE geotype in the clear–sky reduced database.*

Geotype	Number of pixels	Fraction [%]
ocean	8030	13
vegetation	18575	31
desert	33492	56

To directly compare our results with ISCCP, we have selected the associated MS7 ISCCP Pixel Level Cloud Products with a native spatial resolution of 30 km [142]. From these data, we have converted the extracted composite (on 10 days) clear–sky radiances into reflectances using the absolute ISCCP calibration across all satellites participating in this project [20]. Then, for every clear–sky pixel in our reduced database, we have taken the reflectance value associated to the nearest ISCCP data point. To cope for possible differences between ISCCP and EUMETSAT calibrations, we recomputed our cloud–free reflectance database according to ISCCP calibration. The comparisons of both results are given in the second part of tables 4.3 and 4.4, and the associated scatter plots are given in figures 4.6.

Table 4.3 *– Statistics (bias, standard deviation and root mean square deviation) on absolute errors of clear–sky reflectances according to the RGP and ISCCP algorithms for the reduced database.*

	RMIB GERB Processing			ISCCP Processing		
Geotype	bias	stddev	rmsd	bias	stddev	rmsd
ocean	0.003	0.004	0.005	0.017	0.005	0.017
vegetation	-0.012	0.011	0.016	-0.002	0.024	0.024
desert	-0.017	0.016	0.023	-0.004	0.043	0.043

Table 4.4 *– Statistics (bias, standard deviation and root mean square deviation) on relative errors of clear–sky reflectances according to the RGP and ISCCP algorithms in percent for the reduced database.*

	RMIB GERB Processing			ISCCP Processing		
Geotype	bias	stddev	rmsd	bias	stddev	rmsd
ocean	8.4	11.9	14.6	43.0	15.7	45.8
vegetation	-7.0	5.7	9.0	0.4	14.1	14.1
desert	-5.9	5.2	7.9	-0.2	16.2	16.2

As errors for each method have been computed according to a priori two different calibration schemes, we should first check and account for possible discrepancies between them before proceeding with any conclusion based on these results. It can be demonstrated by simply plotting (not shown) the measured reflectances for all (reduced) database clear–sky pixels that ISCCP and EUMETSAT calibration are almost identical. Indeed, such pairs of values have a correlation coefficient of 0.999885 while a linear best fit on these gives the law

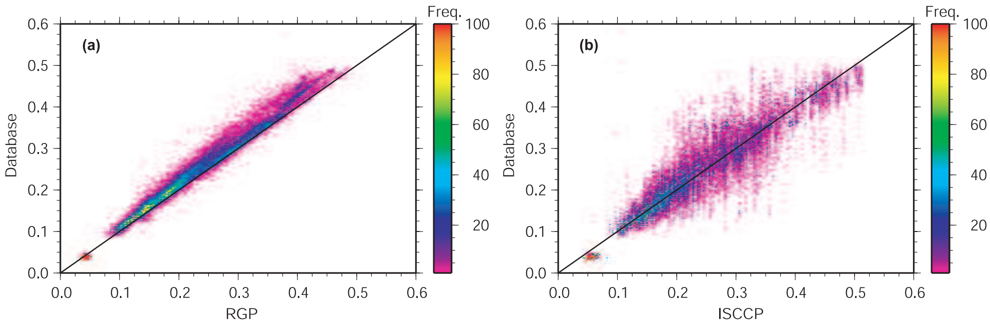

Figure 4.6 *– (a) Estimated RGP and (b) ISCCP clear–sky reflectance vs. clear–sky (reduced) database value.*

$\rho_E = 0.9927 \times \rho_I$. Thus, the above errors in these tables can be directly compared. We notice that the overall error (rmsd) of our method is significantly smaller than for ISCCP. This is also illustrated in figures 4.6 where the ISCCP plot exhibits a larger scatter. Looking at the standard deviation of the relative error in table 4.4, we notice that the scatter due to our method is about 10 % lower than ISCCP for vegetation and desert (surface types associated with large reflectance values), while for ocean which has usually a minimal response in the visible spectrum (≤ 0.05) it is about 4 % lower.

However, except for the ocean, where there seems to be some problem with ISCCP clear–sky algorithm, our scheme systematically has a larger bias than ISCCP. This could result from the three additional effects occurring and contributing to some extent to the signal: (a) variability due to changes in aerosol content, (b) variability induced by the discrete quantification of the detectors (8 bits for MS7) and (c) variations due to the movement of the satellite which are compensated in the image registration process (interpolation) on a fixed geolocation grid. These three effects are clearly illustrated in figure 4.4 before the 240th Julian day where all the previous days have cloud–free conditions while the reflectance time–series exhibits some random fluctuations around its mean clear–sky value. These perturbations can reach up to 10 % of the mean value for desert pixels and other surfaces with high reflectance values such as vegetation. Investigating more closely the sign of the bias in table 4.4, we notice that our method tends to underestimate the clear–sky values over land. This would suggest to increase the threshold above the 5th percentile over these surfaces*.

Moreover, our method was checked to perform well on other time slots. In table 4.5, we have given the statistics on the relative error distribution between RGP clear–sky estimates and associated values of the complete database (including all day–time hours from 8:00 to 16:00 UTC). One can notice these values are nearly identical compared to the ones found in table 4.4. We also performed a sensitivity study (not shown) on the percentile and time period N using the complete database which demonstrated that the chosen values from visual image inspection are giving the overall best results.

However, our database is not adequate to estimate the optimal percentile and time period, N, for each major surface class due to the difficulty of selecting pixels where cloud shadows

*Finding the optimal threshold would be an interesting study object, which has however not been done yet.

Table 4.5 – Statistics (bias, standard deviation and root mean square deviation) on relative errors of clear–sky reflectances according to the RGP for the complete database.

	RMIB GERB Processing			Population	
Geotype	bias	stddev	rmsd	Number of pixels	Fraction [%]
ocean	8.7	11.8	14.7	18855	10
vegetation	-6.5	6.8	9.4	60186	33
desert	-5.9	5.5	8.0	106494	57

occur in their associated time–series. It is primarily due to the fact that our clear–sky database was only built on three days of data. A possible future improvement of our method could be the estimation of such optimal parameters, but this step will need a clear–sky database covering a large temporal period (ideally one year).

4.5 Final remarks and perspectives

The new statistical method we develop to determine the composite clear–sky reflectance images in the visible part of the spectrum uses a priori knowledge of angular variations of surfaces reflectance through the clear–sky CERES broadband ADMs. The strength of these models is that they have been built from experimental data around the world over a long period of time, accounting therefore for correct averaged spatio-temporal responses for each of their surface classes.

Nevertheless, as illustrated in figure 4.7, some limitations appear in the presence of high occurrence of cloud shadows within the considered period of time. As we see, the 60–day values are moved down due to several minima in the recorded radiance time–series. A possible way to solve this weakness could rely on the determination of the optimal percentile and time period, N, for each surface geotype and according possibly to location. However, this requires further investigations through the building of an exhaustive spatial and temporal clear–sky pixels database*. Another technique could be the use of a cloud shadows detection scheme such as the one found in [152] in order to discard the associated reflectance values in the percentile computation.

Moreover, fresh snow covers due to their high visible reflectance responses (same order of magnitude as thick clouds) can lead to a misevaluation by our algorithm of the associated clear–sky values and the cloud properties retrievals. To remedy to this, a snow detection procedure is generally applied in the a posteriori cloud identification scheme, but this is beyond the scope of this chapter.

Finally, this method was shown to perform better than the ISCCP scheme on MS7. This should also hold for other geostationary satellites having similar MS7–*like* wide visible channels. Nevertheless, this technique should be applicable to both SEVIRI visible narrowbands (0.6 μm and 0.8 μm) by simply substituting in our method the CERES shortwave ADMs by the visible Polarization and Directionality of the Earth's Reflectances (POLDER) TOA ADMs as generated by [97].

*This requires visual image interpretation which is beyond the capabilities of a small team.

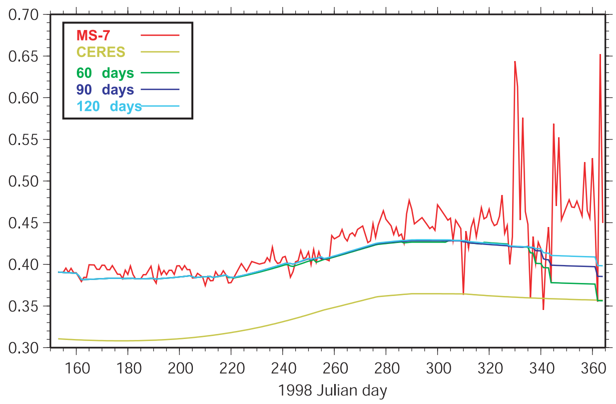

Figure 4.7 *– Meteosat–7 visible reflectance time–series, ρ_m, and its associated clear–sky broadband CERES reflectances, ϱ_c, according to the scene viewing geometry variations from the 12:00 UTC daily measurements over a bright desert pixel (28.13°N, 29.19°E) and our algorithm visible clear–sky predicted values ρ_{cs} for several N.*

Acknowledgments

This study was supported by the Belgian Science Policy Office (DWTC/SSTC) through the PRODEX–6 contract No. 15162/01/NL/SFe(IC).
The ISCCP DX data were obtained from the NASA Langley Research Center Atmospheric Sciences Data Center. The Meteosat–7 data were obtained from the MARF. All graphics and plots were made using The Generic Mapping Tools (GMT) software collection.
The authors are grateful to the anonymous reviewers for all their constructive comments.

Chapter 5

Cloud optical depth and cloud fraction retrievals using Meteosat–7 data*

This chapter describes the developement of a cloud optical depth retrieval and cloud mask algorithm applied to the Meteosat–7 imager and the comparison of its results to a polar retrieved datatset.

Abstract

The Geostationary Earth Radiation Budget (GERB) instrument was launched during the 2002 summer together with the Spinning Enhanced Visible and InfraRed Imager (SEVIRI) on board of the Meteosat Second Generation satellite. This broadband radiometer will aim to deliver near–realtime estimates of the top of the atmosphere radiative fluxes at high temporal resolution thanks to the geostationary orbit. To infer these fluxes, a radiance–to–flux conversion needs to be performed on measured radiances. Since we plan to carry out such a conversion by using the angular dependency models (ADMs) developed from the Clouds and the Earth's Radiant Energy System (CERES) experiment, the GERB ground segment will have to rely on some scene identification on SEVIRI data which mimic as close as possible the one from CERES in order to select the proper ADM. In this chapter, we briefly present the method we used to retrieve cloud optical depth and cloud fraction on footprints made of several imager pixels. We then compare the retrieval of both features on the same targets using nearly time–simultaneous Meteosat–7 imager and CERES Single Satellite Footprint data. The targets are defined as CERES radiometer footprints. We investigate the possible discrepancies between the two datasets according to surface type and cloud phase and, if they exist, suggest some strategies to homogenize GERB retrievals based on CERES ones.

5.1 Introduction

To derive the most accurate top of the atmosphere (TOA) solar fluxes from the measured Geostationary Earth Radiation Budget (GERB) [49, 66] broadband radiances, the Royal

*Adapted transcription of Ipe, A., N. Clerbaux, C. Bertrand, S. Dewitte, and L. Gonzalez, Validation and homogenization of cloud optical depth and cloud fraction retrievals for GERB/SEVIRI scene identification using Meteosat–7 data, *Atmos. Res.*, 72, 17–37, doi:10.1016/j.atmosres.2004.03.010, 2004.

Meteorological Institute of Belgium (RMIB) is planning to use the new angular dependency models (ADMs) from the Clouds and the Earth's Radiant Energy System (CERES) experiment [99]. They are due to replace and outperform the accuracy of the previous Earth Radiation Budget Experiment (ERBE) models [162]. To reach the highest level of confidence in the derived fluxes from the radiance–to–flux angular conversion, it is needed to select and use the corresponding ADM that would be applied by CERES to the measured scene types of each GERB footprint's pixel. This requires to perform a scene identification (sceneID) which gives similar results (i.e. features values) than those used to stratify the CERES ADMs. More precisely, it is crucial to remove any systematic bias between these two sceneID schemes.

As the GERB experiment aims to deliver products on a near–realtime basis (i.e. within 3 hours after the acquisition time), the overall RMIB GERB Processing (RGP) should not take more than the time period between two GERB/SEVIRI series of images (i.e. 15 minutes). In order to cope with this major time constraint, such a sceneID scheme for GERB is committed to remain simple and only extract the smallest needed set of features. It turns out that the minimal set required to select the more relevant ADM is defined by the cloud fraction, the cloud phase, the cloud optical depth and the surface type for each GERB pixel, or more specifically the mean of the feature values of all the Spinning Enhanced Visible and InfraRed Imager (SEVIRI) pixels (3 km at nadir) within this GERB footprint's pixel. The use of CERES ADMs in connection with measured footprints of similar spatial resolution than those used to build these ADMs (i.e., about 10 km at nadir, [184]) certainly avoids any new error source in the radiance–to–flux conversion which could arise from distinct spatial extents of GERB and CERES footprints. Hence, in the following, the term *GERB pixel* or *footprint* will not refer to the native spatial resolution of the instrument (50 km at nadir), but to a pixel's size of about 10 km. To reach such a resolution the GERB broadband measured radiances are being interpolated by some data fusion algorithm with the help of the Spinning Enhanced Visible and InfraRed Imager (SEVIRI) multispectral imager on board of the Meteosat Second Generation (MSG) satellite [148]. Briefly, the high spectral accuracy of GERB is combined with the high spatial resolution of SEVIRI. This is achieved by correcting the broadband radiance estimations from the 11 SEVIRI spectral channels with GERB measurements and by interpolating these correction coefficients to footprints of 3×3 SEVIRI pixels [60].

In this chapter, we shall focus on the determination of the cloud optical depth and cloud fraction. We will present a fast cloud optical depth retrieval algorithm which is not based on an iterative scheme as it is the case for the CERES experiment. Instead, it only uses visible narrowband radiances from an imager to estimate the cloud optical depth. Moreover, it does not require to priorly flag cloudy pixels by some cloud detection scheme (generally based on threshold tests applied to imager narrowband measurements). However, look–up tables computed using a radiative transfer (RT) model are still needed in order to link the measured quantities to cloud optical depth, but an innovative way to parameterize them will be given. The cloud fraction estimation is based on cloudy imager pixels detection within some defined footprint (typically of the size of GERB pixel); the cloudy test being simply a threshold on their associated cloud optical depth. Then, we will illustrate both retrieval schemes by applying them to Meteosat–7 (MS7) visible images. We will show comparisons of the RGP retrieved cloud optical depth and cloud fraction from Meteosat–7 simulated footprints and CERES associated features' values. We will then suggest some correction schemes on GERB cloud optical depth and provide the optimal threshold for cloudy/non–cloudy pixels which mimic as close as possible the CERES cloud optical depth and cloud fraction estimates. Finally, we will propose some strategies for more in–depth future comparisons of CERES and SEVIRI cloud properties' retrievals.

5.2 Cloud properties retrieval algorithms

5.2.1 Cloud optical depth

A cloud optical depth retrieval scheme is usually part of a larger cloud properties inference algorithm which is based on multi–wavelength radiance measurements. Such algorithms can generally be divided into two classes: (a) those using RT calculations combined with a threshold test to detect cloudy pixels and (b) those relying on some clustering techniques in the multidimensional radiance space constituted by several bands. However, due to problems inherent to clustering techniques, the majority of cloud remote sensing studies are based on comparisons with RT computations. Nevertheless, clustering schemes are specifically aimed to deal with only partially cloudy pixels, i.e. low spatial resolution measurements, as shown in [7].

Threshold techniques treat each pixel independently and assume that the pixel can be considered as either completely cloudy or clear–sky. According to the SEVIRI spatial resolution of 3 km (at nadir), this independent pixel approximation (IPA) can be considered as valid in our case. However, it is worth pointing out that correction schemes exist in order to cope with 3–dimensional (3–D) cloud structure and their associated horizontal transport of radiation which can not be anymore neglected at higher spatial resolutions, as it is illustrated in [191]. IPA algorithms rely on the fact that the reflection function of clouds at a non–absorbing narrow band in the visible part of the electromagnetic spectrum is primarily dependent on the cloud optical depth. These schemes can further be divided into two groups: (1) those making use of asymptotic relations for the reflection and transmission functions of optically thick layers ($\tau \gtrsim 9$) as shown in [84] and (2) those using a large set of precomputed values of the reflection function according to various scene viewing geometries and cloud optical depth, τ, as for example in [118].

From the previous considerations, it turns out that the simplest algorithm which still ensures the broadest range of applicability for cloud optical depth retrievals is based on simulated radiances from RT models properly convoluted with the visible narrowband filters of the imager under consideration. For simplicity we have simulated the outgoing radiances $L(\theta_0, \theta, \varphi)$ $[\mathrm{W} \cdot \mathrm{m}^{-2} \cdot \mathrm{sr}^{-1}]$ for a small set of ideal scene types, i.e. pure ground surfaces with spectrally uniform lambertian albedos and two cloud conditions (water or ice) with fixed parameters (altitude and particle size). The scene observing conditions are defined relatively to the local normal to the ground surface where, θ_0, is the Sun's zenith angle, θ, is the satellite's zenith angle and, φ, is the relative azimuth angle defined as the angle between the principal plane (made by the Sun, the surface and its local normal) and the satellite–surface–normal plane ($\varphi = 0$ corresponds to forward scattering). We selected for this work the STREAMER [82] RT code. The definition of the scenes simulated by the RT code, as well as its input parameters, are given in table 5.1. We used for planetary boundary layer standard atmospheric profile the mid–latitude summer properties and we set the aerosol optical model to maritime for ocean and rural for land, both with background tropospheric and stratospheric vertical profiles and finally we used a 50 km visibility. Gaseous absorption and Rayleigh scattering were also included. The cloud optical depths, τ, given at 0.65 μm are chosen according to a pseudo–logarithmic scale. The optically opaque cloudy condition, $\tau = 128$, we used is identical to the one chosen in the CERES experiment, as well as the particle shape for ice clouds. Note that we are only considering single uniform cloud layers in these computations. Moreover, the reflectance model of the ground surfaces used is *Lambertian* as it is also the case for a majority of algorithms found in the literature [7, 84, 118, 119, 137] and in particular for CERES.

Table 5.1 – *Scene parameters used as inputs for the STREAMER code simulations where, α, is the broadband surface albedo, z, is the bottom cloud altitude, h, is the cloud geometrical thickness, r_e, the cloud particle mean effective radius and, τ, the cloud optical depth at 0.65 μm.*

α	$0 \rightarrow 0.8$ by 0.05 steps	
Aerosols	maritime	rural
	background tropos. and stratos. prof.	
Std prof.	mid–latitude summer	
θ_0 [°]	$0 \rightarrow 90$ by 5° steps	
θ [°]	$0 \rightarrow 90$ by 5° steps	
φ [°]	$0 \rightarrow 180$ by 10° steps	
Cloud	water	ice
z [km]	3	9
h [km]	3	1
Shape	spheric	hexagonal
r_e [μm]	8	70
τ	$0, \{10^{-2}, 10^{-1}, 1, 10\} \times \{1, 2, 4, 7\}, 100, 128$	

The common approach found in the literature is, first, to apply a cloud detection scheme using threshold tests on multispectral measurements as, for example, the APOLLO algorithm [144]. Then, for so flagged cloudy pixels, RT computed radiances are used directly as look–up tables to extract the cloud optical depth according to the scene viewing geometry and the measured visible narrowband values (see for example [137]). Instead, we proceed differently. As shown in [119], there is an empirical law between the visible radiance (thus reflectance) and the cloud optical depth which is nearly insensitive to the cloud particle size r_e for visible wavelengths. By introducing the mean cloud amount (or cloud coverage index), C, defined as [24]

$$C(\theta_0, \theta, \varphi, \alpha, \text{phase}, \tau) = \frac{L(\theta_0, \theta, \varphi, \alpha, \text{phase}, \tau) - L(\theta_0, \theta, \varphi, \alpha, \tau = 0)}{L(\theta_0, \theta, \varphi, \text{phase}, \tau = 128) - L(\theta_0, \theta, \varphi, \alpha, \tau = 0)},$$

which can be equivalently expressed in terms of the bidirectional reflectance distribution function (BRDF) ρ as

$$C(\theta_0, \theta, \varphi, \alpha, \text{phase}, \tau) = \frac{\rho(\theta_0, \theta, \varphi, \alpha, \text{phase}, \tau) - \rho(\theta_0, \theta, \varphi, \alpha, \tau = 0)}{\rho(\theta_0, \theta, \varphi, \text{phase}, \tau = 128) - \rho(\theta_0, \theta, \varphi, \alpha, \tau = 0)}, \tag{5.1}$$

(where, $\tau = 0$, represents clear–sky conditions above the ground surface, $\tau = 128$, denotes the opposite boundary limit associated with optically opaque cloudy conditions leading to simulated radiance fields insensitive to surface albedo) this law is rescaled with C values ranging from 0 to 1. This empirical law is easily built from our RT simulated data. The most noticeable fact when plotting this law according to the cloud optical depth is its similar shape for all scene viewing geometries (see figure 5.1). Note that the curve is not saturated at $C = 1$ when $\tau = 128$. This relies on the fact that the reflection function of the optically opaque clouds generated by the RT code is still increasing with the cloud optical depth. Nevertheless, it can be shown that saturation is reached for $\tau \approx 400$. However, to remain in accordance with the

CERES retrievals, we have set $\tau = 128$ as the highest possible cloud optical depth value which can be given by our algorithm.

Due to this characteristic shape we parameterize this relation by using a modified sigmoïd function of the logarithm of the optical depth*, i.e. $C = f(\log \tau)$, where f is defined as

$$f(\log \tau) = \frac{A}{B + 10^{-(\log \tau - \log \tau_0)/\chi}}$$

and relates on 4 parameters (A, B, $\tau_0 > 0$ and $\chi \neq 0$). Note that, in the latter expression, the dependency of C and of the 4 parameters with the scene viewing geometry $(\theta_0, \theta, \varphi)$, surface albedo α and cloud phase is implicitly assumed. Some basic algebra leads us to the compact form

$$C = \frac{A}{B + \left(\frac{\tau_0}{\tau}\right)^{1/\chi}}. \tag{5.2}$$

These 4 parameters can then be adjusted in order to get the closest match between the empirical curve and our modified sigmoïd through a least square fit on the RT data. Practically, the Powell multidimensional fitting method [131] is used. Finally, we end up with a set of 4 parameters (A, B, τ_0 and χ) for each scene viewing geometry, surface albedo and cloud phase instead of twice (C and τ) the number of optical depth values (according to table 5.1 this number is equal to 19). Moreover, the relation between C and τ can be seen as an implicit non–linear interpolation on the discrete τ and C values computed by the RT code. We can directly see the benefit of the simple formulation of our fitting function. Indeed, equation 5.2 can explicitly be solved for the cloud optical depth, leading us to

$$\tau = \frac{\tau_0 \cdot C^{\chi}}{(A - B \cdot C)^{\chi}}, \tag{5.3}$$

with the mathematical constraints of equation 5.2 ($\chi \neq 0$, $\tau_0 > 0$) and setting the retrieved τ value to 128 when $C \geq A/B$ (saturation condition).

Thus, our cloud optical depth retrieval algorithm immediately follows. For each imager pixel:

1. We estimate its cloud phase from the 0.67 and 1.6 μm SEVIRI channels according to [77],

2. According to the clear–sky reflectance estimated as in chapter 4 and the pixel's viewing geometry $(\theta_0, \theta, \varphi)$, we search the associated broadband surface albedo $\widetilde{\alpha}$ corresponding to the closest match between the RT clear–sky imager simulated reflectances $\rho(\theta_0, \theta, \varphi, \widetilde{\alpha}, \tau = 0)$ and this estimated clear–sky value,

3. We compute its associated mean cloud amount value, C using equation 5.1, where the optically opaque cloudy reflectance, $\rho(\theta_0, \theta, \varphi, \widetilde{\alpha}, \text{phase}, \tau = 128)$ is from RT simulation according to the pixel's viewing geometry $(\theta_0, \theta, \varphi)$ and broadband surface albedo $\widetilde{\alpha}$ found in the previous step,

4. We compute its associated cloud optical depth value using equation 5.3 and the 4 fitted parameters for the associated pixel's viewing geometry, broadband surface albedo $\widetilde{\alpha}$ and cloud phase.

*It must be noted that the sigmoïd function of the optical depth only satisfies the boundary value problem of $C = 0$ for $\tau = 0$ asymptotically.

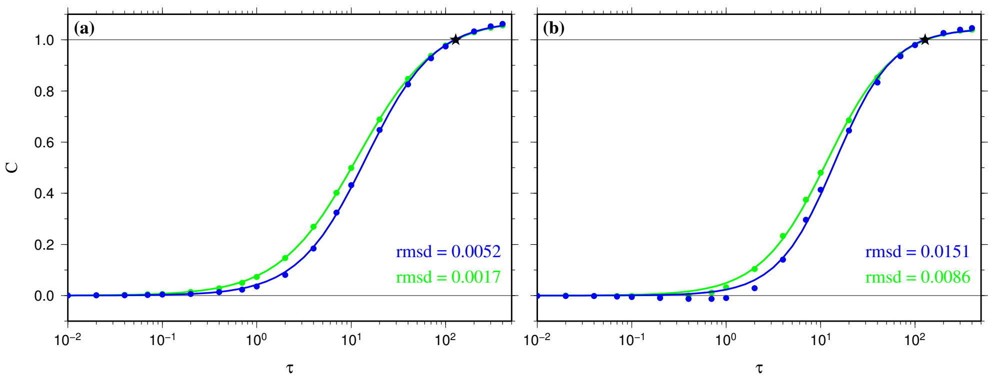

Figure 5.1 *– Mean cloud amount C versus cloud optical depth τ RTM calculations (dot) and associated sigmoïd fit (plain line) for (a) ocean surface albedo ($\alpha = 0.05$) under water cloud and (b) land surface albedo ($\alpha = 0.4$) under ice cloud using the STREAMER RT code. The green curve is associated to $\theta_0 = 10°$, $\theta = 60°$ and $\varphi = 0°$, while the blue curve is for $\theta_0 = 45°$, $\theta = 15°$ and $\varphi = 180°$. The stars (★) are representing the optically opaque cloudy conditions ($\tau = 128$) above the surfaces.*

5.2.2 Cloud fraction

The cloud fraction or cloud cover f is always defined on some footprint (i.e. a set of pixels) and simply consists in the computation of the relative fraction of *cloudy* pixels within that footprint. Major cloud detection algorithms found in literature are based on threshold decision tests related to multispectral radiance measurements for each pixel (see for example [137] or [144]). Moreover, such a cloudy/non–cloudy test is generally applied before any cloud properties retrieval scheme. For GERB, we adopt a different approach. The cloud screening scheme requires that the cloud optical depth retrieval scheme described above has been priorly applied. The pixel is then flagged as cloudy if $\tau > \tau_{\text{thres}}$ where, τ_{thres}, is a constant threshold value (see section 5.4). As mentioned in section 5.1, we are planning to deliver TOA broadband fluxes at an increased spatial resolution of 10 km at nadir compared to the lower native GERB resolution. Therefore, due to the spatial resolution of SEVIRI, the footprint size on which cloud fraction needs to be estimated is 3×3 SEVIRI pixels.

5.3 Data description

To uncover possible discrepancies between GERB and CERES cloud properties retrieval methods and suggest some correction schemes, we compare the cloud optical depth and cloud fraction predicted by both instruments' algorithms. However, during the commissioning period of MSG, SEVIRI measurements will not be available on an operational basis (i.e. realtime dissemination through receiving station). Therefore, the RGP will be tested with Meteosat–7 as the imager. Nevertheless, application of the GERB sceneID scheme on MS7 visible narrowband data and comparisons with CERES will prove useful for the validation of our adopted methodology for cloud optical properties retrievals.

Due to the lack of a 1.6 μm channel on MS7, the cloud phase algorithm can not be directly transposed to this imager. Note that we could use a cloud phase discrimination method based on brightness temperatures estimated from the MS7 11.5 μm thermal channel, but this would require a further validation step. Therefore, as such a scheme would certainly not be used for SEVIRI due to its uncertainties compared to its CERES counterpart, we will rely on the determination of the cloud phase given in the CERES products.

Considering the relatively broad visible channel of MS7 extending up to 1 μm compared to the narrower 0.6 and 0.8 μm SEVIRI bands (see figure 5.2), we are expecting an increase in the amount of radiation absorbed with respect to the cloud particle size as illustrated in [77] for the SEVIRI 1.6 μm channel. Therefore, it will certainly introduce some scattering in GERB retrievals due to our adopted methodology (RT computed radiances were made with a fixed effective particle size for each cloud phase). Rayleigh and aerosol scattering as well as surface albedo tend to increase clear–sky measurements made in this wider visible channel, thus leading to a decrease in sensitivity of the radiance towards cloud optical depth. However, for SEVIRI, our cloud identification scheme will be applied for ocean on 0.8 μm data for minimal sensitivity regarding the surface albedo, Rayleigh and aerosol scattering. For other surface types the 0.6 μm channel will be considered in order to minimize the contribution of the surface albedo in the signal.

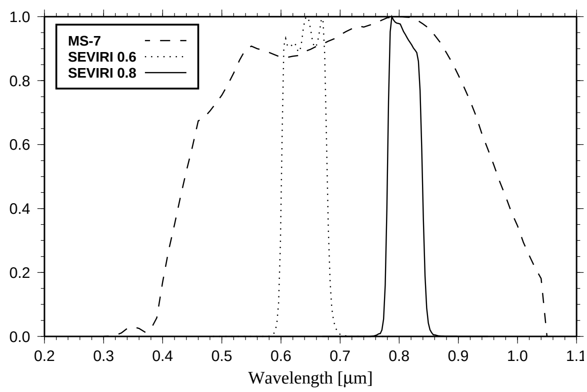

Figure 5.2 *– Meteosat–7 and SEVIRI visible narrowband spectral responses.*

Since CERES ADMs were built from the Tropical Rainfall Measuring Mission (TRMM) satellite measurements using the Visible and InfraRed Spectrometer (VIRS) imager, we shall use the CERES Single Satellite Footprint (SSF) TOA/Surface Fluxes and Clouds products which are generated on a hourly basis. Indeed, this dataset was used for the ADMs production [99]. As the operational phase of MS7 started in the beginning of June 1998, we used for our comparisons 5000 $\times$ 5000 MS7 visible images (about 2.25 km at nadir) from the Meteosat Archive and Retrieval Facility (MARF) of EUMETSAT and CERES SSF data from June 1998 to the end of August 1999 (15 months). Due to an anomaly of the CERES radiometer at the end of August 1998, we priorly use SSF VIRS Edition 2A and VIRS–only Edition 2 a posteriori. However, this change of data has no influence on the cloud parameters retrieval since CERES algorithms are only relying on VIRS data which were still available after the discovery of the anomaly.

To ensure measurements over similar scenes by both satellites (cloud motion due to the wind), our comparisons only take into account CERES footprints and related MS7 pixels measured within 5 minutes around CERES acquisition time. Moreover, in order to limit sensitivity of our retrievals to parallax effects and 3–D cloud structures, we only select for our comparisons CERES footprints which have a maximum tilt angle of 5° between the vectors joining the ground surface to each satellite. By this way, we select close scene viewing geometries for both instruments. In addition, only CERES footprints which are completely characterized by the VIRS imager are considered (i.e. the imager coverage within each footprint is 100 %). Then, for each selected CERES footprint, we compute the mean cloud optical depth and cloud fraction over an equivalent GERB footprint made up of the 5×5 MS7 nearest pixels to the geographical center of the CERES footprint. As previously mentioned, we rely on the CERES sceneID scheme for the cloud phase determination. However, as this feature is an average over the CERES footprint, we do not have access to its associated values at the imager pixel–scale. Therefore, we only consider footprints with pure water or ice clouds according to CERES. Finally, to be able to easily bin our results according to the surface type, we further refine our selection of CERES footprints to those characterized by homogeneous geotypes.

5.4 Comparisons of GERB and CERES cloud properties

As we have seen, the mean cloud optical depth and cloud fraction within each GERB footprint are both linked to the chosen threshold τ_{thres} used to distinguish between cloudy and non–cloudy imager pixels. We already mentioned in the beginning of section 3.2 that such classification is relative to its intended application. Since we want to apply the same ADMs for the GERB radiance–to–flux conversion as CERES, we need to mimic as close as possible the CERES cloud fraction retrievals. It is obvious that variations of τ_{thres} mainly affect low cloud optical depth retrievals, i.e. the detection of thin clouds, while high τ values are nearly insensitive. However, it is known that these thin clouds only have a limited radiative impact. Requiring that the value of this parameter is taken in order that, on average on the studied footprints, the cloud fractions computed by the CERES algorithm are nearly identical to those computed by our scheme guarantees that we detect on average the same amount of cloud coverage than CERES. Practically, we find that a value of $\tau_{\text{thres}} = 0.85$ matches our requirement regarding the mean cloud coverages for both instruments as it is shown in figure 5.3.

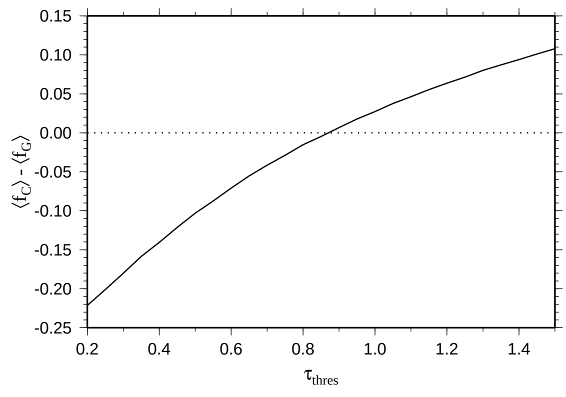

Figure 5.3 *– Difference between CERES and GERB mean fractional cloud cover versus of* τ_{thres}.

To be consistent with the CERES methodology and thus to be able to perform meaningful comparisons between CERES and GERB results, we should convolve the cloud optical properties from imager pixels within GERB footprints with the dynamic CERES point spread function (PSF) as it is done for the retrievals in CERES SSF data. However, due to the increase of programming complexity and computing time, we have discarded these calculations. Nevertheless, it is expected that such an approximation is only introducing a slight bias [61].

5.4.1 Cloud optical depth

The average of cloud optical depth over the equivalent GERB footprint is performed by a natural logarithmic mean on cloudy pixels based on the threshold value τ_{thres}. The range of possible τ values is spreading across 3 decades, while $\log \tau$ is varying almost linearly. This methodology is also adopted in the CERES products. Moreover, to avoid any bias when comparing the cloud optical depths, we only take into account CERES footprints having a single cloud layer as flagged so by the CERES sceneID scheme and corresponding to totally overcast cloudy conditions within the CERES field–of–view (FOV).

Despite the huge set of data used, the selection criteria on the cloud layers, ground surfaces and instruments tilt angle applied for the cloud optical depth comparisons only produce a limited set of pairs of values τ_C and τ_G (see table 5.2). This table lists the different populations according to their CERES surface type and cloud phase. The most noticeable fact is the limited measurements above desert surface compared to others. This is not so surprising since deserts are known to be dry areas, and thus with very low occurrences of clouds (which are the media for precipitation).

Table 5.2 *– Population of GERB and CERES cloud optical depth pairs according to their associated CERES surface type and cloud phase. Only pure footprints according to the CERES mean cloud phase with homogene surface are considered.*

	Water	Ice	Total
Ocean	12646	3645	16291
Vegetation	768	1770	2538
Desert	116	187	303
Total	13530	5602	19132

The comparisons between CERES and GERB cloud optical depth retrieval schemes are illustrated in figure 5.4. For each panel in this figure we chose to plot the natural logarithm of the retrieved τ values in order to display small and large τ with the same order of magnitude. This comparison accounts for collocated footprints associated to nearly time–simultaneous measurements and similar viewing geometries of both imagers. The most noticeable result from these scatterplots is the good agreement between the two retrieval schemes. The correlation coefficients are 0.894 for ocean with water clouds, 0.946 for ocean with ice clouds, 0.874 for vegetation with water clouds, 0.924 for vegetation with ice clouds and 0.886 for desert with ice clouds, but only 0.576 for water clouds above desert (see figure 5.4(e)). The latter can be explained by the fact that the associated dataset population is very small and thus not statistically representative. The same conclusion holds for the linear least square fit. Regarding ice clouds cases, there is a larger scatter of the plots compared to the water phase cases as illustrated by the χ^2 values of the linear fits (as for example 0.094 versus 0.106 for ocean). A

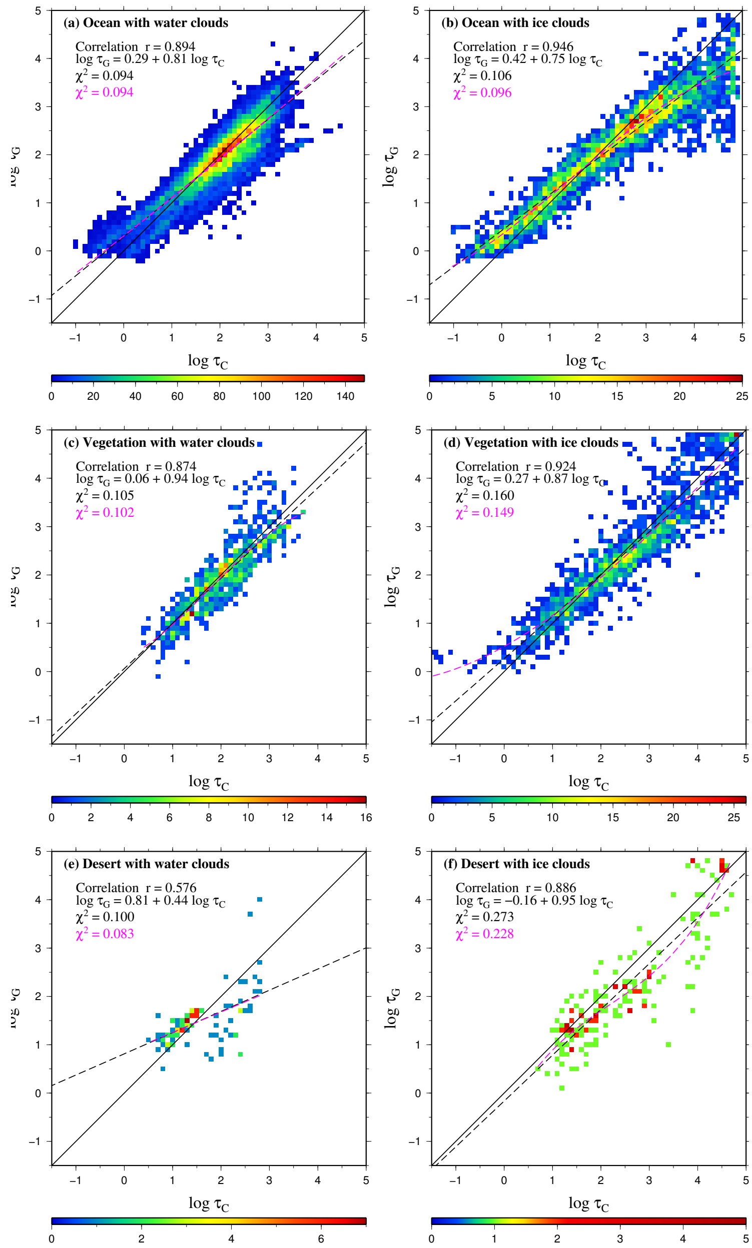

Figure 5.4 *– Natural logarithm of cloud optical depth retrieval pairs* $(\log \tau_C, \log \tau_G)$ *from collocated CERES and GERB footprints according to the different considered surfaces and cloud phases. Plain line represents the ideal case* $\tau_G = \tau_C$ *while dashed line illustrates a robust linear least square fit with respect to outliers [70]. Pink dashed line illustrates the most significant robust polynomial least square fits in terms of confidence on the decrease of residuals [70].*

possible explanation of this effect could be related to the broader distribution of the ice particle effective radii r_e for ice clouds than for water clouds (see figure 5.5). One can argue that using visible radiance measurements, the impact of the ice particle size distribution on the cloud optical depth retrievals should normally be less than the one we show. In fact, we strongly question our assumption regarding the insensitivity of visible radiance to cloud particle size when using MS7 due to its broad visible channel (see figure 5.2) which extends at least partly in the near–infrared region. Moreover, this could also explain the deviation of the linear least square fits relative to the ideal case line.

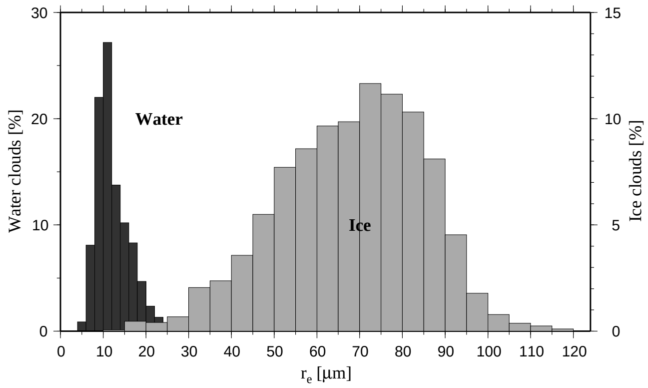

Figure 5.5 *– Normalized histograms of the CERES SSF cloud effective particle size for the selected footprints used in the cloud optical depth comparisons.*

As mentioned previously, the implementation of a scene identification within the RGP is used to select the proper CERES ADMs for the broadband radiance–to–flux conversions. These ADMs are defined over some ranges of cloud optical depth [99]. Hence, the crucial constraint of our retrieval scheme is to select on average the same ADM as the CERES software would (i.e. having a confusion matrix between the two classifications as close as possible diagonal). Such a confusion matrix is shown in table 5.3 for ocean and ice cloud footprints*. As we could expect from the correlation between $\log \tau_C$ and $\log \tau_G$ (figure 5.4(b)) retrievals are located around its diagonal while spreading away with increasing cloud optical depth ranges. However, due to the deviation from the ideal line of the least square fit, the sub–matrices associated to extreme cloud optical depth values are far away from the diagonal line. If diagonal dominance would be fulfilled, then GERB cloud optical depth retrieval scheme would lead on average to a similar selection of ADMs as CERES would. However, these previous results suggest the need to develop some correction strategy in order to adjust GERB retrievals to CERES ones. Such a scheme will be developed later in this chapter.

5.4.2 Cloud fraction

To avoid any bias when comparing the cloud fraction, we only take into account CERES footprints having a single cloud layer as flagged so by the CERES sceneID scheme (there is no restriction on cloud coverage). The population of footprints matching this criterion is given in table 5.4 according to the surface type and cloud phase. We did not perform CERES PSF

*Confusion matrices for figures 5.4(a),(c)–(f) will not be shown to spare space.

Table 5.3 *– Confusion matrix (footprint populations) resulting from the comparisons of CERES ADMs cloud optical depth classifications according to CERES (columns) and GERB (rows) retrievals for ocean and ice cloud footprints. The bold numbers on the diagonal are for cases where the ADMs selected using CERES and GERB cloud optical depth retrievals are identical. ADM class numbers are for the following ranges of cloud optical depth [99]:* 1 = (0 − 0.01), 2 = (0.01 − 1), 3 = (1 − 2.5), 4 = (2.5 − 5), 5 = (5 − 7.5), 6 = (7.5 − 10), 7 = (10 − 12.5), 8 = (12.5 − 15), 9 = (15 − 17.5), 10 = (17.5 − 20), 11 = (20 − 25), 12 = (25 − 30), 13 = (30 − 40), 14 = (40 − 50) *and* 15 = (> 50).

Class	1	2	3	4	5	6	7	8	9	10	11	12	13	14	15r
1	**0.00**														
2		**0.91**	0.08												
3		4.77	**10.32**	1.37	0.03										
4		0.03	2.85	**9.33**	1.32	0.27	0.08	0.03							
5				2.39	**4.14**	1.67	0.69	0.19	0.03		0.05	0.03			
6				0.44	1.95	**2.66**	1.43	0.44	0.27	0.22	0.22	0.11	0.05	0.11	0.49
7					0.33	0.88	**1.59**	1.62	1.15	0.52	0.27	0.25	0.08	0.14	0.41
8						0.14	0.96	**1.37**	1.23	0.82	1.18	0.25	0.55	0.25	0.60
9						0.05	0.16	0.60	**0.85**	1.07	1.26	0.93	0.66	0.19	0.49
10							0.05	0.14	0.44	**0.55**	0.99	0.71	0.91	0.36	0.66
11							0.03	0.03	0.22	0.77	**1.23**	1.45	1.59	0.91	1.48
12									0.05	0.14	0.33	**0.93**	1.04	0.71	2.11
13										0.03	0.08	0.36	**0.74**	0.69	2.83
14												0.05	0.36	**0.16**	2.50
15										0.03	0.05	0.03	0.25	0.19	**3.98**

convolution of our cloud retrievals on MS7 pixels within GERB footprints. Therefore, GERB cloud fraction values are only part of the discrete set made of multiples of $\frac{1}{5\times5} = 0.04$, while they are continuously varying for CERES. To be able to perform meaningful comparisons, we have plotted in figure 5.6 both cloud fractional cover retrievals for ocean footprints. These results have been binned in squared regions according to a bin width of 0.04. It can be noted that there is a good agreement for clear–sky and overcast footprints between both schemes and that these cases are a major contribution to the total population of selected footprints (notice the logarithmic scale of the colorbars in the graphs). Moreover, according to the gray band joining these extreme cloudy conditions in figure 5.6(a), there is also a correlation for intermediate cloud fraction values.

Table 5.4 *– Population of GERB and CERES cloud optical depth pairs according to their associated CERES surface type and cloud phase. Only pure footprints according to the CERES mean cloud phase with homogene surface are considered.*

	Water	Ice	Total
Ocean	40599	4439	45038
Vegetation	4055	2008	6063
Desert	1507	430	1937
Total	46161	6877	53038

However, results are also more scattered than for the cloud optical depth. A horizontal scatter is due to the fact that CERES retrievals are convoluted with the CERES dynamic PSF which is stretching around 72 VIRS pixels [153] and thus taking into account a larger footprint than the expected 5×5 VIRS pixels when estimating cloud fraction. This is clearly illustrated in figure 5.6 where $f_G = 0$ and $f_G = 1$ while $f_C \in (0-1)$. While τ_{thres} has only a limited impact on the low cloud optical depth retrievals, it is a highly sensitive parameter for cloud fraction estimation (which is totally relying on the cloudy/non–cloudy test). In contrast, CERES methodology based on multispectral radiance threshold tests is not directly depending on the retrieved cloud optical depths. This can therefore result in cloudy footprints for which the mean cloud optical depth is below the GERB chosen threshold. This contributes to the horizontal scatter and also to its vertical component as shown in the figure where $f_C = 1$ while $f_G \in (0-1)$. But we can question the validity of such low CERES cloud optical depth retrievals with regards, for example, to the sensitivity in the estimation of the surface albedo.

As the CERES ADMs are also stratified according to some ranges of the cloud fraction [99], the confusion matrix for ocean and water cloud footprints is given in table 5.5*. From this table, it can be noted that while about 34 % of the footprints are identified as totally overcast by CERES, it reaches up to 45 % for GERB. Moreover, GERB is also overestimating the number of footprints in the clear–sky class (15 %) compared to CERES (0.42 %). In fact, it can be noticed that the majority of these GERB retrievals are classified in CERES class 2. This is certainly due to (1) the range used to define classes 1, 2, 12 and 13 on extreme cloud fraction values, (2) the convolution of CERES retrievals which tend to spread their values compared to GERB results, (3) probable CERES cloud optical depths which are below our chosen threshold. As previously mentioned, a possible solution to correctly compare CERES and GERB cloud fractional covers would be to perform CERES PSF convolution on MS7 pixels and only select footprints whose mean cloud optical depth is above τ_{thres}. However, such processes are deferred to a future

*Confusion matrices for other surfaces and phase will not be shown to spare space.

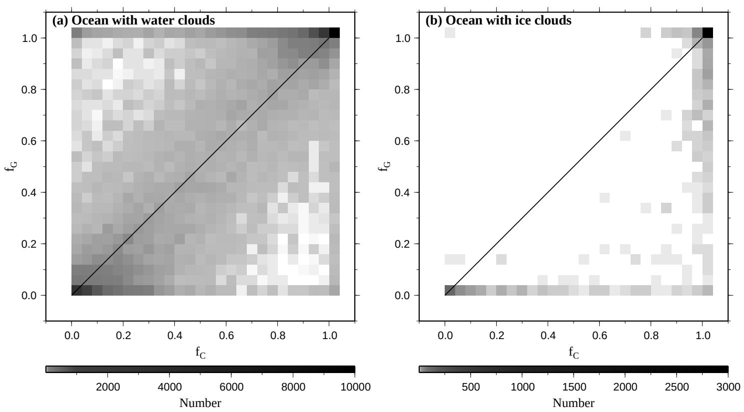

Figure 5.6 *– Histograms of cloud fraction retrieval pairs (f_{C}, f_{G}) from collocated CERES and GERB ocean footprints according to both cloud phases. Plain line represents the ideal case $f_{\mathrm{G}} = f_{\mathrm{C}}$ where both retrieval schemes provide identical values. As can be seen, both histograms are dominated by the extreme cloud fractions (black squares).*

study on SEVIRI data*. Nevertheless, the choice of τ_{thres} is a basic validation of our cloud fraction retrievals as it leads to the same average of cloud fractional cover than CERES.

5.5 Homogenization of GERB cloud optical depths

5.5.1 Method

In this section, we propose a generic homogenization scheme to correct retrievals of a given feature according to some method towards associated reference values. More specifically, the reference values will be taken as the CERES cloud optical depth retrievals while the results which have to be corrected are the outputs of the GERB cloud optical depth algorithm.

As previously mentioned, cloud optical depth values are not convenient to handle due to their large range of variation (about 3 decades). Any attempt to fit directly these optical depths will produce poor results due to the influence of large values compared to small ones. One would expect that retrieval errors increase with increasing optical depth values and thus, any fit should decrease the weights of theses large values accordingly. However, if we consider the logarithm of cloud optical depths, the variation range is implicitly reduced while having an almost linear dependence and therefore these values are more suited to perform meaningful statistical fits.

To perform a statistical fit on $\log \tau$ values we used a mathematical model f (needed to express the correlation between two variables) of the following form: $f(\log \tau) = \mathcal{P}_n(\log \tau)$, where, $\mathcal{P}_n$, is the generic form of a degree n polynomial with coefficients a_i for $i = 0, \ldots, n$. The robust polynomial least square fits with respect to outliers [70] which lead to a significant

*In the meanwhile, we adopted the pragmatic approach when going from MS7 to SEVIRI: we changed the MS7 τ_{thres} by visual inspection of the more recent SEVIRI data.

Table 5.5 *– Confusion matrix (in percent) resulting from the comparisons of CERES ADMs cloud fraction classifications according to CERES (columns) and GERB (rows) retrievals for ocean and water cloud footprints. Bold numbers on the diagonal are for cases where the ADMs selected using CERES and GERB cloud fraction retrievals are identical. ADM class numbers are for the following ranges of cloud fraction [99]:* $1 = (0 - 0.001)$, $2 = (0.001 - 0.1)$, $3 = (0.1 - 0.2)$, $4 = (0.2 - 0.3)$, $5 = (0.3 - 0.4)$, $6 = (0.4 - 0.5)$, $7 = (0.5 - 0.6)$, $8 = (0.6 - 0.7)$, $9 = (0.7 - 0.8)$, $10 = (0.8 - 0.9)$, $11 = (0.9 - 0.95)$, $12 = (0.95 - 0.99)$ *and* $13 = (0.99 - 1)$.

Class	1	2	3	4	5	6	7	8	9	10	11	12	13	Sum
1	**0.40**	10.51	2.41	0.97	0.42	0.21	0.14	0.07	0.05	0.04	0.04	0.03	0.11	15.41
2	0.01	**1.86**	1.41	0.93	0.62	0.24	0.16	0.09	0.05	0.02	0.01	0.01	0.09	5.50
3		0.68	**0.96**	0.76	0.59	0.34	0.20	0.13	0.08	0.04	0.02	0.03	0.07	3.89
4	0.00	0.47	0.82	**1.07**	0.84	0.67	0.40	0.21	0.15	0.08	0.02	0.03	0.10	4.88
5		0.18	0.23	0.47	**0.51**	0.44	0.35	0.23	0.13	0.08	0.03	0.04	0.07	2.78
6		0.18	0.31	0.41	0.52	**0.69**	0.60	0.47	0.29	0.19	0.07	0.06	0.11	3.90
7		0.11	0.12	0.18	0.29	0.38	**0.38**	0.33	0.28	0.22	0.06	0.05	0.06	2.46
8		0.11	0.14	0.16	0.33	0.43	0.57	**0.65**	0.56	0.42	0.17	0.15	0.11	3.79
9	0.00	0.08	0.07	0.10	0.12	0.21	0.35	0.43	**0.51**	0.45	0.14	0.12	0.11	2.71
10		0.12	0.06	0.09	0.14	0.19	0.36	0.56	0.77	**1.04**	0.47	0.49	0.23	4.52
11		0.03	0.04	0.04	0.04	0.05	0.08	0.16	0.29	0.52	**0.32**	0.30	0.18	2.06
12		0.05	0.03	0.03	0.04	0.06	0.09	0.16	0.31	0.60	0.37	**0.69**	0.26	2.68
13	0.01	0.46	0.26	0.24	0.23	0.29	0.36	0.53	0.81	1.61	1.85	6.08	**32.68**	45.42
Sum	0.42	14.86	6.87	5.46	4.69	4.20	4.05	4.03	4.27	5.33	3.57	8.08	34.17	40599

decrease of the residuals for the selected footprints are given in figures 5.4 (pink dashed lines). Having set the number of degrees of freedom $n^\star$ and performed the fit on the dataset, we end up with the expression

$$\log \tau_{\mathrm{G}} = \mathcal{P}_{n^\star}(\log \tau_{\mathrm{C}}) \tag{5.4}$$

where, $\mathcal{P}_{n^\star}$ is the fitted polynomial of degree $n^\star$ with coefficients $a_i^\star$ for $i = 0, \ldots, n^\star$. The next step is to homogenize values for GERB cloud optical depth, $\widetilde{\tau}_{\mathrm{G}}$, in such a way that on average $\log \tau_{\mathrm{C}} = \log \widetilde{\tau}_{\mathrm{G}}$. By substituting the latter formula in equation 5.4, the homogenized cloud optical depths are implicitly given by

$$\mathcal{P}_{n^\star}(\log \widetilde{\tau}_{\mathrm{G}}) = \log \tau_{\mathrm{G}}. \tag{5.5}$$

As we see, the difficulty lies in solving this equation for $\widetilde{\tau}_{\mathrm{G}}$, either explicitly for $n^\star \leq 5$ or iteratively when $n^\star > 5$, for every value τ_{G}. However, robust iterative methods for finding roots of polynomials exist and are described in the literature [131].

5.5.2 Results

Our correction scheme is illustrated for cloud optical depth pairs associated with ocean and ice cloud footprints. It turns out that the fitting model in terms of robustness and significant decrease of the residuals is the third degree polynomial $\mathcal{P}_4(\log \tau_{\mathrm{C}}) = 0.336 + 0.737\ \log \tau_{\mathrm{C}} + 0.076\ (\log \tau_{\mathrm{C}})^2 - 0.017\ (\log \tau_{\mathrm{C}})^3$. Results are given in table 5.6 as a confusion matrix. As we could expect from figure 5.4(b), our retrieval scheme overestimates low cloud optical depth while underestimates high τ values by comparison to CERES. The benefit of our correction method is clearly shown by comparing uncorrected (table 5.3) and homogenized GERB values (table 5.6) where the number of diagonal–dominant elements decreased from 8 to 4 while the off–diagonal elements are balanced, leading to a more symmetric matrix. Finally, it can be noted that adjusted GERB values are now all classified in an adjacent CERES class for those which do not meet the diagonal dominance criterion.

5.6 Conclusions and future work

In this chapter, we have presented cloud optical depth and cloud fraction retrieval algorithms. These schemes will be implemented as part of the SEVIRI scene identification for the RMIB GERB Ground Segment. They are based on a direct inversion method which relies on simulated radiances by a radiative transfer model over specific scenes, composed by a restricted number of ground surfaces and cloudy conditions. The method uses an innovative and efficient parameterization of the inversion look–up tables. Preliminary validation of the cloud optical depth and cloud fraction retrieval algorithms were performed by comparing CERES footprints and Meteosat–7 simulated GERB footprints. These comparisons have shown good correlation between GERB and CERES methods. However, discrepancies occur but they are expected to decrease with the use of the SEVIRI imager thanks to its narrower visible channels compared to Meteosat–7. But it will have to be confirmed by a future validation study on this imager*. Moreover, a correction scheme was also suggested in order to cope with the possible remaining cloud optical depth discrepancies between CERES and SEVIRI retrievals. Its

*In the meanwhile we received cloud properties retrievals from the NASA Langley Cloud and Radiation Research Group which has adapted the CERES sceneID to SEVIRI data. There are still discrepancies but these are not related anymore to differences in footprint.

***Table 5.6** – Confusion matrix (in percent) resulting from the comparisons of CERES ADMs cloud optical depth classifications according to CERES (columns) and GERB (rows) retrievals for ocean and ice cloud footprints for homogenized GERB results. The bold numbers on the diagonal are associated to the case where the ADMs selected using CERES and GERB cloud optical depth retrievals are identical. ADM class numbers are for the following ranges of cloud optical depth [99]:*
$1 = (0 - 0.01)$, $2 = (0.01 - 2.5)$, $3 = (2.5 - 6)$, $4 = (6 - 10)$, $5 = (10 - 18)$, $6 = (18 - 40)$, $7 = (> 40)$.

Class	1	2	3	4	5	6	7	8	9	10	11	12	13	14	15r
1	**0.00**														
2		**4.61**	1.73	0.03											
3		1.07	**9.96**	2.55	0.05										
4		0.03	1.56	**8.64**	1.54	0.33	0.08	0.03							
5				1.81	**3.68**	1.48	0.63	0.19	0.03		0.05	0.03			
6				0.49	1.78	**2.33**	0.91	0.22	0.19	0.08	0.11	0.05	0.05	0.11	0.25
7					0.63	0.93	**1.45**	0.85	0.47	0.30	0.11	0.19		0.05	0.36
8					0.08	0.47	0.96	**1.10**	0.85	0.47	0.36	0.11	0.14	0.11	0.41
9						0.05	0.69	0.99	**0.77**	0.55	0.69	0.16	0.30	0.14	0.30
10						0.05	0.14	0.47	0.91	**0.47**	0.91	0.41	0.33	0.16	0.44
11						0.03	0.11	0.55	0.55	1.07	**1.43**	0.91	0.96	0.16	0.49
12							0.03		0.33	0.49	0.69	**0.74**	0.85	0.41	0.69
13								0.03	0.14	0.55	0.93	1.21	**1.84**	0.85	1.23
14									0.03	0.14	0.25	0.69	0.69	**0.66**	1.54
15										0.03	0.16	0.60	1.07	1.04	**9.85**

efficiency was demonstrated on CERES and MS7 cloud optical depth comparisons. Basic validation of the cloud fraction was performed by choosing the optimal threshold value on cloud optical depth which is the border between cloudy/non–cloudy imager pixels. This value ensures that, on average, our algorithm produces the same cloud coverage as the one computed by the CERES software. Finally, some recommendations were issued for future comparisons such as convolute with CERES point spread function our cloud properties' retrievals.

These cloud optical depth and cloud fraction estimations will be part of the GERB products generated at RMIB. Complete description of their content as well as the algorithms used are available at `http://gerb.oma.be`. Products will be freely available to the scientific community at `ftp://gerb.oma.be`.

Acknowledgments

The CERES SSF data were obtained from the NASA Langley Research Center Atmospheric Sciences Data Center. The Meteosat–7 data were obtained from the Meteosat Archive and Retrieval Facility (MARF). All graphics and plots were made using The Generic Mapping Tools (GMT) software collection of P. Wessel (University of Hawai'i) and W.H.F. Smith (NOAA / NESDIS / NODC).

Chapter 6

Description of the GERB Edition 1 SEVIRI scene identification*

This chapter describes the adaptation of the scene identification initially developed on Meteosat–7 data to the improved SEVIRI imager.

Abstract

The first Geostationary Earth Radiation Budget (GERB) instrument was launched during summer 2002 together with the Spinning Enhanced Visible and InfraRed Imager (SEVIRI) on board the Meteosat–8 satellite. This broadband radiometer aims to deliver near–realtime estimates of solar and thermal radiative fluxes at the top of the atmosphere (TOA) with high temporal resolution thanks to the geostationary orbit. Such a goal is achieved with the L20 GERB processing which generates these fluxes from the directional filtered radiance measurements of the instrument at several spatial resolutions. This processing consists of successive components, one of them being a radiance–to–flux conversion. The conversion is carried out in the solar region by using the shortwave angular dependency models (ADMs) developed from the Tropical Rainfall Measuring Mission Clouds and the Earth's Radiant Energy System experiment. Since these ADMs are stratified according to specific scene properties, the GERB ground segment will have to rely on a scene identification of SEVIRI data which allows us to select the proper ADM.

This chapter presents the method which was developed for this SEVIRI scene identification within the GERB processing for the official Edition 1 release of the L20 products. Detailed discussion on the strategy which was adopted compared to common approaches found in the literature will be given. More specifically, it will introduce an improved method to estimate the TOA clear–sky reflectances in the visible part of the spectrum from geostationary imager data. A cloud properties retrieval scheme will rely on these clear–sky estimates to provide cloud optical depth, cloud phase and cloud fraction within the GERB footprints.

*Adapted transcription of A. Ipe, C. Bertrand, N. Clerbaux, S. Dewitte and L. Gonzalez Sotelino, The GERB Edition 1 products SEVIRI scene identification – Part I: Methodology, *under review at IEEE Trans. Geosci. Remote Sens.*, 2010.

6.1 Introduction

THE fundamental driving force for weather and climate is the net radiation received at the top of the atmosphere (TOA) [125]. The Earth radiation budget (ERB) is the balance between the incoming radiation from the Sun and the outgoing reflected and scattered solar radiation plus the thermal infrared emission to space.

In the mid 60's, Earth–orbiting satellites began to play an important role in measurements of the Earth's radiation flux (see e.g., [68]). Raschke et al. [132] developed radiation budget maps using measurements from a scanning radiometer which had a number of narrow bands. However, due to the intermittent operation of the instrument, it was necessary to accumulate a month of data in order to produce a map of albedo and outgoing longwave radiation (OLR). Their work provided a new view of the flow of energy in the Earth–atmosphere system. It also demonstrated the need for radiometers designed for radiation budget measurements and the need for models with which to analyze the data.

A major accomplishment of the 80's was the design, launch and data processing of satellite–based moderate resolution broadband fluxes in the Earth Radiation Budget Experiment (ERBE) [9]. However, it is known that the ERBE observations suffer from some restrictions, including limited angular models used to convert directional radiances to fluxes, poor scene identification capabilities needed to accurately estimate cloud radiative forcing, and very limited diurnal sampling [185].

The Clouds and the Earth's Radiant Energy System (CERES) [184] experiment marked the beginning of a new generation of instruments and greatly improved radiation budget products. CERES instruments were launched aboard the Tropical Rainfall Measuring Mission (TRMM) [89] in November 1997 and on the Earth Observing System (EOS) Terra and Aqua satellites in December 1999 and May 2002, respectively. CERES is designed to provide multiple view angles. This allows for better transformation of radiances to fluxes and improved scene identification thanks to the on board narrowband imager (VIRS on TRMM, MODIS on Terra/Aqua). It results in improved estimates of cloud radiative forcing. Although the processing of CERES data is expected to be combined with geostationary satellite imaging data, the maximum four observations per day is not expected to fully resolve the diurnal cycle. Geostationary data is then used to supplement the CERES observations by resolving the diurnal variations between them. The geostationary fluxes are produced through radiance narrowband–to–broadband and radiance–to–flux conversions.

The diurnal sampling issue is being addressed with the Geostationary Earth Radiation Budget (GERB) instrument [66, 67] on board the Meteosat Second Generation (MSG) [148]. GERB is a European effort supplementing the polar orbiting broadband measurements made by the Scanner for Radiation Budget (ScaRaB) [79]. It has been designed to exploit the geostationary orbit to make unique ERB measurements over Europe and Africa in a shortwave and a totalwave channel with a temporal sampling of 5 minutes 30 seconds. Based on such measurements, the aim of the GERB project is to deliver on a near–realtime basis TOA solar and thermal fluxes to the science community with a target accuracy of about 5 $\mathrm{W \cdot m^{-2}}$. Such a goal is achieved by the synergistic use of the multispectral Spinning Enhanced Visible and InfraRed Imager (SEVIRI) data within the L20 GERB Processing [52] performed at the Royal Meteorological Institute of Belgium (RMIB). This processing consists in applying successively a spectral modeling, a radiance–to–flux conversion and a resolution enhancement of the products at a higher spatial resolution (typically 10 km) than the native GERB instrument sampling (about 45 km at nadir).

This chapter is presented in two parts. In Part I (this chapter) we focus on the major requirement needed by the radiance–to–flux conversion scheme in the solar region. Angular dependency models (ADMs) play a key role in the conversion of directional radiance to TOA flux. Since the relationship between directional radiance and TOA flux that is described by ADMs differs considerably for various scenes (clear–sky surfaces, cloud properties, etc. . .), the accuracy of the radiance–to–flux conversion relies on the selection of the most representative ADM for each scene. Building such ADMs requires polar orbiting satellites, because these satellites observe a specific scene with variable viewing geometries during consecutive overpasses. This is not possible from geostationary satellites, which have fixed viewing geometries. Thus, the ADMs from TRMM which is on a 35° precessing polar orbit have been selected. Since these models were stratified according to the CERES scene identification [111, 116, 117], a simple but robust scene identification was implemented within the GERB processing to provide the basic features needed to properly select the ADM for every scene, i.e. surface geotype, cloud thermodynamic phase, cloud optical depth and cloud fraction. In the following, we will justify the selected approach and give a detailed description of the algorithms implemented with all their ancillary data. In Part II (chapter 7) we will present a detailed step–by–step error analysis as well as extensive comparison results with CERES retrievals.

6.2 Surface geotype

The CERES TRMM ADMs are classified according to some specific surface types [99]. This fixed surface map is derived from the Global Land Cover Map (version 1.2) dataset produced by the International Geosphere Biosphere Program (IGBP) [16]. The 17 IGBP surfaces are then aggregated into 5 classes—ocean, desert, low–to–moderate and moderate–to–high vegetation, ice/snow—according to the grouping shown in table 6.1. The desert class is further split in a dark and bright desert type according to their albedos. Thus, it was decided to adopt a similar approach for the SEVIRI scene identification. It simply consists in a spatial downscaling and regriding of the CERES surface map from 1 km to the native SEVIRI field–of–view (FOV) (3 km at nadir) by only retaining the most represented class within each SEVIRI pixel.

Since desert surfaces can exhibit large albedo differences and thus different anisotropic behavior, these were separated into bright and dark desert according to the CERES classification which lead to the 6 CERES TRMM ADMs surface types (see [99] for discussion). The final SEVIRI geotype map used in the GERB processing is illustrated in figure 6.1 and it can be found within the L20 GERB product files [52]. However, it is anticipated that the lack of dynamic snow/ice detection scheme in the current Edition 1 implementation will result in inaccurate cloud properties retrievals over such surfaces. Moreover, the misspecification of the underlying surface type for the radiance–to–flux conversion through the ADM selection will lead to large errors in the associated fluxes. This issue will be addressed in future Edition processing by the use of a snow/ice detection algorithm which was recently developed [18].

Table 6.1 *– Merging of the 17 IGBP surfaces into ocean, desert, low–to–moderate and moderate–to–high vegetation, ice / snow.*

ADM name	IGBP name
ocean	water
desert	open shrubland, barren or sparsely vegetated
low–to–moderate vegetation	savannas, grassland, permanent wetland, cropland, urban and built–up, cropland/natural vegetation mosaic
moderate–to–high vegetation	evergreen needleleaf forest, evergreen broadleaf forest, deciduous needleleaf forest, deciduous broadleaf forest, mixed forest, closed shrubland, woody savannas
ice/snow	permanent snow and ice

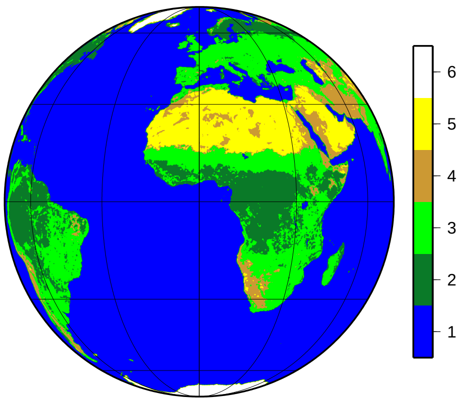

Figure 6.1 *– Geotype map for SEVIRI FOV where 1 is for ocean, 2 for moderate–to–high vegetation cover, 3 for low–to–moderate vegetation cover, 4 for dark desert, 5 for bright desert and 6 for snow or ice.*

6.3 Cloud properties

Since the GERB experiment aims to deliver products on a near–realtime basis (i.e. within 3 hours after the acquisition time), the overall RMIB GERB Processing (RGP) has to be done in the time period between two series of SEVIRI images, i.e. 15 minutes. To cope with this major time constraint, the adaptation of the CERES scene identification [111] to SEVIRI was not considered. Instead, we only retrieve the needed features to correctly apply the ADMs, i.e. cloud thermodynamic phase, cloud optical depth and cloud fraction. Nevertheless, we shall compare both schemes in Part II as it is crucial to select similar ADMs as CERES algorithm would. This will ensure that no spurious bias is introduced in the GERB TOA fluxes. The RMIB GERB Processing (RGP) retrieval starts by inferring the cloud thermodynamic phase for each SEVIRI pixel, and is then followed by retrieving cloud optical depth from visible narrowband radiances. This is achieved through the independent pixel approximation, i.e. by neglecting the horizontal transport of radiation in the atmosphere, while we make the assumption that pixels can only be either purely overcast or clear–sky. Such retrieval relies on the fact that the reflection function of clouds at non–absorbing narrowbands in the visible part of the electromagnetic spectrum is primarily dependent on the cloud optical depth [118]. It uses a set of look–up tables (LUTs) of narrowband visible radiances computed using a radiative transfer model (RTM) for a restricted number of ideal scenes (see for example [137]). Finally, instead of relying on complex imager multispectral threshold tests whose values have to be tuned specifically to each imager as usually found in the literature (see for example [144]), the cloud flag is simply based on a threshold test of the cloud optical depth and therefore remains consistent with this retrieval.

The method used for each SEVIRI pixel can be summarized by the following algorithm (see figure 6.2):

1. compute its TOA clear–sky reflectance in the 0.6 and 0.8 μm visible bands (see section 6.3.1),
2. determine the potential cloud thermodynamic phase using a fixed threshold on the 10.8 μm brightness temperature (see section 6.3.2),
3. using the proper 0.6 or 0.8 μm visible reflectance, derive the cloud optical depth through comparisons with the associated TOA clear–sky reflectance and look–up tables from 1–dimensional (1–D) RTM computations (see section 6.3.3),
4. assign a cloudy/non–cloudy flag from a threshold test on the cloud optical depth (see section 6.3.4),

Since the CERES ADMs have been built using measurements of about 10 km at nadir [181], we have chosen to perform the radiance–to–flux conversion within the GERB processing at a similar spatial resolution, i.e. 3×3 SEVIRI pixels' footprints (approximately 9 km). This minimizes any error which can arise from mixing data with distinct spatial extents. Thus, these retrieved cloud properties are averaged over such footprints and these mean properties are used to select an ADM most likely corresponding to the observed scene within each footprint. The cloud fraction is defined as the number of *cloudy* pixels divided by the total number of valid pixels (*clear*, *cloudy* and *shadow*) provided that the number of *clear* and *cloudy* pixels represent the majority, the mean cloud optical depth as the logarithmic average over all cloudy flagged SEVIRI pixels, while the mean cloud thermodynamic phase is defined as the average over the same SEVIRI pixels.

6.3.1 TOA composite clear–sky reflectances

The estimation of TOA clear–sky visible reflectances or albedos is a mandatory step of nearly all scene identification algorithms which aim to retrieve cloud optical parameters, as illustrated in the literature [141]. Indeed, they are used to provide reference values for the computation of the cloud optical depth using the RTM LUTs (see section 6.3.3) as well as to derive properties at the surface through inversion schemes. The major algorithms found in literature are inadequate for several reasons. First, they are not designed for the geostationary platform which implies large scene geometry variations with time (see figure 6.3(c)). Moreover, they

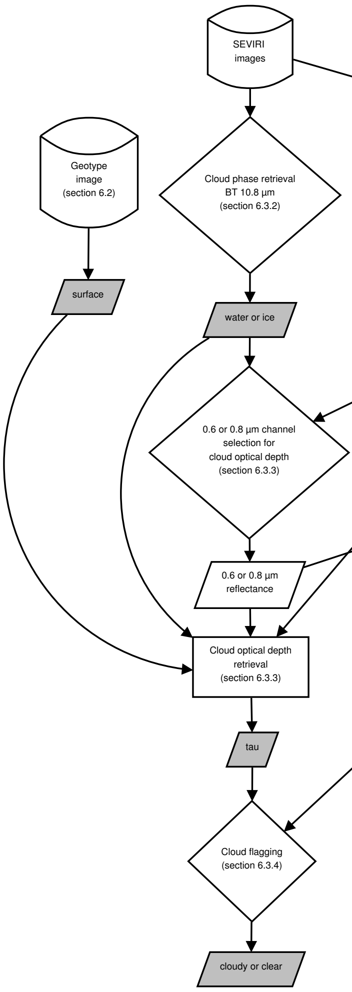

Figure 6.2 *– Flow diagram of the cloud properties retrieval scheme: gray–filled boxes denote the features needed for ADM selection while the dashed box is a weekly processing.*

do not usually retain the high temporal sampling of the imager nor its native spatial resolution. Therefore, we have developed a new method to compute the TOA clear–sky reflectance for the Meteosat–7 visible broadband which addresses the previous requirements (see chapter 4) and we are using its straightforward adaptation to the 0.6 and 0.8 μm visible channels of Meteosat–8. In the following we briefly recall the basic algorithm. Then, we investigate its refinements to solve its surface variability and sun–glint issues.

6.3.1.1 Basic algorithm

This method is based on the same common assumptions of numerous algorithms found in the literature (see chapter 4 for a non–exhaustive list): clear–sky visible reflectance variations are smaller in time than in space (especially over land), and surface reflectance variations are smaller than variations induced by observed clouds. Therefore, successive snapshots of the same target can be used for the estimation of the TOA visible clear–sky reflectances through the concept of time–series. It is worth pointing out that snow covered surfaces exhibit visible reflectances of the same order of magnitude than clouds which violate the commonly used assumptions for the clear–sky algorithm. Thus, it is expected that clear–sky estimated reflectances as well as cloud properties retrievals over snow covered regions will be highly unreliable.

According to the previous assumptions the TOA visible reflectance time–series of a SEVIRI pixel at a given day–time is a function of surface temporal variations, seasonal illumination changes and cloudiness. Surface temporal variations mainly occur over vegetation due to its life cycle which rules the cover fraction and spectral signature. However, for most of Africa, vegetated surfaces are stable (evergreen forests) while for the rest of the SEVIRI FOV we make the assumption that they remain stable over a restricted time period. Therefore, the time–series for each pixel in each visible channel can be split into two components: a base curve representative of clear–sky conditions which is only a function of illumination variations, and an additive noise representing the cloudy contributions above the surface (high spikes in the reflectance time–series as illustrated in figures 6.3(a)-(b)). Nevertheless, additional effects may occur such as cloud shadows in broken cloud fields which result in a significant decrease of the measured reflectance as shown in figure 6.3. Varying aerosol content usually leads to its increase, too. Thus, to extract the base curve, we need some knowledge about the variations of the TOA clear–sky visible reflectances according to scene geometry. Such information is provided by the CERES shortwave ADMs which allow us to compute climatological TOA clear–sky broadband reflectances for 6 coarse classes of geotypes (see section 6.2).

We make the assumption that the clear–sky SEVIRI visible reflectance base curve, $\rho_{\text{cs}}^{\text{sv}}$, and the associated clear–sky shortwave CERES curve, $\rho_{\text{cs}}^{\text{cr}}$, only differ by a multiplication factor over a restricted time period (N days). Thus, for a given day d and time t, a composite clear–sky image is built by using for each pixel and visible SEVIRI band:

$$\rho_{\text{cs}}^{\text{sv}}(d,t) = \alpha_{\text{cs}}^{\text{sv}}(d,t) \cdot \rho_{\text{cs}}^{\text{cr}}(d,t) \tag{6.1}$$

where $\alpha_{\text{cs}}^{\text{sv}}$ is the SEVIRI multiplication factor. This value is selected to keep 3 measurement values of the reflectances ρ^{sv} below the clear–sky SEVIRI base curve $\alpha_{\text{cs}}^{\text{sv}} \cdot \rho_{\text{cs}}^{\text{cr}}$ over a N–days time period. This is similar to estimate

$$\alpha_{\text{cs}}^{\text{sv}}(d,t) = \text{4th lowest value of } \frac{\rho^{\text{sv}}(\star,t)}{\rho_{\text{cs}}^{\text{cr}}(\star,t)} \tag{6.2}$$

where $\star$ represents the observations during the period $d - N$ till d and N is the number of days used for the estimation of the multiplication factor. We have chosen the 4th lowest value for the multiplication factor because it represents a good compromise for shadow and cloud filtering. Indeed, we have observed that a lower value would lead to an unacceptable sensitivity to shadow occurrences while a higher would result in an overestimation of the clear–sky reflectance. Since some parts of the African tropical land area exhibit persistent cloudiness over more than 20 days [104], the time period N should accordingly not be chosen below.

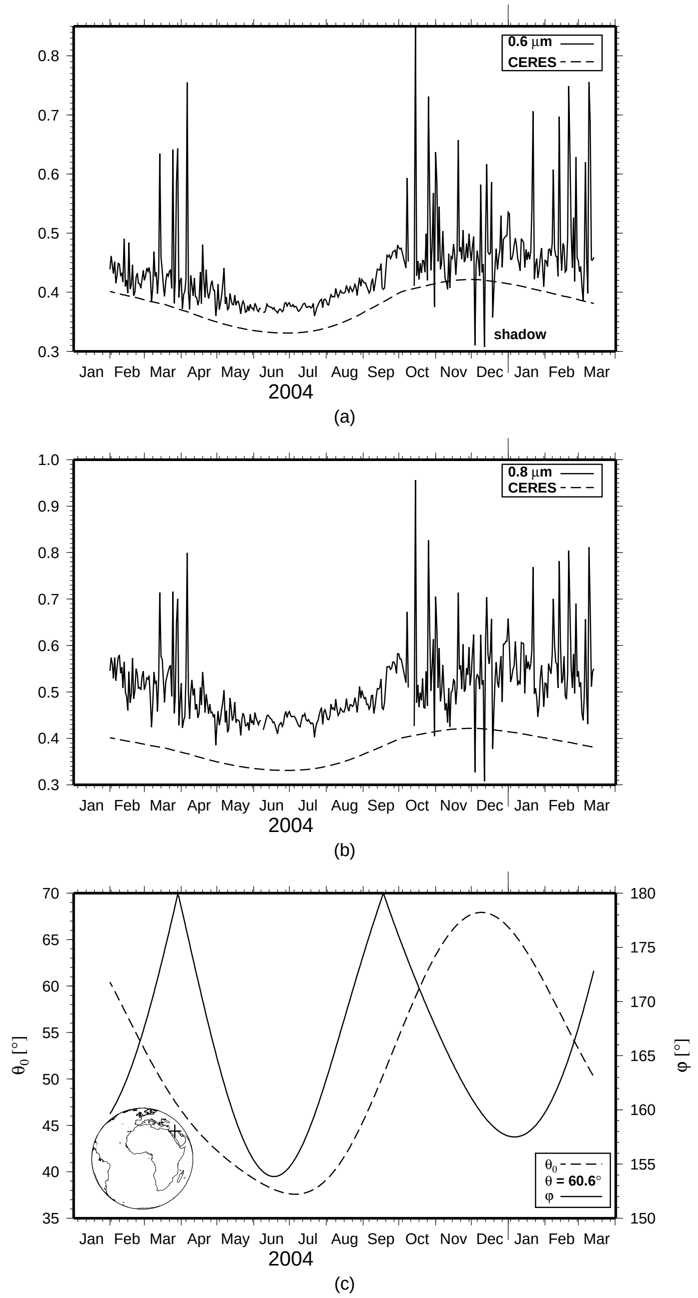

***Figure 6.3** – Meteosat–8 visible reflectance time–series ρ^{sv} and associated clear–sky shortwave CERES reflectances ρ^{cr}_{cs} for (a) 0.6 µm and (b) 0.8 µm, according to (c) scene viewing geometry variations (θ_0 = solar zenith angle, θ = viewing zenith angle, and φ = relative azimuth angle) for daily 12:00 UTC measurements over a bright desert pixel (42.54 N, 29.98 E).*

Moreover, bearing in mind our assumption on the stability of surface reflectances over this time period, its value should also not exceed 60 days.

6.3.1.2 Surface variability

As we mentioned in the previous section, the time period N has to range between 20 and 60 days. However, fast transient seasonal changes can be observed in specific regions, mainly between the Sahara desert and the equatorial evergreen forests, i.e. the Sahel. Figure 6.4 illustrates such changes in the latter region by displaying two false–color images acquired within a time interval of less than 60 days. The displacement of the border between those two geotypes is obvious. Therefore, the time period should not be constant across the whole FOV but instead should be varying, to take into account areas exhibiting rapid surface variability as well as locations with persistent cloudiness.

The most adequate time period for each pixel relies on the climatology of cloud frequencies from the International Cloud Climatology Project (ISCCP) [140]. By taking into account the constraints about persistent cloudiness and transient surface variability areas, we have created a mapping to calculate the time period N for every pixel within the FOV when applied to the ISCCP D2 annual mean cloud cover as shown in figure 6.5. More specifically, we have taken into account three constraints for building it. First, regions with the lowest cloud occurrences should not use less than 20 days to build their clear–sky to remain insensitive to cloud shadows (lowest plateau in figure 6.5(b)). Second, areas with persistent cloudiness such as the tropical rain forest and Western Europe should not consider more than 60 days for stability of surface reflectances (highest plateau in figure 6.5(b)). Third, for the Sahel region, a time period of 30 days have shown to perform well and removes the cloud artefacts due to the seasonal changes of the vegetation (middle plateau in figure 6.5(b)). Finally, linear transitions between the different plateaus are selected for simplicity.

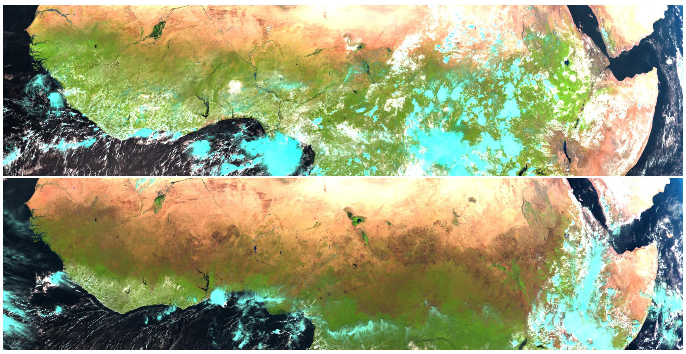

Figure 6.4 *– False color images using the* 1.6, 0.8 *and* 0.6 *µm channels of the Sahel region for October 10 (top) and December 8 (bottom) 2003 at 12:00 UTC (green: vegetation; dark blue: water; light brown and yellow: desert; dark brown: savannah; magenta: ice clouds; white: water and thin ice clouds).*

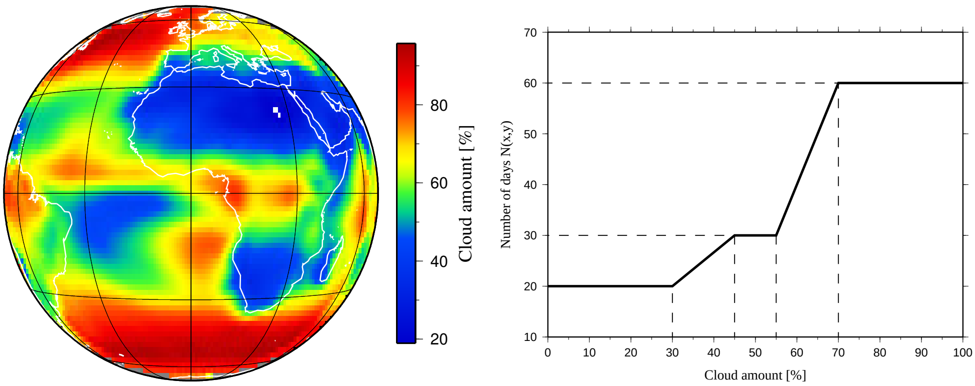

(a) (b)

Figure 6.5 *– (a) ISCCP D2 annual mean cloud cover for SEVIRI FOV and (b) time period mapping of the cloud amount derived from (a) and figure 6.4 by visual interpretation.*

6.3.1.3 Sun–glint

Due to the geostationary orbit, the sun–glint effect, i.e. the intense specular reflection of sun light on the ocean surface, is extensively observed during several hours in the FOV of the satellite. This is illustrated by the figure 6.6 showing the probability of sun–glint [174] for September 15 2004 at 12:00 UTC according to the QuikSCAT [17] monthly mean ocean wind climatology. Since the maximum probability spot is following the Sun movement, this phenomenon affects a large region of the Atlantic ocean throughout the day. It results in a high variability of the ocean reflectance within even a short period of time. Thus, our assumption on $\alpha_{\mathrm{cs}}^{\mathrm{sv}}$ being constant over N days (see section 6.3.1.1) is no longer valid. As a matter of fact, this method would systematically underestimate the ocean clear–sky reflectance for pixels entering the affected area.

To overcome this limitation, we choose to parametrize $\alpha_{\mathrm{cs}}^{\mathrm{sv}}$ according to the tilt angle Ψ between the specular reflection and the viewing direction defined as

$$\Psi = \operatorname{acos}(\sin\theta \sin\theta_0 \cos\varphi + \cos\theta \cos\theta_0). \tag{6.3}$$

Such approach is relying on theoretical radiative transfer calculations (libRadtran [105]) for a typical clear ocean scene with a fixed 5 $\mathrm{m \cdot s^{-1}}$ wind speed using the Cox–Munk ocean reflectance model [38] and specific scene geometries in 2004: solstices (June and December 21) corresponding to extreme Sun positions and the Spring equinox (March 21) associated to a symmetric Sun position with respect to the equatorial plane. These computations are then used to estimate theoretical SEVIRI–like FOVs for the 0.6, 0.8 μm and shortwave channels. For each selected day and repeat cycle between 7:00 and 17:00 UTC, theoretical $\widehat{\alpha}_{\mathrm{cs}}^{\mathrm{sv}}$ values were computed from the theoretical reflectances at the 0.6, 0.8 μm and shortwave bands according to the tilt angle Ψ (see figure 6.7(a)). Finally a least square fit using the following model was performed

$$\widehat{\alpha}_{\mathrm{cs}}^{\mathrm{sv}} = a_i\, e^{-b_i \Psi^3 - c_i \Psi^2} + d_i. \tag{6.4}$$

The root mean square deviation (rmsd) of these fits are ranging from 0.002 (March 21) and 0.023 (June and December 21) to 0.091. Moreover, the minimum values are reached near

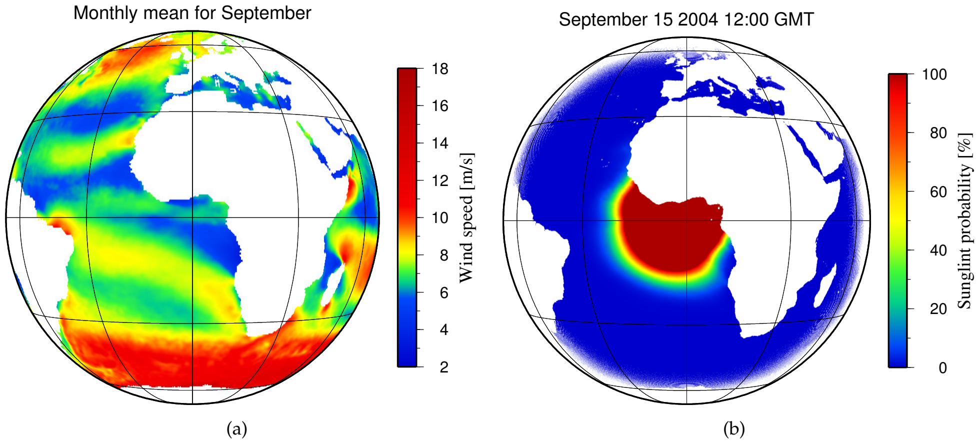

Figure 6.6 *– QuikSCAT monthly wind speed climatology for September (a) and associated sun–glint probability (b).*

12:00 UTC, while the rmsd is increasing as time moves away from noon. Its highest values are occurring near 7:00 and 17:00 UTC. Such U–shape for the diurnal rsmd curves can be explained by the fact that the solar and viewing zenith angles over the sun–glint area are increasing as time moves away from noon. This results in spurious artifacts in the RTM simulations due to the limitations of the plane–parallel formalism at large zenith angles exacerbated by the peaked response of the Cox–Munk surface model around the direction of specular reflection ($\Psi = 0$).

By comparing all these fits, one can note that they share similar b_i and c_i coefficients and hence exhibit the same shape as it is illustrated in figure 6.7(b) (green curves). Thus, making the assumption that the mean shape of these fits is valid for all geometries, we get

$$\begin{aligned} \alpha_{\mathrm{cs}}^{\mathrm{sv}} &= \left(M^{\mathrm{sv}} - m^{\mathrm{sv}}\right) \langle e^{-b_i\Psi^3 - c_i\Psi^2} \rangle + m^{\mathrm{sv}} \\ &= \left(M^{\mathrm{sv}} - m^{\mathrm{sv}}\right) e^{-6.939\Psi^3 - 1.128\Psi^2} + m^{\mathrm{sv}} \end{aligned} \tag{6.5}$$

where $\langle \cdots \rangle$ denotes the ensemble mean (red curve in figure 6.7(b)), $M^{0.6,0.8} = 0.9$, $m^{0.6} = 0.7$ and $m^{0.8} = 0.4$. m^{sv} were chosen empirically to match measured $\alpha_{\mathrm{cs}}^{\mathrm{sv}}$ in the outer neighborhood of the sun–glint area, while M^{sv} is empirically obtained as the maximum value of $\alpha_{\mathrm{cs}}^{\mathrm{sv}}$ in the sun–glint area. This model is then applied in the processing for $\Psi < 1$ radian (mean model cut–off value).

6.3.1.4 Additive offset to $\rho_{\mathrm{cs}}^{\mathrm{sv}}$

It can be shown that if the clear–sky value $\rho_{\mathrm{cs}}^{\mathrm{sv}}$ is directly used in the cloud optical depth retrieval scheme described in section 6.3.3, it results in false cloudy detection of obvious clear–sky areas. Since there is a high uncertainty when detecting thin clouds due to the error of the clear–sky reflectance estimation, we try to minimize false cloudy detection. Therefore, an empirical offset Δ^{sv} is added to $\rho_{\mathrm{cs}}^{\mathrm{sv}}$. Its value was selected according to the uncertainty of the

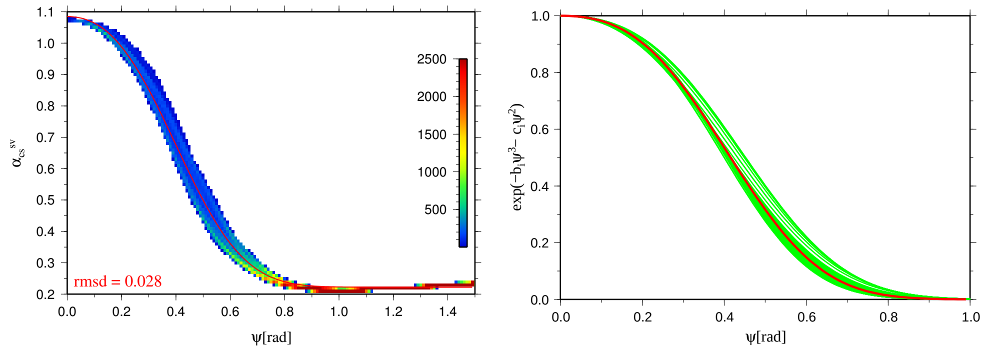

(a) (b)

***Figure 6.7** – Histogram of the theoretical $\alpha_{\rm cs}^{\rm sv}$ values according to the tilt angle Ψ for March 21 2004 at 14:00 UTC and its associated least square fitted curve in red (a) and least square fitted curves for every mentioned day and repeat cycle with their averaged curve in red (b).*

clear–sky reflectances to avoid false cloud detection. $\Delta^{0.6} = 0.025$ and $\Delta^{0.8} = 0$ fulfill this constraint while preserving simplicity thanks to their constant values. Finally, the value used in the retrieval algorithm $\widetilde{\rho}_{\rm cs}^{\rm sv}(d,t)$ is then given by

$$\widetilde{\rho}_{\rm cs}^{\rm sv}(d,t) = \rho_{\rm cs}^{\rm sv}(d,t) + \Delta^{\rm sv}. \tag{6.6}$$

6.3.1.5 Computation of TOA composite clear–sky images

As mentioned previously, the algorithm is run at the SEVIRI pixel–level for both visible channels. Each SEVIRI image being 3712×3712 pixels large, the near–realtime constraint of the GERB processing currently forbids the estimation of these images on a daily basis due to the limited amount of computing resources available. Therefore, the estimation of $\alpha_{\rm cs}^{\rm sv}$ outside the sun–glint area is only performed once a week, while $\rho_{\rm cs}^{\rm sv}(d,t)$ is computed for every day d and each repeat cycle t according to equation 6.1 with the associated $\rho_{\rm cs}^{\rm cr}(d,t)$. It is worth recalling that the geometrical dependency of $\alpha_{\rm cs}^{\rm sv}$ according to pixel coordinates (x,y) and time (d,t) is implicit. However, we plan to remove this limitation in future releases of products. An example of the estimated clear–sky visible reflectance images for the 0.6 and 0.8 μm channels is given in figure 6.8(b) as a false–color composite.

6.3.2 Cloud thermodynamic phase

The cloud thermodynamic phase detection test is the first step of the cloud properties retrieval scheme. It is used to properly select the ADM of the studied scene and the LUT for the cloud optical depth estimation algorithm. Because this test is performed prior to the cloud flag test, it always assigns to each SEVIRI pixel a cloud phase even if it is later declared as clear–sky. Nevertheless, at the end of the processing the cloud phase attribute will be reassigned to *undefined* if the pixel is detected as clear–sky.

During the development of the prototypal scene identification (sceneID) on Meteosat–7 (MS7) data (see chapter 5), it was foreseen that the future 1.6 μm SEVIRI channel would enable efficient detection of the cloud phase. The literature review (see chapter 3, section 3.3.2) demonstrated that this approach is successful for thick clouds only. Indeed, the satellite signal is essentially originating from these clouds. It implies that thick water and ice clouds can be separated according to the different spectral behavior of their absorption (see figure 2.7). However, for thin clouds, the contribution of the surface to the measurements is significantly larger. Therefore, without an accurate characterization of the surface (or TOA clear–sky) reflectances in this band, thin water and ice clouds can not be discriminate since they are exhibiting similar TOA near–infrared (NIR) reflectances. Such estimation of the clear–sky NIR reflectance is in practice difficult to achieve without ancillary information. The MODIS Atmosphere Science Team (MAST) initially planned to use for Moderate Resolution Imaging Spectroradiometer (MODIS) a threshold test on the ratio $\rho_{1.6}/\rho_{0.6}$ but reached the same conclusion and implemented an IR–only technique [85, 130].

The cloud thermodynamic phase test relies here on the fact that in the vicinity of 11 μm, for an optically thick cloud the cloud top brightness temperature is usually not larger than 1 K from its physical temperature. This is due to the high emissivity of both water and ice and the atmospheric transmission [30]. Therefore, the following index allows us to discriminate between water and ice clouds

$$\Phi = \begin{cases} 0 & \text{if} \quad \mathrm{BT}_{10.8} > \mathrm{BT}_{\max} \\ \frac{\mathrm{BT}_{\max}-\mathrm{BT}_{10.8}}{\mathrm{BT}_{\max}-\mathrm{BT}_{\min}} & \text{if} \quad \mathrm{BT}_{\min} \leq \mathrm{BT}_{10.8} \leq \mathrm{BT}_{\max} \\ 1 & \text{if} \quad \mathrm{BT}_{10.8} < \mathrm{BT}_{\min} \end{cases} \tag{6.7}$$

where $\mathrm{BT}_{10.8}$ is the brightness temperature estimated from the 10.8 μm SEVIRI channel radiance using the standard EUMETSAT formula [149] and $\mathrm{BT}_{\max}$ (resp. $\mathrm{BT}_{\min}$) is a maximum (minimum) empirical threshold value. For $\mathrm{BT}_{\max} = 265$ K and $\mathrm{BT}_{\min} = 245$ K chosen for the processing, this index is ranging between 0 (pure water) and 1 (pure ice). For the ADM selection, since no ADM consists of mixed cloud phase, the pixel is reassigned as pure ice if this value is above 0.5 while it is assigned to pure water otherwise. One can show that this simply reduces to the following test

$$\begin{aligned} \mathrm{BT}_{10.8} &\geq \mathrm{BT}_{\mathrm{thres}} \Rightarrow \text{water cloud} \\ \mathrm{BT}_{10.8} &< \mathrm{BT}_{\mathrm{thres}} \Rightarrow \text{ice cloud} \end{aligned} \tag{6.8}$$

where $\mathrm{BT}_{\mathrm{thres}}$ is then equal to 255 K in accordance with Wolters et al. [189]. However, this mixed cloud phase index Φ is used in the remaining of the GERB processing for the high resolution products. We are aware that such a crude cloud phase retrieval scheme suffers from several limitations. Supercooled water clouds will surely be misidentified as ice clouds, while many thin cirrus clouds will be misclassified as water clouds. An example of the estimated cloud thermodynamic phase image is given in figure 6.8(f).

6.3.3 Cloud optical depth

Our scheme relies on simulated outgoing radiances L from the plane–parallel STREAMER [82] RTM convoluted with the associated filters of both SEVIRI visible channels. These simulations were run for a set of simple scenes with varying cloud optical depth τ. For simplicity, we have only considered pure ground surfaces with uniform single layer and phase clouds as described in table 6.2. The scene geometries are defined relatively to the local normal of the surface with θ_0 and θ being the solar and viewing zenith angles and φ the relative azimuth angle ($\varphi = 0$ corresponds to the forward scattering). In order to remain consistent with the ADM geotype classification (section 6.2), input ground surfaces were selected accordingly and their characteristics are also given in table 6.2. The broadband albedo is simply a scaling factor applied to the spectral signature of the geotype. Note that for low–to–moderate and moderate–to–high vegetation covers which consist in a broad range of IGBP classes (see table 6.1) and therefore are exhibiting the highest variations, we consider two subclasses for both. The values of τ were selected to match a pseudo–logarithmic scale while the optically opaque cloudy condition $\tau = 128$ and the particle shape for ice clouds are identical to those considered for the CERES scene identification.

Table 6.2 *– Scene parameters used as input for the STREAMER code simulations where z is the bottom cloud altitude, h the cloud geometrical depth, r_e the cloud particle mean effective radius and, τ the cloud optical depth at 0.6 μm.*

Ground surfaces		
Type	Model	Broadband albedo
ocean	open sea water	–
bright desert	dry sand	0.28
dark desert	dry grass	0.20
low–to–mod veg. 1	grass	0.18
low–to–mod veg. 2	grass	0.16
mod–to–high veg. 1	deciduous forest	0.15
mod–to–high veg. 2	coniferous forest	0.15
Aerosol profiles	maritime for ocean and rural for others, background tropospheric and stratospheric profiles,	
Standard profile	mid–latitude summer	
Cloud properties		
Phase	water	ice
z (km)	3	9
h (km)	3	1
Particle shape	spheric	hexagonal
Phase function	Henyey–Greenstein	double Henyey–Greenstein
Particle size distrib.	Hu and Stamnes [69]	Key et al. [83]
r_e (μm)	12	70
τ	$0, \{10^{-2}, 10^{-1}, 1, 10\} \times \{1, 2, 4, 7\}, 100, 128$	
Scene geometries		
θ_0 (°)	$0 \rightarrow 90$ by 5° steps	
θ (°)	$0 \rightarrow 90$ by 5° steps	
φ (°)	$0 \rightarrow 180$ by 5° steps	

The LUTs mentioned in section 6.3 are not directly used to retrieve the cloud optical depth from the measured visible narrowband radiances as it is commonly performed in the literature (see Rossow and Garder [137] for example). As shown in Nakajima and Nakajima [119] the radiance is empirically linked to the cloud optical depth while it is nearly insensitive to the cloud particle size r_e for visible wavelengths. By reformulating the mean cloud amount (or cloud coverage index) C as defined in Cano et al. [24] in terms of reflectance ρ^{sv}, one gets

$$C(\theta_0, \theta, \varphi, s, \mathrm{phase}, \tau) = \frac{\rho^{\mathrm{sv}}(\theta_0, \theta, \varphi, s, \mathrm{phase}, \tau) - \rho^{\mathrm{sv}}(\theta_0, \theta, \varphi, s, \tau = 0)}{\rho^{\mathrm{sv}}(\theta_0, \theta, \varphi, s, \mathrm{phase}, \tau = 128) - \rho^{\mathrm{sv}}(\theta_0, \theta, \varphi, s, \tau = 0)}, \tag{6.9}$$

where $\tau = 0$ represents clear–sky conditions above the ground surface and $\tau = 128$ denotes the optically opaque cloudy conditions leading to simulated radiance fields which are insensitive to the ground surface s. Then this empirical law is simply rescaled with C values ranging from 0 to 1.

In chapter 5 we have shown that this law can be parametrized using a modified sigmoïd function of the logarithm of the cloud optical depth, i.e.

$$C = \frac{A}{B + 10^{-(\log \tau - \log \tau_0)/\chi}} \tag{6.10}$$

which is uniquely determined by the four parameters A, B, $\tau_0 > 0$ and $\chi \neq 0$. We have omitted for notation simplicity their dependency to the scene geometries (θ_0, θ, φ), ground surface and cloud phase as it is also the case for the mean cloud amount C. Note that the reflection function generated by these simulations does not yet reach the asymptotic value of C for the optically opaque cloudy conditions ($\tau = 128$). However, to be consistent with CERES retrievals, we have set $C = 1$ for $\tau \geq 128$, the highest possible cloud optical depth value which will be retrieved by our algorithm. Then, the parameters A, B, τ_0 and χ are obtained through a least square fit on the theoretical simulations values by using the Powell multidimensional fitting approach [131]. Solving equation 6.10 for τ, one gets

$$\tau = \begin{cases} \dfrac{\tau_0 \, C^{\chi}}{(A - BC)^{\chi}} & \text{for } C < A/B \\ 128 & \text{for } C \geq A/B \end{cases} \tag{6.11}$$

with $\chi \neq 0$ and $\tau_0 > 0$.

Therefore, our cloud optical depth retrieval scheme immediately follows; for each SEVIRI pixel:

1. we compute the denominator of the right hand side of equation 6.9 for both 0.6 and 0.8 μm channels knowing the surface geotype s from section 6.2, the cloud phase from section 6.3.2, the composite clear–sky reflectance $\widetilde{\rho}^{\mathrm{sv}}_{\mathrm{cs}}$ from section 6.3.1 for $\rho^{\mathrm{sv}}(\theta_0, \theta, \varphi, s, \tau = 0)$ and using the theoretical optically opaque cloudy reflectance $\rho^{\mathrm{sv}}(\theta_0, \theta, \varphi, s, \mathrm{phase}, \tau = 128)$,

2. we select the channel sv with the highest denominator in equation 6.9, i.e. the one associated with the highest sensitivity to the cloud signal compared to the clear–sky response, and we compute its mean cloud amount C substituting $\rho^{\mathrm{sv}}(\theta_0, \theta, \varphi, s, \mathrm{phase}, \tau)$ by its reflectance measurement unless its denominator is below a threshold of 0.2 for which our algorithm ends by flagging the pixel as *uncontrasted*,

3. we finally estimate its cloud optical depth with equation 6.11 and the parameters A, B, τ_0 and χ which are function of $(\theta_0, \theta, \varphi, s, \mathrm{phase})$ unless C is below a threshold of -0.1 which corresponds to the flag *shadowed*.

Note that due to the limitations of 1–D RTMs for geometries reaching grazing solar and viewing zenith angles, we only perform the estimation of cloud optical depth for zenith angles (θ_0 and θ) below 80°. An example of the estimated cloud optical depth image is given in figure 6.8(c).

6.3.4 Cloud flag

The chosen parametrization of the mean cloud amount with respect to the cloud optical depth given in equation 6.10 only fulfills asymptotically the boundary clear–sky condition, i.e. $C = 0$ for $\tau \to 0$. Thus, one can expect that the previous algorithm will always retrieve cloud optical depth values strictly above 0. Because small values are not significant compared to the retrieval error, we have decided to set all τ values below τ_{thres} to the clear–sky condition $\tau = 0$. In section 5.4 we found that a value of 0.85 for τ_{thres} is ensuring that, on average, MS7 and CERES are detecting the same cloud coverage over their footprints. We therefore start by considering this value for SEVIRI. However, due to the different visible spectral characteristics of MS7 and SEVIRI (see figure 5.2), it has to be adapted. This adjustment to 0.6 is performed through visual image inspection over a period of about one week to decrease the number of misidentified cloudy pixels when it is set to 0.85 without significantly increase the number of detected false clouds. In addition, such threshold has to be locally increased for mixed SEVIRI ocean/land pixels which can exhibit significant changes in their visible reflectance time–series. This is due to the rectification errors, when regriding the SEVIRI images, which come from the movement of the satellite around its nominal position. It is especially true on coastlines, but it can also appear for mixed land pixels. These significant differences between composite and measured clear–sky reflectances lead to false cloud detection for these pixels. To overcome such issue, we compute an image based τ_{thres} for each pixel (x, y) on the composite clear–sky $\rho_{\text{cs}}^{\text{sv}}$ reflectance associated to the visible channel sv with the highest dynamic as

$$\tau_{\text{thres}} = \min\left[\tau_{\max}, 0.6 + \beta\left(\max_{3\times3}\rho_{\text{cs}}^{\text{sv}} - \min_{3\times3}\rho_{\text{cs}}^{\text{sv}}\right)\right] \tag{6.12}$$

where we have omitted the dependency to (d, t) for notation simplicity and the min (respect. max) denotes a minimum (respect. maximum) search in a 3×3 window around the pixel. It is found that $\tau_{\max} = 3$ and $\beta = 30$ are values that give good results in heterogeneous Earth surface boundary regions. Thus, for a region with low contrast, i.e. typically made of an homogeneous surface type, τ_{thres} will be close to 0.6, while for areas characterized with heterogeneous surfaces such as coastlines, this value will be increased close to $\tau_{\max}$. This last step can be summarized as follows: if $\tau(x, y) < \tau_{\text{thres}}(x, y)$ then the pixel is flagged *clear–sky* with its τ value set to 0 and cloud phase set to *undefined* otherwise it is flagged *cloudy*. An example of the dynamic τ_{thres} images is given in figure 6.8(d) while the estimated cloud flag image is given in figure 6.8(e). Note that the area over Europe corresponding to large τ_{thres} values (up to 3) can be explained by fresh snow covered surfaces. Indeed, as mentioned in section 6.2, the GERB scene identification currently lacks a dynamic snow detection scheme and these pixels were processed into the composite clear–sky estimation scheme. However, such snow covered surfaces are characterized by high and extremely variable visible reflectances which do not satisfy the assumptions of the algorithm for the calculation of TOA composite clear–sky reflectances (see section 6.3.1.1). This results in inaccurate as well as spatially noisy clear–sky estimated reflectances and thus high τ_{thres} values.

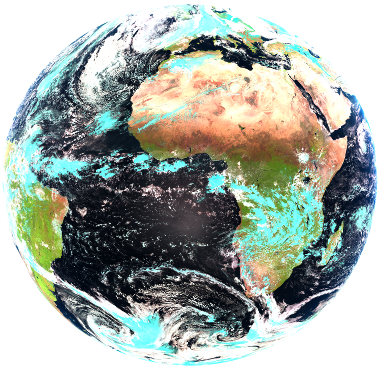

(a) False color visible reflectances (red = 1.6 μm, green = 0.8 μm, blue = 0.6 μm)

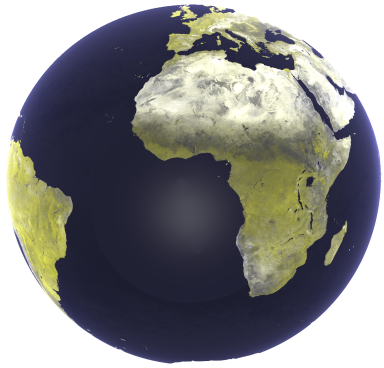

(b) False color visible clear–sky reflectances (red = 0.8 μm, green = 0.8 μm, blue = 0.6 μm)

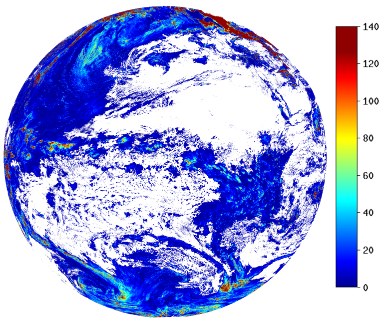

(c) Cloud optical depth

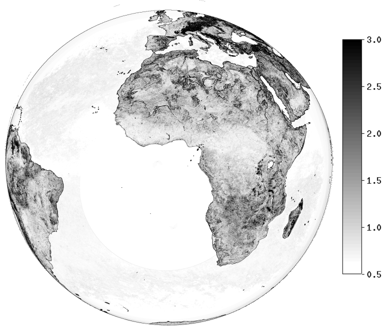

(d) Dynamic τ_{thres}

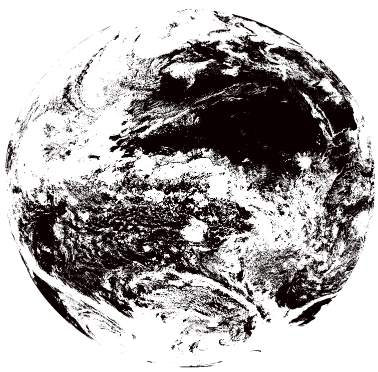

(e) Cloud flag (white = cloudy, black = clear–sky)

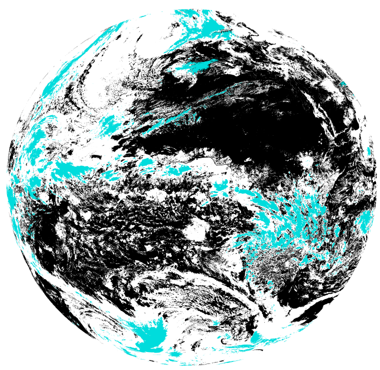

(f) Cloud phase (cyan = ice, white = water)

***Figure 6.8** – Examples of SEVIRI cloud products generated by the GERB scene identification for January 17 at 12:00 UTC.*

6.4 Conclusion

In this chapter, we described the scene identification scheme which is applied to the SEVIRI data within the GERB processing to build the GERB Edition 1 product dataset. Detailed information on the cloud properties retrieval algorithm was given as well as ancillary data. More specifically, an improved method to estimate TOA composite clear–sky visible reflectance from the geostationary orbit was presented. It allows to perform a cloud detection together with a cloud optical depth estimation using solely visible reflectance data from an imager. The simplicity of this scene identification allows it to be routinely operated on realtime data streams. RMIB has been successfully running this scheme on Meteosat–8 data and a previous version on the Meteosat–7 imager.

Loeb et al. [96] stressed the importance of using the same scene identification scheme in both development and application of ADMs for determining TOA fluxes. Since this is not operationally achievable, we need to ensure that the GERB scene identification matches as close as possible the CERES retrievals to avoid any bias in the ADM selection for the radiance–to–flux conversion scheme. This will be addressed in the following chapter 7 which is devoted to the validation of the GERB scene identification. Briefly, we plan to compare the GERB cloud properties to the CERES retrievals which are estimated from the same SEVIRI input dataset. The availability of the CERES retrievals from SEVIRI is made possible thanks to the adaptation and the dedicated processing of the CERES scene identification by the NASA Langley Cloud and Radiation Research Group. Indeed, it will allow a pixel–to–pixel comparison to be performed without any consideration about spatial or spectral instruments' differences as it is usually the case. Discrepancies between both schemes will be investigated and quantified from a temporal, spatial and angular perspective. Furthermore, the so–called GERB–like processing based only on SEVIRI data will be run on both GERB and CERES cloud properties retrievals. It will enable study of the impact of the discrepancies between GERB and CERES scene identifications on the estimation of GERB–like TOA solar fluxes. Such assessment will certainly point out current limitations of the GERB scheme and will thus suggest improvements for the Edition 2 version of the algorithm*.

Acknowledgments

The QuikSCAT monthly mean wind data were obtained from the CERSAT located in IFREMER, Plouzoné (France).

The authors would like to thank Dr. D. Caprion from the Climate Monitoring SAF (CM-SAF) at the Royal Meteorological Institute of Belgium and Dr. C. Dupuy from Total Petrochemicals Research Feluy, Belgium, for their comments on the manuscript.

This work was supported by the Research Directorate of the European Commission under contract GERBEC, the Belgian Science Policy Office (BELSPO) under contract PRODEX 5–8 and by European Organisation for the Exploitation of Meteorological Satellites (EUMETSAT) under contract EUMETGERB.

*see section 7.4 in chapter 7

Chapter 7

Validation of the GERB Edition 1 SEVIRI scene identification*

This chapter describes the comparisons of the cloud properties retrievals between the previously described scene identification and a reference scene identification both applied to the same SEVIRI data.

Abstract

The processing of Geostationary Earth Radiation Budget (GERB) radiance measurements implies a radiance–to–flux conversion scheme which is based for the solar part of the spectrum on explicit angular dependency models developed from the recorded Tropical Rainfall Measuring Mission Clouds and the Earth's Radiant Energy System (CERES) directional radiances. To properly select such models for every GERB footprint, a scene identification relying on the Spinning Enhanced Visible and InfraRed Imager (SEVIRI) was developed to provide the required cloud properties.

This chapter compares the results of the GERB and CERES scene identification schemes when applied to SEVIRI data. Discrepancies are analyzed and quantified according to the various features of the GERB algorithm. Possible dependencies with the ancillary composite clear–sky estimation scheme as well as spatial and angular factors over the SEVIRI field–of–view are investigated. Limitations in the current GERB Edition 1 processing are pointed out and various improvements are suggested for future Edition processing. Finally, an objective comparison between GERB–like top–of–the–atmosphere solar fluxes estimated using both GERB and CERES scene identification retrievals is performed to assess instantaneous as well as averaged flux errors which can be expected from discrepancies of these retrievals.

7.1 Introduction

THIS chapter is the second of a two–part series. In the first part (see chapter 6), we described the development of the methods used in the Geostationary Earth Radiation Budget (GERB) scene identification (sceneID) based on Spinning Enhanced Visible and InfraRed

*Adapted transcription of A. Ipe, C. Bertrand, N. Clerbaux, S. Dewitte and L. Gonzalez Sotelino, The GERB Edition 1 products SEVIRI scene identification – Part II: Validation, *under review at IEEE Trans. Geosci. Remote Sens.*, 2010.

Imager (SEVIRI) data. Such sceneID is mandatory to perform the radiance–to–flux conversion within the GERB L20 processing in the solar wavelength region through the selection of angular dependency models (ADMs). However, the usefulness of this sceneID goes beyond this single step as its retrievals are also included within the end–user products. This is of prime interest for the science community as it allows users to perform studies on specific processes, such as clouds or aerosols [95] radiative forcing or derive monthly and monthly diurnal cycle solar clear–sky flux products [58], for example.

Here, we focus on the validation of these algorithms through an extensive comparison with a reference dataset. We also investigate the impact of the discrepancies between the GERB and the Clouds and the Earth's Radiant Energy System (CERES) sceneIDs on the ADM selection through the resulting errors in top of the atmosphere (TOA) solar fluxes. Finally a step–by–step error analysis on each feature derived by the sceneID and used in the radiance–to–flux conversion scheme is performed.

As mentioned in chapter 6, it has been stressed in the literature that it is important to use the same sceneID scheme for both development and application of ADMs [96]. However, operational constraints forced us to adopt a different strategy, i.e. to specifically develop a basic sceneID providing solely the needed features to adequately select the most relevant CERES Tropical Rainfall Measuring Mission (TRMM) broadband shortwave ADMs. Therefore, to validate the GERB sceneID, we present a comparison between GERB and CERES retrievals on SEVIRI data and quantify their expected differences as well as their impact on GERB solar fluxes where the CERES sceneID is taken as a reference.

This chapter is structured as follows. We start in section 7.2 with a brief discussion on the surface type used within the GERB sceneID. Then, we perform in section 7.3 detailed analyses on the accuracy of the retrieved cloud properties as well as on their ancillary clear–sky reflectances by using a reference dataset. Temporal, spatial and angular dependencies on the comparison errors are studied. In section 7.4, the impact of misidentification on GERB–like TOA solar fluxes compared to the CERES reference scheme is assessed. We finally conclude in section 7.5 and suggest possible improvements for future Edition processing.

7.2 Surface geotype

As mentioned in chapter 6, CERES TRMM ADMs were stratified according to a spatially and temporally fixed surface cover map. To avoid any bias due to the surface geotype in the GERB processing, we explicitly used the same dataset which was simply regrided according to the SEVIRI field–of–view.

Even if there is no misclassification of surface types between the GERB processing and the CERES TRMM ADMs, one may argue that the use of ADMs which were specifically built over the TRMM tropical latitude band (38° N – 38° S), and thus are not representative of the vegetation in the higher latitudes such as in Europe, is not totally adequate. Moreover, a fixed surface map does not take into account the seasonal cycles of the vegetation growth and decay in the Sahel and Europe regions [19]. Nevertheless, such considerations are beyond the scope of the error analysis performed in this chapter. New seasonal and latitudinal ADMs are currently being developed to address this issue in future Edition processing.

As already mentioned in chapter 6, seasonal snow/ice covered surfaces are currently misidentified. The cloud properties retrieval scheme is then run over unspecified snow/ice covered pixels. Since snow reflectance is bright and highly variable in the visible wavelengths, low confidence on the accuracy of these retrievals is expected. We are thus planning to use for the Edition 2 processing a dynamic snow/ice detection scheme which was specifically developed for the GERB operational environment [18] prior to the cloud properties retrieval. This will spare these snow/ice pixels from further being processed. Note that techniques to retrieve cloud properties over snow/ice covered surfaces are available in the literature [129]. These basically consist in the transposition of the usual cloud properties retrieval principle based on an absorbing and non–absorbing water channel to two near–infrared absorbing bands. This channel substitution is done because snow/ice exhibits a reduced reflectance compared to its response in the visible spectral domain. However, the implementation of this method over the relative low number of snow/ice pixels observed in the SEVIRI field–of–view (FOV) is not foreseen as a short–term improvement.

7.3 Cloud properties

During the initial development phase of the GERB processing on Meteosat–7 (MS7) imager, we tried to validate the GERB cloud properties retrievals against CERES TRMM Single Satellite Footprint (SSF) products (see chapter 5). The CERES SSF products provide instantaneous TOA fluxes with the complete CERES sceneID over 10 km footprint averaged measurements [184, 185]. However, for meaningful comparisons with this distinct instrument dataset, we had to collect only nearly coangular and simultaneous measurements between TRMM Visible and InfraRed Spectrometer (VIRS) and MS7 imagers. Even considering about 15 months of day–time data did not allow us to perform detailed comparisons due to the small number of remaining CERES SSF footprints satisfying such criteria. Moreover, considerations about the use of two imagers with different spectral characteristics to derive cloud properties and their convolution with the CERES point spread function over SSF footprints introducing spurious discrepancies suggested us to adopt another strategy.

7.3.1 Dataset

Rather than comparing GERB and CERES retrievals over footprints covered by several imager pixels, we opt for a direct one–to–one imager pixel comparison methodology. The NASA Langley Cloud and Radiation Research Group led by Dr. P. Minnis which is in charge of the CERES sceneID has adapted this scheme to the processing of geostationary data. A subsampled version is routinely running on data from the operational SEVIRI instrument [115]. Briefly, this scheme consists in first applying a series of cascading multispectral threshold tests to perform the cloud masking over the FOV [116]. These threshold tests are applied on brightness temperatures (BTs), BT differences, reflectances and ratios of reflectances. Monthly clear–sky estimates are used as references [161] and the thresholds are dynamically computed according to ancillary data from numerical weather analyses and forecasts (temperature, water vapor, wind and ozone profiles). The output of this cloud masking is then passed to the cloud properties retrieval module [117]. It is based on distinct algorithms for day– and night–time. The day–time algorithm, called VISST for Visible Infrared Solar–infrared Split window Technique, relies primarily on the 0.6, 3.9, 10.8 and 12 μm SEVIRI channels. It uses a parametrization of theoretical radiance calculations for several water and ice particle size distributions as well as atmospheric profiles from weather forecast models to retrieve cloud optical properties (cloud optical thickness, effective particle radius, liquid and ice water path, cloud thermodynamic phase, cloud top and base pressure and temperature, etc. . .) by matching the calculations to the measurements.

To compare the GERB and CERES sceneID retrievals, we have selected one week of SEVIRI data, from March 11 to 17 2007, where the previously mentioned adapted CERES sceneID was specifically run once a day at 12:00 UTC and at the full native spatial resolution (3 km at nadir). It is only possible to consider one repeat cycle (slot) per day due to the required CERES processing time of about 3 hours for each slot. Every pixel of this CERES dataset is then reprojected according to its longitude and latitude to the SEVIRI geolocated grid by using EUMETSAT prescribed formulas [36]. This drastically simplifies the comparisons between GERB and CERES retrievals providing extensive pixel statistics thanks to the one–to–one pixel relationship. One may argue that only considering one hour per day lacks generality. This choice was made due to the large amount of resources required for the computation of the CERES/VISST dataset. The extensive SEVIRI FOV allows to investigate various scene geometry configurations, except those in the vicinity of the sunrise and sunset. Nevertheless, the reciprocity principle [170] allows us to extend all conclusions about the viewing zenith angle to the solar zenith angle. It is worth pointing out that the CERES sceneID used to generate this associated SEVIRI dataset is an updated version of the CERES sceneID used to derive the TRMM ADMs. Therefore, this will undoubtedly have some impact on the consistency of the comparisons. Nevertheless, since the GERB cloud properties' retrievals are included in the GERB L20 products for the users' convenience, it seems to us more meaningful to perform comparisons and suggest improvements relatively to a recent CERES sceneID instead of the previous TRMM ADMs' version with known weaknesses which are now solved.

In the following, discrepancies between GERB and CERES are discussed according to their spatial distribution within the SEVIRI FOV as well as to their temporal dependency on the weekly clear–sky estimation, i.e. age of clear–sky in days (see chapter 6, section 6.3.1.5). We have chosen to summarize the results according to 3 coarse surface types–ocean, vegetation and desert–simply by combining in a single geotype each CERES pair for vegetation and desert. We shall use either CERES or Visible Infrared Solar–Infrared Split Window Technique (VISST) to designate the same dataset.

7.3.1.1 Geolocation

For meaningful comparisons, we must first ensure that there is no offset between the geolocations used by the GERB and CERES sceneIDs. Since the CERES retrievals are reprojected on the SEVIRI grid according to the geographical coordinates included in these products, we can compute the correlation between the 0.6 μm channel reflectance images from GERB and CERES processing. Letting the sub–satellite pixel coordinates (C_x, C_y) vary from the EUMETSAT prescribed values $(1856, 1856)$ (pixel numbering starts at 0) when reprojecting the CERES data [36], we get a mapping of the correlation coefficient between both images according to these coordinates (not shown). The (C_x, C_y) values associated to the higher correlation match the former EUMETSAT prescribed values, thus confirming that the grids of both schemes are identical.

7.3.1.2 Calibration

One possible source of discrepancy between GERB and CERES cloud properties retrievals could also arise from different calibration schemes used. The GERB processing is using coefficients provided by EUMETSAT within the SEVIRI products [62, 63]. In contrast, CERES needs geostationary ancillary inputs in its processing to accurately model the diurnal cycle. A specific inter–calibration scheme compatible with VIRS on TRMM, MODIS on Terra and Aqua and GOES satellites was developed to provide consistent measurements between the different instruments and thus to avoid any spurious offset [112–114]. This difference in the calibrations for the SEVIRI 0.6 μm channel is about 2.5 % higher for CERES (result from a robust linear fit [131] on March 12 2007 at 12:00 UTC). This will undoubtedly impact the quality of the comparisons between the two sceneIDs. It is worth pointing out that the scattering around the fit is due to the time–dependent inter–calibration.

7.3.2 TOA composite clear–sky reflectances

When developing the TOA composite clear–sky reflectance algorithm on Meteosat–7 (see chapter 4), its accuracy was estimated on a clear–sky pixels database. This database was simply built by visually selecting cloud–free pixel areas within the Meteosat–7 imagery. However, such a process is time–consuming while not fully assuring that cloud contaminated pixels are excluded from the selection. Thus, for an exhaustive validation on SEVIRI data, we select a clear–sky pixels database made of all the pixels which are classified as clear–sky by the CERES sceneID over the whole SEVIRI FOV. For each of these pixels, one is able to compute the error between the GERB clear–sky estimated reflectance ρ_{cs}^{sv} and the *true* clear–sky reflectance ρ^{sv} which is directly measured by SEVIRI in both instrument's visible bands.

7.3.2.1 Temporal error analysis

Tables 7.1 and 7.2 summarize the mean and standard deviation of the absolute errors distribution $\rho^{sv} - \rho_{cs}^{sv}$. One can notice that our composite clear–sky estimation scheme tends to underestimate the actual clear–sky reflectances in both channels. Moreover, there is no obvious dependency of the mean and the standard deviation of the absolute errors with the age of the clear–sky estimation ratio α_{cs}^{sv} (see chapter 6, section 6.3.1 equation 6.2) for any surface type.

Since the average reflectance of the 3 coarse geotypes significantly differs, we have plotted in figure 7.1 the mean of the relative error distribution $\langle(\rho^{sv} - \rho_{cs}^{sv})/\rho^{sv}\rangle$ for this clear–sky pixels database according to the age of the clear–sky estimation. We can see that the highest relative errors are occurring for ocean surfaces for both channels where they range between 12 and 16 % for 0.6 μm (see panel (a)) and between 16 and 22 % for 0.8 μm (see panel (b)), respectively. There is also a small increase of the errors according to the age of the clear–sky for this geotype. This is consistent with the fact that the average spectral response of ocean surfaces is reduced compared to other surface types and is lower at 0.8 than 0.6 μm. Similarly, vegetation and desert covers exhibit lower clear–sky relative errors in both bands due to their higher spectral signatures compared to ocean. Typical relative errors over desert are between 1 and 2 % at 0.6 μm (see panel (a)) and 2 to 3 % at 0.8 μm (see panel (b)) while ranging for vegetation from 3 to 8 % (resp. 3 to 6 %).

***Table 7.1** – Mean and standard deviation of the distribution of the absolute errors $\rho^{sv} - \rho^{sv}_{cs}$ according to the age of the clear–sky for 0.6 μm.*

Age	Ocean		Vegetation		Desert	
[days]	mean	stddev	mean	stddev	mean	stddev
0	0.0108	0.0130	0.0108	0.0160	0.0035	0.0103
1	0.0114	0.0134	0.0085	0.0173	0.0031	0.0104
2	0.0123	0.0130	0.0102	0.0164	0.0030	0.0096
3	0.0124	0.0127	0.0092	0.0166	0.0032	0.0104
4	0.0119	0.0125	0.0114	0.0162	0.0040	0.0112
5	0.0117	0.0132	0.0136	0.0177	0.0050	0.0119
6	0.0126	0.0130	0.0120	0.0185	0.0040	0.0122

***Table 7.2** – Mean and standard deviation of the distribution of the absolute errors $\rho^{sv} - \rho^{sv}_{cs}$ according to the age of the clear–sky for 0.8 μm.*

Age	Ocean		Vegetation		Desert	
[days]	mean	stddev	mean	stddev	mean	stddev
0	0.0095	0.0126	0.0190	0.0235	0.0094	0.0212
1	0.0104	0.0131	0.0197	0.0240	0.0108	0.0218
2	0.0101	0.0129	0.0145	0.0229	0.0091	0.0186
3	0.0101	0.0123	0.0104	0.0228	0.0065	0.0177
4	0.0104	0.0122	0.0136	0.0251	0.0070	0.0194
5	0.0104	0.0126	0.0143	0.0243	0.0107	0.0206
6	0.0115	0.0123	0.0161	0.0253	0.0081	0.0225

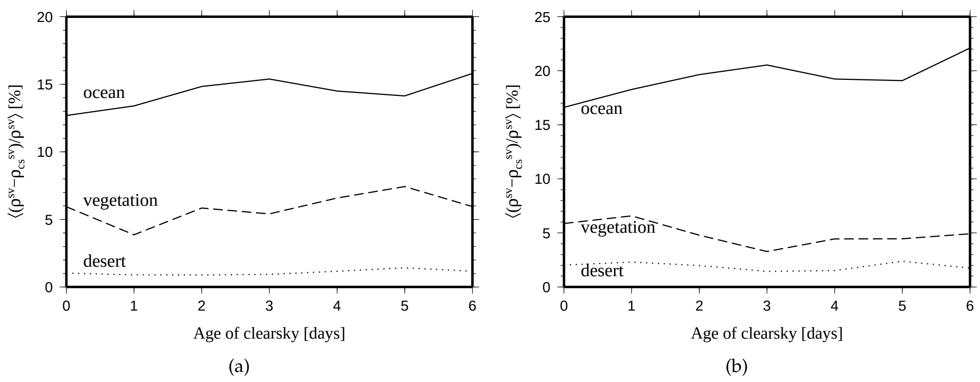

***Figure 7.1** – Mean of the relative error distribution $\langle (\rho^{sv} - \rho^{sv}_{cs}) / \rho^{sv} \rangle$ according to the age of the clear–sky estimation for pixels flagged as clear–sky by the VISST algorithm and the (a) 0.6 and (b) 0.8 μm SEVIRI channels.*

7.3.2.2 Overall error analysis

Panels in figure 7.2 display the relative frequency histograms of the absolute error $\rho^{\mathrm{sv}} - \rho^{\mathrm{sv}}_{\mathrm{cs}}$ distributions for the same surface classes. In the insets of figure 7.2, their associated cumulative histograms are shown. We notice that the peaks of all the histograms are occurring between 0 and 0.005 and that all distributions are right–tailed. If we jointly consider the mean μ (bias) and standard deviation σ (scattering) as an overall error quality criterion, we see that any cloud optical depth retrieval scheme based on our TOA visible clear–sky estimations would minimize uncertainties due to the surface contribution if we use the 0.8 μm channel over the ocean and the 0.6 μm spectral band over vegetation and desert (see figure 2.12). This is in agreement with the fact that we choose to dynamically select the visible channel exhibiting the highest sensitivity for the difference between clear–sky and cloudy conditions for every pixel in the cloud optical depth retrieval (see chapter 6, section 6.3.3). Since the reflected radiation for a given cloud is almost constant in the visible wavelengths [74], this choice is solely driven by the spectral response of the clear–sky surfaces recalling that the reflectance for ocean is smaller at 0.8 than 0.6 μm, while it is higher for vegetation and desert [8]. Specifically, it can be shown that the dynamic channel selection is always considering the 0.8 μm band for ocean and the 0.6 μm for land. Moreover, despite the fact that GERB clear–sky reflectances are underestimated, the empirical selection of 0.025 for the 0.6 μm clear–sky additive offset Δ^{sv} (see chapter 6, section 6.3.1.4, equation 6.6) is ensuring that at least 80 % of the clear–sky pixels will be correctly classified as illustrated by the cumulative histograms in figure 7.2 panels (a,c,e). In contrast, we notice that for the 0.8 μm band, our null empirical value is not adequate.

7.3.2.3 Sun–glint

In chapter 6, we noted that our method for clear–sky estimation in sun–glint regions fails due to fast transient changes of visible reflectances. Therefore, we suggested to model the TOA clear–sky ocean response in the sun–glint using radiative transfer simulations with a Cox–Munk surface reflectance formalism [38]. To check such a model, we have plotted in figure 7.3 the absolute clear–sky errors $\rho^{\mathrm{sv}} - \rho^{\mathrm{sv}}_{\mathrm{cs}}$ averaged by tilt angle Ψ bins (angle between the specular reflection and the viewing direction for ocean clear–sky reflectances). It can be observed that the clear–sky error significantly jumps when changing from the clear–sky sun–glint model to the standard scheme. This will certainly imply a discontinuity of the cloudy pixels statistics around the transition region. It is obvious from the curve of figure 7.3(a) that our empirical choice for M^{sv} and m^{sv} (see chapter 6, section 6.3.1.3, equation 6.5) at 0.6 μm is not optimal. Indeed, the underestimation of the *true* clear–sky values ρ^{sv} is higher near the central sun–glint spot ($\Psi = 0$) than it is on its border. However, such behavior is drastically reduced for the 0.8 μm band as seen in figure 7.3(b) where the underestimation of our sun–glint model is smoother and lower than for regions where our standard clear–sky estimation scheme is applied ($\Psi > 0$).

7.3.2.4 Summary

The results from the previous sections can be summarized as follows. Errors on clear–sky estimations in both visible SEVIRI channels have a limited sensitivity to the aging of the clear–sky estimation ratio $\alpha^{\mathrm{sv}}_{\mathrm{cs}}$. Nevertheless, a small trend exists for ocean. Moreover, our scheme

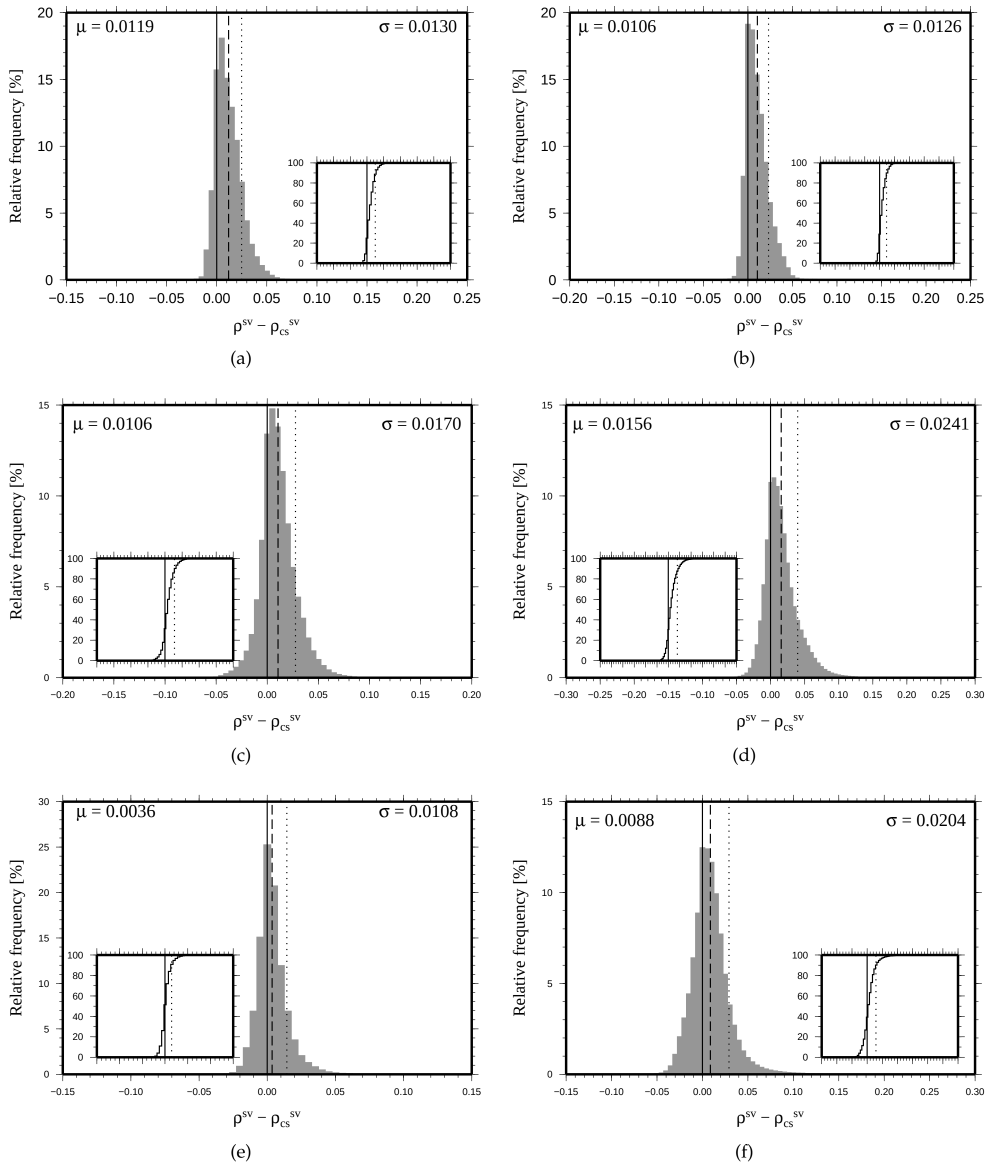

Figure 7.2 *– Relative frequency histograms of the absolute error $\rho^{\mathrm{sv}} - \rho^{\mathrm{sv}}_{\mathrm{cs}}$ distributions for ocean (a,b), vegetation (c,d) and desert (e,f), for the 0.6 (a,c,e) and 0.8 µm (b,d,f) SEVIRI channels, respectively. In inset, the associated cumulative histogram is also plotted (same abscissa scale). The plain line marks the $\rho^{\mathrm{sv}}_{\mathrm{cs}} = \rho^{\mathrm{sv}}$ condition, while the dashed is for the mean μ and the dotted is for the mean plus the standard deviation $\mu + \sigma$. Data from March 11 to 17 2007 are considered altogether.*

systematically underestimates the *true* clear–sky values. This suggests that the selected value of the $\alpha^{\mathrm{sv}}_{\mathrm{cs}}$ (see chapter 6, section 6.3.1.1, equation 6.2) should be increased by considering

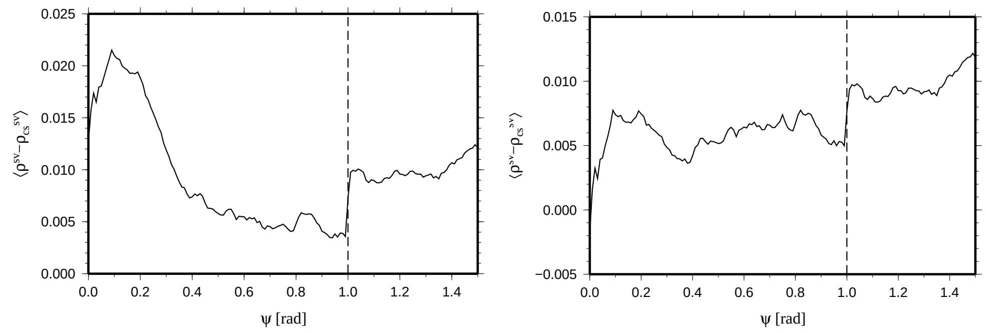

(a) (b)

***Figure 7.3** – Bin–averaged absolute clear–sky errors $\langle \rho^{\mathrm{sv}} - \rho_{\mathrm{cs}}^{\mathrm{sv}} \rangle$ according the tilt angle Ψ for the (a) 0.6 and (b) 0.8 μm SEVIRI channels, respectively. The vertical dashed line marks the limit of the domain where the clear–sky sun–glint model is applied. Data from March 11 to 17 2007 are considered altogether.*

the fifth or sixth lowest value in future Edition processing rather than the 4th as currently done. The optimal value should be selected as the one leading to lowest clear–sky errors when comparing with the VISST dataset.

For sun–glint affected areas, our empirical choice of the sun–glint model parameters leads to a sudden change of the clear–sky errors and thus in cloud sensitivity around its limit of application domain. To reduce the resulting bias in L20 GERB products for future Edition processing, an objective tuning of these parameters should be based again on comparisons with the CERES dataset.

7.3.3 Cloud flag

In this section, we investigate the discrepancies of the cloud masks associated to the GERB and CERES sceneIDs. We start by studying a possible temporal dependency according to the aging of the clear–sky estimation ratio. Then, we analyze the spatial distribution of the discordance between the two cloud masks.

7.3.3.1 Temporal error analysis

Table 7.3 gives the cloud fraction, i.e. the number of cloudy pixels out of the total *valid* common pixels, over the SEVIRI FOV for the GERB and CERES cloud masks according to the age of the clear–sky estimation ratio. We observe a good agreement between the two schemes with the highest difference being about 3 %. Moreover, the aging of the clear–sky estimation ratio does not noticeably impact these results. This confirms that the adjustment made by visual image inspection to the MS7 τ_{thres} value is almost optimal for SEVIRI.

It is anticipated that the cloud detection sensitivity is different according to the geotype and thus it is expected that the discrepancies between the GERB and VISST cloud masks could also vary according to the geotype. Thus we decided to study these differences according to

Table 7.3 *– Cloud fraction over the SEVIRI FOV for GERB and CERES sceneIDs according to the age of the clear–sky data. Only pixels which were validly retrieved as clear–sky or cloudy by both schemes are considered in the statistics.*

Age [days]	GERB [%]	CERES [%]
0	56.89	54.15
1	56.01	52.68
2	56.56	53.34
3	59.46	58.47
4	59.02	59.22
5	61.08	60.09
6	60.19	60.16

the 3 coarse surface types (ocean, vegetation and desert). In table 7.4, the discrepancies between the GERB and VISST cloud masks are given relative to CERES taken as reference. We can note that there is no significant dependency with the aging of the clear–sky estimation. While over vegetation and desert surfaces, our scheme tends to misclassify more cloudy than clear–sky pixels (from the CERES point of view), it is the opposite for ocean. This imbalance of misclassifications is in contradiction to what would be expected for vegetation and desert due to the underestimation of the clear–sky reflectances which we previously reported in section 7.3.2. A possible explanation could be that the applied threshold τ_{thres} of about 0.6 (see chapter 6, section 6.3.4) on the cloud optical depth for the cloudy/non–cloudy test is too high, thus classifying too many thin clouds as clear–sky. Nevertheless, by adding figures from CL/cs and cs/CL and subtracting from 100 %, the fraction of common classification between GERB and CERES is between 88 and 91 % for ocean and 85 and 90 % for vegetation and desert.

Table 7.4 *– Discrepancies in percent between the GERB and CERES cloud masks for the different geotypes according to the age of the clear–sky. CL/cs (resp. cs/CL) designates the fraction of the CERES clear–sky (cloudy) pixels flagged as cloudy (clear–sky) by the GERB sceneID relative to the overall validly processed pixels.*

Age	Ocean		Vegetation		Desert	
[days]	CL/cs	cs/CL	CL/cs	cs/CL	CL/cs	cs/CL
0	8.96	1.27	3.97	9.61	2.28	7.89
1	9.92	1.43	4.97	9.89	1.68	8.19
2	10.04	1.67	4.69	9.97	1.57	7.71
3	7.97	1.63	3.23	11.82	2.39	9.55
4	7.13	1.71	3.93	13.34	2.45	12.70
5	7.74	1.69	4.91	11.95	2.10	10.76
6	6.54	2.07	3.99	11.16	1.65	9.82

7.3.3.2 Overall error analysis

To investigate the spatial dependency of the discrepancies between both cloud masks, we have plotted in figure 7.4 the frequencies of CL/cs and cs/CL labeled pixels over the SEVIRI

FOV.

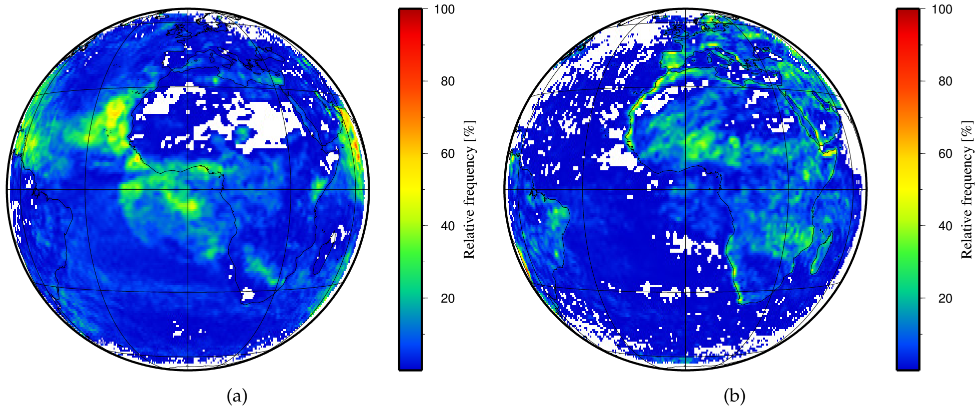

Figure 7.4 *– Spatial relative frequency distribution of the discrepancies between GERB and CERES cloud masks for the (a) CL/cs and (b) cs/CL pixels. Data from March 11 to 17 2007 is considered altogether and results are binned over* $1^\circ \times 1^\circ$ *grid boxes.*

It is clear from figure 7.4(a) that the imbalance of discrepancies towards CL/cs pixels over the ocean (see table 7.4) is due to the fact that Saharan dust bursts are detected as clouds by our algorithm while CERES is identifying them as clear–sky and that we are inaccurately modeling the sun–glint clear–sky reflectances as it was previously demonstrated in section 7.3.2.3. Moreover, the enlarged discordance over the Arabian Sea could also be explained by high load of aerosols in the atmosphere as observed by Moderate Resolution Imaging Spectroradiometer (MODIS) due to sand dust blown off the coast. Careful inspection of this figure also shows that GERB sceneID tends to identify more clouds over the African tropical rainforest than CERES in these regions exhibiting periods of consecutive cloudy conditions reaching up to 60 days.

In figure 7.4(b), we can observe that a significant amount of the discrepant cs/CL pixels are located in the Sahel and Great Lakes regions. As already mentioned, the threshold on cloud optical thickness for the cloud flag test could be larger than it should be over land and therefore the GERB sceneID is falsely detecting thin clouds (cirrus or fog) as clear–sky. This is supported by figure 7.5 where we have plotted the cumulative histogram of the retrieved CERES cloud optical depth τ_C for the discrepant cs/CL pixels of figure 7.4(b). Indeed, about 50 % of those pixels are associated by CERES to a cloud optical depth lower than 1.

7.3.3.3 Summary

Even if both GERB and CERES schemes give similar overall cloud fraction statistics over the whole FOV, discrepancies occur over the various surface types. This suggests that the threshold value used on cloud optical thickness for the cloud flag test should be adapted to a lower value in future Edition processing. The optimal value could be the one resulting in a balance of misidentification between cloudy and clear–sky pixels with respect to the CERES cloud flagging. Moreover, applying distinct threshold values according to geotypes should also be

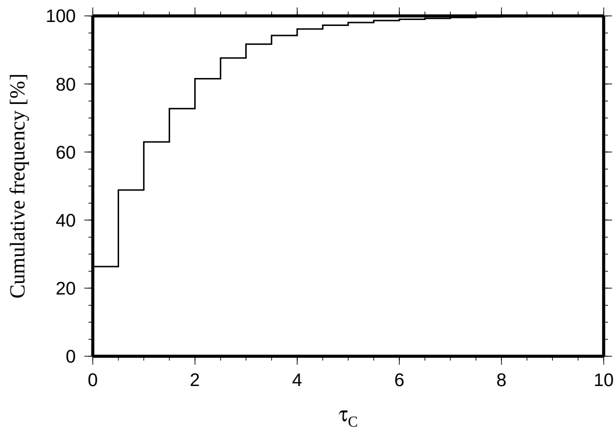

Figure 7.5 *– Cumulative histogram of the retrieved CERES cloud optical depth τ_C for the cs/CL pixels.*

investigated.

Considering the spatial distribution of the discrepancies, we noticed that thick dust clouds are falsely detected as clouds over the ocean by the GERB sceneID. Nevertheless, we intend to apply for future Edition processing a clear–sky restoral scheme [21] to reclassify cloudy dust aerosol pixels as clear–sky using SEVIRI thermal channels. Another issue is that we tend to falsely flag thin clouds as clear–sky. This is especially the case over land where it seems that the threshold of about 0.6 on cloud optical depth is more problematic than over the ocean. Therefore this value should be adapted to a lower value according to the CERES results. Finally, our scheme exhibits a lower sensitivity to detect clouds in the area where the sun–glint clear–sky model is applied. This leads to a systematical misidentification of clear–sky pixels compared to its neighborhood.

7.3.4 Cloud thermodynamic phase

In this section, we investigate the discrepancies of the cloud thermodynamic phases between GERB and CERES. We are anticipating significant discordance between both cloud phase retrievals due to the crude phase inference scheme implemented within the GERB processing (see chapter 6, section 6.3.2). Since it simply consists in thresholding the 10.8 μm SEVIRI brightness temperature, we expect to falsely flag all supercooled water clouds as ice. Moreover, it is well known in the literature that thin clouds such as cirrus have only a limited impact on the response of a single infrared channel compared to the contribution of their underlying surface [73]. Thus these thin clouds will almost certainly be mistaken as water clouds if their associated cloud optical depth is above the cloud detection threshold τ_{thres}. Furthermore, discrepancies will also be caused by the fact that our scheme does not correct for the increased atmospheric path length at high viewing zenith angles. We start by studying the day by day discrepancies. Then, we analyze the spatial distribution of the discordance between the two cloud phase schemes.

Table 7.5 gives the ice cloud fraction over the SEVIRI FOV for both GERB and CERES as well as their relative difference (CERES taken as reference) according to the day of the month. It obviously illustrates that our threshold test on a single brightness temperature leads to a systematic underestimation of the fraction of ice clouds up to 43 % relatively to CERES results.

Table 7.5 *– Ice cloud fraction over the SEVIRI FOV for GERB and CERES sceneIDs and their relative difference according to the day (March 2007).*

Day	GERB [%]	CERES [%]	Rel. diff. [%]
11	20.52	32.60	37.05
12	19.96	32.56	38.72
13	16.81	29.22	42.47
14	18.72	32.06	41.60
15	19.45	34.11	42.99
16	19.91	33.47	40.53
17	21.30	37.00	42.43

In table 7.6 we have collected statistics on the discrepancies between GERB and CERES (taken as reference) cloud phases according to the three coarse geotypes for each day. We notice that the i/w cases, i.e. when GERB misidentifies the phase as ice instead of water, are not sensitive to the surface type and represent less than 2 % of the total amount of cloudy pixels, detected by both methods. Therefore, it seems that supercooled water clouds will only have a limited impact due to their low occurrence. As already noticed in table 7.5, it confirms that the GERB phase retrieval fails to correctly identify ice clouds in the vast majority of cases. The relative imbalance between the figures of ocean and land surfaces could be due to the fact that ocean surface temperatures are more spatially and temporally stable, thus allowing the brightness temperature test to correctly capture an increased amount of ice clouds (between 5 and 11 %).

Table 7.6 *– Discrepancies in percent between the GERB and CERES cloud phases for the different geotypes according to the day (March 2007). w/i (resp. i/w) designates the fraction of the CERES ice (water) cloudy pixels flagged as water (ice) clouds by GERB relative to the overall pixels commonly flagged by GERB and CERES as cloudy.*

Day	Ocean		Vegetation		Desert	
	w/i	i/w	w/i	i/w	w/i	i/w
11	12.62	1.17	19.77	0.51	18.08	0.49
12	13.41	1.06	19.18	0.52	21.67	0.74
13	13.83	1.72	19.09	0.45	15.22	0.49
14	14.13	1.51	25.35	0.62	13.06	0.88
15	15.20	1.24	26.80	0.58	17.43	1.36
16	13.15	1.13	24.43	1.07	23.19	1.22
17	16.16	0.84	27.44	1.08	22.57	0.68

To study the spatial dependency of the discrepancies between both cloud phase retrievals, we have plotted in figure 7.6 the frequencies of i/w and w/i pixels relatively to the overall local number of pixels where both retrievals could be inferred. These statistics were collected in $1^\circ \times 1^\circ$ grid boxes of pixels over the SEVIRI FOV.

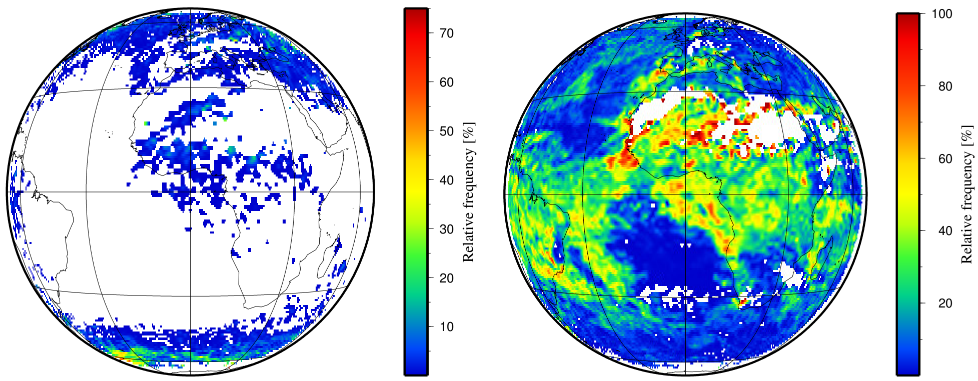

(a) (b)

Figure 7.6 *– Spatial relative frequency distribution of the discrepancies between GERB and CERES cloud phases for (a) i/w and (b) w/i pixels. Data from March 11 to 17 2007 are considered altogether and results are binned over* $1^\circ \times 1^\circ$ *grid boxes.*

From figure 7.6(a), we observe that most of the discordance where GERB is falsely assigning ice phase instead of water (CERES taken as reference) is located in the austral region. This is not surprising due to the low temperatures associated to the surface (ocean or sea ice) which can falsely trigger the brightness temperature threshold test.

However, as already mentioned, the majority of the discrepancies occurs where GERB wrongly selects water instead of ice phase. Their spatial distribution is illustrated in figure 7.6(b). It is clear that the Equator region displays large frequencies due to the heavy convection processes occurring in this area. These result in clouds extending up to an altitude of 10 km where only ice particles exist in their upper part. Another location of large discrepancies occurs over the Sahara desert. It seems that the GERB phase retrieval scheme fails to detect thin cirrus clouds due to the high surface temperature which tends to mask the response of this type of clouds in the measured signal. This assumption is confirmed in figure 7.7 where we have plotted the cumulative histogram of the CERES retrieved cloud optical depth for these falsely water flagged pixels. Indeed, it shows that ice clouds associated to an optical depth of less than 2 represent about 70 % of the total population.

To summarize, we have shown that as expected the rather simplistic GERB cloud phase detection results in large systematic discrepancies. Their high imbalance towards misidentification of thin cirrus clouds leads to their inhomogeneous spatial distribution which will certainly have some impact on the estimation of instantaneous as well as averaged TOA solar fluxes. Therefore, for the future Edition 2 processing, we plan to drastically modify this scheme by including information from other SEVIRI channels. The MODIS multispectral cloud phase retrieval adapted to SEVIRI instruments [190] could be considered.

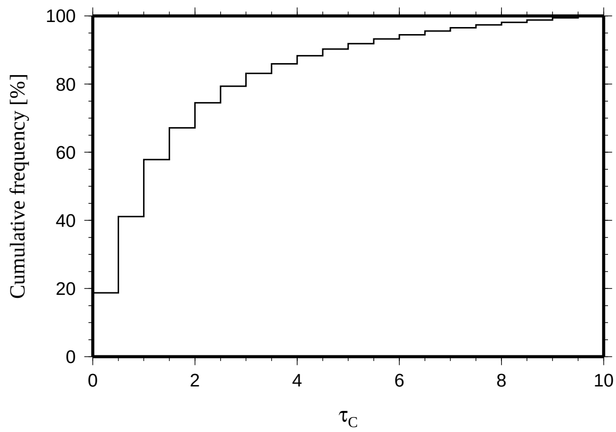

***Figure 7.7** – Cumulative histogram of the retrieved CERES cloud optical depth τ_C for the w/i pixels.*

7.3.5 Cloud optical depth

In this section, we investigate the discrepancies of the cloud optical depth retrievals between the GERB and CERES sceneIDs. As already mentioned in section 7.3.1.2, the difference between the calibrations used in GERB and CERES schemes for the visible SEVIRI channels will undoubtedly result in differences for the cloud optical depth even if all other parameters of GERB and CERES were identical. However, this assumption will remain qualitative as both schemes are tuned to their respective calibration and thus any quantitative assessment of the impact of sceneID differences would require drastic changes to one of the algorithms.

Moreover, as demonstrated in section 7.3.2, the GERB sceneID systematically underestimates the true clear–sky reflectances. Thus, it is expected that cloud optical depth values from GERB will be overestimated compared to CERES. Indeed, this is confirmed in figure 7.8 where we have plotted the relative frequency histograms of the difference of the logarithm of the cloud optical depths between GERB and CERES for the 3 coarse surface types and both cloud phases. The highest discrepancies occur for ocean. This is not surprising recalling the fact that our scheme produces the highest relative errors for the associated clear–sky reflectance estimation as illustrated in figure 7.1 compared to the other geotypes. In figure 7.8(a), one can notice two modes (around 0 and μ) in the ocean and water clouds histogram. It can be shown that the mode around 0 is associated the cloud optical depth retrievals over pixels within the domain of the clear–sky sun–glint model ($\Psi < 1$) while the other is related to the percentile approach for $\Psi \geq 1$. This is consistent with the behavior of the absolute clear–sky errors shown in figure 7.3(b) as the 0.8 μm channel is usually selected from our highest cloud sensitivity criterion.

Another source of discrepancy between both schemes can arise from the look–up tables (LUTs) used in the inversion from reflectance to cloud optical depth. Those LUTs were generated with different radiative transfer models (RTMs) and with different input parameters such as, for example, surface reflectances, cloud altitudes and particle radii as well as output geometries, respectively. This is well reflected in figure 7.9 where we have plotted the average of $\log_{10} \tau_G - \log_{10} \tau_C$ according to the viewing zenith angle θ for both cloud phases. It is ob-

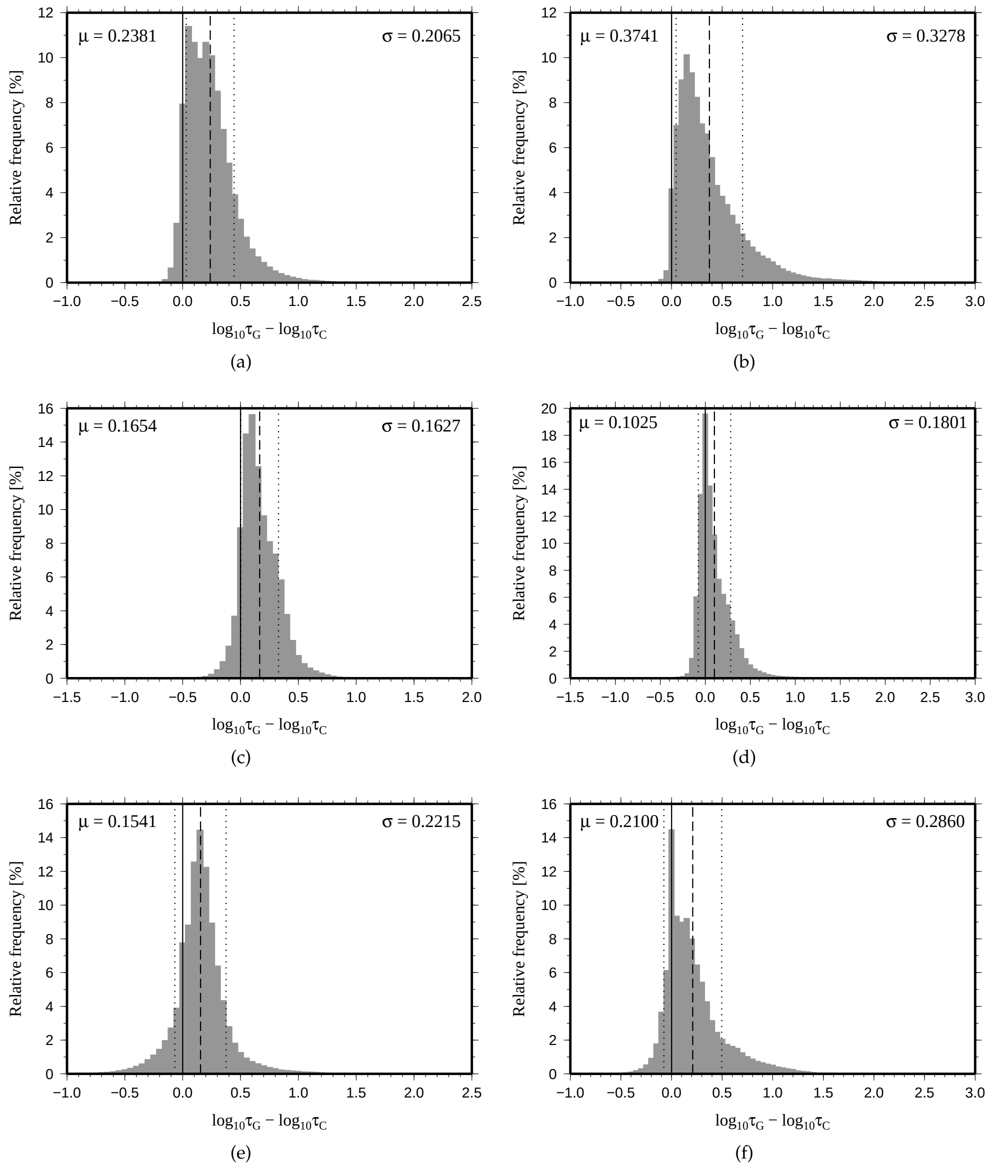

Figure 7.8 *– Relative frequency histograms of* $\log_{10}\tau_G - \log_{10}\tau_C$ *distributions between GERB and CERES cloud optical depths for ocean (a,b), vegetation (c,d) and desert (e,f), for water (a,c,e) and ice (b,d,f) clouds, respectively. The plain line marks the* $\tau_G = \tau_C$ *condition, while the dashed line is for the mean* μ *and the dotted lines are for the mean plus/minus the standard deviation* $\mu \pm \sigma$*. Data from March 11 to 17 2007 are considered altogether.*

vious that discrepancies are strongly related to the viewing direction and it is anticipated that a similar effect occurs for the illumination zenith angle in virtue of the reciprocity principle.

Indeed, RTMs used to compute the LUTs are based on the plane–parallel assumption and thus limitations of their physics parametrization is reached at large solar and viewing zenith angles. Moreover, the STREAMER [82] RTM used within the GERB processing may not be fully adequate to perform simulations over the SEVIRI visible channels as the physics parametrization of this model is averaged in much larger spectral bands. From the insets of figure 7.9, we notice that the relative azimuth angle φ of a majority of pixels within the SEVIRI FOV are about 180°, i.e. located in the backscattering region of the cloud phase function, for the period of year and time of day (12:00 UTC) considered. While the CERES LUTs were computed using accurate cloud phase function parametrizations, the STREAMER RTM used to build the GERB LUTs is only considering the simplistic (double) Henyey–Greenstein phase function for water (ice) clouds. But, as stressed in section 2.4.2, these models are unable to capture the detailed structure of the real cloud phase functions. The fact that the distribution of the relative azimuth angles is peaked around the backscattering direction only exacerbates such limitations. Nevertheless, the double Henyey–Greenstein phase function seems to perform better for ice clouds than its simple version for water clouds as illustrated by the lower errors for ice than water clouds associated to viewing zenith angles between 15 and 55°. This is probably due to the fact that it provides some estimation of the backward peak for ice clouds, while it does not for water clouds.

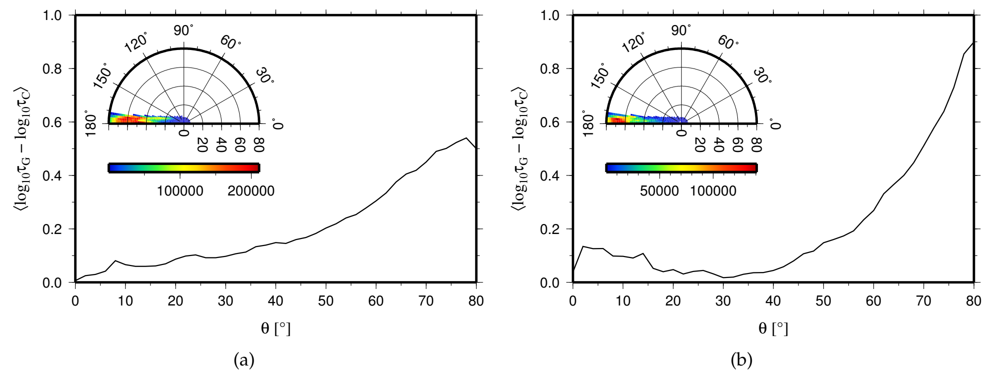

Figure 7.9 *– Bin–averaged* $\log_{10}\tau_G - \log_{10}\tau_C$ *according to viewing zenith angle* θ *bins of 2° for the (a) water and (b) ice clouds. In inset, the associated histogram of the viewing geometries* (θ, φ) *is shown as polar plot. Data from March 11 to 17 2007 is considered altogether.*

To summarize, we have shown that a systematic bias exists between GERB and CERES cloud optical depth retrievals with higher GERB values. This can be related to the associated underestimation of clear–sky reflectances. Discrepancies between retrievals clearly also demonstrate a dependency on the geometry. This is not surprising due to the distinct RTMs and parameters used to compute the LUTs as well as their underlying plane–parallel assumption. Finally, we assume that the band–model which was used prior to generate Meteosat–7 LUTs (see chapter 5) may not be sufficient to accurately simulate the SEVIRI narrowband measurements. Therefore, the use of other RTMs should be investigated for the calculations of the GERB LUTs in the future Edition 2 processing, such as the line–by–line spectral libRadtran [105] model that is still based on plane–parallel theory or a Monte Carlo model with one–dimensional input parameters, together with an accurate parametrization of the cloud phase function for both water and ice clouds.

7.4 TOA GERB–like solar fluxes

In the previous sections, we have assessed the discrepancies of the retrieved cloud properties due to GERB and CERES sceneIDs. These properties are used in the processing to derive the GERB TOA solar fluxes by applying to each footprint a specific ADM. Therefore, the fact that both GERB and CERES retrievals do not match implies a misselection of the ADMs in the radiance–to–flux conversion. This results in differences between fluxes when considering either the GERB or CERES scheme.

To investigate such discordances, we have run what we call the GERB–like processing using both cloud properties as input. This processing solely uses SEVIRI multispectral data to simulate GERB broadband radiances and applies the ADMs to the latter to estimate GERB–like TOA fluxes [52, 67] over 3×3 SEVIRI pixels (about 9 km at nadir). Such fluxes are not yet *corrected* with the actual GERB measurements. Nevertheless, these quantities give a valuable insight about the impact of ADM misselection. We have to stress that a rigorous analysis on the final GERB products is not possible because the full GERB processing of data from one repeat cycle requires data from the previous and the next repeat cycles from GERB and SEVIRI due to the needed temporal interpolations (GERB and SEVIRI acquisition times are asynchronous). Moreover, an extensive validation has been performed through scene–type comparisons between the various GERB L20 products and the associated CERES SSF footprints [35].

In the following of this section, F_G designates the TOA GERB–like solar fluxes which are generated using the GERB sceneID features, while F_C is associated to the fluxes estimated from CERES sceneID parameters. We investigate the GERB-like flux errors according to the GERB cloud fraction, cloud thermodynamic phase and cloud optical depth. Since fluxes are only available in GERB Edition 1 products for sun–glint tilt angles larger than 25°, we have decided to constrain these analyzes of GERB–like flux errors over such area. Finally, the spatial distribution of these errors is given without any restriction over the FOV.

7.4.1 Cloud fraction

We have computed in table 7.7 the mean and standard deviation of the relative flux errors $(F_G - F_C)/F_C$ according to the different geotypes and GERB cloud fraction bins as well as their overall statistics. We can notice that for footprints classified as clear–sky by GERB (cloud fraction of 0), the mean relative error is positive and less than 0.8 % for every surface type, meaning that on average the GERB sceneID is slightly overestimating the GERB–like fluxes compared to CERES. For totally overcast GERB footprints corresponding to a cloud fraction of 100 %, it remain positive but reaches up to 2.42 % for desert. In contrast, footprints associated to intermediate cloud fractions tend to be generally negative with values as low as −4.95 % for desert proving that GERB–like fluxes are underestimated compared to CERES. Nevertheless, the overall relative error statistics when considering all surfaces and cloudy conditions are about 0.31 % on average. The standard deviation figures on the other side only provide limited information on the relative error distribution. Indeed they are heavily biased by large relative error values typically resulting when one scheme identifies the footprint as clear–sky while it is overcast for the other, even if the occurrence of such errors is low as illustrated by the cumulative histogram of the relative flux errors $(F_G - F_C)/F_C$ in figure 7.10. The relative frequency histogram of this figure shows that the error distribution is more or less symmetric around the origin with more than 45 % of the footprints having a relative error of about 0.

Table 7.7 *– Mean and standard deviation of the relative flux errors $(F_G - F_C)/F_C$ according to the different geotypes and GERB cloud fraction as well as their overall statistics. Data from March 11 to 17 2007 are considered altogether.*

Cloud fraction	Ocean		Vegetation		Desert		All	
[%]	mean	stddev	mean	stddev	mean	stddev	mean	stddev
0	0.78	4.77	0.38	14.24	0.19	8.27	0.46	9.71
$0-10$	-	-	-	-	-	-	-	-
$10-20$	-4.70	7.94	-1.71	8.81	-4.09	8.90	-3.74	8.41
$20-30$	-4.08	7.85	-3.09	8.51	-4.95	8.71	-3.86	8.14
$30-40$	-3.63	7.67	-0.30	8.53	-1.83	8.95	-2.50	8.17
$40-50$	-3.76	7.75	-1.11	8.33	-2.40	8.95	-2.85	8.11
$50-60$	-3.56	7.72	-1.20	7.57	-1.42	9.07	-2.71	7.85
$60-70$	-3.20	7.55	-2.08	7.49	-2.23	8.68	-2.81	7.62
$70-80$	-3.02	7.43	0.41	7.82	0.98	9.74	-1.72	7.89
$80-90$	-2.19	7.38	-0.63	7.50	-0.09	9.07	-1.60	7.57
$90-100$	-	-	-	-	-	-	-	-
100	1.41	10.70	1.52	7.79	2.42	7.38	1.46	10.07
All pixels	0.28	9.43	0.47	10.82	0.14	8.36	0.31	9.69

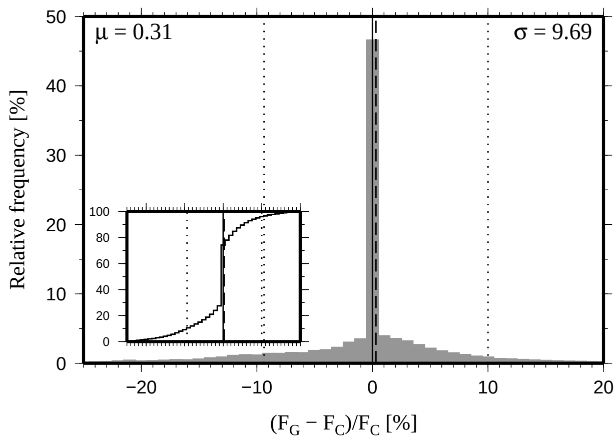

Figure 7.10 *– Relative frequency histogram of the relative flux errors $(F_G - F_C)/F_C$. In inset, the associated cumulative histogram is also plotted (same abscissa scale). The plain line marks the $F_G = F_C$ condition, while the dashed is for the mean μ and the dotted is for the mean plus/minus the standard deviation $\mu \pm \sigma$. Data from March 11 to 17 2007 are considered altogether.*

7.4.2 Cloud optical depth and thermodynamic phase

To assess the dependency of the cloud optical depth as well as the ice cloud fraction within the footprints on the GERB–like fluxes, we have computed in table 7.8 the mean of the relative flux errors $(F_G - F_C)/F_C$ which have been binned according to the GERB cloud optical depth and ice cloud fraction. We can notice that either for almost pure water and ice cloud footprints, we are underestimating GERB–like fluxes for cloud optical depth up to 4. Moreover, such underestimation is significantly higher (up to 10.65 %) for thin ice clouds ($0.6 < \tau_G < 2$) while it is mostly occurring over desert (not shown). For pure clouds associated to cloud optical depth above 4, we tend to overestimate the fluxes with the largest fluxes differences being related to the highest cloud optical depths as well as to ice clouds. This is consistent with the fact that the GERB sceneID is increasingly overestimating the cloud optical depth compared to the CERES sceneID. By examining the various columns of this table, we can notice that, for a fixed cloud optical depth bin, the magnitude of the relative flux errors reaches its highest level for ice cloud fraction around 50 %. This is symptomatic of the fact that the retrieval of the cloud thermodynamic phase is only relying on a single $\mathrm{BT}_{10.8}$ threshold test concomitantly with a non–optimal choice of the threshold value.

7.4.3 Spatial distribution

The spatial distribution of the averaged relative flux errors $\langle (F_G - F_C)/F_C \rangle$ is plotted in figure 7.11. We can observe that for a majority of footprints within the FOV the average of the relative error is close to 0. The aerosol dust event which occurred during that week is clearly pointed out by negative relative flux errors of about $-5 - 10$ % off the West coast of the Sahara desert. However, these values are by no mean accurate. The current implementation within the GERB processing implies that clear–sky ocean ADMs are used over thin dust clouds while cloudy models are applied to thick dust clouds. It was demonstrated in the literature that using such clear–sky models for GERB fluxes lead to a mean overestimation of about $12\ \mathrm{W \cdot m^{-2}}$ over dust cloudy scenes [22]. In contrast, applying cloudy ADMs results in an averaged underestimation of about $1\ \mathrm{W \cdot m^{-2}}$. Moreover, this study also showed that instantaneous flux errors vary between 0 and $55\ \mathrm{W \cdot m^{-2}}$ depending on the geometry and dust optical depth. As we already mentioned, it is anticipated for the future Edition 2 processing to correctly detect dust clouds in the sceneID, estimate their aerosol optical depth and apply the aerosol ADMs which were developed specifically for GERB in [22].

One can also notice in figure 7.11 that errors tend to increase at grazing viewing zenith angles (see figure 7.12(b)) as well as in the Austral region as it is expected from the discussions of the previous sections. Moreover, sun–glint affected areas over the Gulf of Guinea also exhibit larger errors (up to about 25 %) as anticipated from our previous results on cloud properties. This is supported by figure 7.12(a) where we plotted the relative flux errors which were averaged over bins of the sun–glint tilt angle Ψ. Finally, the largest errors occur over Scandinavia and a possible explanation could be that the surface is covered by snow which is only correctly identified as clear–sky by CERES. Nevertheless, as snow TRMM ADMs are not available even the CERES associated GERB–like fluxes F_C should be taken as highly inaccurate.

7.5 Conclusion

In this chapter, we have described the comparisons performed to assess the accuracy of the GERB Edition 1 sceneID on SEVIRI. Such validation was carried out by using a reference dataset resulting from the processing of SEVIRI data with an adapted CERES sceneID. How-

Table 7.8 *– Mean of the relative flux errors* $(F_G - F_C)/F_C$ *according to the GERB cloud optical depth and ice cloud fraction and overall (cloudy) statistics. Data from March 11 to 17 2007 are considered altogether.*

Ice cloud fraction	Cloud optical depth								
[%]	0.6 – 1	1 – 2	2 – 4	4 – 8	8 – 16	16 – 32	32 – 64	64 – 128	Overall
0	-5.14	-3.81	-0.55	0.83	2.55	2.89	2.67	3.99	-0.50
0 – 10	-2.57	-4.60	-4.71	-1.41	3.02	3.42	3.13	2.45	-0.27
10 – 20	-4.89	-4.82	-5.86	-2.72	3.06	4.50	4.36	2.83	0.23
20 – 30	-6.41	-4.98	-6.42	-4.02	2.20	4.63	5.69	3.81	0.54
30 – 40	-7.35	-5.59	-6.77	-4.97	1.06	4.13	6.58	4.83	0.49
40 – 50	-7.22	-5.95	-7.09	-5.61	0.02	3.11	6.81	6.01	-0.02
50 – 60	-2.15	3.31	3.12	4.22	8.57	11.71	15.82	19.59	9.52
60 – 70	-4.18	2.80	2.97	3.48	6.47	8.95	13.13	18.53	7.66
70 – 80	-7.42	1.26	2.83	3.35	5.96	7.75	12.04	15.18	6.58
80 – 90	-6.12	-0.20	2.83	3.36	5.99	7.44	11.54	14.52	6.33
90 – 100	-5.89	-1.34	2.86	3.12	5.81	7.00	10.17	12.95	6.00
100	-10.22	-10.65	-0.49	3.02	4.80	4.24	4.54	7.40	4.59
Overall	-5.13	-3.83	-1.06	0.66	3.38	4.26	5.30	7.75	0.31

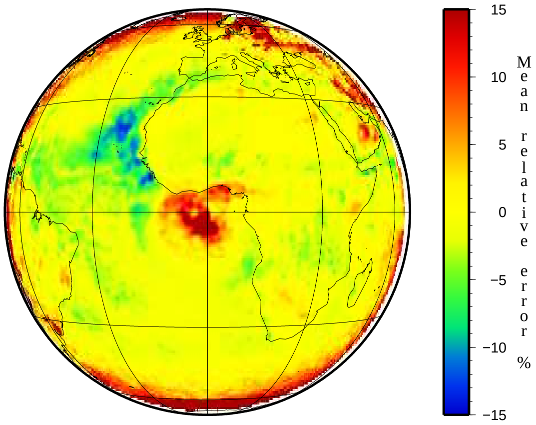

Figure 7.11 *– Spatial distribution of the mean relative flux errors $\langle (F_G - F_C)/F_C \rangle$. Data from March 11 to 17 2007 (12:00 UTC) are considered altogether and results are binned over $1^\circ \times 1^\circ$ grid boxes.*

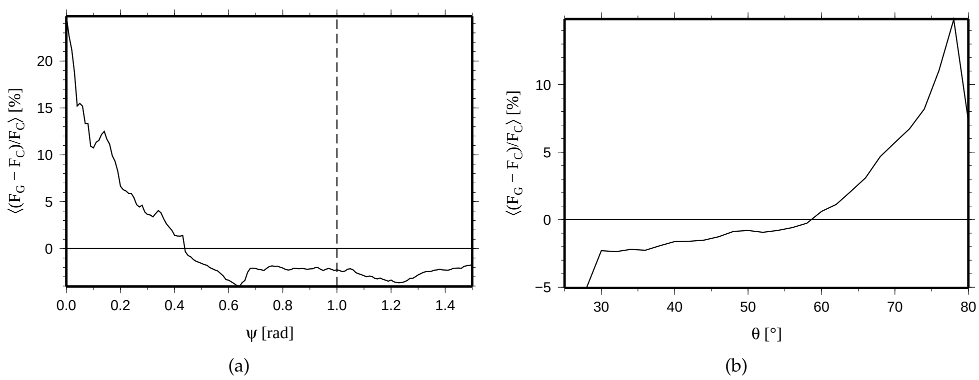

Figure 7.12 *– Bin-averaged relative flux errors $\langle (F_G - F_C)/F_C \rangle$ according to (a) the sun–glint tilt angle Ψ and (b) the viewing zenith angle θ for $\Psi > 1$. Data from March 11 to 17 2007 are considered altogether.*

ever, differences in the applied calibration of both schemes were identified and are qualitatively expected to impact the comparisons.

We found that the estimated relative errors on the composite clear–sky reflectances are about 1 % for desert, $3 - 8$ % for vegetation and $12 - 22$ % for ocean over both SEVIRI visible channels. We also demonstrated that the weekly update of the clear–sky estimation ratio has a limited effect on these errors. However the systematic underestimation of these reflectances should be decreased in future Edition processing as they have a direct impact on the cloud detection and cloud optical depth retrievals. Moreover, the developed sun–glint clear–sky reflectance model seems promising but an objective tuning of its parameters should be performed to reduce its inhomogeneity on cloud sensitivity.

Concerning the cloud flag, even if the average cloud fraction over the whole FOV gives similar results compared to CERES, discrepancies occur according to the surface type. This suggests that different thresholds for distinct surfaces would possibly be appropriate. This still has to be investigated in future developments. It would improve thin cloud identification, especially over land. Furthermore, correct identification of dust clouds as clear–sky with an estimation of their aerosol optical depth should imperatively be carried out in future GERB processing.

One of the major weaknesses of the current GERB Edition 1 sceneID is the cloud thermodynamic phase retrieval. It was demonstrated that the simplistic fixed threshold test on a single thermal channel which was implemented in regards to the operational constraints is unsuitable as it results in large systematic underestimation of the ice cloud population. Thus, the thermodynamic phase of thin cirrus as well as mid–level convective clouds has a higher probability to be misidentified as water. Therefore, users who wish to composite GERB fluxes by cloud type should be aware of this issue. Since several phase detection schemes exist in the literature, we plan to implement in the Edition 2 processing the method giving the best compromise between its accuracy and complexity for an operational implementation.

The lack of a snow detection scheme in the GERB sceneID also prevents a correct estimation of the fluxes through the selection of snowy clear–sky ADMs for snow covered surfaces. Combined with the limitations of the cloud thermodynamic phase retrieval, seasonal sea ice in Austral regions can be misidentified as ice clouds over the ocean. This problem is expected to be solved in the next Edition processing by the implementation of a snow detection algorithm [18].

As we already mentioned, the systematic bias of the cloud optical depth values can be related to a large part to the underestimation of the clear–sky reflectances. We also suggested that the narrow SEVIRI bands may not be adequately simulated by our selected RTM for the computation of the LUTs. Thus, we may consider in the future to use another RTM but such investigation is part of the long–term perspectives.

Finally, we tried to assess the impact of the misidentification on the GERB–like solar fluxes. It is obvious that any discrepancy between GERB and CERES sceneIDs at native SEVIRI resolution will lead to flux differences due to the distinct ADM selection in the radiance–to–flux conversion scheme. Such flux comparisons exhibit a relative error of about 0.31 % on average over the whole FOV. But the errors for specific scene types are significantly higher. Indeed, the fluxes for thin cirrus (as identified by the GERB sceneID) are underestimated up to 11 % compared to the CERES sceneID, while they are always overestimated ($2.55 - 7.40$ %) for thick pure water and ice clouds ($\tau_G > 8$). Moreover, mixed cloud phase scenes have their highest errors for an ice cloud fraction of about 50 % which results from the limitation of a single BT threshold test for cloud thermodynamic phase detection. To overcome such issues a multispectral cloud phase detection scheme will be implemented as part of the GERB Edition 2 sceneID. Flux errors also exhibit a viewing zenith angle dependency ranging from -2 % for $\theta = 30°$ to 15 % for $\theta = 78°$. Furthermore, we notice that even with a correct identification and characterization of thick dust, the use of cloudy ADMs instead of specific aerosol models leads to a mean solar flux underestimation of 1 $W \cdot m^{-2}$, while instantaneous errors are ranging between 0 and 55 $W \cdot m^{-2}$ [22]. For thin dust, the use of clear–sky ADMs instead of specific aerosol models leads to a mean solar flux overestimation of about 12 $W \cdot m^{-2}$. Thus it is foreseen to include these newly developed aerosol ADMs within the future Edition 2 processing.

Acknowledgments

This work was supported by the Research Directorate of the European Commission under contract GERBEC, the Belgian Science Policy Office (BELSPO) under contract PRODEX 5–8 and by European Organisation for the Exploitation of Meteorological Satellites (EUMETSAT) under contract EUMETGERB.

The CERES/VISST images were obtained from the NASA Langley Cloud and Radiation Research Group, `http://angler.larc.nasa.gov/satimage/products.htm`. We are thankful to Dr. P. Minnis and R. Palikonda from the NASA Langley Cloud and Radiation Research Group for the dedicated VISST processing of the SEVIRI data at native resolution over the full disk.

Chapter 8

Cloud detection using IR SEVIRI channels for GERB*

This chapter describes the development of a self-adaptive night–time cloud detection algorithm on SEVIRI IR data at native pixel–level allowing to estimate dynamically cloudy thresholds and using only a single climatological ancillary dataset.

Abstract

The first Geostationary Earth Radiation Budget (GERB) instrument was launched during summer 2002 together with the Spinning Enhanced Visible and InfraRed Imager (SEVIRI) on board of the Meteosat–8 satellite. This broadband radiometer aims to deliver near–realtime estimates of solar and thermal radiative fluxes at the top of the atmosphere (TOA) with high temporal resolution thanks to the geostationary orbit. Such a goal is achieved with the L20 GERB processing which generates these fluxes from the directional filtered radiance measurements of the instrument at several spatial resolutions. This processing consists of successive components, one of them being a radiance–to–flux conversion. The conversion is carried out in the solar wavelength region by using information from a scene identification developed for application to SEVIRI data. This scene identification estimates the cloud mask over the whole SEVIRI/GERB field–of–view with solely visible SEVIRI channels. While this method gives good results during day–time, it cannot be applied during night–time. Nevertheless, cloud mask information is valuable to study clouds and aerosols thermal radiative forcing. Thus, a night–time cloud mask would benefit to the GERB flux products in the thermal infrared (IR) region.

In this chapter, we describe a new cloud detection method using exclusively IR SEVIRI channels and a single climatological ancillary dataset. It is aimed to supplement the day–time GERB scene identification by providing cloud mask information in the GERB L20 products during night–time. Such method is based on a clustering approach on 60–days brightness temperature time–series at pixel–scale. Its strength lies in the fact that this technique does not make use of any fixed threshold values but instead adapts itself to the measurements. Despite the fact that it tends to systematically miss low warm water clouds (stratocumulus) due to their limited contrast compared to clear–sky conditions, it achieves better

*Adapted transcription of A. Ipe, L. Gonzalez Sotelino, C. Bertrand, E. Baudrez, N. Clerbaux, I. Decoster, S. Dewitte, S. Nevens and A. Velazquez Blazquez, Cloud detection using IR SEVIRI channels for GERB, *under review at Remote Sens. Environ.*, 2010.

detection with only 2 IR bands than the operational EUMETSAT CLM scheme. Our method is equipped with the NWCSAF CMa spatial texture cloud filter. The NWCSAF CMa is used as the golden standard for all comparisons.

8.1 Introduction

THE Geostationary Earth Radiation Budget (GERB) experiment aims to deliver to the science community top of the atmosphere (TOA) broadband solar and thermal fluxes on a near–realtime basis from a geostationary orbiting platform [66, 67]. The high temporal and spatial samplings of such climate record make it an ideal tool to study regional– as well as global–scale processes over an extensive time period of currently 7 years. Moreover, it is also providing an independent validation dataset to compare to current general circulation models (GCMs) outputs. This is being routinely perform on the UK Meteorological Office Unified Model [3], allowing to assess for example improvements of the tropical convective scheme of this model.

The first 2 GERB broadband radiometers are currently flying on board of the Meteosat Second Generation satellites (Meteosat–8 and –9) as co–passenger of the Spinning Enhanced Visible and InfraRed Imager (SEVIRI) main payload while it is expected that 2 more similar platforms will be launched in the future. Since GERB instruments are providing directional radiance measurements in the shortwave ($0.3 - 4$ μm) and longwave ($4 - 100$ μm) regions of the electromagnetic spectrum, a radiance–to–flux conversion scheme is adopted in the processing of their data [52]. These are first transformed into solar and thermal radiances through an unfiltering step [33, 34]. Then, a specific approach is followed for each source of radiation. The Clouds and the Earth's Radiant Energy System (CERES) shortwave angular dependency models (ADMs) from the Tropical Rainfall Measuring Mission (TRMM) are used to infer the solar TOA fluxes from their associated radiances [99] thanks to a scene identification performed on the companion SEVIRI imager (see chapters 5 and 6). In contrast, thermal fluxes are estimated through implicit thermal ADMs from non–linear regressions on spectral imager measurements [32].

Since an explicit scene identification and thus a cloud detection method is only needed for the solar part of the processing, i.e. during day–time, GERB products currently lack cloud mask information during night–time. Indeed, the adopted strategy in the processing is to exclusively consider visible imager channels to retrieve cloud properties since it is assumed that only such properties will significantly impact the TOA solar fluxes. Nevertheless, a specific cloud detection scheme is required to compute cloud radiative forcing during night–time.

Various cloud detection algorithms are found in the literature. They can generally be split into two groups depending if they rely or not on numerical weather prediction (NWP) forecasts or reanalyses, such as temperature and water vapor profiles, to estimate their thresholds in multispectral reflectance and brightness temperature (BT) tests. The brightness temperature is the associated temperature of a black body emitting the same amounts of radiation as for the SEVIRI measurements. State–of–the–art schemes such as the Moderate Resolution Imaging Spectroradiometer (MODIS) operational processing [2, 85, 130], the CERES VINT [116] and the Nowcasting and Very Short–Range Forecasting SAF (NWCSAF) [47] algorithms rely at night on numerous BT and brightness temperature difference (BTD) threshold tests. These tests are designed to be sensitive to specific cloud types. It is therefore needed to estimate the associated threshold values between cloudy and clear–sky conditions for all observed scenes in the field–of–view (FOV). Since the infrared measurements are impacted by the water vapor profile in the atmosphere as well as by the emissivity of the surface and clouds, the CERES and NWCSAF algorithms use NWP profiles together with surface emissivity climatologies as best guess to estimate their various clear–sky thresholds. MODIS, on the other hand, is only considering static thresholds varying over the FOV.

As previously mentioned, one goal of the GERB project is to act as an independent validation dataset for GCMs. It is thus questionable to use, in its processing, output fields of any model. Moreover, since cloud masking is only a small module of the whole processing, the near–realtime constraint of the project discards complex methods. Finally, the MODIS cloud detection was developed for low Earth orbit (LEO) imagers and would thus require significant tuning of its thresholds to efficiently work on geostationary scene geometries. Any change in the imager calibration would also result in a systematic bias of the delivered cloud mask. Therefore, it was decided to develop a specific night–time cloud detection scheme for the GERB processing. Since only infrared measurements are planned to be used, it is expected to give consistent results for day and night.

This chapter is organized as follows. Section 8.2 describes the adopted strategy and the assumptions. The algorithm and the ancillary data are then detailed in section 8.3. The input dataset considered in the following as well as examples of ancillary data and results of our scheme are illustrated in section 8.4. In section 8.5, we perform comprehensive comparisons between our algorithm and 2 operational cloud mask schemes. We discuss the expected limitations of our technique at the end of this section. Finally, we conclude and suggest possible investigations for future work in section 8.6.

8.2 Assumptions

A similar strategy as the one developed for the estimation of the TOA visible clear–sky reflectances within the GERB processing (see chapters 4 and 7) is adopted. Specifically, we are considering for every SEVIRI pixel its previous 60–days BT time–series at the same repeat cycle (day–time or slot) for a given infrared (IR) channel. This 60–days time period is a safeguard to ensure that at least several clear–sky events occurs over each pixel, even for the persistent cloudy regions over the Tropics. Such a $BT_{10.8}$ time–series is shown in figure 8.1 for the vegetation surface type. We can notice that thick cold clouds are characterized by low BT spikes, while the upper envelope of the time–series can be associated to clear–sky conditions. It is obvious that intermediate values can be related to thin (cirrus) or warm (stratocumulus) clouds.

Since we are only considering measurements in the infrared part of the spectrum, the geometric variability of the scenes can be assumed to be limited to the viewing zenith angle θ which is constant over the whole pixel time–series. However, water vapor absorption can be significant in the IR channels. This implies that TOA clear–sky BTs are modulated according to the state of the atmosphere. Moreover, surface temperatures exhibit a memory effect depending on the atmospheric conditions of the previous hours and days (clouds decreasing temperature, rainfall modifying surface emissivity). Thus, clear–sky BTs variability cannot be neglected, but we make the assumption that it is not larger than the BT signature of thin or warm clouds.

We can then summarize the main assumptions of the following algorithm. The samples

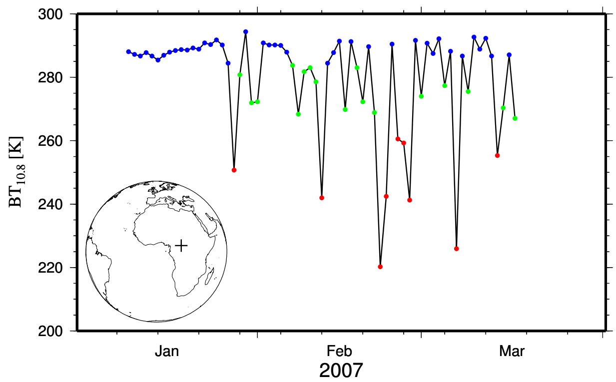

Figure 8.1 *– 60–days time–series of the SEVIRI 10.8 µm BT over a vegetation pixel at 0:00 UTC. The color of each sample indicates the resulting classification from our clustering algorithm when considering 3 classes (red: thick cold cloud; green: thin or warm (low) cloud; blue: clear–sky).*

of the 60–days time–series for a given channel and every pixel can be grouped at most in 3 classes according to their decreasing values of BT: (1) clear–sky, (2) thin or warm (low) clouds and (3) thick cold clouds.

8.3 Algorithm

Since the absolute level of clear–sky BTs can change drastically over the FOV, our method should adapt and find itself the BT boundaries of the clear–sky class. It was thus decided to select the unsupervised k nearest neighbor (*kNN*) clustering scheme [53]. Such technique has already been used in the literature. Indeed, [48] investigated its applicability to the three Meteosat channels (visible, IR and water vapor) for cloud type classification, while [5] applied this classifier to directional textural features of Meteosat–4 data for cloud detection. Compared to these previous studies, the novel approach of our method lies in the fact that we are not considering spatial but instead temporal samples of the same pixel to classify.

8.3.1 Clustering scheme

The *kNN* clustering scheme relies on some metric $d(x^{(n)}, C_k)$ to estimate the "distance" between a sample $x^{(n)}$ and a cluster center or *centroïd* C_k in the features space. The algorithm starts from a initial guess of the K $C_k^{(0)}$ centroïds in the features space:

Step 1 Let $i = 0$.

Step 2 For each sample $x^{(n)}$ where $n = 1, \ldots, N$ (here $N = 60$ days), assign it the class $k^\star$ which has the nearest centroïd $C_{k^\star}^{(i)}$, i.e.

$$d(x^{(n)}, C_{k^\star}^{(i)}) = \min_{k=1,\ldots,K} d(x^{(n)}, C_k^{(i)}).$$

Step 3 For each class k where $k = 1, \dots, K$, update its associated centroïd $C_k^{(i+1)}$ according to the samples $x^{(n)}$ which were assigned to it in the previous step such as

$$C_k^{(i+1)} = \frac{1}{N_k} \sum_{n=1}^{N} \delta_{nk} \cdot x^{(n)},$$

where $\delta_{nk} = 1$ if $x^{(n)} \in C_k^{(i)}$ and $\delta_{nk} = 0$ otherwise.

Step 4 For each class k, check if the updated centroïd $C_k^{(i+1)}$ is within a distance δ of the initial centroïd $C_k^{(i)}$. If this test which is equivalent to

$$\max_{k=1,\dots,K} d(C_k^{(i)}, C_k^{(i+1)}) < \delta$$

is satisfied, then the clustering has converged and we can stop. Otherwise, let $i = i + 1$ and go to step 2.

The convergence distance δ is usually set to the limit of significance where two centroïds are not differing anymore according to the physics of the problem. Any value below such limit would result in an overkill to reach the convergence criterion.

Section 8.3.3 will detail the importance of the initialization step of the centroïds for a meaningful convergence of the clustering to the final classification.

8.3.2 Metric used

As stated in section 8.2, the extent of the clear–sky class is due to the natural variability of the surface temperature, atmospheric state and surface emissivity over 60 days. It is obvious that the distribution of the clear–sky BTs of any thermal channels is asymmetric. Indeed, clear–sky BTs cannot be above some $\mathrm{BT}^{(\max)}$ value which is the highest BT over the 60 days period, while the lower the BTs, the lower their probability. Such distribution has more or less the shape of a log–normal random variable.

Due to the semi–finite property of the clear–sky distribution and its log–normal shape, one could be tempted to use a metric d associated to the log–normal density function for the clustering. However, the estimation of its parameters at each iteration from the mean and standard deviation of its current samples as well as the issue that some samples could be located outside the domain where the density function is defined, makes such function too complex to use. To overcome such problem and for the sake of simplicity, we have decided to approximate such density function $p_k(BT)$ with a normal distribution. It results that each centroïd C_k is defined by its mean μ_k and standard deviation σ_k, while the metric $d(x^{(n)}, C_k)$ is the linear discriminant function which, for classes following a normal distribution, reduces to

$$d(x^{(n)}, C_k) = \frac{(x^{(n)} - \mu_k)^2}{2\sigma_k^2} + \log \sigma_k$$

where $x^{(n)}$ represents the $\mathrm{BT}^{(n)}$ samples over the 60–days time period, if we assume that the prior probability to belong to every class C_k is identical to avoid using any knowledge of cloud occurrence statistics and bias our classifier. Thus, the update of centroïds $C_k^{(i+1)}$ at iteration $(i+1)$ is simply the recomputation of μ_k and σ_k according to the samples belonging to $C_k^{(i)}$. Such modeling is illustrated in figure 8.2.

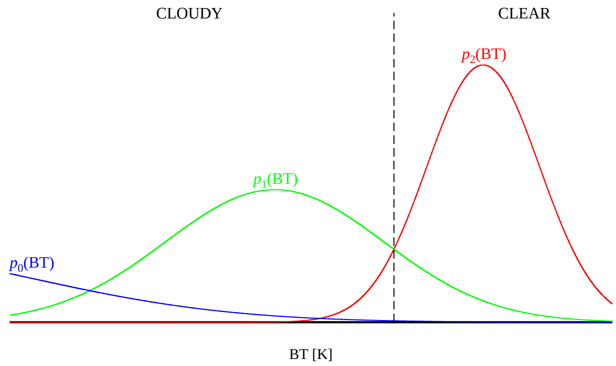

***Figure 8.2** – Normal probability densities modeling for the 3 clusters C_k.*

Since we are considering for the classification the brightness temperatures, it is reasonable to select for the convergence distance δ a value of 0.01 K. Indeed, this value is 10 times smaller than the measurement error of the most accurate SEVIRI IR channel [149].

It is worth pointing out that we also applied this clustering to a logarithmic transform of the $\mathrm{BT}^{(n)}$ samples and considered that the population within each class follows a normal distribution. However, comparisons similarly performed as in section 8.5 (not shown) demonstrated lower classification confidence than the abovementioned approach.

8.3.3 Initialization scheme

The unsupervised clustering technique is extremely simple yet powerful, but it suffers from a major drawback in the sense that its results are depending on the initialization of the clusters' locations $C_k^{(0)}$ [53]. This issue is usually addressed in the literature by a Monte Carlo scheme [164]. It consists to repeat the clustering a large number of times by varying the initialization. One is then able to build up some probability density function of the clustering results and select the optimal solutions accordingly. Such technique is however unrealistic given our constraint of operational processing.

Instead, we have developed a method to make a crude estimation of the width Δ of the clear–sky class which allows us to initialize $C_k^{(0)}$. This is achieved by considering 10 years (from 1991 to 2001) of skin surface temperatures T_s from the European Centre for Medium–Range Weather Forecasts (ECMWF) ReAnalysis project (ERA–40) [169] which are available every 6 hours on a $0.25° \times 0.25°$ grid. The main assumption is that the surface temperature is the major factor of variation of the satellite's BTs and that we are neglecting the contribution of the atmosphere. Therefore, the skin surface temperature can be used as a proxy [46].

These data once reprojected into the SEVIRI FOV are used to compute for every pixel and each of the 4 times of day t

$$\Delta(d,t) = T_s^{(\max)} - T_s^{(\min)} \tag{8.1}$$

at a given date d from the previous 60–days T_s time–series. We can finally estimate a climatology of Δ for every pixel by taking the 95 % percentile of instantaneous $\Delta(d,t)$ values acquired in a total period of 10 years. Such climatology can be generated either on a monthly or a seasonal basis. However, to simplify the implementation of the (linear) interpolation scheme according to the current date, a monthly climatology is considered. It is worth pointing out that the satellite's BTs are affected by the limb darkening effect while such effect is neglected when the skin surface temperatures are reprojected. Nevertheless, its impact is limited due to the fact that only the width of the clear–sky class, i.e. a difference of temperatures (equation 8.1), is considered.

The initialization scheme of the 3 $C_k^{(0)}$ centroïds is the following (from clear–sky to thick clouds):

1. For $C_2^{(0)}$: $\mu_2^{(0)} = \mathrm{BT}^{(\max)} - \frac{1}{2}\Delta$ and $\sigma_2^{(0)} = \Delta/3.25$,
2. For $C_1^{(0)}$: $\mu_1^{(0)} = \mu_2^{(0)} - \Delta$ and $\sigma_1^{(0)} = \Delta/3.25$,
3. For $C_0^{(0)}$: $\mu_0^{(0)} = \mathrm{BT}^{(\min)}$ and $\sigma_0^{(0)} = \Delta/3.25$, provided that it is meaningful ($\mu_0^{(0)} < \mu_1^{(0)} - \frac{1}{2}\Delta$).

In some restricted cases where 3 clusters cannot be initialized, we fall back on a 2 clusters' search problem ($C_2^{(0)}$ and $C_1^{(0)}$). If the samples do not allow us to initialize 2 distinct clusters at a distance Δ, no clustering is performed. The time–series is then assumed to be entirely clear–sky and the pixel is flagged accordingly.

The initial estimation of the clear–sky standard deviation $\sigma_2^{(0)}$ from the difference Δ between the maximum and minimum samples of a population is given by [158]. The choice of the same value for the initial cloudy standard deviations $\sigma_1^{(0)}$ and $\sigma_0^{(0)}$ is only done to ensure that the clear–sky class has an initial width of Δ.

We have to stress that despite the fact that we rely on NWP ancillary data, their impact is mitigated since only a derived climatology is used in our method for the initial locations of the clusters $C_k^{(0)}$, while other algorithms use reanalyzes of the current day to estimate their threshold values between clear–sky and cloudy conditions.

8.4 Results

Even if our method can be applied to the SEVIRI 3.9 μm band during night–time, its contamination by solar reflected radiation during day–time, infringing our assumptions in section 8.2, prevents its use. Moreover, this channel is almost exclusively used in major cloud detection schemes found in the literature on BTD threshold tests. Indeed, the fact that the water cloud emissivity is lower in this channel [71] allows to specifically discriminate warm (low) clouds from the clear–sky surface signal during night–time. However, our algorithm cannot be applied to BTD time–series since such differences are highly dependent on the atmospheric state (water vapor content and temperature profile) which can drastically changed from day to day resulting in the superposition of both clear–sky and cloudy scenes' classes. Therefore, only the SEVIRI thermal channels, i.e. at 8.7, 10.8 and 12 μm, will be considered in the following.

8.4.1 Dataset

For the sake of simplicity, we have selected one week of SEVIRI data, from March 11 to 17 2007, on which our algorithm was applied. Indeed, this week was also selected to perform the validation of the GERB Edition 1 products SEVIRI scene identification (see chapter 7), thus limiting the amount of storage needed. Since the climatological Δ dataset is only available every 6 hours, we can restrict our comparisons to an hourly basis without any loss of generality instead of the 15 minutes SEVIRI repeat cycle.

8.4.2 Monthly climatology Δ of the clear–sky class' width

A typical illustration of the climatological dataset Δ used as ancillary information for the clear–sky class' initialization is given in figure 8.3 for March at 0:00 UTC. It is worth pointing out that the ECMWF ERA dataset is neglecting the somehow limited diurnal cycle of the sea surface temperature by assuming a constant daily value. This results in a constant daily climatology Δ over the ocean for each month.

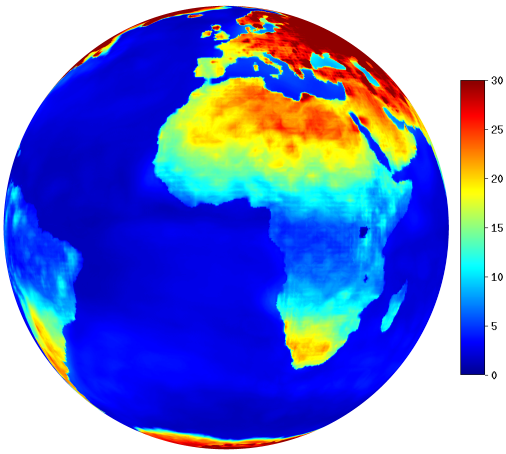

***Figure 8.3** – Monthly climatology of Δ [K] for March 15 at 0:00 UTC.*

8.4.3 Example of cloud masks

Figure 8.4 summarizes the results of our technique applied to the 8.7, 10.8 and 12.0 μm channels as a false–color composite image for March 11 2007 at 0:00 UTC. The overall level of agreement between these 3 masks is about 92.19 %. However, it varies according to the geotype with 90.52 % for ocean, 94.19 % for vegetation and 96.47 % for desert.

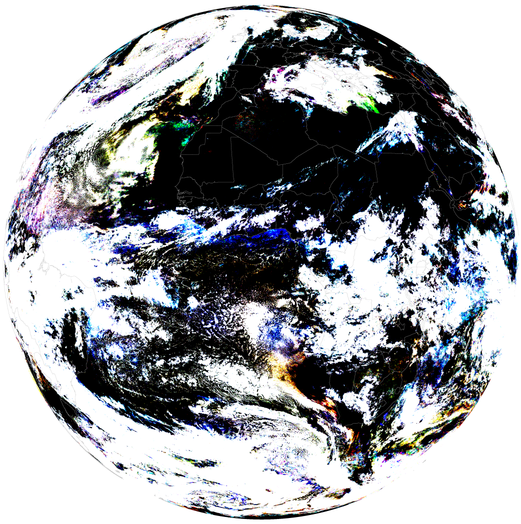

Figure 8.4 *– False–color composite from the 8.7 (red), 10.8 (green) and 12.0 μm (blue) cloud masks on March 11 2007 at 0:00 UTC. White pixels are flagged cloudy, while the blacks are associated to clear–sky in the 3 channels by our algorithm. Red / green / blue pixels are flagged cloudy only by their associated band's cloud mask, while cyan / yellow / magenta pixels are flagged by two associated cloud masks.*

One has to note that the clustering technique adopted in our scheme does not compromise the near–realtime constraint of the GERB processing. Such constraint requires that the overall processing time for one repeat cycle should not exceed 15 minutes which is the available time frame between 2 SEVIRI acquisitions. An optimized implementation allows our method to run in less than 5 minutes on a single i7 core requiring as little as 200 MB of RAM to process a single IR channel from one repeat cycle.

8.4.4 Sensitivity to the initialization scheme

As we already mentioned in section 8.3.1, the result of any clustering algorithm is sensitive to the initial clusters' locations. It was implicitly assumed in section 8.3.3 that a realistic choice of these locations based on a derived skin surface temperatures climatology should alleviate this problem. To test this assumption, we have ran our algorithm by considering a ± 10 % variation of the clear–sky class' width Δ which in turns results in a different estimation of the initial parameters of the classes' distributions.

Table 8.1 illustrates such analysis which is limited to 4 hours of a single day. As expected, the highest sensitivity occurs at noon. Indeed, it is around that time of the day that the temperatures reach their highest values and therefore that the classes are the widest. One can also note that the sensitivity increases with the wavelength of the SEVIRI channel. Nevertheless, according to this table, a change of 10 % on Δ only results at most in a variation of 1.76 % of the pixels for the cloud classification.

***Table 8.1** – Number of pixels (in percent) associated to a different cloud flag according to a multiplication factor of Δ relatively to a factor of 1.0 for March 11 2007.*

Band [μm]	Factor	00:00	06:00	12:00	18:00
	0.9	1.29	1.30	1.43	1.32
8.7	1.0	0.00	0.00	0.00	0.00
	1.1	1.19	1.20	1.26	1.19
	0.9	1.35	1.35	1.59	1.34
10.8	1.0	0.00	0.00	0.00	0.00
	1.1	1.24	1.22	1.39	1.20
	0.9	1.53	1.49	1.76	1.55
12	1.0	0.00	0.00	0.00	0.00
	1.1	1.39	1.36	1.55	1.34

8.5 Comparisons

In the following we compare our method to 2 other algorithms which are routinely applied to SEVIRI data. The first scheme is the Cloud Mask (CLM) available from the Meteorological Product Extraction Facility (MPEF) at EUMETSAT [100] which is disseminated together with the Level 1.5 SEVIRI radiances to the users' community. Its products are currently embedded within the GERB Edition 1 L20 data, due to the lack of native cloud mask information during night–time in the GERB processing. The second method is the Cloud Mask (CMa) algorithm from the NWCSAF [47]. Such scheme currently represents a state–of–the–art technique for satellite cloud detection. Thus, its associated dataset will be considered as the reference truth to which our results and the MPEF CLM will be compared (reference dataset).

8.5.1 Datasets

As we mentioned in the introduction, both schemes rely on threshold tests either on single or pairs of channels compared against clear–sky predicted values. For night–time, only IR information is used through BTs and BTDs while during day–time, visible and near–infrared (NIR) (1.6 μm) observations supplement them through reflectances and differences of reflectances (MPEF CLM). Moreover, textural tests based on spatial standard deviation of BTs, reflectances and BTDs (NWCSAF CMa) are also applied on available measurements.

It is obvious that our IR–only scheme can not compete with algorithms fully exploiting the additional visible and NIR measurements available during day–time. Therefore, we will restrict the comparisons to night–time scenes to select the best merging scheme in section 8.5.2.

8.5.1.1 MPEF CLM

The MPEF CLM was developed to provide a "robust, efficient, easy–to–maintain and accurate cloud processing tool" [100]. The clear–sky visible and NIR thresholds are inferred by building weekly reflectance maps from previous days' clear–sky results, while values for the differences of reflectances are estimated using linear relationships of static coefficients with measured reference reflectances. On the other side, the clear–sky BT thresholds are first guessed by averaging neighboring clear–sky pixels BTs from the previous repeat cycle provided that the averaging is statistically meaningful. Otherwise, the previous technique is applied to the current repeat cycle. However, if the BT standard deviation of those neighboring clear–sky pixels is large, then the clear–sky BT values are estimated at TOA through radiative transfer computations using ECMWF NWP global forecast pressure, temperature and humidity profiles together with skin surface temperatures. The clear–sky BTD thresholds are then computed using linear relationships of static coefficients with the previously inferred clear–sky BTs. Spatial texture tests based on standard deviation over 3×3 SEVIRI pixels for a visible as well as an IR channel are also used to detect clouds. Finally, it is worth noting that the MPEF CLM products, at least for the considered comparison week, are limited to viewing zenith angles below 70°.

8.5.1.2 NWCSAF CMa

Unlike the MPEF CLM scheme, the NWCSAF CMa algorithm gives a central role to the ECMWF NWP forecasts (skin surface temperature, integrated water vapor and ozone contents) for the IR channels' tests. Indeed, TOA clear–sky BT and BTD thresholds are estimated from radiative transfer model look–up tables according to these forecast fields, scene geometries and the surface types as well as elevation and climatological ancillary datasets. A similar approach is adopted for TOA clear–sky visible and NIR reflectance thresholds which are inferred from the Cox–Munk ocean model [38] or monthly climatological land surface reflectances.

Moreover, since emphasis of the NWCSAF CMa algorithm was given for nowcasting and very short term forecasting, false cloud detection and cloud misdetection have to be limited. This is achieved by applying to the threshold values corrective factors or offsets tuned according to a manual training database.

The spatial texture tests based on standard deviation over 3×3 SEVIRI visible reflectances, BTs and BTDs can raise some concerns about their adequacy. Indeed, if we consider as a theoretical construct the ideal case of a perfect clear–cut cloud border from one pixel to its neighbor, it is obvious that this neighboring clear–sky pixel will exhibit a larger spatial standard deviation than a pixel completely surrounded by clear–sky scenes. Therefore, it will be flagged as cloudy resulting in an artificial growth of the cloud's size. This is illustrated in figure 8.5 representing the comparisons between the MPEF CLM and NWCSAF CMa cloud masks over the Southern area of the Atlantic ocean where pixels only flagged as cloudy by the NWCSAF CMa local spatial textures tests are highlighted in white. Thus to objectively perform the following comparisons, the results of an "augmented" GERB IR method consisting to apply the NWCSAF CMa spatial filtering as a post–processing will also be considered.

8.5.2 Merging scheme

The strength of our method lies in the fact that it can be independently applied to each SEVIRI IR window channel. However, as illustrated in figure 8.4, these results are only differing by a small amount of pixels since information extracted from these single channel signals are more

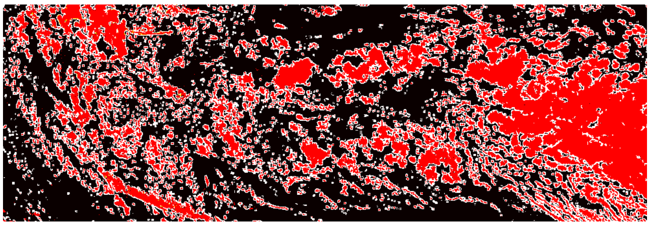

***Figure 8.5** – MPEF CLM and NWCSAF CMa comparison map for an area located in the Southern part of the Atlantic ocean on March 11 2007 at 0:00 UTC. Agreement between the 2 cloud masks corresponds to black (clear–sky) and red (cloudy), while white is associated to pixels only flagged as cloudy by the NWCSAF CMa local spatial texture tests.*

or less correlated. This is due to surface emissivities having limited variations over those 3 channels as well as to channel weighting functions over altitude for cloudy scenes [126]. Nevertheless, we could wonder if the results from these 3 channels could be either partially or completely exploited for pixels which do not reach unanimity. To investigate such assumption, table 8.2 gives the ocean pixels relative statistics according to the cloud flag in each channel with respect to the NWCSAF CMa cloud flag. It is expected that an agreement between the 3 channels' cloud masks is associated to the highest amount of correctly identified pixels (72.40 % for clear–sky and 95.63 % for cloudy scenes). However, agreements between any pair of channels' cloud masks do not allow meaningful statistical discrimination. Similar tables for vegetation and desert pixels (not shown) lead to the same conclusion.

***Table 8.2** – Statistics of ocean pixels according to their 8.7, 10.8 and 12 μm channel cloud masks (cs=clear–sky, CL=cloudy) with respect to their NWCSAF CMa flag (cloud contaminated and opaque cloudy classes are aggregated) and their relative fraction in percent for March 11 2007 at 0:00 UTC.*

GERB IR cloud masks			NWCSAF CMa		Pixels
8.7 μm	10.8 μm	12 μm	cs	CL	fraction
cs	cs	cs	72.40	27.60	38.49
cs	cs	CL	56.99	43.01	3.13
cs	CL	cs	39.70	60.30	0.83
CL	cs	cs	26.39	73.61	1.15
cs	CL	CL	40.59	59.41	1.86
CL	cs	CL	37.58	62.42	0.76
CL	CL	cs	18.33	81.67	1.75
CL	CL	CL	4.37	95.63	52.03

Therefore, our proposed merging scheme is to only consider a single channel's cloud mask per surface type. It is obvious that the band associated to the largest dynamic range of the measured signal, thus allowing for the best delineation, between clear–sky and cloudy conditions for a specific geotype will exhibit the highest cloud detection confidence. Since such analysis which is only achievable through theoretical radiative transfer calculations is out of the scope of this chapter, we will select for each geotype the channel's cloud mask giving the best comparisons' results with respect to the NWCSAF CMa cloud flag.

Table 8.3 gives the daily averages in percent of pixels where the GERB IR cloud mask agrees with the reference dataset restricted to the night scenes for the 3 broad geotypes and IR channels. Since the number of night scenes within the FOV varies with the time of day, these averages are weighted accordingly. We have also computed the weekly means of those daily averages with their associated uncertainties at 2σ. One can notice that it is not possible to conclude which channel is the most statistically suitable for each surface type. Nevertheless, it makes sense to select the channel associated to the highest weekly mean agreement with the NWCSAF CMa for each geotype, which is the 8.7 μm band for ocean surface type and the 12 μm channel for land geotypes (vegetation and desert). Thus, in the following, such merging of the channels' cloud masks is considered for the GERB IR cloud detection.

8.5.3 Intercomparisons

We first investigate the performance of the GERB IR and the MPEF CLM cloud detection schemes with respect to the NWCSAF CMa dataset during night–time SEVIRI measurements. As we mentioned previously, such conditions guarantee that no day–time measurements are being used in the MPEF CLM and NWCSAF CMa processing. We then similarly investigate their cloud detection skills during day–time conditions where it is expected that the GERB IR method will give degraded results.

8.5.3.1 Night–time

We have computed the weighted averages in percent of pixels where the MPEF CLM and GERB IR cloud masks agree with the reference dataset restricted to the night scenes for the 3 geotypes and independently from the surface type in table 8.4. Since no spatial textural filtering is performed within the GERB IR cloud detection algorithm compared to the 2 other schemes, we also have calculated the agreement with an "augmented" GERB IR method by performing the NWCSAF CMa spatial filtering as post–processing (denoted in table by "GERB IR+"). As expected, the "augmented" GERB IR method always performs better than without the spatial filter.

It can be noted that the MPEF CLM systematically exhibits a lower agreement than the standard GERB IR cloud detection over all geotypes for night–time conditions. The difference of performance is limited for ocean (0.39 %) and vegetation (0.42 %) between these 2 schemes. It is however significantly larger for desert (3.69 %). This demonstrates that our clustering scheme on BT time–series of a single IR channel over warm surfaces is particularly well suited compared to multispectral threshold tests. Moreover, the benefit of the filtering process in the "augmented" GERB IR method drastically increases the cloud detection performance over the ocean to reach almost the same level than over vegetation. This can be explained by the fact that such filtering is more efficient for ocean than vegetation and desert surfaces since the ocean clear–sky BTs are more spatially homogeneous. Ocean surfaces thus fulfill more easily the standard deviation threshold tests at clouds' edges.

8.5.3.2 Day–time

Table 8.5 similarly gives the weighted means in percent of the MPEF CLM and GERB IR cloud masks' agreement with the reference dataset restricted to the day scenes for the 3 geotypes as

Table 8.3 *– Weighted daily means according to the number of night pixels of the hourly pixels' agreement (in percent) between the NWCSAF CMa and the GERB IR cloud masks for August 11–17 2007 for the 3 IR channels and geotypes. The uncertainties on the means are given at* 2σ.

Geotype	Band [μm]	11	12	13	14	15	16	17	mean
ocean	8.7	84.95	86.75	86.67	86.07	85.95	86.19	86.26	86.12 ± 0.45
	10.8	84.70	86.45	86.43	85.77	85.91	86.22	86.18	85.95 ± 0.46
	12	83.12	85.05	85.22	84.26	84.22	84.78	84.57	84.46 ± 0.53
vegetation	8.7	88.81	88.06	88.41	88.33	86.55	86.78	85.63	87.50 ± 0.90
	10.8	89.41	88.83	89.12	89.32	87.76	88.08	86.85	88.47 ± 0.72
	12	89.78	89.25	89.58	89.99	88.60	89.05	87.64	89.12 ± 0.61
desert	8.7	94.34	94.69	95.19	94.99	91.94	91.30	89.61	93.13 ± 1.66
	10.8	95.18	95.55	95.84	95.65	93.25	92.98	91.75	94.30 ± 1.23
	12	95.57	95.83	96.21	95.92	93.89	93.84	93.02	94.88 ± 0.96

Table 8.4 *– Weighted means according to the number of night pixels of the hourly pixels' agreement (in percent) of the MPEF CLM, GERB IR cloud masks with respect to the NWCSAF CMa cloud mask for August 11–17 2007. GERB IR+ designates the GERB IR cloud mask supplemented with the NWCSAF CMa spatial texture filter.*

Cloud mask	Geotype			
	ocean	vegetation	desert	all
MPEF CLM	85.73	88.70	91.19	87.20
GERB IR	86.12	89.12	94.88	88.02
GERB IR+	89.97	90.67	96.02	90.94

well as independently from the surface type. It is obvious that the use of the additional SEVIRI visible and NIR measurements which are available during day–time is an asset for both the MPEF CLM as well as the NWCSAF CMa algorithms compared to the GERB IR cloud detection. Indeed, typical clouds which do not exhibit a distinct signature in the thermal IR channels from the background clear–sky scenes such as stratocumulus can be easily detected by their highly reflective behavior in the visible spectrum while their associated clear–sky reflectance is very low. This explains the lower performance of the GERB IR method compared to the MPEF CLM for ocean and vegetation while it is the reverse for desert which is characterized by a high visible albedo, thus limiting the sensitivity of visible channels to clouds' detection over such surfaces.

Table 8.5 *– Weighted means according to the number of day pixels of the hourly pixels' agreement (in percent) of the MPEF CLM, GERB IR cloud masks with respect to the NWCSAF CMa cloud mask for August 11–17 2007. GERB IR+ designates the GERB IR cloud mask supplemented with the NWCSAF CMa spatial texture filter.*

Cloud mask	Geotype			
	ocean	vegetation	desert	all
MPEF CLM	84.13	89.24	90.27	86.21
GERB IR	82.91	83.27	93.11	84.32
GERB IR+	88.06	85.99	93.70	88.27

8.5.3.3 All–time

In this section we perform the overall comparisons by considering all together the hourly day and night scenes over one week. These results are given in table 8.6. One can notice that the performance of the GERB IR method almost reaches the MPEF CLM for ocean but it is lower for vegetation when the complete diurnal cycle is taken into account. However, the GERB IR scheme still outperforms the MPEF CLM algorithm for desert. If the performance of the MPEF CLM is slightly higher for all geotypes than for the GERB IR method (86.70 % instead of 86.17 %), it is the reverse when the latter is supplemented by the NWCSAF spatial filtering (89.60 % compared to 86.70 %).

Due to the fact that MPEF CLM and NWCSAF CMa algorithms make use of the visible and

***Table 8.6** – Means of the hourly pixels' agreement (in percent) of the MPEF CLM, GERB IR cloud masks with respect to the NWCSAF CMa cloud mask for August 11–17 2007. GERB IR+ designates the GERB IR cloud mask supplemented with the NWCSAF CMa spatial texture filter.*

Cloud mask	Geotype			
	ocean	vegetation	desert	all
MPEF CLM	84.93	88.97	90.73	86.70
GERB IR	84.51	86.20	94.00	86.17
GERB IR+	89.01	88.33	94.87	89.60

NIR SEVIRI channels during day–time, it is expected that the cloud detection skills of both the MPEF CLM as well as the GERB IR schemes are varying during the course of the day. Therefore, we have plotted in figure 8.6 the hourly comparisons averaged over one week. One can notice that the MPEF CLM method is exhibiting large diurnal variations of its performance for land surfaces. It is particularly obvious for desert where the probability of detection (POD) drops of about 18 % in the morning and 10 % in the beginning of the afternoon. This clearly points out some problems in the MPEF CLM processing over such surfaces. In contrast, the curve associated to ocean is smoother denoting a smaller sensitivity of its multispectral tests with respect to the availability of additional information during day–time. Concerning the standard and "augmented" GERB IR techniques, there is a drop in their cloud detection performances around 12:00 as expected, the larger drop occurring for vegetation. Consistently with table 8.6, we can observe that both GERB IR techniques demonstrate significantly lower PODs than the MPEF CLM for an extended period of the day over vegetation compared to the ocean and desert.

As previously mentioned, the satellite's measured radiances are affected by the limb darkening effect. Such effect is due to the increased optical path length through the atmosphere with increasing viewing zenith angles. It results in a larger contribution of the colder atmosphere to the measured signal and thus in the decrease of the BT. This effect is expected to reduce the BT difference between clear–sky and cloudy scenes and therefore the performance of our algorithm at low viewing zenith elevation. Moreover, it is expected that our assumption consisting to neglect the impact of the atmospheric path length in the estimation of the clear–sky class' width Δ at large zenith viewing angles is not valid anymore. Such facts are illustrated in figure 8.7 where we have plotted the POD according to the viewing zenith angle θ. It can be noted that the detection performances of both GERB IR(+) and MPEF CLM schemes drastically decrease compared to the NWCSAF CMa algorithm. As expected, our GERB IR method is worse at higher viewing zenith angles (60°) than the MPEF CLM since it only relies on 2 channels (see section 8.5.2 for the reduction of 3 channels to 2) while it delivers similar results elsewhere. Nevertheless, when coupled with the NWCSAF CMa spatial texture cloud filter, our GERB IR+ technique outperforms the MPEF CLM at any viewing zenith angles. It is worth pointing out that the variations of these curves for viewing zenith angles below 60° can be explained by the inhomogeneous distribution of geotypes in the FOV.

8.5.3.4 Limitations

Considering the assumptions of section 8.2, it is obvious that scenes characterized by low BT contrast between cloudy and clear–sky conditions, i.e. when clear–sky and thin or warm low

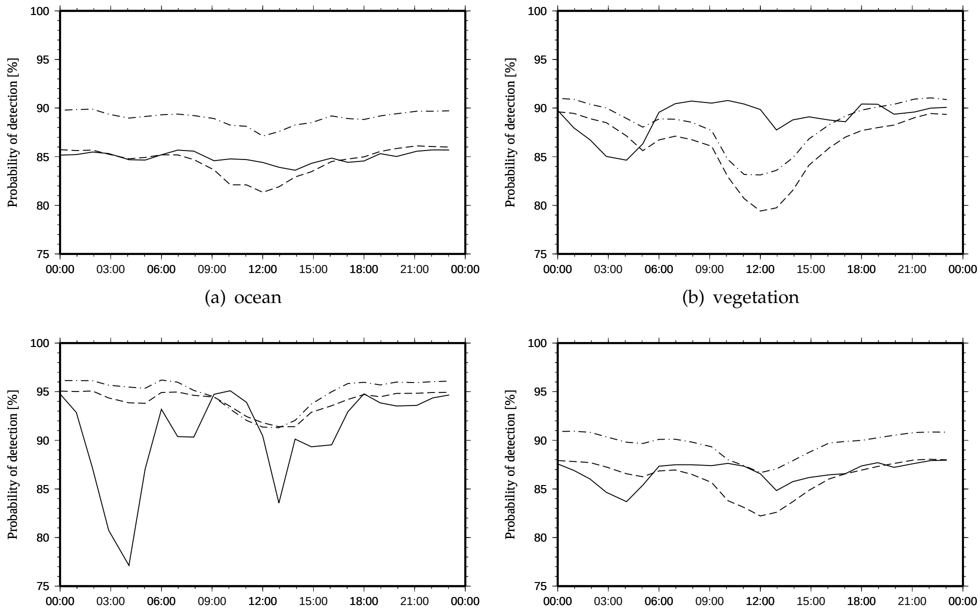

(a) ocean (b) vegetation

(c) desert (d) all surfaces

Figure 8.6 *– Hourly means of the weekly pixels' agreement (in percent) of the MPEF CLM (plain), GERB IR (dashed) and GERB IR+ (dotted–dashed) cloud masks with respect to the NWCSAF CMa cloud mask over (a) ocean, (b) vegetation, (c) desert and (d) all surfaces for August 11–17 2007. GERB IR+ designates the GERB IR cloud mask supplemented with the NWCSAF CMa spatial texture filter. The time scale corresponds to the SEVIRI repeat cycles.*

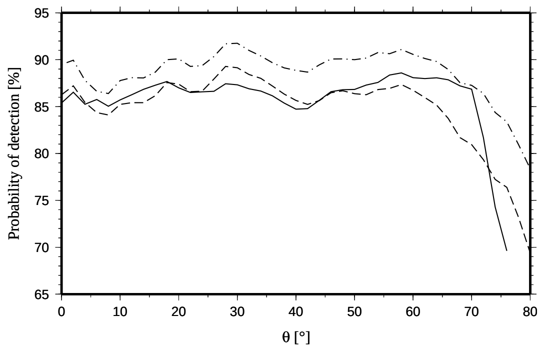

Figure 8.7 *– Means of the weekly pixels' agreement (in percent) of the MPEF CLM (plain), GERB IR (dashed) and GERB IR+ (dotted–dashed) cloud masks with respect to the NWCSAF CMa cloud mask binned according to the viewing zenith angle θ for August 11–17 2007. GERB IR+ designates the GERB IR cloud mask supplemented with the NWCSAF CMa spatial texture filter.*

clouds classes are overlapping, will be missed by our scheme as clear–sky. This is especially the case for low warm clouds (stratocumulus) over the ocean whose satellite signal results in a BT decrease of only a couple of K compared to their associated clear–sky ocean. The region depicted in figure 8.8 typically illustrates such issue. We have plotted in panel 8.8(a) the comparison between the GERB IR+ and NWCSAF CMa cloud masks where the eggplant color designates pixels identified as clear–sky by the GERB algorithm while being specifically detected as cloudy by the NWCSAF low water cloud threshold test ($BTD_{10.8-3.9}$ or $BTD_{12-3.9}$). Panel 8.8(b) represents the SEVIRI 8.7 μm BT whose color scale ranges from 274 to 290 K used over water surfaces in the GERB IR+ scheme. It is obvious that these eggplant colored areas are characterized by BTD between cloudy and neighboring clear–sky pixels of only about 2 K.

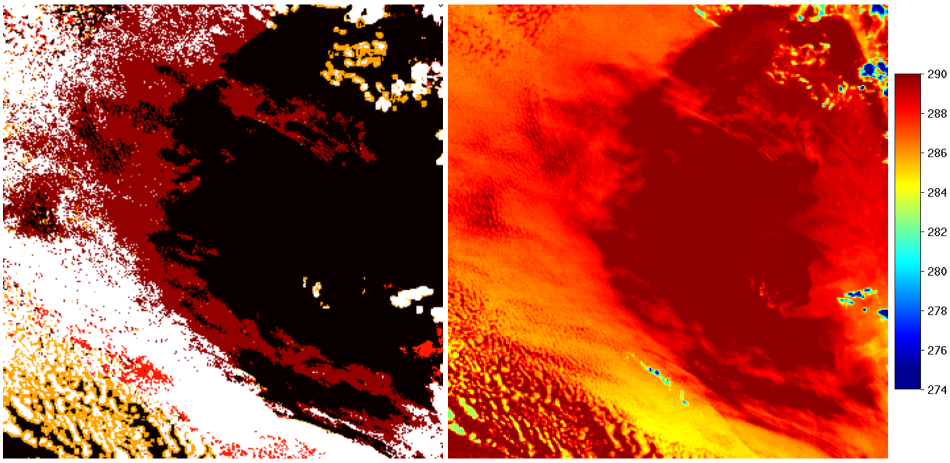

(a) (b)

__Figure 8.8__ – (a) GERB IR+ and NWCSAF CMa comparison map for an ocean area located in the West of the Namibian coast on March 11 2007 at 0:00 UTC. The eggplant color designates pixels identified as clear–sky by the GERB algorithm while being specifically detected as cloudy by the NWCSAF low water cloud threshold test ($BTD_{10.8-3.9}$ or $BTD_{12-3.9}$). Orange color is associated to pixels flagged clear–sky by the GERB algorithm and cloudy by any other combination of NWCSAF threshold tests. Red depicts pixels detected as cloudy by the GERB and as clear–sky by the NWCSAF schemes. Agreement between the 2 cloud masks corresponds to black (clear–sky) and white (cloudy). (b) Associated SEVIRI 8.7 μm BT measurements.

Similarly, cloud edges in broken cloud fields are also falsely detected as clear–sky by our method. This is shown in the lower left corner of panel 8.8(a) in orange. From panel 8.8(b) we can notice that such pixels also lack a sufficient SEVIRI 8.7 μm BT contrast with respect to clear–sky conditions.

8.6 Conclusions

This chapter presents a novel technique for cloud detection in geostationary imagery using only thermal IR channels. It is based on a yet simple but robust approach that for every pixel clear–sky and cloudy conditions of a 60–days BT time–series are drawn from clear–sky and cloudy normal distributions of BTs. Such modeling allows us to perform a *kNN* clustering approach to estimate their parameters and thus to classify all BTs of the time–series as clear–

sky or cloudy. Instead of relying on NWP or reanalysis fields computed at the acquisition time of the imagery to classify as it is usually the case for operational algorithms found in the literature, our clustering scheme is initialized using a realistic width of the BT clear–sky class. Such width is estimated from a 10–years climatology of reanalysis skin surface temperatures. Therefore, our algorithm is only making use of the satellite measurements and of an ancillary clear–sky class' width dataset for its initialization. It avoids fixed threshold values but instead dynamically estimates these values thanks to the clustering technique.

Comparisons of our technique and of the MPEF CLM scheme with respect to the state–of–the–art NWCSAF CMa algorithm have shown that we generally outperform the MPEF processing during night–time as well as during day–time even if the latter makes use of the additional satellite's visible and NIR information while we only use a single selected thermal IR band for ocean and another single channel for land geotype supplemented by the NWCSAF CMa spatial texture filter. However, results should be mitigated during day–time over vegetation since it is the MPEF CLM which is exhibiting better cloud detection performance in this case. This can be explained by the larger heterogeneity of this geotype's BT response, thus broadening its associated clear–sky distribution which then tends to overlap with the intermediate cloudy conditions.

One would expect a reduced angular accuracy of our method compared to MPEF due to the fact that our ancillary dataset used for the initialization of the clustering is not corrected for the increasing atmospheric optical path length at large zenith viewing angles while it is the case for the MPEF thresholds. It turns out to be otherwise: our detection performance is always higher than for the MPEF algorithm. Nevertheless, we notice in the comparisons with the NWCSAF CMa technique a large decrease of performance from 70° on. A possible improvement could be to consider a TOA clear–sky BTs climatology from satellite's measurements including large viewing zenith angle measurements to estimate an new ancillary dataset.

Despite the fact that our method exhibits better results than the MPEF scheme, we have identified specific conditions for which it systematically fails. Indeed, warm low clouds above ocean are typically characterized by a difference in their thermal signature of a few K compared to their associated clear–sky scenes. Both clear–sky and intermediate cloudy BT distributions tend to overlap and are thus infringing the assumptions of our technique. It results that such stratocumulus scenes are falsely classified as clear–sky. Nevertheless, preliminary investigations have shown that a simple $BTD_{10.8-3.9}$ threshold test inspired by the MODIS cloud detection algorithm can drastically decrease this level of misidentification. The selection of a threshold value of 6 K promisingly increased the stratocumulus detection performance from 44 to 71 % (according to NWCSAF low water cloud threshold test) for March 11 2007 at 0:00 UTC. However, further work is still required to assess the optimum value over day– and night–time.

Further improvements could also be investigated. The ECMWF ERA–40 dataset used to compute our ancillary clear–sky class' width stops in 2001. It results that the last 10 years are not considered and hence changes in surface temperature that could have occurred are ignored. To avoid any resulting bias in our cloud detection, a more recent skin surface temperatures climatology should be used to estimate our ancillary initialization dataset. Moreover, such ECMWF dataset is only currently available on a 6–hourly basis which is too limited to fully resolve the diurnal cycle, especially in the thermal IR region. It is foreseen in the future to increase this sampling to 8 times per day (every 3 hours) but this would require the complete recomputation of the ERA–40 dataset. Furthermore, the skin surface temperatures are currently used all together to estimate the clear–sky class' width Δ, even if they are associated to cloudy conditions. In the future, such cloudy skin surface temperatures could be screened to only take into account clear–sky conditions for the computation of Δ. Finally, we have performed our comparisons by considering as reference the NWCSAF CMa product. However, since this algorithm uses different multispectral tests during day– (visible, NIR and thermal IR) and night–time (thermal IR), its cloud detection performance is varying with time. A completely independent validation of our method could be performed by comparing its results with CloudSat [155] products. However, such low orbiting platform raises some concerns about the simultaneity, collocation and spatial coverage of its acquisitions when compared to SEVIRI measurements.

Acknowledgments

This work was supported by the European Organisation for the Exploitation of Meteorological Satellites (EUMETSAT) under contract EUMETGERB.

Chapter 9

Summary and perspectives

THIS work is exclusively focused on the scene identification scheme developed within the Geostationary Earth Radiation Budget (GERB) L20 operational processing performed at Royal Meteorological Institute of Belgium (RMIB). As explained previously, such scheme holds a central position in the radiance–to–flux conversion of the GERB shortwave measurements. In this scope, we had to develop a scene identification (sceneID) algorithm allowing to select the state–of–the–art Clouds and the Earth's Radiant Energy System (CERES) shortwave angular dependency models (ADMs). This step required a specific approach in the cloud properties estimation. Therefore, a near–realtime processing chain was prototyped on Meteosat–7 (MS7) data prior to the launch of the first GERB instrument.

The literature review showed the importance of an adequate estimation of the clear–sky conditions to accurately perform cloud optical depth retrievals. This explains why we have devoted a significant amount of time to the development and the validation of a novel composite top of the atmosphere (TOA) clear–sky visible reflectances algorithm. The next step was to select the best approach for estimating the needed cloud properties according to the processing constraints, mainly the near–realtime delivery of the products. We decided to implement a non–iterative cloud optical depth retrieval method relying on comparisons with fixed radiative transfer model (RTM) calculations without any *a priori* knowledge of clouds in the field–of–view (FOV). Such comparisons were achieved through an innovative look–up tables (LUTs) parameterization, relative to the previously estimated clear–sky reflectances. The cloud thermodynamic phase detection was limited to a crude threshold test on the infrared (IR) brightness temperature (BT) because the MS7 imager had only 3 channels (visible, window IR and water vapor), knowing that the estimation of the cloud optical depth is ambiguous for thin clouds using only visible information. Finally, a cloud conservative cloud flag was derived for pixels whose cloud optical depth is above a fixed threshold. We then performed to some extent consistency checks between GERB and CERES cloud properties retrievals. However, the adopted strategy to compare averaged properties over almost simultaneous collocated and coangular GERB–like and CERES footprints showed its limits despite the fact that more than 15 months of day–time data was considered. Indeed, issues resulting from the reduced number of cloudy pairs available over desert surfaces led to unreliable statistics. Other surfaces exhibited discrepancies to the expected one–to–one relationship between GERB and CERES retrievals. These discrepancies could be explained by the large MS7 visible band extending up to the near–infrared (NIR) region and resulting in a significant sensitivity of its measurements to the cloud particle size. We also investigated a possible correction scheme (homogenization) on GERB cloud optical depths to improve their matching with CERES retrievals. However, such transformation was not considered further in this work. Instead, we opted for an accurate analysis of the discrepancies allowing to identify the current limitations of the GERB sceneID.

Once Spinning Enhanced Visible and InfraRed Imager (SEVIRI) data were routinely available, we carried out the adaptation of the previously developed sceneID to this new imager. Compared to the single visible channel of MS7, we had to deal with a pair of narrower visible bands for SEVIRI. This required to modify the composite clear–sky visible reflectances algorithm to take into account the increased sensitivity with respect to vegetation growing and changing seasons especially in the Sahel region. The cloud optical depth LUTs were simply recomputed for the two SEVIRI channels using the same RTM. Since these channels are significantly narrower than the band parameterization of the RTM, a lower reliability for the SEVIRI imager is observed. Comparisons between GERB and CERES retrievals both on SEVIRI sceneID data suggested that our clear–sky reflectance estimations are systematically underestimated. Sun–glint retrievals also suffer from systematic overestimation of cloud occurrences due to the empirical choice of parameters in the developed sun–glint visible clear–sky reflectances model. Moreover, the cloud thermodynamic phase detection implemented in the first edition of the RMIB GERB Processing (RGP) software collection is limited to a crude threshold test on the 10.8 μm BT. This results in a significant underestimation of the ice clouds occurrence compared to the CERES sceneID. Comparisons of the GERB and CERES sceneID retrievals also highlighted the need of a fresh snow/ice as well as an aerosol dust detection scheme, prior to any cloud properties retrieval, to avoid current misidentification of such events with clouds. All these issues result in discrepancies in the TOA solar fluxes due to ADM misselection compared to the CERES sceneID.

Finally, we performed a feasibility study on a cloud detection algorithm using only SEVIRI IR channels without any use of numerical weather prediction (NWP) ancillary information as it is usually the case with the major cloud detection schemes. We showed that such algorithm, simply relying on measurements and on a clustering approach using a climatology for its initialization, exhibits an overall performance in cloud detection similar to the operational European Organisation for the Exploitation of Meteorological Satellites (EUMETSAT) Meteorological Product Extraction Facility (MPEF) scheme when the Nowcasting and Very Short–Range Forecasting SAF (NWCSAF) cloud mask product is considered as reference.

The following summarizes our contributions to the field in the scope of an operational implementation:

- development of a composite TOA clear–sky visible reflectance algorithm using temporal information from geostationary Earth orbit (GEO) imagers providing results at the native spatial resolution of the imager, by (i) taking into account the scene geometry variability over the time–series, the spatial climatology of the cloud coverage for the length of the time–series as well as (ii) suggesting a theoretical model for the clear–sky reflectances in sun–glint affected areas,

- development of a non–iterative cloud optical depth retrieval scheme for GEO imagers using weekly updated TOA clear–sky visible reflectances and a parameterization of the LUTs for fast inversion, together with a consistent cloud mask through a threshold test on the cloud optical depth,

- development of a self–adaptive night–time cloud detection method using temporal information from GEO imagers providing results at the native spatial resolution of the imager, by using only a single IR band over the ocean, another IR channel over the land and a climatological ancillary dataset allowing to estimate dynamically cloudy threshold values.

Future perspectives can be divided into two groups depending on their short–term or long–term horizon. Short–term improvements are foreseen to be part of the Edition 2 RGP as updates or tuning of current operational schemes. Long–term perspectives are usually either additional features to products or completely new investigations on methods which could achieve better accuracy. It is needless to say that the CERES cloud properties dataset, even limited to a single day–time over one week, is invaluable in the objective assessment of the discrepancies between GERB and CERES sceneIDs as well as in any tuning of parameters.

As we mentioned previously, our clear–sky algorithm is underestimating the true values. We are thus planning, in a short–term perspective, to increase the rank (percentile) of the selected ratio (see chapter 6, section 6.3.1.1) which is used to infer the clear–sky reflectance. Such selection of the rank could even be performed according to the surface type. Moreover, the parameters of the clear–sky sun–glint reflectance model need to be chosen to avoid any spatial discontinuity at the border as well as artefacts within the sun–glint region in the cloud mask. While these improvements could be achieved empirically and their validity tested against CERES retrievals, the estimation of the sun–glint model parameters could also be dynamically derived using our newly developed IR cloud mask. Concerning the long–term view, our clear–sky algorithm could benefit from recent techniques found in literature for the estimation of the envelope upper/lower curve from a noisy (clouds) reflectance time–series* [26, 78, 180].

The detailed comparisons between GERB and CERES cloud thermodynamic phase retrievals illustrated that our current implementation (threshold test on the 10.8 μm BT) is inadequate and exhibits a systematic underestimation in the detection of ice clouds. As shown in the literature review, several multispectral techniques are available. However for the Edition 2 processing, we will most probably use the Moderate Resolution Imaging Spectroradiometer (MODIS)–like IR scheme [130]†. Indeed, it was found that such method shows small instantaneous bias for thick clouds with respect to ground–based observations [190]. For the long–term, the use of the 1.6 μm SEVIRI channel could be foreseen, but the knowledge of the surface albedo or the TOA clear–sky reflectance would be required.

To avoid any misclassification of oceanic aerosol dust clouds or fresh snow/ice as clouds, the Edition 2 sceneID will first rely on an IR multispectral aerosol dust detection [21] and on a developed snow/ice identification [18] prior to the cloud properties retrieval. State–of–the–art ice crystals bulk properties parameterizations are appearing in recent literature [15]. Their incorporation within user–friendly RTMs such as libRadTran [105] together with precomputed Mie calculations for water clouds together with the increase of computing power‡, enables us to perform the complete update of the LUTs used in the cloud optical depth inversion. It is expected that this LUT inversion will benefit (1) from the improved cloud models compared to

*However, such techniques are assuming either a positive or negative contribution of the noise to the base signal. Thus, in our case, cloud shadows which are characterized by lower reflectances than clear–sky scenes should be priorly identified and filtered out to only keep the positive noisy contribution associated to cloudy scenes.

†We could also possibly check if any improvement over this method could be achieved by considering the Strabala *et al.* [157] algorithm.

‡allowing a drastic increase of the angular nodes (from 5 to 2° step) together with the number of streams (from 48 to 192)

the double Henyey–Greenstein phase function parameterization and (2) from the LUTs stratification according to the surface albedo. Moreover, we already assumed that the SEVIRI channels, being significantly narrower than the band parameterization of the STREAMER RTM, certainly results in inaccuracies in Edition 1 LUTs. Thus, such issue will definitely be mitigated for Edition 2 thanks to the line–by–line RTM used (libRadtran). The GERB and CERES comparisons also revealed a problem with the fixed threshold value used to flag clear–sky and cloudy scenes. This needs to be addressed for the next edition processing possibly by considering a different threshold according to the surface type. Again, an objective tuning of this threshold could be performed by selecting the values such that the mean cloud fraction over the SEVIRI FOV matches between GERB and CERES sceneIDs. In a long–term perspective, our cloud properties retrieval would certainly benefit from the use of the 1.6 μm channel allowing to select the best ice crystal shape and cloud particle size LUT within an iterative scheme. This would require first some knowledge on the surface albedo or the TOA clear–sky reflectance in that band. The free availability of 3–dimensional (3–D) Monte Carlo RTMs will open new perspectives. One possible investigation could be the use of such code in 1–dimensional (1–D) mode to overcome the intrinsic limitations of plane–parallel radiative transfer (RT) modeling at low zenith angles, since any accuracy level is achievable providing sufficient computing time. However, both perspectives will require significant computing power both operationally and offline, which is still difficult to achieve nowadays at reasonable costs.

Finally, our IR cloud detection scheme could benefit as suggested for our clear–sky reflectance algorithm from recent techniques in the estimation of the envelope upper curve from a noisy (clouds) BT time–series. This would not only provide a cloud mask but also TOA clear–sky BT for several IR channels, thus allowing to estimate the cloud radiative forcing in such bands and possibly in the whole thermal region.

List of acronyms and abbreviations

1–D 1–dimensional

3–D 3–dimensional

ADM . . . . angular dependency model

APOLLO . . . . . AVHRR Processing scheme Over cLoudy Land and Ocean

ASTEX . . . . . . Atlantic Stratocumulus Transition Experiment

ATSR . . . . Along Track Scanning Radiometer

AVHRR . . . . . . Advanced Very High Resolution Radiometer

BB . . . . broadband

BBR . . . . broadband radiometer

BRDF . . . . bidirectional reflectance distribution function

BT . . . . brightness temperature

BTD . . . . brightness temperature difference

CERES . . . . . . Clouds and the Earth's Radiant Energy System

CLAVR . . . . . . Cloud Advanced Very High Resolution Radiometer

CMSAF . . . . . . Climate Monitoring SAF

ECMWF . . . . . European Centre for Medium–Range Weather Forecasts

EOS . . . . Earth Observing System

ERB . . . . Earth radiation budget

ERBE . . . . Earth Radiation Budget Experiment

EUMETSAT . . . . European Organisation for the Exploitation of Meteorological Satellites

FDTD . . . . finite–difference time domain
FIRE . . . . First ISCCP Regional Experiment
FOV . . . . field–of–view

GCM . . . . general circulation model
GEO . . . . geostationary Earth orbit
GERB . . . . Geostationary Earth Radiation Budget
GOES . . . . Geostationary Operational Environment Satellite

HIRS . . . . High–Resolution Infrared Sounder
HIS . . . . High–spectral resolution Interferometer Sounder

IGBP . . . . International Geosphere Biosphere Program
IPA . . . . independent pixel approximation
IR . . . . infrared
ISCCP . . . . . . International Cloud Climatology Project
IWC . . . . ice water content
IWP . . . . ice water path

kNN . . . . k–nearest neighbours

LEO . . . . low Earth orbit
LUT . . . . look–up table
LWC . . . . liquid water content
LWP . . . . liquid water path

MARF . . . . . . Meteosat Archive and Retrieval Facility
MAS . . . . MODIS Airborne Simulator
MAST . . . . . . MODIS Atmosphere Science Team
MERIS . . . . . . Medium Resolution Imaging Spectrometer
MODIS . . . . . . Moderate Resolution Imaging Spectroradiometer
MPEF . . . . Meteorological Product Extraction Facility
MS7 . . . . Meteosat–7
MSG . . . . Meteosat Second Generation

MTI . . . . Multispectral Thermal Imager

NIR . . . . near–infrared

NN . . . . neural network

NOAA . . . . . . National Ocean and Air Administration

NWCSAF . . . . . Nowcasting and Very Short–Range Forecasting SAF

NWP . . . . numerical weather prediction

OCA . . . . optimal cloud analysis

OLR . . . . outgoing longwave radiation

POD . . . . probability of detection

POLDER . . . . . Polarization and Directionality of the Earth's Reflectances

PSF . . . . point spread function

RAL . . . . Rutherford Appleton Laboratory

RGP . . . . RMIB GERB Processing

RMIB . . . . Royal Meteorological Institute of Belgium

RT . . . . radiative transfer

RTM . . . . radiative transfer model

SAF . . . . Satellite Application Facility

ScaRaB . . . . . . Scanner for Radiation Budget

sceneID . . . . . . scene identification

SEVIRI . . . . . . Spinning Enhanced Visible and InfraRed Imager

SORCE . . . . . . Solar Radiation and Climate Experiment

SSF . . . . Single Satellite Footprint

SST . . . . sea surface temperature

TIM . . . . Total Irradiance Monitor

TOA . . . . top of the atmosphere

TRMM . . . . . . Tropical Rainfall Measuring Mission

UTC . . . . Universal Time Convention

VIIRS . . . . Visible–InfraRed Imaging Radiometer Suite

VIRS . . . . Visible and InfraRed Spectrometer

VISST . . . . Visible Infrared Solar–Infrared Split Window Technique

WCRP . . . . . . World Climate Research Program

Bibliography

[1] S.A. Ackerman, W.L. Smith, J.D. Spinhirne, and H.E. Revercomb. The 27–28 October 1986 FIRE IFO cirrus case study: psectral properties of cirrus clouds in the 8–12 μm window. *Mon. Wea. Rev.*, 118:2377–2388, 1990. 35

[2] S.A. Ackerman, K.I. Strabala, W.P. Menzel, R.A. Frey, C.C. Moeller, and L.E. Gumley. Discriminating clear sky from clouds with MODIS. *J. Geophys. Res.*, 103(D24):32141–32157, 1998. 31, 122

[3] R.P. Allan, A. Slingo, S.F. Milton, and M.A. Brooks. Evaluation of the Met Office global forecast model using Geostationary Earth Radiation Budget (GERB) data. *Quart. J. R. Meteorol. Soc.*, 133:1993–2010, 2007. 122

[4] U. Amato, A. Antoniados, V. Cuomo, L. Cutillo, M. Franzese, L. Murino, and C. Serio. Statistical coud detection from SEVIRI multispectral images. *Remote Sens. Environ.*, 112: 750–766, 2008. 28

[5] Z. Ameur, S. Ameur, A. Adane, H. Sauvageot, and K. Bara. Cloud classification using the textural features of Meteosat images. *Int. J. Remote Sensing*, 25(21):4491–4503, 2004. 29, 124

[6] A. Arking. Latitudinal distribution of cloud cover from TIROS III photographs. *Science*, 143:569–572, 1964. 27

[7] A. Arking and J.D. Childs. Retrieval of cloud cover parameters from multispectral satellite images. *J. Appl. Meteorol. Clim.*, 24:322–333, 1985. 29, 35, 39, 63, 64

[8] A.M. Baldridge, S.J. Hook, C.I. Grove, and G. Rivera. The ASTER spectral library version 2.0. *Remote Sens. Environ.*, 113(4):711–715, 2009. doi: 10.1016/j.rse.2008.11.007. 25, 103

[9] B.R. Barkstrom. The Earth Radiation Budget Experiment (ERBE). *B. Am. Meteorol. Soc.*, 65(11):1170–1186, 1984. 80

[10] B.A. Baum and J.D. Spinhirne. Remote sensing of cloud properties using the MODIS airborne simulator imagery during SUCCESS – 3. Cloud overlap. *J. Geophys. Res.*, 105: 11793–11804, 2000. 38

[11] B.A. Baum, V. Tovinkere, J. Titlow, and R.M. Welch. Automated cloud classification of global AVHRR data using a fuzzy logic approach. *J. Appl. Meteorol.*, 36:1519–1540, 1997. 23, 28

[12] B.A. Baum, P.F. Soulen, K.I. Strabala, M.D. King, S.A. Ackerman, and W.P. Menzel. Remote sensing of cloud properties using the MODIS airborne simulator imagery during SUCCESS – 2. Cloud thermodynamic phase. *J. Geophys. Res.*, 105:11781–11792, 2000. 36

[13] B.A. Baum, A.J. Heymsfield, P. Yang, and S.T. Bedka. Bulk scattering models for the remote sensing of ice clouds. Part 1: Microphysical data and models. *J. Appl. Meteorol.*, 44:1885–1895, 2005. 17, 19

[14] B.A. Baum, P. Yang, A.J. Heymsfield, S. Platnick, M.D. King, Y.-X. Hu, and S.T. Bedka. Bulk scattering models for the remote sensing of ice clouds. Part 2: Narrowband models. *J. Appl. Meteorol.*, 44:1896–1911, 2005.

[15] B.A. Baum, P. Yang, S.L. Nasiri, A.K. Heidinger, A.J. Heymsfield, and J. Li. Bulk scattering models for the remote sensing of ice clouds. Part 3: High resolution spectral models from 100 to 3250 cm^{-1}. *J. Appl. Meteorol. Clim.*, 46:423–434, 2007. 17, 19, 143

[16] A.S. Belward, J.E. Estes, and K.D. Kline. The IGBP–DIS 1–km landcover data set DISCover: A project overview. *Photogramm. Eng. Rem. Sens.*, 65(9):1013–1020, 1999. 81

[17] A. Bentamy, P. Queffeulou, Y. Quilfen, and K. Katsaros. Ocean surface wind fields estimated from satellite Active and Passive microwave instruments. *IEEE Trans. Geosci. Remote Sens.*, 37(5):2469–2486, 1999. 88

[18] C. Bertrand, L. Gonzalez, A. Ipe, and N. Clerbaux. Improvement in the GERB short wave flux estimations over snow covered surfaces. *Adv. Space Res.*, 41(7):1894–1905, 2008. 81, 99, 119, 143

[19] C. Bertrand, A. Ipe, N. Clerbaux, and L. Gonzalez. GERB SW flux anomalies over the Sahel region: an ADM related issue. In *Proc. 37th COSPAR Scientific Assembly*, Montréal, Canada, 2008. 98

[20] C.L. Brest, W.B. Rossow, and M. Roiter. Updated of Radiance Calibration for ISCCP. *J. Atmos. Ocean. Tech.*, 14:1091–1109, 1997. 57

[21] H.E. Brindley and J.E. Russel. Improving GERB scene identification using SEVIRI: Infrared dust detection strategy. *Remote Sens. Environ.*, 104(4):426–446, 2006. doi: 10.1016/j.rse.2006.05.019. 43, 108, 143

[22] H.E. Brindley and J.E. Russell. Assessing the errors in shortwave radiative fluxes inferred from the Geostationary Earth Radiation Budget (GERB) instrument in the presence of dust aerosol. *J. Appl. Meteorol.*, 47(6):1659–1680, 2008. doi: 10.1175/2007jamc1723.1. 116, 120

[23] J.C. Buriez, C. Vanbauce, F. Parol, P. Goloub, M. Herman, B. Bonnel, Y. Fouquart, P. Couvert, and G. Sèze. Cloud detection and derivation of cloud prperties from POLDER. *Int. J. Remote Sensing*, 18(13):2785–2813, 1997. 39

[24] D. Cano, J.M. Monget, M. Albuisson, H. Guillard, N. Regas, and L. Wald. A method for the determination of the global solar radiation from meteorological satellite data. *Sol. Energy*, 37:31–39, 1986. 64, 93

[25] B. Carlin, Q. Fu, U. Lohmann, G.G. Mace, K. Sassen, and J.M. Comstock. High–cloud horizontal inhomogeneity and solar albedo bias. *J. Climate*, 15:2321–2339, 2002. 30

[26] J. Chen, P. Jönsson, M. Tamura, Z. Gu, B. Matsushita, and L. Eklundh. A simple method for reconstructing a high–quality NDVI time–series data set based on the Savitzky–Golay filter. *Remote Sens. Environ.*, 91:332–344, 2004. doi: 10.1016/j.rse.2004.03.014. 143

[27] H. Chepfer, P. Goloub, J. Spinhirne, P.H. Flamant, M. Lavorato, L. Sauvage, G. Brogniez, and J. Pelon. Cirrus cloud properties derived from POLDER–1/ADEOS polarized radiances: First validation using ground–based lidar network. *J. Appl. Meteorol.*, 39:154–168, 2000. 37

[28] Y.S. Choi, C.H. Ho, M.H. Ahn, and Y.S. Kim. Enhancement of the consistency of MODIS thin cirrus with cloud phase by adding 1.6 μm reflectance. *Int. J. Remote Sensing*, 26(21): 4669–4680, 2005. 36

[29] P. Chylek and C. Borel. Mixed phase cloud water/ice structure from high spatial resolution satellite data. *J. Geophys. Res.*, 31(L14104), 2004. doi: 10.1029/2005GL020428. 36

[30] P. Chylek, S. Robinson, M.K. Dubey, M.D. King, Q. Fu, and W.B. Clodius. Comparison of near–infrared and thermal infrared cloud phase detections. *J. Geophys. Res.*, 111(D20203), 2006. 36, 91

[31] P.F. Clapp. Global cloud cover for seasons using TIROS nephanalyses. *Mon. Wea. Rev.*, 92:495–507, 1964. 27

[32] N. Clerbaux, S. Dewitte, L. Gonzalez, C. Bertand, B. Nicula, and A. Ipe. Outgoing longwave flux estimation: improvement of angular modelling using spectral information. *Remote Sens. Environ.*, 85:389–395, 2003. 122

[33] N. Clerbaux, S. Dewitte, C. Bertrand, D. Caprion, B. De Paepe, L. Gonzalez, A. Ipe, and J. Russell. Unfiltering of the Geostanionnary Earth Radiation Budget (GERB) data. Part I: Shortwave radiation. *J. Atmos. Ocean. Tech.*, 25(7):1087–1105, 2008. 122

[34] N. Clerbaux, S. Dewitte, C. Bertrand, D. Caprion, B. De Paepe, L. Gonzalez, A. Ipe, and J. Russell. Unfiltering of the Geostanionnary Earth Radiation Budget (GERB) data. Part II: Longwave radiation. *J. Atmos. Ocean. Tech.*, 25(7):1106–1117, 2008. 122

[35] N. Clerbaux, J.E. Russell, S. Dewitte, C. Bertrand, D. Caprion, B. De Paepe, L. Gonzalez Sotelino, A. Ipe, R. Bantges, and H.E. Brindley. Comparison of GERB instantaneous radiance and flux products with CERES Edition–2 data. *Remote Sens. Environ.*, 113:102–114, 2009. 114

[36] Coordination Group for Meteorological Satellites. LRIT/HRIT Global Specification. Technical Report CGMS 03, EUMETSAT, Darmstadt, Germany, 1999. 100

[37] C. Cornet, H. Isaka, B. Guillement, and F. Szczap. Neural network retrieval of cloud parameters of inhomogeneous clouds from multispectral and multiscale radiance data: feasibility study. *J. Geophys. Res.*, 109:D12203, 2004. 28

[38] C. Cox and W. Munk. Measurement of the roughness of the sea surface from photographs of the sun's glitter. *J. Opt. Soc. Am.*, 44:838–850, 1954. 88, 103, 131

[39] D. Crommelynck and S. Dewitte. Metrology of total solar irradiance monitoring. *Adv. Space Res.*, 24:195–204, 1999. 1

[40] D. Crommelynck and V. Domingo. Solar Irradiance Observations. *Science*, 225:180–181, 1984.

[41] D. Crommelynck, V. Domingo, and C. Fröhlich. The Solar Variations (SOVA) experiment in the EURECA space platform. *Adv. Space Res.*, 11:83–87, 1991.

[42] D. Crommelynck, A. Fichot, V. Domingo, and R. Lee III. SOLCON solar constant observations from the ATLAS missions. *Geophys. Res. Lett.*, 23:2293–2296, 1996.

[43] D.A. Crommelynck, R.W. Brusa, and V. Domingo. Results of the solar constant experiment onboard Spacelab 1. *Sol. Phys.*, 107:1–9, 1987. 1

[44] A.B. Davis, A. Marshak, E. Kassianov, and G.M. Stokes. Three–dimensional radiative transfer makes its mark. *EOS Trans. AGU*, 80(51):622–624, 1999. 29

[45] J. Delanoë and R.J. Hogan. Combined CloudSat–CALIPSO–MODIS retrievals of the properties of ice clouds. *J. Geophys. Res.*, 115(D00H29), 2010. doi: 10.1029/2009JD012346. 27

[46] R.P. d'Entremont and G.B. Gustafson. Analysis of geostationary satellite imagery using a temporal–differencing technique. *Earth Interact.*, 7:1–25, 2003. 126

[47] M. Derrien and H. Le Gléau. MSG/SEVIRI cloud mask and type for SAFNWC. *Int. J. Remote Sensing*, 26(21):4707–4732, 2005. doi: 10.1080/01431160500166128. 33, 40, 122, 130

[48] M. Desbois, G. Sèze, and G. Szejwach. Automatic classification of clouds on Meteosat imagery: application to high–level clouds. *J. Appl. Meteorol.*, 21:401–412, 1982. 29, 124

[49] S. Dewitte, N. Clerbaux, L. Gonzalez, A. Hermans, A. Ipe, A. Joukoff, and G. Sadowski. Generation of GERB unfiltered radiances and fluxes. In *Proc. EUMETSAT Meteorological Satellite Data Users' Conference*, volume P.29, Bologna, Italy, 2000. 61

[50] S. Dewitte, A. Joukoff, D. Crommelynck, R.B. Lee III, R. Helizon, and R.S. Wilson. Contribution of the SOLCON program to the long term total solar irradiance observation. *J. Geophys. Res.*, 106:759–766, 2001. 1

[51] S. Dewitte, D. Crommelynck, and A. Joukoff. Total solar irradiance observations from DIARAD/VIRGO. *J. Geophys. Res.*, 109:A02102, 2004. 1

[52] S. Dewitte, L. Gonzalez, N. Clerbaux, A. Ipe, C. Bertrand, and B. De Paepe. The Geostationary Earth Radiation Budget Edition 1 data processing algorithms. *Adv. Space Res.*, 41 (11):1906–1913, 2008. 3, 80, 81, 114, 122

[53] R.O. Duda, P.E. Hart, and D.G. Stork. *Pattern Classification — Second Edition*. Wiley Interscience, New York, 2001. 124, 126

[54] J.Ph. Duvel, M. Viollier, P. Raberanto, R. Kandel, M. Haeffelin, L.A. Pakhomov, V.A. Golovko, J. Mueller, R. Stuhlmann, and the International ScaRaB Scientific Working Group. The ScaRaB–Resurs earth radiation budget dataset and first results. *B. Am. Meteorol. Soc.*, 82:1397–1408, 1998. 2

[55] E. Ebert. A pattern recognition technique for distinguishing surface and cloud types in the polar regions. *J. Appl. Meteorol. Clim.*, 26:1412–1427, 1987. 23, 28

[56] H. Eichler, A. Ehrlich, M. Wendisch, G. Mioche, J.-F. Gayet, M. Wirth, C. Emde, and A. Minikin. Influence of ice crystals shape on retrieval of cirrus optical thickness and effective radius: a case study. *J. Geophys. Res.*, 114:D19203, 2009. doi: 10.1029/2009JD012215. 39, 45

[57] A. Feijt, P. de Valk, and S. van der Veen. Cloud detection using Meteosat imagery and numerical weather prediction model data. *J. Appl. Meteorol.*, 39:1017–1030, 2000. 33

[58] J.M. Futyan and J.E. Russell. Developing clear–sky flux products for the Geostationary Earth Radiation Budget experiment. *J. Appl. Meteorol.*, 44(9):1361–1374, 2005. 98

[59] L. Gómez–Chova, G. Camps–Valls, J. Calpe–Maravilla, L. Guanter, and J. Moreno. Cloud–screening algorithm for ENVISAT/MERIS multispectral images. *IEEE Trans. Geosci. Remote Sens.*, 45(12):4105–4118, 2007. doi: 10.1109/TGRS.2007.905312. 29

[60] L. Gonzalez, A. Hermans, S. Dewitte, A. Ipe, G. Sadowski, and N. Clerbaux. Resolution enhancement of GERB data. In *Proc. EUMETSAT Meteorological Satellite Data Users' Conference*, volume P.29, Bologna, Italy, 2000. 62

[61] L. Gonzalez Sotelino. GERB–CERES Intercomparisons — Update. personal communication, 2008. 69

[62] Y. Govaerts and M. Clerici. MSG-1/SEVIRI Solar Channels Calibration Commissioning Activity Report. Technical Report EUM/MSG/TEN/04/0024, EUMETSAT, Darmstadt, Germany, 2004. 101

[63] Y. Govaerts, A. Arriaga, and J. Schmetz. Operational vicarious calibration of the MSG/SEVIRI solar channels. *Adv. Space Res.*, 28(1):21–30, 2001. 44, 51, 101

[64] A. Gruber and J.S. Winston. Earth–atmosphere radiative heating based on NOAA scanning radiometer measurements. *B. Am. Meteorol. Soc.*, 59:1570–1573, 1978. 54

[65] G.M. Hale and M.R. Querry. Optical constants of water in the 200nm to 200 μm wavelength region. *Appl. Opt.*, 12:555–563, 1973. 18

[66] J.E. Harries and D. Crommelynck. The Geostationary Earth Radiation Budget Experiment on MSG–1 and its potential applications. *Adv. Space Res.*, 24(7):915–919, 1999. 3, 61, 80, 122

[67] J.E. Harries, J.E. Russel, J.A. Hanafin, H. Brindley, J. Futyan, J. Rufus, S. Kellock, G. Matthews, R. Wrigley, A. Last, J. Mueller, R. Mossavati, J. Ashmall, E. Sawyer, D. Parker, M. Caldwell, P.M. Allan, A. Smith, M.J. Bates, B. Coan, B.C. Stewart, D.R. Lepine, L.A. Cornwall, D.R. Corney, M.J. Ricketts, D. Drummond, D. Smart, R. Cutler, S. Dewitte, N. Clerbaux, L. Gonzalez, A. Ipe, C. Bertrand, A. Joukoff, D. Crommelynck, N. Nelms, D.T. Llewellyn-Jones, G. Butcher, G.L. Smith, Z.P. Szewczyk, P.E. Mlynczak, A. Slingo, R.P. Allan, , and M.A. Ringer. The Geostationary Earth Radiation Budget Project. *B. Am. Meteorol. Soc.*, 86:945–960, 2005. 3, 80, 114, 122

[68] F.B. House, A. Gruber, G.E. Hunt, and A.T. Mecherikunnel. History of Satellite Missions and Measurements of the Earth Radiation Budget (1957–1984). *Rev. Geophys.*, 24:357–377, 1986. 80

[69] Y.X. Hu and K. Stamnes. An accurate parameterization of the radiative properties of water clouds suitable for use in climate models. *J. Climate*, 6(4):728–742, 1993. 92

[70] P.J. Huber. Robust estimation of a location parameter. *Ann. Math. Stat.*, 35:73–101, 1964. 70, 74

[71] G.E. Hunt. Radiative properties of terrestrial clouds at visible and infra-red thermal window wavelengths. *Quart. J. R. Meteorol. Soc.*, 99:346–369, 1973. 127

[72] K.D. Hutchison. Application of AVHRR/3 imagery for the improved detection of thin cirrus clouds and specification of cloud–top phase. *J. Atmos. Ocean. Tech.*, 16:1885–1899, 1999. 37

[73] T. Inoue. On the temperature and effective emissivity determination of semitransparent cirrus clouds by bispectral measurements in the 10 μm window region. *J. Meteor. Soc. Japan*, 63:88–98, 1985. 108

[74] H. Ishida and T.Y. Nakajima. Development of an unbiased cloud detection algorithm for a spaceborne multispectral imager. *J. Geophys. Res.*, 114:D07206, 2009. doi: 10.1029/2008JD010710. 32, 103

[75] H. Iwabuchi. Efficient Monte Carlo methods for radiative transfer modeling. *J. Atmos. Sci.*, 63:2324–2339, 2006. 29

[76] H. Iwabuchi and T. Hayasaka. Effects of cloud horizontal inhomogeneity on the optical thickness retrieved from moderate–resolution satellite data. *J. Atmos. Sci.*, 59:2227–2242, 2002. 30

[77] D. Jolivet and A.J. Feijt. Cloud thermodynamic phase and particle size estimation using the 0.67 and 1.6 μm channels from meteorological satellites. *Atmos. Chem. Phys. Discuss.*, 3:4461–4488, 2003. 36, 65, 67

[78] Y. Julien and J.A. Sobrino. Comparison of cloud–reconstruction methods for time series of composite NDVI data. *Remote Sens. Environ.*, 114:618–625, 2010. doi: 10.1016/j.rse.2009.11.001. 143

[79] R. Kandel, M. Viollier, P. Raberanto, J.Ph. Duvel, L.A. Pakhomov, V.A. Golovko, A.P. Trishchenko, J. Mueller, E. Raschke, R. Stuhlmann, and the International ScaRaB Scientific Working Group. The ScaRaB earth radiation budget dataset. *B. Am. Meteorol. Soc.*, 79:765–783, 1998. 2, 80

[80] S. Kato and A. Marshak. Solar zenith and viewing geometry–dependent errors in satellite retrieved cloud optical thickness: Marine stratocumulus case. *J. Geophys. Res.*, 114:D01202, 2009. doi: 10.1029/2008JD010579. 47

[81] S. Kato, L.M. Hinkelman, and A. Cheng. Estimate of satellite–derived cloud optical thickness and effective radius errors and their effect on computed domain–averaged irradiances. *J. Geophys. Res.*, 111:D17201, 2006. doi: 10.1029/2005JD006668. 30

[82] J. Key and A.J. Schweiger. Tools for atmospheric radiative transfer: Streamer and FluxNet. *Comp. Geosci.*, 24(5):443–451, 1998. 20, 63, 91, 113

[83] J. Key, P. Yang, B. Baum, and S. Nasiri. Parameterization of shortwave ice cloud optical properties for various particle habits. *J. Geophys. Res.*, 107(D13):4181, 2002. 20, 92

[84] M.D. King. Determination of the scaled optical thickness of clouds from reflected solar radiation measurements. *J. Atmos. Sci.*, 44:1734–1751, 1987. 20, 39, 43, 63, 64

[85] M.D. King, W.P. Menzel, Y.J. Kaufman, D. Tanré, B. Gao, S. Platnick, S.A. Ackerman, L.A. Remer, R. Pincus, and P.A. Hubanks. Cloud and aerosol properties, precipitable water, and profiles of temperature and water vapour from MODIS. *IEEE Trans. Geosci. Remote Sens.*, 41(2):442–458, 2003. 31, 35, 40, 44, 91, 122

[86] G. Kopp, G. Lawrence, and G. Rottman. The Total Irradiance Monitor (TIM): Science Results. *Sol. Phys.*, 230(1):129–140, 2005. 9

[87] W. Krebs, H. Mannstein, L. Bugliaro, and B. Mayer. Technical note: a new day– and night–time Meteosat Second Generation Cirrus Detection Algorithm MeCIDA. *Atmos. Chem. Phys. Discuss.*, 7:10933–10969, 2007. 37

[88] K.T. Kriebel, G. Gessel, M. Kästner, and H. Mannstein. The cloud analysis tool APOLLO: improvements and validations. *Int. J. Remote Sensing*, 24:2389–2408, 2003. 31

[89] C. Kummerow, W. Barnes, T. Kozu, J. Shiue, and J. Simpson. The Tropical Rainfall Measuring Mission (TRMM) sensor package. *J. Atmos. Ocean. Tech.*, 15(3):809–817, 1998. 2, 80

[90] J. Lean and D. Rind. Climate forcing by changing solar radiation. *J. Climate*, 11:3069–3094, 1998. 9

[91] J. Li, W.P. Menzel, Z. Yang, R.A. Frey, and S.A. Ackerman. High–spatial–resolution surface and cloud–type classification from MODIS multispectral band measurements. *J. Appl. Meteorol.*, 42:204–226, 2003. 28

[92] Z. Li and H.G. Leighton. Narrowband to Broadband Conversion with Spatially Autocorrelated Reflectance Measurements. *J. Appl. Meteorol.*, 31:421–432, 1992. 54

[93] K.N. Liou. *An Introduction to Atmospheric Radiation — Second Edition*. Academic Press, San Diego, 2002. 7, 13, 14, 42

[94] N.G. Loeb and J.A. Coakley Jr. Inference of marine stratus cloud optical depth from satellite measurements: Does 1D theory apply ? *J. Climate*, 11(2):215–233, 1998. 47

[95] N.G. Loeb and S. Kato. Top–of–atmosphere direct radiative effect of aerosols from the Clouds and the Earth's Radiant Energy System Satellite instrument (CERES). *J. Climate*, 15:1474–1484, 2002. 98

[96] N.G. Loeb, P.O. Hinton, and R.N. Green. Top–of–atmosphere albedo estimation from angular distribution models: a comparison between two approaches. *J. Geophys. Res.*, 104 (D24):31255–31260, 1999. 96, 98

[97] N.G. Loeb, F. Parol, J.Cl. Buriez, and C. Vanbauce. Top–of–atmosphere albedo estimation from angular distribution models using scene identification from satellite cloud property retrievals. *J. Climate*, 13:1269–1285, 2000. 59

[98] N.G. Loeb, K. Loukachine, N.M. Smith, B.A. Wielicki, and D.F. Young. Angular distribution models for top–of–atmosphere radiative flux estimation from the Clouds and the Earth's Radiant Energy System instrument on the Tropical Rainfall Measuring Mission satellite – Part II: Validation. *J. Appl. Meteorol.*, 42(12):1748–1769, 2003. 4

[99] N.G. Loeb, N.M. Smith, S. Kato, W.F. Miller, S.K. Kupta, P. Minnis, and B.A. Wielicki. Angular distribution models for top–of–atmosphere radiative flux estimation from the Clouds and the Earth's Radiant Energy System instrument on the Tropical Rainfall Measuring Mission satellite – Part I: Methodology. *J. Appl. Meteorol.*, 42(2):240–265, 2003. 4, 52, 53, 62, 67, 71, 72, 73, 75, 77, 81, 122

[100] H.J. Lutz. Scenes and Cloud Analysis from Meteosat Second Generation (MSG) Observations. In *Proc. EUMETSAT Meteorological Satellite Data Users' Conference*, volume P.39, Weimar, Germany, 2003. 130

[101] A. Macke, P.N. Francis, G.M. McFarquhar, and S. Kinne. The role of ice particle shapes and size distributions in the single scattering properties of cirrus clouds. *J. Atmos. Sci.*, 55:2874–2883, 1998. 45

[102] A. Macke, D.L. Mitchell, and L.V. Bremen. Monte Carlo radiative transfer calculations for inhomogeneous mixed phase clouds. *Phys. Chem. Earth, Ser. B*, 24(3):237–241, 1999. 29

[103] A. Marshak, A. Davis, R.F. Cahalan, and W. Wiscombe. Nonlocal independent pixel approximation: direct and inverse problems. *IEEE Trans. Geosci. Remote Sens.*, 36(1):192–205, 1998. 30

[104] E. Matthews and W.B. Rossow. Regional and seasonal variations of surface reflectances from satellite observations at 0.6 μm. *J. Appl. Meteorol. Clim.*, 26:170–202, 1987. 50, 51, 54, 85

[105] B. Mayer and A. Kylling. The libRadtran software package for radiative transfer calculations – description and examples of use. *Atmos. Chem. Phys.*, 5:1855–1877, 2005. 21, 22, 88, 113, 143

[106] S. Mekaoui and S. Dewitte. Total Solar Irradiance absolute level from DIARAD/SOVIM on the International Space Station. *Adv. Space Res.*, submitted, 2009. 1

[107] P. Minnis. Viewing zenith angle dependence of cloudiness determined from coincident GOES East and GOES West data. *J. Geophys. Res.*, 94(D2):2303–2320, 1989. 44

[108] P. Minnis and E.F. Harrison. Diurnal Variability of Regional Cloud and Clear–Sky Radiative Parameters Derived from GOES Data. Part I: Analysis Method. *J. Appl. Meteorol. Clim.*, 23:993–1011, 1984. 33, 50

[109] P. Minnis and E.F. Harrison. Diurnal Variability of Regional Cloud and Clear–Sky Radiative Parameters Derived from GOES Data. Part III: November 1978 Radiative Parameters. *J. Appl. Meteorol. Clim.*, 23:1032–1051, 1984. 50, 54

[110] P. Minnis, D.P. Garber, and D.F. Young. Parameterizations of reflectance and effective emittance for satellite remote sensing of cloud properties. *J. Atmos. Sci.*, 55(22):3313–3339, 1998. 35, 46

[111] P. Minnis, D.F. Young, B.A. Wielicki, P.W. Heck, X. Dong, L.L. Stowe, and R. Welch. CERES cloud properties derived from multispectral VIRS data. In *Proc. Symp. on Remote Sensing*, volume 3867, pages 91–102, Florence, Italy, 1999. 81, 82

[112] P. Minnis, L. Nguyen, D.R. Doelling, D.F. Young, W.F. Miller, and D.P. Kratz. Rapid Calibration of Operational and Research Meteorological Satellite Imagers. Part I: Evaluation of Research Satellite Visible Channels as References. *J. Atmos. Ocean. Tech.*, 19:1233–1249, 2002. 32, 101

[113] P. Minnis, L. Nguyen, D.R. Doelling, D.F. Young, W.F. Miller, and D.P. Kratz. Rapid Calibration of Operational and Research Meteorological Satellite Imagers. Part II: Comparison of Inrared Channels. *J. Atmos. Ocean. Tech.*, 19:1250–1266, 2002. 32

[114] P. Minnis, D.R. Doelling, L. Nguyen, W.F. Miller, and V. Chakrapani. Assessment of the visible channel calibrations of the TRMM VIRS and MODIS on Aqua and Terra. *J. Atmos. Ocean. Tech.*, 25:385–400, 2008. 101

[115] P. Minnis, L. Nguyen, R. Palikonda, P.W. Heck, D.A. Spangenberg, D.R. Doelling, J.K. Ayers, W.L. Smith Jr., M.M. Khaiyer, Q.Z. Trepte, L.A. Avey, F.-L. Chang, C.R. Yost, T.L. Chee, and S. Sun–Mack. Near-real time cloud retrievals from operational and research meteorological satellites. In *Proc. SPIE Europe Remote Sens.*, volume 7107(2), Cardiff, UK, 2008. 30, 99

[116] P. Minnis, Q.Z. Trepte, S. Sun-Mack, Y. Chen, D.R. Doelling, D.F. Young, D.A. Spangenberg, W.F. Miller, B.A. Wielicki, R.R. Brown, S.C. Gibson, and E.B. Geier. Cloud detection in nonpolar regions for CERES using TRMM VIRS and Terra and Aqua MODIS data. *IEEE Trans. Geosci. Remote Sens.*, 46(11):3857–3884, 2008. 32, 41, 44, 81, 99, 122

[117] P. Minnis, S. Sun-Mack, D.F. Young, P.W. Heck, D.P. Garber, Y. Chen, D.A. Spangenberg, R.F. Arduini, Q.Z. Trepte, W.L. Smith, Jr., J.K. Ayers, S.C. Gibson, W.F. Miller, V. Chakrapani, Y. Takano, K.N. Liou, and Y. Xie. CERES Edition–2 cloud property retrievals using TRMM VIRS and Terra and Aqua MODIS data, Part I: Algorithms. *IEEE Trans. Geosci. Remote Sens.*, submitted, 2010. 30, 41, 44, 81, 99

[118] T.Y. Nakajima and M.D. King. Determination of the optical thickness and effective particle radius of clouds from reflected solar radiation measurements. Part I: Theory. *J. Atmos. Sci.*, 47:1878–1893, 1990. 20, 39, 43, 63, 64, 83

[119] T.Y. Nakajima and T. Nakajima. Wide–area determination of cloud micropysical properties from NOAA AVHRR measurements for FIRE and ASTEX regions. *J. Atmos. Sci.*, 52:4043–4059, 1995. 40, 64, 92

[120] S.L. Nasiri and B.A. Baum. Daytime multilayerd cloud detection using multispectral imager data. *J. Atmos. Ocean. Tech.*, 21:1145–1155, 2004. 38

[121] W. O'Hirok and C. Gautier. A three–dimensional radiative transfer model to investigate the solar radiation wihtin a cloudy atmosphere: Part I. Spatial effects. *J. Atmos. Sci.*, 55: 2162–2179, 1998. 29

[122] L. Oreopoulos, R.F. Cahalan, A. Marshak, and G. Wen. A new normalized difference cloud retrieval technique applied to Landsat radiances over the Oklahoma ARM site. *J. Appl. Meteorol.*, 39:2305–2321, 2000. 30

[123] M.J. Pavolonis and A.K. Heidinger. Daytime cloud overlap detection from AVHRR and VIIRS. *J. Appl. Meteorol.*, 43:762–778, 2004. 38

[124] M.J. Pavolonis, A.K. Heidinger, and T. Uttal. Daytime global cloud typing from AVHRR and VIIRS: algorithm description, validation, and comparisons. *J. Appl. Meteorol.*, 44: 804–826, 2005. 36, 38

[125] J.P. Peixoto and A.H. Oort. *Physics of Climate*. American Institute of Physics, New York, NY, 1992. 80

[126] G.W. Petty. *A First Course in Atmospheric Radiation — Second Edition*. Sundog Publishing, Madison, 2006. 7, 13, 15, 24, 34, 132

[127] R. Pincus, M. Szczodrak, J. Gu, and P. Austin. Uncertainty in cloud optical depth estimates made from satellite radiance measurements. *J. Climate*, 8:1453–1462, 1995. 44, 45

[128] S. Platnick. Approximations for horizontal photon transport in cloud remote sensing problems. *J. Quant. Spect. Rad. Trans.*, 68:75–99, 2001. 30

[129] S. Platnick, J.Y. Li, M.D. King, H. Gerber, and P.V. Hobbs. A solar reflectance method for retrieving the optical thickness and droptlet size of liquid water clouds over snow and ice surfaces. *J. Geophys. Res.*, 106:15185–15199, 2001. 42, 99

[130] S.E. Platnick, M.D. King, S.A. Ackerman, W.P. Menzel, B.A. Baum, J.C. Riédi, and R.A. Frey. The MODIS cloud products: Algorithms and examples from Terra. *IEEE Trans. Geosci. Remote Sens.*, 41(2):459–473, 2003. 31, 35, 40, 41, 44, 91, 122, 143

[131] W.H. Press, W.T. Vetterling, S.A. Teukolsky, and B.P. Flannery. *Numerical Recipes in C. The Art of Scientific Computing. Second Edition*. Cambridge University Press, Cambridge, 1992. 65, 76, 93, 101

[132] E. Raschke, T.H. Vonder Haar, W.R. Bandeen, and M. Pasternak. The Annual Radiation Balance of the Earth–Atmosphere System During 1969–70 from Nimbus 3 Measurements. *J. Atmos. Sci.*, 30(3):341–364, 1973. 80

[133] M. Reuter, W. Thomas, P. Albert, M. Lockhoff, R. Weber, K.–G. Karlsson, and J. Fischer. The CM–SAF and FUB cloud detection schemes for SEVIRI: validation with synoptic data and initial comparison with MODIS and CALIPSO. *J. Appl. Meteorol.*, 48:301–316, 2009. doi: 10.1175/2008JAMC1982.1. 28

[134] R.A. Roebeling, A.J. Feijt, and P. Stammes. Cloud property retrievals for climate monitoring: Implications of differences between Spinning Enhanced Visible and Infrared Imager (SEVIRI) on Meteosat–8 and Advanced Very High Resolution Radiometer (AVHRR) on NOAA–17. *J. Geophys. Res.*, 111:D20210, 2006. doi: 10.1029/2005JD006990. 30, 36, 40, 44

[135] J.K. Roskovensky and K.N. Liou. Detection of thin cirrus from 1.38 μm/0.65 μm reflectance ratio combined with the 8.6–11 μm brightness temperature difference. *Geophys. Res. Lett.*, 30(19):1985, 2003. doi: 10.1029/2003GL018135. 37

[136] J.K. Roskovensky and K.N. Liou. Detection of thin cirrus using a combination of 1.38 μm reflectance and window brightness temperature difference. *J. Geophys. Res.*, 108(D18): 4570, 2003. doi: 10.1029/2002JD003346. 37

[137] W.B. Rossow and L.C. Garder. Cloud detection using satellite measurements of infrared and visible radiances for ISCCP. *J. Climate*, 6:2341–2369, 1993. 33, 50, 64, 66, 83, 92

[138] W.B. Rossow and A.A. Lacis. Global, Seasonal Cloud Variations from Satellite Radiance Measurements. Part II: Cloud properties and radiative effects. *J. Climate*, 3(11):1204–1253, 1990. 39, 43

[139] W.B. Rossow and R.A. Schiffer. ISCCP cloud data products. *B. Am. Meteorol. Soc.*, 72: 2–20, 1991. 33, 39

[140] W.B. Rossow and R.A. Schiffer. Advances in Understanding Clouds from ISCCP. *B. Am. Meteorol. Soc.*, 80(11):2261–2288, 1999. 33, 35, 87

[141] W.B. Rossow, L.C. Garder, and A.A. Lacis. Global, Seasonal Cloud Variations from Satellite Radiance Measurements. Part I: Sensitivity of Analysis. *J. Climate*, 2:419–458, 1989. 39, 43, 50, 51, 83

[142] W.B. Rossow, A.W. Walker, D.E. Beuschel, and M.D. Roiter. International Satellite Cloud Climatology Project (ISCCP) Documentation of New Cloud Datasets. Technical Report WMO/TD–No. 737, World Meteorological Organization, Geneva, Switzerland, 1996. 57

[143] K. Saitwal, M.R. Azimi-Sadjadi, and D. Reinke. A multichannel temporally adaptive system for continuous cloud classification from satellite imagery. *IEEE Trans. Geosci. Remote Sens.*, 41(5):1098–1104, 2003. doi: 10.1109/TGRS.2003.813550. 28

[144] R.W. Saunders. An automated scheme for the removal of cloud contamination from AVHRR radiances over western Europe. *Int. J. Remote Sensing*, 7:867–888, 1986. 30, 64, 66, 83

[145] R.W. Saunders and K.T. Kriebel. An improved method for detecting clear sky and cloudy radiances from AVHRR data. *Int. J. Remote Sensing*, 9:123–150, 1988. 31, 37

[146] G. Schaepman–Strub, M.E. Schaepman, T.H. Painter, S. Dangel, and J.V. Martonchik. Reflectance quantities in optical remote sensing—definitions and case studies. *Remote Sens. Environ.*, 103:27–42, 2006. doi: 10.1016/j.rse.2006.03.002. 24

[147] R.A. Schiffer and W.B. Rossow. The International Satellite Cloud Climatology Project (ISCCP): the first project of the World Climate Research Program. *B. Am. Meteorol. Soc.*, 66:1498–1505, 1983. 33, 35

[148] J. Schmetz, P. Pili, S. Tjemkes, D. Just, J. Kerkmann, S. Rota, and A. Ratier. An introduction to Meteosat Second Generation (MSG). *B. Am. Meteorol. Soc.*, 83(7):977–992, 2002. 3, 44, 62, 80

[149] J. Schmetz, P. Pili, S. Tjemkes, D. Just, J. Kerkmann, S. Rota, and A. Ratier. Supplement to An introduction to Meteosat Second Generation (MSG): SEVIRI Calibration. *B. Am. Meteorol. Soc.*, 83(7):992–992, 2002. 91, 126

[150] J.J. Simpson and J.R. Stitt. A procedure for the detection and removal of cloud shadow from AVHRR data over land. *IEEE Trans. Geosci. Remote Sens.*, 36(3):880–897, 1998. 43

[151] J.J. Simpson, T. McIntire, Z. Jin, and J.R. Stitt. Improved cloud top height retrieval under arbitrary viewing and illumination conditions using AVHRR data. *Remote Sens. Environ.*, 72:95–110, 2000. 43

[152] J.J. Simpson, J.R. Stitt, and Z. Jin. Cloud Shadow Detection under Arbitrary Viewing and Illumination Conditions. *IEEE Trans. Geosci. Remote Sens.*, 38(2):972–976, 2000. 43, 59

[153] G.L. Smith. Effects of time response on the point spread function of a scanning radiometer. *Appl. Opt.*, 33:7031–7037, 1994. 73

[154] G.L. Smith, R.N. Green, E. Raschke, L.M. Avis, J.T. Suttles, B.A. Wielicki, and R. Davies. Inversion methods for satellite studies of the Earth's Radiation Budget: development of algorithms for the ERBE mission. *Rev. Geophys.*, 24:407–421, 1986. 2

[155] G.L. Stephens, D.G. Vane, R.J. Boain, G.G. Mace, K. Sassen, Z. Wang, A.J. Illingworth, E.J. O'Connor, W.B. Rossow, S.L. Durden, S.D. Miller, R.T. Austin, A. Benedetti, C. Mitrescu, and The CloudSat Science Team. The CloudSat Mission and the A–Train: A New Dimension of Space-Based Observations of Clouds and Precipitation. *B. Am. Meteorol. Soc.*, 83(12):1771–1790, 2002. 140

[156] L.L. Stowe, P.A. Davis, and E.P. McClain. Scientific basis and initial evaluation of the CLAVR–1 global clear/cloud classification algorithm for the Advanced Very High Resolution Radiometer. *J. Atmos. Ocean. Tech.*, 16:656–681, 1999. 31

[157] K.I. Strabala, S.A. Ackerman, and W.P. Menzel. Cloud properties inferred from 8–12 μm data. *J. Appl. Meteorol.*, 33:212–229, 1994. 35, 143

[158] A. Stuart and K. Ord. *Kendall's Advanced Theory Of Statistics (Volume 1: Distribution Theory) — Sixth Edition*. Wiley, New York, 1994. 127

[159] C.J. Stubenrauch, V. Briand, and W.B. Rossow. The Role of Clear–Sky Identification in the Study of Cloud Radiative Effects: Combined Analysis from ISCCP and the Scanner of Radiation Budget. *J. Appl. Meteorol.*, 41:396–412, 2002. 50

[160] S. Sun-Mack, P. Minnis, Y. Chen, R.F. Arduini, and D.F. Young. Visible clear–sky and near–infrared surface albedos derived from VIRS and MODIS data for CERES. *IEEE Trans. Geosci. Remote Sens.*, submitted, 2008. 32, 41

[161] S. Sun-Mack, P. Minnis, Y. Chen, R.F. Arduini, and D.F. Young. Visible clear–sky and near–infrared surface albedos derived from VIRS and MODIS data for CERES. *IEEE Trans. Geosci. Remote Sens.*, submitted, 2008. 99

[162] J.T. Suttles, R.N. Green, P. Minnis, G.L. Smith, W.F. Staylor, B.A. Wielicki, I.J. Walker, D.F. Young, V.R. Taylor, and L.L. Stowe. Angular radiation models for the earth–atmosphere system. Vol. I: Shortwave radiation. Technical Report RP–1184, NASA, USA, 1988. 53, 62

[163] V.R. Taylor and L.L. Stowe. Reflectance characteristics of uniform earth and cloud surfaces derived from Nimbus 7 ERB. *J. Geophys. Res.*, 89:4987–4996, 1984. 52

[164] S. Theodoridis and K. Koutroumbas. *Pattern Recognition — Fourth Edition*. Academic Press, London, 2009. 126

[165] G.E. Thomas and K. Stamnes. *Radiative Transfer in the Atmosphere and Ocean*. Cambridge University Press, Cambridge, 1999. 7

[166] S.M. Thomas, A.K. Heidinger, and M.J. Pavolonis. Comparison of NOAA's operational AVHRR–derived cloud amount to other satellite–derived climatologies. *J. Climate*, 17: 4805–4822, 2004. 31

[167] K.E Trenberth, J.T. Fasullo, and J. Kiehl. Earth's global energy budget. *B. Am. Meteorol. Soc.*, 90(3):311–323, 2009. 2

[168] S. Twomey and K.J. Seton. Inferences of gross microphysical properties of clouds from spectral reflectance measurements. *J. Atmos. Sci.*, 37:1065–1069, 1980. 39

[169] S.M. Uppala, P.W. Kallberg, A.J. Simmons, U. Andrae, V. Da Costa Bechtold, M. Fiorino, J.K. Gibson, J. Haseler, A. Hernandez, G.A. Kelly, X. Li, K. Onogi, S. Saarinen, N. Sokka, R.P. Allan, E. Andersson, K. Arpe, M.A. Balmaseda, A.C.M. Beljaars, L. van de Berg, J. Bidlot, N. Bormann, S. Caires, F. Chevallier, A. Dethof, M. Dragosavac, M. Fisher, M. Fuentes, S. Hagemann, E. Holm, B.J. Hoskins, L. Isaksen, P.A.E.M. Janssen, R. Jenne, A.P. McNally, J.F. Mahfouf, J.J. Morcrette, N.A. Rayner, R.W. Saunders, P. Simon, A. Sterl, K.E. Trenberth, A. Untch, D. Vasiljevic, P. Viterbo, and J. Woollen. The ERA–40 re–analysis. *Quart. J. R. Meteorol. Soc.*, 131(612):2961–3012, 2005. 126

[170] H.C. van de Hulst. *Multiple Light Scattering: Tables, Formulas and Applications*. Academic Press, New York, 1980. 100

[171] T. Várnai and A. Marshak. Statistical analysis of the uncertainties in cloud optical depth retrievals caused by three–dimensional radiative effects. *J. Atmos. Sci.*, 58:1540–1548, 2001. 46

[172] T. Várnai and A. Marshak. View angle dependence of cloud optical thicknesses retrieved by Moderate Resolution Imaging Spectroradiometer (MODIS). *J. Geophys. Res.*, 112:D06203, 2007. doi: 10.1029/2005JD006912. 47

[173] T. Várnai and A. Marshak. MODIS observations of enhanced clear sky reflectance near clouds. *Geophys. Res. Lett.*, 36:L06807, 2009. doi: 10.1029/2008GL037089. 46

[174] M. Viollier, D. Tanré, and P.Y. Deschamps. An algorithm for remote sensing of water color from space. *Bound. Layer Meteor.*, 18:247–267, 1980. 88

[175] J. Wang, M.R. Azimi-Sadjadi, and D. Reinke. A temporally adaptive classifier for multispectral imagery. *IEEE Trans. Neural Networks*, 15(1):159–165, 2004. doi: 10.1109/TNN.2003.820622. 28

[176] M. Wang and M.D. King. Correction of Rayleigh scattering effects in cloud optical thickness retrievals. *J. Geophys. Res.*, 102(D22):25915–25926, 1997. 42

[177] P.H. Wang, M.P. McCormick, L.R. Poole, W.P. Chu, G.K. Yue, G.S. Kent, and K.M. Skeens. Tropical high cloud characteristics derived from SAGE II extinction measurements. *Atmos. Res.*, 34:53–83, 1994. 37

[178] S.G. Warren. Optical constants of ice from the ultraviolet to the microwave. *Appl. Opt.*, 23:1026–1225, 1984. 18

[179] P.D. Watts, C.T. Mutlow, A.J. Baran, and A.M. Zavody. Study on cloud properties derived from Meteosat Second Generation observations. Technical Report ITT 97/181, EUMETSAT, Darmstadt, Germany, 2001. 30

[180] R.A. Weekley, R.K. Goddrich, and L.B. Cornman. An algorithm for classification and outlier detection of time–series data. *J. Atmos. Ocean. Tech.*, 27:94–107, 2010. doi: 10.1175/2009JTECHA1299.1. 143

[181] B. Wielicki, B.R. Barkstrom, E.F. Harrison, R.B. Lee, G.L. Smith, and J.E. Cooper. Clouds and the Earth's Radiant Energy System (CERES): an earth observing system experiment. *B. Am. Meteorol. Soc.*, 77:853–868, 1996. 83

[182] B.A. Wielicki and L. Parker. On the determination of cloud cover from satellite sensors: the effect of sensor spatial resolution. *J. Geophys. Res.*, 97(D12):12799–12823, 1992. 45

[183] B.A. Wielicki, R.D. Cess, M.D. King, D.A. Randall, and E.F. Harrison. Mission to Planet Earth: role of clouds and radiation in climate. *B. Am. Meteorol. Soc.*, 76(11):2125–2153, 1995. 2

[184] B.A. Wielicki, B.R. Barkstrom, E.F. Harrison, R.B. Lee III, G.L. Smith, and J.E. Cooper. Clouds and the Earth's Radiant Energy System (CERES): An Earth observing system experiment. *B. Am. Meteorol. Soc.*, 77(5):853–868, 1996. 2, 62, 80, 99

[185] B.A. Wielicki, B.R. Barkstrom, B.A. Baum, T.P. Charlock, R.N. Green, D.P. Kratz, R.B. Lee III, P. Minnis, G.L. Smith, T. Wong, D.F. Young, R.D. Cess, J.A. Coakley Jr., D.A.H. Crommelynck, L. Donner, R. Kandel, M.D. King, A.J. Miller, V. Ramanathan, D.A. Randall, L.L. Stowe, and R.M. Welch. Clouds and the Earth's Radiant Energy Systems (CERES): Algorithm Overview. *IEEE Trans. Geosci. Remote Sens.*, 36(4):1127–1141, 1998. 80, 99

[186] E.M. Wilcox, Harshvardhan, and S. Platnick. Estimate of the impact of aborbing aerosol over cloud on the MODIS retrievals of cloud optical thickness and effective radius using two independent retrievals of liquid water path. *J. Geophys. Res.*, 114:D05210, 2009. doi: 10.1029/2008JD010589. 43

[187] R.C. Willson, H. Hudson, and M. Woodard. The inconstant solar constant. *Sky and Telescope*, 67:501–503, 1984. 1

[188] W.J. Wiscombe. Improved Mie scattering algorithms. *Appl. Opt.*, 19:1505–1509, 1980. 17, 19

[189] E. Wolters, R. Roebeling, and A. Feijt. Quantitative assessment of cloud phase determination from SEVIRI using ground-based cloud radar and lidar. In *Proc. EUMETSAT Meteorological Satellite Conference*, volume P.48, Helsinki, Finland, 2006. 91

[190] E.L.A. Wolters, R.A. Roebeling, and A.J. Feijt. Evaluation of cloud–phase retrieval methods for SEVIRI on Meteosat–8 using ground–based lidar and cloud radar data. *Int. J. Remote Sensing*, 47:1723–1738, 2008. doi: 10.1175/2007JAMC1591.1. 35, 36, 41, 110, 143

[191] K. Wyser, W. O'Hirok, C. Gautier, and C. Jones. Remote sensing of surface solar irradiance with corrections for 3–D cloud effects. *Remote Sens. Environ.*, 80:272–284, 2002. 30, 63

[192] P. Yang, H. Wei, H.L. Huang, B.A. Baum, Y.X. Hu, M.I. Mishchenko, and Q. Fu. Scattering and absorption property database of various nonspherical ice particles in the infrared and far-infrared spectral region. *Appl. Opt.*, 44:5512–5523, 2005. 17, 19

[193] Y. Yang and L. Di Girolamo. Impacts of 3–D radiative effects on satellite cloud detection and their consequences on cloud fraction and aerosol optical depth retrievals. *J. Geophys. Res.*, 113:D04213, 2008. doi: 10.1029/2007JD009095. 29, 46

List of publications

Peer–reviewed journals

[1] C. Bertrand, N. Clerbaux, **A. Ipe**, and L. Gonzalez. Estimation of the 2002 Mount Etna eruption cloud radiative forcing from Meteosat–7 data. *Remote Sens. Environ.*, 87(2-3): 257–272, 2003.

[2] C. Bertrand, N. Clerbaux, **A. Ipe**, and L. Gonzalez. Corrigendium to Estimation of the 2002 Mount Etna eruption cloud radiative forcing from Meteosat–7 data. *Remote Sens. Environ.*, 90(1):135, 2004.

[3] C. Bertrand, N. Clerbaux, **A. Ipe**, S. Dewitte, and L. Gonzalez. Angular distribution models anisotropic correction factors and mixed clear scene types: a sensitivity study. *IEEE Trans. Geosci. Remote Sens.*, 43(1):92–102, 2005.

[4] C. Bertrand, N. Clerbaux, **A. Ipe**, S. Dewitte, and L. Gonzalez. Angular distribution models anisotropic correction factors and sun glint: a sensitivity study. *Int. J. Remote Sensing*, 27(9):1741–1757, 2006.

[5] C. Bertrand, J. Futyan, **A. Ipe**, L. Gonzalez, and N. Clerbaux. Diurnal asymmetry in the GERB SW Fluxes. *IEEE Trans. Geosci. Remote Sens.*, 44(12):3585–3600, 2006.

[6] C. Bertrand, L. Gonzalez, **A. Ipe**, and N. Clerbaux. Improvement in the GERB short wave flux estimations over snow covered surfaces. *Adv. Space Res.*, 41(7):1894–1905, 2008.

[7] N.J. Cerf, **A. Ipe**, and X. Rottenberg. Cloning of Continuous Quantum Variables. *Phys. Rev. Lett.*, 85(8):1754–1757, 2000. ISSN 0031–9007.

[8] N. Clerbaux, S. Dewitte, L. Gonzalez, C. Bertand, B. Nicula, and **A. Ipe**. Outgoing Longwave Flux Estimation: Improvement of Angular Modelling Using Spectral Information. *Remote Sens. Environ.*, 85:389–395, 2003.

[9] N. Clerbaux, **A. Ipe**, C. Bertrand, Dewitte S., B. Nicula, and L. Gonzalez. Evidence of Azimuthal Anisotropy for the Thermal Infrared Radiation Leaving the Earth's Atmosphere. *Int. J. Remote Sensing*, 24:3005–3010, 2003.

[10] N. Clerbaux, S. Dewitte, C. Bertrand, D. Caprion, De Paepe B., L. Gonzalez, **A. Ipe**, and J. Russell. Unfiltering of the Geostanionnary Earth Radiation Budget (GERB) data. Part I: Shortwave Radiation. *J. Atmos. Ocean. Tech.*, 25(7):1087–1105, 2008.

[11] N. Clerbaux, S. Dewitte, C. Bertrand, D. Caprion, De Paepe B., L. Gonzalez, **A. Ipe**, and J. Russell. Unfiltering of the Geostanionnary Earth Radiation Budget (GERB) data. Part II: Longwave Radiation. *J. Atmos. Ocean. Tech.*, 25(7):1106–1117, 2008.

[12] N. Clerbaux, J.E. Russell, S. Dewitte, C. Bertrand, D. Caprion, B. De Paepe, L. Gonzalez Sotelino, **A. Ipe**, R. Bantges, and H.E. Brindley. Comparison of GERB instantaneous radiance and flux products with CERES Edition–2 data. *Remote Sens. Environ.*, 113(1): 102–114, 2009.

[13] B. De Paepe, A. Ignatov, S. Dewitte, and **A. Ipe**. Aerosol retrieval over ocean from SEVIRI for the use in GERB's Earth radiation budget analysis. *Remote Sens. Environ.*, 112:2455–2468, 2008.

[14] S. Dewitte, L. Gonzalez, N. Clerbaux, **A. Ipe**, C. Bertrand, and B. De Paepe. The Geostationary Earth Radiation Budget Edition 1 data processing algorithms. *Adv. Space Res.*, 41 (11):1906–1913, 2008.

[15] J. E. Harries, J. E. Russell, J. A. Hanafin, H. Brindley, J. Futyan, J. Rufus, S. Kellock, G. Matthews, R. Wrigley, A. Last, J. Mueller, R. Mossavati, J. Ashmall, E. Sawyer, D. Parker, M. Caldwell, P. M. Allan, A. Smith, M. J. Bates, B. Coan, B. C. Stewart, D. R. Lepine, L. A. Cornwall, D. R. Corney, M. J. Ricketts, D. Drummond, D. Smart, R. Cutler, S. Dewitte, N. Clerbaux, L. Gonzalez, **A. Ipe**, C. Bertrand, A. Joukoff, D. Crommelynck, N. Nelms, D. T. Llewellyn-Jones, G. Butcher, G. L. Smith, Z. P. Szewczyk, P. E. Mlynczak, A. Slingo, R. P. Allan, and M. A. Ringer. The Geostationary Earth Radiation Budget Project. *B. Am. Meteorol. Soc.*, 86(7):945–960, 2005.

[16] **A. Ipe**, N. Clerbaux, C. Bertrand, Dewitte S., and L. Gonzalez. Pixel–scale composite TOA clear–sky reflectances for Meteosat–7 visible data. *J. Geophys. Res.*, 108(D19):4612–4612, 2003.

[17] **A. Ipe**, N. Clerbaux, C. Bertrand, Dewitte S., and L. Gonzalez. Validation and homogenisation of cloud optical depth and cloud fraction retrievals for GERB/SEVIRI scene identification using Meteosat–7 data. *Atmos. Res.*, 72:17–37, 2004.

[18] **A. Ipe**, C. Bertrand, N. Clerbaux, Dewitte S., and L. Gonzalez. The GERB Edition 1 products SEVIRI scene identification – Part I: Methodology. *IEEE Trans. Geosci. Remote Sens.*, submitted, 2010.

[19] **A. Ipe**, C. Bertrand, N. Clerbaux, Dewitte S., and L. Gonzalez. The GERB Edition 1 products SEVIRI scene identification – Part II: Validation. *IEEE Trans. Geosci. Remote Sens.*, submitted, 2010.

[20] **A. Ipe**, L. Gonzalez Sotelino, C. Bertrand, E. Baudrez, N. Clerbaux, I. Decoster, S. Dewitte, S. Nevens, and A. Velazquez Blazquez. Cloud detection using IR SEVIRI channels for GERB. *Remote Sens. Environ.*, submitted, 2010.

Conference proceedings

[1] **A. Ipe**, C. Bertrand, N. Clerbaux, S. Dewitte, L. Gonzalez, and B. Nicula. Validation and homogenization of cloud properties retrievals for RMIB GERB/SEVIRI scene identification. In *Proc. SPIE Europe Remote Sens.*, volume 4882, Crete, Greece, 2002.

[2] **A. Ipe**, C. Bertrand, D. Caprion, N. Clerbaux, S. Dewitte, and L. Gonzalez. Pixel–based composite TOA clearsky reflectances for SEVIRI visible images. In *Proc. EUMETSAT Meteorological Satellite Data Users' Conference*, volume P.46, Dubrovnik, Croatia, 2005.

[3] **A. Ipe**, C. Bertrand, N. Clerbaux, S. Dewitte, and L. Gonzalez. The GERB Edition 1 products SEVIRI scene identification. In *Proc. SPIE Europe Remote Sens.*, volume 6745, Florence, Italy, 2007.